THESE POUR OBTENIR LE GRADE DE DOCTEUR DE L'ECOLE NATIONALE SUPERIEURE DE CHIMIE DE MONTPELLIER

En Chimie et Physico Chimie des Matériaux

École doctorale Sciences Chimiques Balard

Unité de recherche Ingénierie et Architectures Macromoléculaires (IAM)

Développement de nanocomposites $BaTiO_3$ @ polymère fluoré pour les matériaux diélectriques et comme liant de cathode dans les batteries lithium

Présentée par **Fatima Ezzahra BOUHARRAS**
Le 21 Juillet 2020

Sous la direction de **Mustapha RAIHANE**
et **Bruno AMEDURI**

Devant le jury composé de

Hamid KEDDAMI, Professeur, UCAM	Président et Rapporteur
Cristina IOJOIU, Directrice de Recherche, Grenoble INP	Rapporteur
Valter CASTELVETRO, Professeur, Univ. de Pise-Italie	Rapporteur
Vasile HULEA, Professeur, ENSCM	Examinateur
Mourad AROUS, Professeur, Université Sfax-Tunisie	Examinateur
Nicolas LOUVAIN, Maitre de conférences, Univ. de Montpellier	Examinateur
Mustapha RAIHANE, Professeur, UCAM	Directeur de thèse
Bruno AMEDURI, Directeur de Recherche, ENSCM	Directeur de thèse

Presentation of Thesis

Name and surname of author: BOUHARRAS Fatima Ezzahra

Title: "*Development of $BaTiO_3$@fluorinated polymer nanocomposites for dielectric materials and as a binder of cathode in Lithium Battery*".

Supervisor:

- **Name, surname and grade** : RAIHANE Mustapha, PES C
- **Laboratory an institution**: Laboratoire de la Chimie Organométallique et Macromoléculaire-Matériaux Composites (LCO2MC); Faculty of Sciences and Technologies of Marrakesh; cadi Ayyad University; Marrakesh-Morocco.

Co-Supervisor:

- **Name, surname and grade** : AMEDURI Bruno
- **Laboratory and institution** : Institut Charles Gerhardt de Montpellier, Ecole Nationale Supérieure de Chimie ; Montpellier-France.

This thesis work has been realized in:

- Laboratoire de la Chimie Organométallique et Macromoléculaire-Matériaux Composites ; Faculté des Sciences et Techniques de Marrakech (Morocco).
- Institut Charles Gerhardt de Montpellier, Ecole Nationale Supérieure de Chimie de Montpellier (France).
- Physics Department, University of Pisa (Italy).

Period of the thesis work: 2016-2020

Support and frameworks:

- Centre National pour la Recherche Scientifique et Technique (CNRST) (7UCA2016).
- Moroccan Ministry of High Education and Research Activities (MESRSFC) in the framework of *Centre d'Etudes Doctorales* (CEDoc) project.

- The European Credit Mobility Erasmus+ Ka107 (Physics Department, Pisa University: spring semester, 2019).

Articles in peer-reviewed journals:

1- **Fatima Ezzahra BOUHARRAS**, Mustapha RAIHANE, Gilles SILLY, Cedric Totee and Bruno AMEDURI; Core shell structured Poly(Vinylidene Fluoride) -*grafted*- $BaTiO_3$ nanocomposites prepared via Reversible Addition-fragmentation chain transfer (RAFT) polymerization of VDF for high energy storage capacitors, *Polymer Chemistry*, **2019**,10, 891-904.

2- **Fatima Ezzahra BOUHARRAS**, Mustapha RAIHANE, and Bruno AMEDURI; Recent Progress on Core-Shell Structured $BaTiO_3$/Fluorinated Polymers Nanocomposites for High Energy Storage: Synthesis, Dielectric properties and Applications; *Progress in Materials Science*, 113, **2020**, 100670.

Articles in progress:

1- **Fatima Ezzahra BOUHARRAS,** Mustapha RAIHANE, Nicolas LOUVAIN, Mohamed BACCOUR and Bruno AMEDURI; Evaluation of core–shell poly(vinylidene fluoride)-grafted-Barium titanate (PVDF-g-$BaTiO_3$) nanocomposites as a cathode binder in batteries (submitted to Solid State Ionics Journal).

2- **Fatima Ezzahra BOUHARRAS,** Simone CAPACCIOLI, Massimiliano LABARDI, Mustapha RAIHANE, Abdelghani HAJLANE and Bruno AMEDURI; Synthesis and characterizations of core double shell structured nanocomposite based on Polyvinylidene fluoride-grafted-$BaTiO_3$/P(VDF-HFP) films (to be submitted).

3- **Fatima Ezzahra BOUHARRAS,** Massimiliano LABARDI, Simone CAPACCIOLI, Mustapha RAIHANE, Bruno AMEDURI; Dielectric characterization of core-shell structured Poly(Vinylidene Fluoride) -grafted- $BaTiO_3$ nanocomposites (to be submitted).

4- **Fatima Ezzahra BOUHARRAS**, Mustapha RAIHANE, and Bruno AMEDURI; Chapter 2: Recent Advances in Vinylidene fluoride copolymers and their applications as nanomaterials. In-Engineered Polymer Nanocomposites for Energy Harvesting Applications**;** Elsevier.

Communications:

1- Mustapha RAIHANE, **Fatima Ezzahra BOUHARRAS**, Gilles SILLY, Bruno AMEDURI; *$BaTiO_3$/PVDF Nanocomposites from RAFT & Click Chemistry* ; Fluoropolymer 2018 Conference; June 24-27, 2018; Denver, Colorado, USA.

2- Mustapha RAIHANE, **Fatima Ezzahra BOUHARRAS**, Mohammed LAHCINI, Gilles Silly, Cedric TOTEE, Bruno AMEDURI, *Core shell structured Poly(vinylidene fluoride)-grafted-*$BaTiO_3$*/ nanocomposites prepared via RAFT polymerization of VDF for high energy storage capacitors*; European Polymer Congress; Crête (Greece); June 9-14, 2019.

3- **Fatima Ezzahra BOUHARRAS**, Mustapha RAIHANE, Gilles SILLY, Cedric Totee and Bruno AMEDURI; *Nanocomposites core shell PVDF-g-*$BaTiO_3$ *synthétisé par la polymérisation radicalaire contrôlée par transfert de chaîne réversible par addition-fragmentation,* 47ème journées d'études des polymères du Groupe Français d'études et d'applications des Polymères, from 29 Septembre to 4 Octobre 2019, Bordeaux.

Abstract

Nanocomposite materials present unique physico-chemical properties that cannot be obtained using one component. Thus, the improvement in the properties of such materials have resulted in major interest for versatile fields. Dielectric nanocomposite materials with high energy density exhibit promising performances for energy storage applications. Major efforts have been conducted to combine the efficient properties and high dielectric constant of ceramics with the flexibility and easy processing of polymers. Thus, this thesis focuses on the development and characterizations of nanocomposites based on $BaTiO_3$ ceramic and fluoropolymers. First, the synthesis of PVDF-*g*-$BaTiO_3$ was realized using RAFT polymerization of VDF from the surface of functionalized nanoparticles, using different $BaTiO_3$ concentrations, and the effect of such percentage on the final properties was studied. Results showed the successful grafting of PVDF leading to nanocomposites with enhanced thermal stability. Furthermore, the successful grafting of PVDF onto the functionalized nanoparticles was mainly proved by HRMAS NMR spectroscopy, which was used for the first time to characterize the prepared nanocomposites. The dielectric properties of such materials were investigated, and reveals the existence of three relaxations: the first one was attributed to the well-known β secondary relaxation in PVDF, the second one was assigned to the crystalline fraction in the polymer, while the third relaxation was assigned to interfacial polarization arising from the presence of fillers and impurities in the system. However, the relaxation related to glass transition temperature could not be observed due to the high crystallinity of the polymer. Solution blending strategy was also used to prepare nanocomposite materials consisting of PVDF-*g*-$BaTiO_3$/P(VDF-*co*-HFP) and the prepared films were fully characterized. The uniform distribution of PVDF-*g*-$BaTiO_3$ nanocomposites in the copolymer matrix leads to enhanced mechanical performances resulting in increased Young's modulus. Then, to supply an application for the prepared PVDF-*g*-$BaTiO_3$ nanocomposites, those later were used as binder to prepare cathode material for batteries. Calendering procedure was used to prepare the electrode films and enabled to obtain uniform structure and enhanced cycling performances.

Keywords: Barium titanate, fluoropolymers, PVDF, dielectric constant, grafting, polymerizations, batteries.

Résumé

Les matériaux nanocomposites présentent des propriétés physico-chimiques uniques qui ne peuvent être obtenues en utilisant un seul composant. Ainsi, l'amélioration des propriétés de ces matériaux a suscité un intérêt majeur dans différents domaines. Les matériaux nanocomposites diélectriques à haute densité d'énergie présentent des performances prometteuses pour les applications de stockage d'énergie. Des efforts importants ont été menés pour combiner la constante diélectrique élevée de la céramique avec la flexibilité et la facilité de mise en œuvre des polymères. Ainsi, cette thèse porte sur le développement et la caractérisation de nanocomposites à base de céramique $BaTiO_3$ et de polymères fluorés. Dans un premier temps, la synthèse de PVDF-*g*-$BaTiO_3$ a été réalisée en utilisant la polymérisation RAFT du VDF à partir de la surface des nanoparticules fonctionnalisées, en utilisant différentes concentrations en $BaTiO_3$, et l'effet de ce pourcentage sur les propriétés finales a été étudié. Les résultats ont montré que le greffage du PVDF a été réalisé avec succès, conduisant à des nanocomposites avec une stabilité thermique améliorée. De plus, le succès du greffage du PVDF a été principalement prouvé par la spectroscopie RMN HRMAS, qui a été utilisée pour la première fois pour caractériser les nanocomposites préparés. Les propriétés diélectriques de ces matériaux ont été étudiés et révèlent l'existence de trois relaxations : la première a été attribué à la relaxation secondaire β dans le PVDF, la seconde a été liée à la fraction cristalline dans le polymère, tandis que la troisième relaxation a été attribué à la polarisation interfaciale résultant de la présence de charges et d'impuretés dans le système. Cependant, la relaxation liée à la température de transition vitreuse n'a pas pu être observé en raison de la cristallinité élevée du polymère. Le procédé de mélange en solution a été également utilisé pour préparer des matériaux nanocomposites constitués de PVDF-*g*-$BaTiO_3$/P(VDF-*co*-HFP) et les films préparés ont été entièrement caractérisés. La dispersion uniforme des nanocomposites PVDF-*g*-$BaTiO_3$ dans la matrice de copolymère a conduit à des performances mécaniques améliorées. Ensuite, pour fournir une application pour les nanocomposites PVDF-*g*-$BaTiO_3$ préparés, ces derniers ont été utilisés comme liant pour préparer un matériau de cathode pour les batteries. La procédure de calandrage a été utilisée pour préparer les films d'électrode et a permis d'obtenir une structure uniforme et des performances de cyclage améliorées.

Mots clés : Titanates de barium, polymères fluorés, PVDF, constante diélectrique, greffage, polymérisations, batteries.

ملخص

تتميز المواد المركبة النانوية بخواص فيزيائية-كيميائية فريدة، لا يمكن الحصول عليها بمكون واحد. وبالتالي، فإن التحسين من خصائص هذه المواد يدفع إلى اهتمام كبير في عدة مجالات. تتصف المواد العازلة للكهرباء ذات الكثافة العالية من الطاقة بأداء واعد في مجال تخزين الطاقة، بحيث بذلت جهود كبيرة للجمع بين ثابت العزل العالي للسيراميك وكذلك المرونة وسهولة المعالجة للبوليمرات.

وبالتالي، تركز هذ الأطروحة على تطوير مواد مركبة نانوية باستخدام السيراميك $BaTiO_3$ و البوليميرات الفلورية. أولا، تم تطوير مواد مركبة $PVDF\text{-}g\text{-}BaTiO_3$ باستعمال بلمرة RAFT للمونومير VDF من سطح الجسيمات الوظيفية النانوية، باستخدام تركيزات مختلفة من $BaTiO_3$ ، و قد تمت دراسة تأثير هذه النسب على الخواص النهائية. أظهرت النتائج أن عملية إقحام PVDF قد أثبت بشكل أساسي من خلال تقنية HRMAS NMR، التي استخدمت لأول مرة لتحليل هذه المواد. تمت كذلك دراسة الخواص العازلة، وكشفت عن وجود ثلاثة استرخاءات، بحيث أن الاسترخاء الأول يعود إلى الاسترخاء الثانوي في PVDF، بينما يعزى الثاني للجزء البلوري في البوليمير، والأخير يعود عن الاستقطاب البيني الناتج عن وجود مواد وشوائب في النظام. في حين أنه لم يتم ملاحظة الاسترخاء المتعلق بدرجة انتقال الزجاج بسبب التبلور العالي للبوليمير.

لقد تم استخدام تقنية ''Solution blending'' لتحضير مواد مركبة نانوية مصنوعة من المركبات النانوية $PVDF\text{-}g\text{-}BaTiO_3$ المدمجة ضمن الكوبوليمير P(VDF-*co*-HFP) . أدى التشتت الموحد للمركبات النانوية $PVDF\text{-}g\text{-}BaTiO_3$ في الكوبوليمير إلى تحسين الأداء الميكانيكي. لتوفير تطبيق للمواد النانوية المعدة، تم استخدامها كرابط لإعداد مادة الكاثود في البطاريات. ثم كذلك استخدام تقنية التقويم لإعداد مواد ذو بنية موحدة وتحسين أداء وفعالية البطاريات.

الكلمات المفتاحية: ثيتانات الباريوم، البوليميرات المفلورة، ثابت العزل الكهربائي، إقحام، البلمرة، البطاريات

Acknowledgements

This join thesis was conducted in collaboration with four teams: “Laboratory of Organometallic and Macromolecular chemistry-Composite Materials (LCO2MC) of Cadi Ayyad University in Morocco, “Ingénierie et Architectures Macromoléculaires (IAM)” and “Aggrégats, Interfaces et Matériaux pour l’énergie (AIME)” teams of the Institut Charles Gerhardt (ICGM) in France and “Physics Department” of University of Pisa in Italy.

Financial support was provided by the French Government (Campus France Maroc), *Centre National pour la Recherche Scientifique et Technique* in Morocco (CNRST (7UCA2016)), Moroccan Ministry of High Education and Research Activities (MESRSFC) in the framework of *Centre d’Etudes Doctorales* (CEDoc) project and the European Credit Mobility Erasmus+ Ka107 (Physics Department, Pisa University: spring semester, 2019).

First and foremost, I would like to thank my mentors, **Mustapha RAIHANE** and **Bruno AMEDURI** for their guidance, expertise, valuable advices and immense knowledge that made it possible for me to work on such topic. Thank you for providing me the opportunity of working not only in your groups, but also the chance to collaborate with other researcher groups as well.

I would like to thank professors **Simone CAPACCIOLI** and **Massimiliano LABARDI** for providing me the opportunity to work in their research group and for instructing me to Broadband dielectric spectroscopy.

A special thank is also addressed to Professor **Nicolas LOUVAIN** for giving me the chance to work in the AIME team. Thank you for sharing your knowledge and experience with me; it has been an honor and a great pleasure to work with you.

A huge gratitude to **Claire NEGRELL** for instructing me on the various machines at IAM team. I would also like to thank **Gilles SILLY** and **Cédric TOTEE** for their assistance in HRMAS NMR spectroscopy.

A great thank to my teammates from LCO2MC laboratory: **Oumayma JENNAH**, **Asma SOFYANE**, **Taha EL ASSIMI**, **Abdelmalek BRIK**, **Abderrahmane NABGUI**, **Ismail ADOUMAZ**, **Jamal CHABBI** and **Nouaamane El IDRISSI**.

I would also like to thank my colleagues from IAM team: **Maxime COLPAERT**, **Qizhi YANG**, **Roberto MORALES**, **Marc-Adrien TRONCHE**, **Gérald LOPEZ**, **Mohammed WEHBI**, **Panagiotis FALIREAS**, **Fernando REIS DA CUNHA**, **Enrique FOLGADO**, **Nadim EID**, **Benoit BRIOU**, **Isaac SHIN** and **Hiroki FUKUMOTO**.

I would like to thank all the members of AIME team for the direct and indirect help during my stay. A special knowledge to **Julien FULLENWARTH**, **Sanghoon KIM** and **Mohamed BACCOUR** for instructing and help on the various equipment and machines.

I am extremely grateful to **Soukaina AJOUGUIM**, **Samira MOUKANNAA**, **Ouafa MOUJAHID**, **Meriem LATIFI**, **Ilyasse IZANZAR** and **Imad MARFOUQ**, for being the best friends and both listening and given energy. Thank you all for your support and encouragement, well before starting my PhD.

I associate my thanks also to **Imane MOUMENE**, **Hend AMRAOUI** and **Denada ARIFAJ** for the unforgettable memories in Pisa.

In the end, I would like to thank my brothers **Mourad, Rida** and **Ahmed** who have always supported, helped and encouraged me. A special thank is also addressed to all **BOUHARRAS** and **MEZRIOUI**'s cousins and family.

Finally, I want to express my deepest thanks to my mother **Touria MEZRIOUI** and my deceased father **Abdelaziz BOUHARRAS**. Thank you for instilling in me the basic values of life and giving me every chance to succeed. Your love carry me and guide me every day. No words can express the love, esteem and respect that I have had always for you.

To my parents,

This work is the fruit of your sacrifices that you have made for my education and training.

Index

List of Figures

Chapter I:

Chapter II:

Chapter III:

Chapter IV:

Chapter V:

Chapter VI:

List of Schemes

Chapter I

Chapter II:

Chapter III:

List of Tables

Chapter I:

Chapter III:

Chapter IV:

Chapter V:

Chapter VI:

List of abbreviations and acronyms

ATRP: Atom transfer radical polymerization

BT: Barium titanate

C2: Phthalic acid

CSPE: Composite solid polymer electrolyte

CTFE: Chlorotrifluoroethylene

CFE: Chlorofluoroethylene

F3C2: 4-(trifluoromethyl)phthalic acid

F4C: 2,3,4,5-tetrafluorobenzoic acid

F4C2: Tetrafluorophthalic acid

P5F: Poly{2,5-bis[(2,3,4,5,6-pentafluoro) oxycarbonyl]styrene}

P7F or PM7F: Poly{2,5-bis[(2,3,5,6-tetrafluoro-4-trifluoromethyl)oxycarbonyl]styrene}

PAC : Sodium polyacrylate

PGMA : Poly(glycidyl methacrylate)

PHEMA : Poly(2-hydroxylethyl methacrylate)

PHFDA : Poly(1H,1H,2H,2H-heptadecafluorodecyl acrylate)

PMMA : Poly(methyl methacrylate)

PTFEMA : Poly(2,2,2,trifluoroethyl methacrylate)

PTFMPCS or P3F: Poly{2,5-bis[(4- trifluoromethoxyphenyl)oxycarbonyl]styrene}

RAFT: Reversible addition fragmentation chain transfer agent

SPE: Solid polymer electrolyte

TrFE: Trifluoroethylene

VDF: Vinylidene fluoride

ε: Dielectric permittivity

General Introduction

Dielectric materials with high dielectric constants have attracted significant attention in the recent years due to their wide range of potential applications in electronic industry, such as multilayer, embedded, and high energy density capacitors [1–7]. The energy density, U_e, characterizing the storage capacity of dielectric materials, can be defined as $U_e=1/2\varepsilon\varepsilon_0 E_b^2$, where E_b, ε and ε_0 are the electric breakdown strength, the dielectric constant and the vacuum dielectric constant of the materials, respectively [4,6–8]. Therefore, the energy density can be enhanced either by increasing the dielectric constant or increasing the electric breakdown strength of the materials.

High dielectric constant can be obtained from the traditional ceramic materials such as $BaTiO_3$ (BT). However, they generally suffer from relatively low breakdown strength and processing issues. On the other hand, polymers have numerous merits (*e.g.,* high electric breakdown strength, low dielectric loss, flexibility, easy processing, and low cost) for dielectric applications, but the low dielectric constant (*e.g.*, < 5-11) limits their applications in the next generation of energy storage devices [9]. Combining the advantages of ceramics and polymers namely preparing high dielectric constant ceramics-based polymer nanocomposites has been used as a strategy to prepare high energy density materials [2,6,7,10]. In fact, the unique physicochemical properties (*e.g.,* large surface energy) of nanoparticles inevitably cause aggregation and inhomogeneity in the polymer matrix [11], particularly in the case of high nanoparticle loading. It has been well recognized that the aggregation of nanoparticles gives a rise to electron conduction for a high dielectric loss, very low breakdown strength and undesirable porosity and voids resulting in deteriorated electrical properties in polymer nanocomposites [12]. Typical challenges include the realization of homogeneous nanoparticle dispersions and the tailoring of polymer/nanoparticle interfaces. Therefore, their surface modification and functionalization, including coupling agents or flexible polymers [13–20], are powerful tools to enhance the nanoparticles-polymer compatibility, resulting in homogeneous dispersion of nanoparticles and thus significantly enhanced the energy density of the resulting nanocomposites.

Ferroelectric fluorinated polymers [*e,g.,* poly(vinylidene fluoride), PVDF] based nanocomposites have received much attention for high tech applications such as high energy density materials because of their high dielectric constants (~10 at 1 kHz) [6,7,21–27]. Despite having many potential benefits, the final properties of these nanocomposites are closely associated with the material processing methods. Conventional synthesis methods (*e.g.,* simple mechanical blending [28] and solution mixing [13]) result in undesirable electric properties (*e.g.,* decreased breakdown strength). Many studies have been devoted to the preparation and dielectric properties of the nanocomposites comprised of PVDF-based polymers with different surfaces modified $BaTiO_3$ nanoparticles [16,29–36]. Prateek *et al.* [5] comprehensively reviewed the use of ferroelectric PVDF binary/ ternary copolymers (*e.g*., poly(VDF-*co*-hexafluoropropylene) P(VDF-HFP), poly(VDF-*co*-trifluoroethylene) P(VDF-TrFE), poly(VDF-*co*-chlorotrifluoroethylene) P(VDF-CTFE) and P(VDF-TrFE-CTFE) terpolymer)/$BaTiO_3$ nanoparticles as potential components in dielectric nanocomposite materials for high energy density capacitor applications. However, VDF based-copolymers are generally immiscible with most organic and inorganic materials because of the low surface energy of the fluoropolymers, and the traditional strategies (*e.g.,* solution mixing) used for the nanoparticles modification by hydrocarbon modifier still lead to filler agglomeration and voids within the final nanocomposite even with high BT loadings [37].

To overcome this disadvantage, surface functionalization of $BaTiO_3$ nanoparticles with fluorinated coupling agents (*e.g.,* perfluoroalkylsilane [16], fluoro phthalic acid [32,38]), and fluorinated polymers (*i.e.,* poly(2,2,2-trifluoroethyl methacrylate) [39], poly(1H,1H,2H,2H-perfluorooctyl methacrylate) [40], poly(2,2,2-trifluoroethyl acrylate) and poly(1H,1H,2H,2H-hepta decafluorodecyl acrylate) [41] and poly(2,5-bis[(4-trifluoromethoxyphenyl)oxycarbonyl] styrene) [4]), have been used to enhance the interface fluorinated modifiers/ PVDF-based polymers using blending solution. However, these methods, even if the interaction forces between PVDF polymers and fluorinated modified BT are stronger than the non-fluorinated ones, still have some limitations in realizing the full potential of high permittivity polymer nanocomposites because the modifiers themselves usually do not play a significant role in the property enhancement energy storage of the nanocomposites [2].

To realize the full potential of nanoparticles to enhance the properties of polymer nanocomposites, significant efforts have recently been devoted to the design and synthesis of core–shell polymer/nanoparticles. More recently, the preparation of structured core-shell high dielectric constant nanoparticles by surface initiated *in-situ* controlled radical polymerization (or RDRP) such as atom transfer radical polymerization (ATRP) [39,42], and reversible addition-fragmentation chain transfer (RAFT) [4,43,44] polymerization received much interest via the "*grafting from*" technique [2,40–42]. Comparatively to conventional methods, this technique provides many advantages such as : (i) the polymer shell layers coated on the nanoparticle surfaces are robustly bonded on the nanoparticle surfaces (by chemical bonds), resulting in a strong nanoparticle/matrix interface and preventing nanoparticle aggregation; (ii) the nanocomposites can be directly achieved from core–shell nanoparticles using the shell layer as a matrix, which allows the preparation of high quality, highly filled nanocomposites (*e.g.,* free of defects, such as voids and pores [12]). In addition, the nanoparticle concentration can be adjusted by tuning the monomer/ initiator functionalized nanoparticles feed ratio. Thus, the objective of this thesis work is the synthesis and characterization of well-structured nanocomposites based on $BaTiO_3$ ceramics embedded within a fluoropolymer matrix for energy storage applications.

To provide an overview of each chapter that follow, chapter 1 is a general state of art, which updates various strategies to design $BaTiO_3$-fluoropolymer nanocomposites. It describes also the synthesis and properties of $BaTiO_3$ and fluoropolymers, highlights the importance of the surface treatment of nanoparticles by fluorinated agents or polymers, and then reports surveys on the applications of such materials.

Chapter 2 describes in detail protocols used to obtain F-polymer-*grafted*-$BaTiO_3$ nanocomposites and the instrumental techniques used to characterize the different prepared materials.

Chapter 3 deals with the synthesis of a nanocomposite materials based on PVDF grafted onto functionalized $BaTiO_3$ using the reversible addition fragmentation chain transfer polymerization (RAFT) of VDF. It demonstrates also the different analyses that enables to prove the successful grafting of PVDF onto the ceramic nanoparticles, namely with ^{1}H and ^{19}F HRMAS-NMR spectroscopy which was used for the first time to characterize such nanocomposites.

Chapter 4 displays a detail study on the dielectric properties of the prepared nanocomposites using broadband dielectric spectroscopy, which is considered as a sensitive technique to study the structural properties in polymeric systems. It describes the main relaxations observed for the pure PVDF as well as for the prepared nanocomposites and study the effect of addition of such ceramic nanoparticles on the final properties.

Chapter 5 exposes the preparation of a core double shell system consisting of PVDF-*grafted*-$BaTiO_3$ embedded within a poly(VDF-*co*-HFP) copolymer using a solution blending method. The designed films are fully characterized using spectroscopic, thermal and morphological analyses. Dielectric and mechanical properties are also investigated.

Chapter 6 deals with the application of the PVDF-*grafted*-$BaTiO_3$ nanocomposites as a binder to prepare cathode material in batteries. The effect of calendering process on the electrochemical performances is also explored.

Finally, the Conclusion summaries all the results obtained during this thesis and the perspectives consist on the future works regarding the enhancement of the different properties and other potential applications for these nanocomposites.

References

[1] Z.-M. Dang, J.-K. Yuan, S.-H. Yao, R.-J. Liao, Flexible Nanodielectric Materials with High Permittivity for Power Energy Storage, Adv. Mater. 25 (2013) 6334–6365. doi:10.1002/adma.201301752.

[2] X. Huang, P. Jiang, Core-Shell Structured High-k Polymer Nanocomposites for Energy Storage and Dielectric Applications, Adv. Mater. 27 (2015) 546–554. doi:10.1002/adma.201401310.

[3] Q. Li, K. Han, M.R. Gadinski, G. Zhang, Q. Wang, High Energy and Power Density Capacitors from Solution-Processed Ternary Ferroelectric Polymer Nanocomposites, Adv. Mater. 26 (2014) 6244–6249. doi:10.1002/adma.201402106.

[4] S. Chen, X. Lv, X. Han, H. Luo, C.R. Bowen, D. Zhang, Significantly improved energy density of BaTiO3 nanocomposites by accurate interfacial tailoring using a novel rigid-fluoro-polymer, Polym. Chem. 9 (2018) 548–557. doi:10.1039/C7PY01914A.

[5] Prateek, V.K. Thakur, R.K. Gupta, Recent Progress on Ferroelectric Polymer-Based Nanocomposites for High Energy Density Capacitors: Synthesis, Dielectric Properties, and Future Aspects, Chem. Rev. 116 (2016) 4260–4317. doi:10.1021/acs.chemrev.5b00495.

[6] Q. Wang, L. Zhu, Polymer nanocomposites for electrical energy storage, J. Polym. Sci. Part B Polym. Phys. 49 (2011) 1421–1429. doi:10.1002/polb.22337.

[7] L. Zhu, Q. Wang, Novel Ferroelectric Polymers for High Energy Density and Low Loss Dielectrics, Macromolecules. 45 (2012) 2937–2954. doi:10.1021/ma2024057.

[8] B. Chu, Z. Xin, R. Kailiang, N. Bret, L. Minren, W. Qing, F. Bauer, Q.M. Zhang, A Dielectric Polymer with High Electric Energy Density and Fast Discharge Speed, Science (80-.). 313 (2006) 334–336. doi:10.1126/science.1127798.

[9] J. Pan, K. Li, J. Li, T. Hsu, Q. Wang, Dielectric characteristics of poly(ether ketone ketone) for high temperature capacitive energy storage, Appl. Phys. Lett. 95 (2009) 22902. doi:10.1063/1.3176219.

[10] Z.-M. Dang, J.-K. Yuan, J.-W. Zha, T. Zhou, S.-T. Li, G.-H. Hu, Fundamentals, processes and applications of high-permittivity polymer–matrix composites, Prog. Mater. Sci. 57 (2012) 660–723. doi:10.1016/J.PMATSCI.2011.08.001.

[11] N. Guo, S.A. DiBenedetto, P. Tewari, M.T. Lanagan, M.A. Ratner, T.J. Marks, Nanoparticle, Size, Shape, and Interfacial Effects on Leakage Current Density, Permittivity, and Breakdown Strength of Metal Oxide−Polyolefin Nanocomposites: Experiment and Theory, Chem. Mater. 22 (2010) 1567–1578. doi:10.1021/cm902852h.

[12] M. Seo, M.A. Hillmyer, Reticulated Nanoporous Polymers by Controlled Polymerization-Induced Microphase Separation, Science (80-.). 336 (2012) 1422–1425. doi:10.1126/science.1221383.

[13] P. Kim, S.C. Jones, P.J. Hotchkiss, J.N. Haddock, B. Kippelen, S.R. Marder, J.W. Perry, Phosphonic Acid-Modified Barium Titanate Polymer Nanocomposites with High Permittivity and Dielectric Strength, Adv. Mater. 19 (2007) 1001–1005. doi:10.1002/adma.200602422.

[14] C. Guo, M. Fuji, Effect of silicone coupling agent on dielectric properties of barium titanate/silicone elastomer composites, Adv. Powder Technol. 27 (2016) 1162–1172. doi:10.1016/J.APT.2016.03.028.

[15] Z.-M. Dang, H.-Y. Wang, H.-P. Xu, Influence of silane coupling agent on morphology and dielectric property in BaTiO3/polyvinylidene fluoride composites, Appl. Phys. Lett. 89 (2006) 112902. doi:10.1063/1.2338529.

[16] X. Zhang, Y. Ma, C. Zhao, W. Yang, High dielectric constant and low dielectric loss hybrid nanocomposites fabricated with ferroelectric polymer matrix and BaTiO3 nanofibers modified with perfluoroalkylsilane, Appl. Surf. Sci. 305 (2014) 531–538. doi:10.1016/J.APSUSC.2014.03.131.

[17] P. Kim, N.M. Doss, J.P. Tillotson, P.J. Hotchkiss, M.-J. Pan, S.R. Marder, J. Li, J.P. Calame, J.W. Perry, High Energy Density Nanocomposites Based on Surface-Modified BaTiO3 and a Ferroelectric Polymer, ACS Nano. 3 (2009) 2581–2592. doi:10.1021/nn9006412.

[18] A. Toor, H. So, A.P. Pisano, Improved Dielectric Properties of Polyvinylidene Fluoride Nanocomposite Embedded with Poly(vinylpyrrolidone)-Coated Gold Nanoparticles, ACS Appl. Mater. Interfaces. 9 (2017) 6369–6375. doi:10.1021/acsami.6b13900.

[19] K. Yang, X. Huang, J. He, P. Jiang, Strawberry-like Core-Shell Ag@Polydopamine@BaTiO3 Hybrid Nanoparticles for High-k Polymer Nanocomposites with High Energy Density and Low Dielectric Loss, Adv. Mater. Interfaces. 2 (2015) 1500361. doi:10.1002/admi.201500361.

[20] H. Luo, D. Zhang, C. Jiang, X. Yuan, C. Chen, K. Zhou, Improved Dielectric Properties and Energy Storage Density of Poly(vinylidene fluoride-co-hexafluoropropylene) Nanocomposite with Hydantoin Epoxy Resin Coated BaTiO3, ACS Appl. Mater. Interfaces. 7 (2015) 8061–8069. doi:10.1021/acsami.5b00555.

[21] Y. Song, Y. Shen, H. Liu, Y. Lin, M. Li, C.-W. Nan, Improving the dielectric constants and breakdown strength of polymer composites: effects of the shape of the BaTiO3 nanoinclusions, surface modification and polymer matrix, J. Mater. Chem. 22 (2012) 16491. doi:10.1039/c2jm32579a.

[22] H. Tang, Y. Lin, H.A. Sodano, Synthesis of High Aspect Ratio BaTiO3 Nanowires for High Energy Density Nanocomposite Capacitors, Adv. Energy Mater. 3 (2013) 451–456. doi:10.1002/aenm.201200808.

[23] L. Zhu, Exploring Strategies for High Dielectric Constant and Low Loss Polymer Dielectrics, J. Phys. Chem. Lett. 5 (2014) 3677–3687. doi:10.1021/jz501831q.

[24] P. Martins, A.C. Lopes, S. Lanceros-Mendez, Electroactive phases of poly(vinylidene fluoride): Determination, processing and applications, Prog. Polym. Sci. 39 (2014) 683–706. doi:10.1016/J.PROGPOLYMSCI.2013.07.006.

[25] D.W. Smith, S.T. Iacono, S.S. Iyer, Handbook of fluoropolymer science and technology, Wiley, 2014. https://www.wiley.com/en-us/Handbook+of+Fluoropolymer+Science+and+Technology+-p-9780470079935 (accessed

February 7, 2018).

[26] B. Ameduri, H. Sawada, Fluorinated Polymers, Royal Society of Chemistry, Cambridge, 2016. doi:10.1039/9781782629368.

[27] T. Soulestin, V. Ladmiral, F.D. Dos Santos, B. Améduri, Vinylidene fluoride- and trifluoroethylene-containing fluorinated electroactive copolymers. How does chemistry impact properties?, Prog. Polym. Sci. 72 (2017) 16–60. doi:10.1016/j.progpolymsci.2017.04.004.

[28] G. Subodh, V. Deepu, P. Mohanan, M.T. Sebastian, Dielectric response of high permittivity polymer ceramic composite with low loss tangent, Appl. Phys. Lett. 95 (2009) 62903. doi:10.1063/1.3200244.

[29] S. Liu, S. Xue, W. Zhang, J. Zhai, Enhanced dielectric and energy storage density induced by surface-modified BaTiO3 nanofibers in poly(vinylidene fluoride) nanocomposites, Ceram. Int. 40 (2014) 15633–15640. doi:10.1016/J.CERAMINT.2014.07.083.

[30] L. Gao, J. He, J. Hu, Y. Li, Large Enhancement in Polarization Response and Energy Storage Properties of Poly(vinylidene fluoride) by Improving the Interface Effect in Nanocomposites, J. Phys. Chem. C. 118 (2014) 831–838. doi:10.1021/jp409474k.

[31] T. Zhou, J.-W. Zha, R.-Y. Cui, B.-H. Fan, J.-K. Yuan, Z.-M. Dang, Improving Dielectric Properties of BaTiO3/Ferroelectric Polymer Composites by Employing Surface Hydroxylated BaTiO3 Nanoparticles, ACS Appl. Mater. Interfaces. 3 (2011) 2184–2188. doi:10.1021/am200492q.

[32] K. Yu, Y. Niu, F. Xiang, Y. Zhou, Y. Bai, H. Wang, Enhanced electric breakdown strength and high energy density of barium titanate filled polymer nanocomposites, J. Appl. Phys. 114 (2013) 174107. doi:10.1063/1.4829671.

[33] K. Yu, Y. Niu, Y. Zhou, Y. Bai, H. Wang, Nanocomposites of Surface-Modified BaTiO3 Nanoparticles Filled Ferroelectric Polymer with Enhanced Energy Density, J. Am. Ceram. Soc. 96 (2013) 2519–2524. doi:10.1111/jace.12338.

[34] H.-J. Ye, W.-Z. Shao, L. Zhen, Tetradecylphosphonic acid modified BaTiO3 nanoparticles and its nanocomposite, Colloids Surfaces A Physicochem. Eng. Asp. 427 (2013) 19–25. doi:10.1016/J.COLSURFA.2013.02.068.

[35] S.F. Mendes, C.M. Costa, C. Caparros, V. Sencadas, S. Lanceros-Méndez, Effect of filler size and concentration on the structure and properties of poly(vinylidene fluoride)/BaTiO3 nanocomposites, J. Mater. Sci. 47 (2012) 1378–1388. doi:10.1007/s10853-011-5916-7.

[36] Y. Zhang, L. Li, B. Wang, J. Zhang, E. Wang, Influence of coupling agent on microcosmic morphology and dielectric properties of energy-storage nanocomposite, (2014) 805–810. doi:10.1007/s10854-013-1649-5.

[37] J.Y. Li, L. Zhang, S. Ducharme, Electric energy density of dielectric nanocomposites, Appl. Phys. Lett. 90 (2007) 132901. doi:10.1063/1.2716847.

[38] Y. Niu, Y. Bai, K. Yu, Y. Wang, F. Xiang, H. Wang, Effect of the Modifier Structure on the Performance of Barium Titanate/Poly(vinylidene fluoride) Nanocomposites for Energy Storage Applications, ACS Appl. Mater. Interfaces. 7 (2015) 24168–24176. doi:10.1021/acsami.5b07486.

[39] X. Zhang, S. Zhao, F. Wang, Y. Ma, L. Wang, D. Chen, C. Zhao, W. Yang, Improving dielectric properties of BaTiO3/poly(vinylidene fluoride) composites by employing core-shell

structured BaTiO3@Poly(methylmethacrylate) and BaTiO3@Poly(trifluoroethyl methacrylate) nanoparticles, Appl. Surf. Sci. 403 (2017) 71–79. doi:10.1016/j.apsusc.2017.01.121.

[40] X. Zhang, H. Chen, Y. Ma, C. Zhao, W. Yang, Preparation and dielectric properties of core–shell structural composites of poly(1H,1H,2H,2H-perfluorooctyl methacrylate)@BaTiO3 nanoparticles, Appl. Surf. Sci. 277 (2013) 121–127. doi:10.1016/J.APSUSC.2013.03.178.

[41] K. Yang, X. Huang, Y. Huang, L. Xie, P. Jiang, Fluoro-Polymer@BaTiO3 Hybrid Nanoparticles Prepared via RAFT Polymerization: Toward Ferroelectric Polymer Nanocomposites with High Dielectric Constant and Low Dielectric Loss for Energy Storage Application, Chem. Mater. 25 (2013) 2327–2338. doi:10.1021/cm4010486.

[42] M. Ejaz, V.S. Puli, R. Elupula, S. Adireddy, B.C. Riggs, D.B. Chrisey, S.M. Grayson, Core-shell structured poly(glycidyl methacrylate)/BaTiO3 nanocomposites prepared by surface-initiated atom transfer radical polymerization: A novel material for high energy density dielectric storage, J. Polym. Sci. Part A Polym. Chem. 53 (2015) 719–728. doi:10.1002/pola.27485.

[43] M. Zhu, X. Huang, K. Yang, X. Zhai, J. Zhang, J. He, P. Jiang, Energy Storage in Ferroelectric Polymer Nanocomposites Filled with Core–Shell Structured Polymer@BaTiO3 Nanoparticles: Understanding the Role of Polymer Shells in the Interfacial Regions, ACS Appl. Mater. Interfaces. 6 (2014) 19644–19654. doi:10.1021/am504428u.

[44] K. Yang, X. Huang, L. Xie, C. Wu, P. Jiang, T. Tanaka, Core-shell structured polystyrene/BaTiO3 hybrid nanodielectrics prepared by in situ RAFT polymerization: A route to high dielectric constant and low loss materials with weak frequency dependence, Macromol. Rapid Commun. 33 (2012) 1921–1926. doi:10.1002/marc.201200361.

Chapter I: State of art

Recent Progress on Core-Shell Structured $BaTiO_3$@polymer/Fluorinated Polymers Nanocomposites for High Energy Storage: Synthesis, Dielectric Properties and Applications[1]

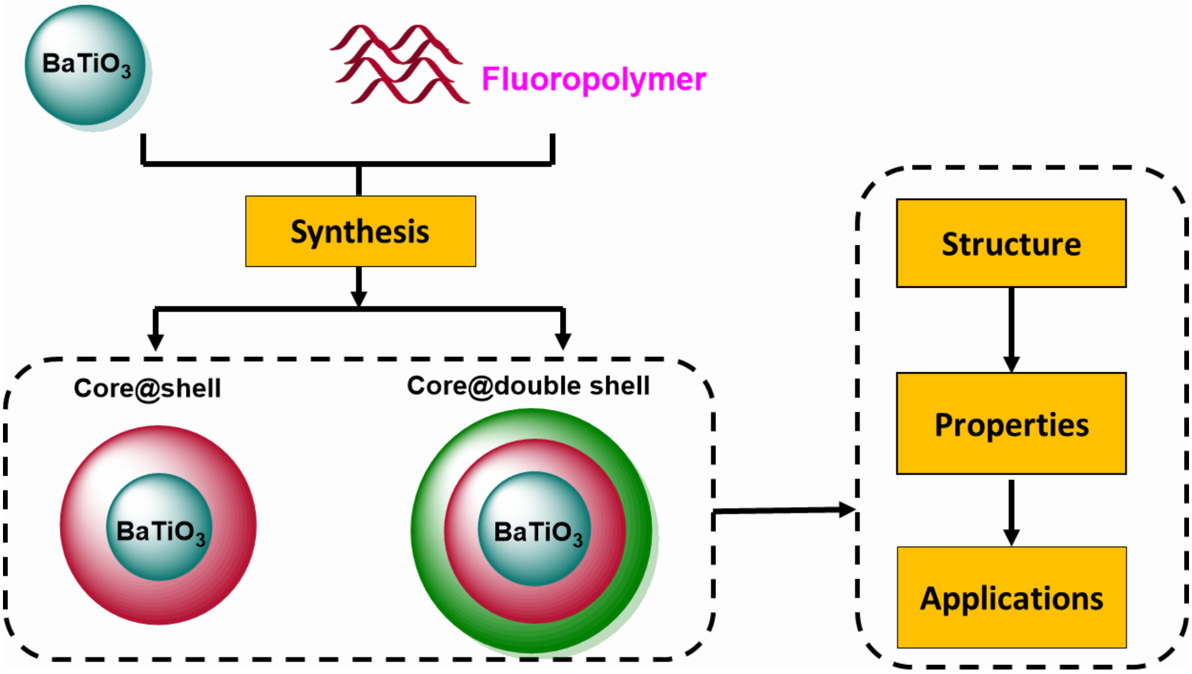

---

[1] This chapter has been published in **Progress in Materials Science** Journal: ***Bouharras et al., Progress in Materials Science, 113, 2020, 100670.***

I.1. Introduction

A nanocomposite is a multiphase material in which one of the components has at least one dimension of a nanometric scale. These nanocomposite materials can be classified according to their matrix group to ceramic, metal or polymer matrix nanocomposite [1]. For the last category that is of interests in the present review, the system consists on polymer matrix containing nanofillers dispersed in it, which results in outstanding properties, resulting in nanocomposite with high potentials [2,3].

In the recent years, dielectric nanocomposites with high energy density have received a great interest because of their wide range use in several applications such as electronic industry [4–9]. Generally, the energy density of a dielectric material can be illustrated as $U = \frac{1}{2}\ \varepsilon_0\ \varepsilon_r\ E^2$ where ε_0, ε_r and E are the permittivity of the free space (8.854 $\times 10^{-14}$ F/cm), relative permittivity and electric breakdown strength, respectively. Thus, obtaining high energy densities can be achieved either by increasing the relative permittivity and/or the electric breakdown strength of the material. Great efforts have been made to achieve both high dielectric permittivity and high breakdown strength. In fact, high permittivities could be obtained with ceramic nanoparticles and the most studied one is $BaTiO_3$ (~3000) [10–15], while high breakdown strength could be achieved with polymers like PVDF and VDF-copolymers (5000 KV/cm) [16–18]. By combining both these materials, a high energy density nanocomposite could be obtained. So far, a large number of polymers have been used in the synthesis of dielectric nanocomposites by introducing $BaTiO_3$ nanoparticles into fluoropolymer matrices (*e.g.*, PVDF [19–21], and VDF copolymers such as poly(vinylidene fluoride-*co*-trifluoroethylene) poly(VDF-*co*-TrFE) [22], poly(vinylidene fluoride-*co*-chlorotrifluoroethylene) poly(VDF-*co*-CTFE),[23] poly(vinylidene fluoride-*ter*-trifluoroethylene-*ter*-chlorofluoroethylene)) or non-fluoropolymer matrices (*e.g.*, poly(methyl methacrylate) (PMMA)[24] or poly(glycidyl methacrylate) (PGMA) [25]). Actually, PVDF and VDF copolymers have received particular attention due to the fact that they present the highest dielectric constants among all polymeric materials (6-12) thanks to the strong C-F dipole moment [26–28].

Apart from the polymeric matrix and the ceramic nanofiller, the interface between the different components plays a major role in the dielectric properties. Thus, it is considered as a third phase in the nanocomposite system [29]. Todd *et al.* [30] developed a model called the "interphase power law" in order to study the complex permittivity of the composite system.

To do so, this model uses the permittivities and the volume fractions of the filler, polymer and the interface region. The suggested model provides insight into the role of the interface and its effect on dielectric permittivity. Tanaka *et al.* [31] proposed a model to understand the dielectric properties of a nanocomposite material (Figure 1). They considered that the interface of a spherical inorganic nanoparticle embedded into a polymer matrix consists on three layers:

(i) The bonded layer (~ 1 nm): this layer corresponds to a transition layer where the polymer and the nanoparticles are bonded by coupling agent such as a silane.
(ii) The bound layer (several nm): called also the interfacial layer, where the polymer chains are strongly bounded and/or interacted to both the bond layer and the nanoparticle surface.
(iii) The loose layer (several tens of nm): this region has a poor interaction with the second layer.

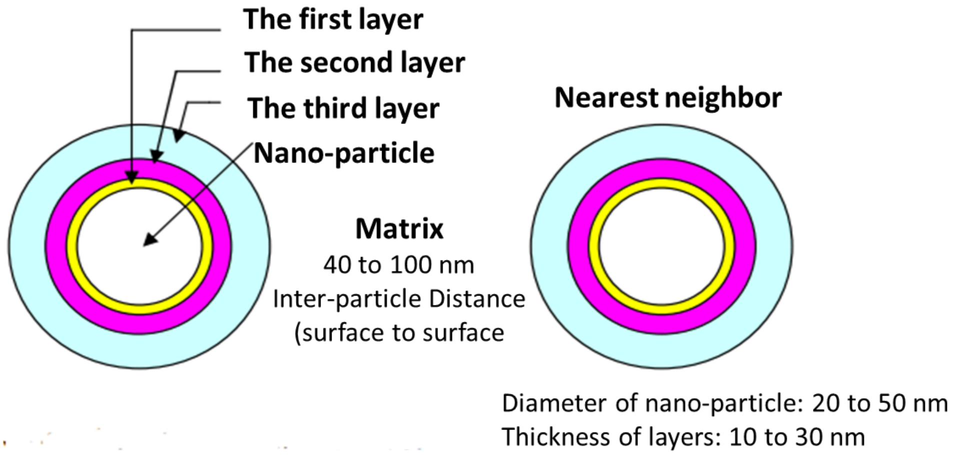

Figure 1. Multi-core model for nano-particle – polymer interfaces. Reproduced with permission from [31]. Copyright 2005 IEEE Xplore Digital library.

Thus, the interfacial region between the nanoparticles and the polymer must be considered since it contributes in the dielectric properties of the nanocomposite. Therefore, in addition to the choice of the nanoparticle and the polymer matrix, the selection of an appropriate pre-treatment of nanoparticles is crucial to obtain high energy density nanocomposites.

This review summarizes the recent work established on nanocomposites based on barium titanate (BT) as a filler and fluoropolymer as a matrix. After reminding the synthesis and properties of BT and fluoropolymers in the two first parts, the different strategies used to produce such nanocomposites are summarized in a third one. The fourth section highlights the importance of the surface treatment of nanoparticles by fluorinated agents or polymers, and then reports surveys on the design of nanocomposites made by one core of BT and double shell of polymer named as "core@double shell" system. The fifth part will cover the applications followed by the conclusion and perspectives.

I.2. $BaTiO_3$ ceramic fillers

I.2.1. Structure and crystallization

Barium titanate (BT) is one of the best ferroelectric ceramic and a good candidate for a wide range of applications due to its excellent dielectric, ferroelectric and piezoelectric properties [32,33]. It is also a dielectric material that belongs to the group having a structure of perovskite material of chemical formula $A(II)B(IV)O_3$, whose crystalline structure is a face centered cube [34]. The divalent ions occupy the top corner of the cell while the tetravalent ions are placed at the center of the cube whereas O^{2-} ions are located at the center of each face (Figure 2a). However, as the temperature decreased, crystallographic changes in $BaTiO_3$ occur and it goes through successive phase transitions: it undergoes a paraelectric to ferroelectric transition to a tetragonal structure at 120 °C (Curie temperature, Tc), it is orthorhombic between -90 and 5 °C and, finally, it is rhombohedral below -90 °C (Figure 2b) [35,36].

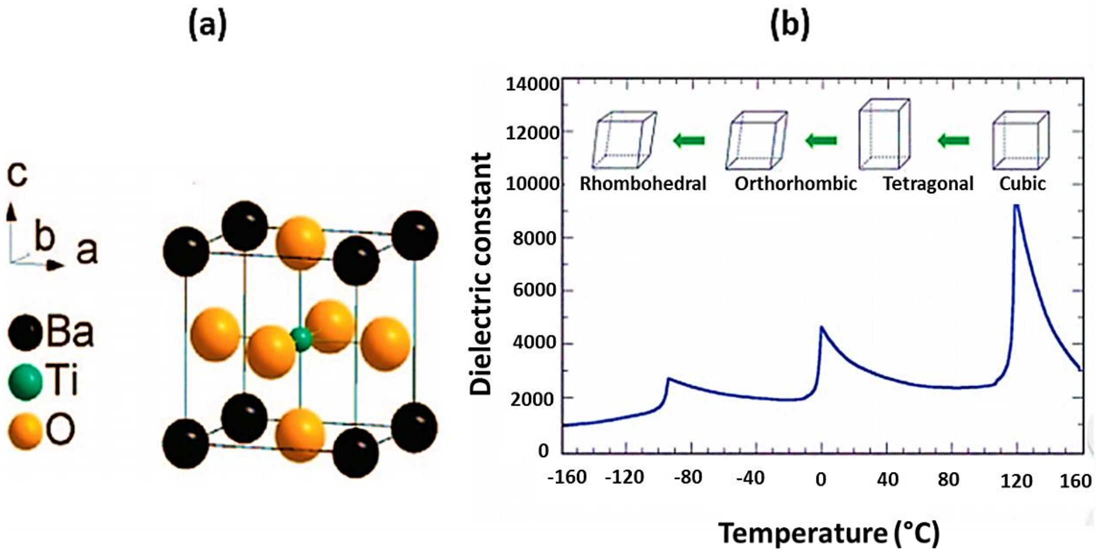

Figure 2. (a) Unit cell of $BaTiO_3$. Reproduced with permission from [32]. Copyright 2008 American Chemical Society, and (b) Barium titanate dielectric constant as a function of

temperature. Reproduced with permission from [37]. Copyright 2012 IEE Xplore Digital Library.

I.2.2. Synthesis of Barium titanate

$BaTiO_3$ presents a wide range of applications in the field of electronics thanks to its high dielectric permittivity [38–41]. In order to achieve the desired properties and practical applications, the quality of the $BaTiO_3$ powders is very important, which depends strongly on their synthesis method. Several routes to prepare BT have been reported by different authors, mentioned below.

I.2.2.1. Hydro/solvothermal synthesis

The hydro- or solvothermal method is a wet chemical preparation of $BaTiO_3$ powder that involves solutions, gels or suspensions subjected to temperatures and pressures ranging from room temperature to 1000 °C and from atmospheric pressure to 100 MPa, respectively [42–44]. The chemical synthesis utilizes the reaction of $Ba(OH)_2$ and a titanium source, according to reaction 1.

$$Ba(OH)_2 + TiO_2 \rightarrow BaTiO_3 + H_2O \qquad (1)$$

The synthesis process is carried out in stainless steel autoclave without any agitation, under heating and pressure. The final material exhibits different properties depending on the experimental conditions. As an example, Hao *et al.* [45] synthesized monodispersed $BaTiO_3$ and studied the effect of different parameters on the growth-up mechanism of $BaTiO_3$ nanocrystals. Temperature, considered as the most important factor that influences the reaction, was studied and it was found that the increase of temperature leads to a decrease of grain size of $BaTiO_3$ nanopowders. However, the opposite effect was observed with the concentration. The grain size of nanopowders was found to decrease by decreasing the concentration, as it was shown by SEM (Figure 3).

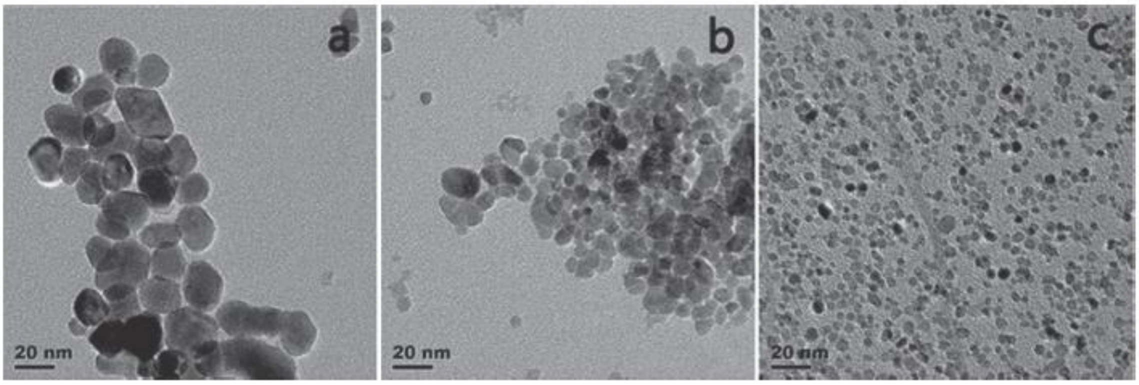

Figure 3. TEM images of the $BaTiO_3$ nanoparticles synthesized at 180 °C for 12 h at the concentration of (a) 3 mol/L, (b) 1.5 mol/L, (c) 0.75 mol/L. Reproduced with permission of [45]. Copyright 2013 The Ceramic Society of Japan.

I.2.2.2. Solid state synthesis

The solid state is considered as the most conventional synthesis method that can be achieved from reaction between TiO_2 and $BaCO_3$ (equation 2). To get $BaTiO_3$, the reactants are first mixed in order to reduce agglomerate and promote their homogeneity, then, are subjected to high temperatures in the region of 1000 °C [46–48].

$$BaCO_3 + TiO_2 \rightarrow BaTiO_3 + CO_2 \qquad (2)$$

However, this method produces relatively coarse and agglomerated particles, which is not suitable for most applications. In order to get fine-grained powders, alternative processing methods have been developed with chemical routes using non-oxide precursors [49,50].

I.2.2.3. Sol-gel synthesis

Barium titanate could be also synthesized using sol-gel method to yield a crystalline material at much lower temperatures than usually required for solid-state reactions [51]. This method involves the use of hydrolysis to form gels from metal oxides before subjecting them on a post processing to obtain high purity $BaTiO_3$ [52–54]. As shown in Table 1, different starting materials could be used to obtain $BaTiO_3$. Mazdiyasni *et al*. [55] used barium isopropoxyde derived from high purity Ba metal, while Flaschen *et al*. [56] involved $Ba(OH)_2$. However, it is found that high purity Ba (99.99 %) could be achieved by using barium isopropoxyde as a starting material [52].

Table 1. Comparison of Starting Materials for the Synthesis of Barium Titanate. Reproduced with permission of [57]. Copyright 1988 American Ceramic Society.

Starting materials	**Comments**
$BaCO_3$ and TiO_2	High-temperature process; lower purity; cheaper raw materials
$Ba(OH)_2$ and $Ti(OC_3H_7)_4$	Ba alkoxide not required
BaO-derived precursor and $Ti(OC_3H_7)_4$	Reaction chemistry uncertain; effect of impurities needs to be studied
Ba-derived $Ba(OC_3H_7)_4$ and $Ti(OC_3H_7)_4$	Ultrafine, stoichiometric and high-purity powders are obtained; expensive reagents needed.

I.2.3. Dielectric properties

The properties of ferroelectric materials are closely related to their crystalline structure, which can be closely related to their size [58–60]. Indeed, the permittivity of the ferroelectric ceramic is also strongly dependent on the size of the grains. Zhao *et al* . [61] reported the effect of grain size of $BaTiO_3$ on its dielectric permittivity. Figure 4 shows the variation of the dielectric permittivity of $BaTiO_3$ particles at different sizes. At 1200 nm, the profile is similar to the bulk material with a curie temperature (Tc) of about 120 °C, associated with a sharp transition from ferroelectric to paraelectric phase and ε_{max} up to 5000. When the particle size decreases to 300 nm, the Tc decreases with a wider phase transition and a $\mathcal{E}_{max}$ around 3500. Finally, at 50 nm, no phase transition was observed and ε_{max} goes below 1000.

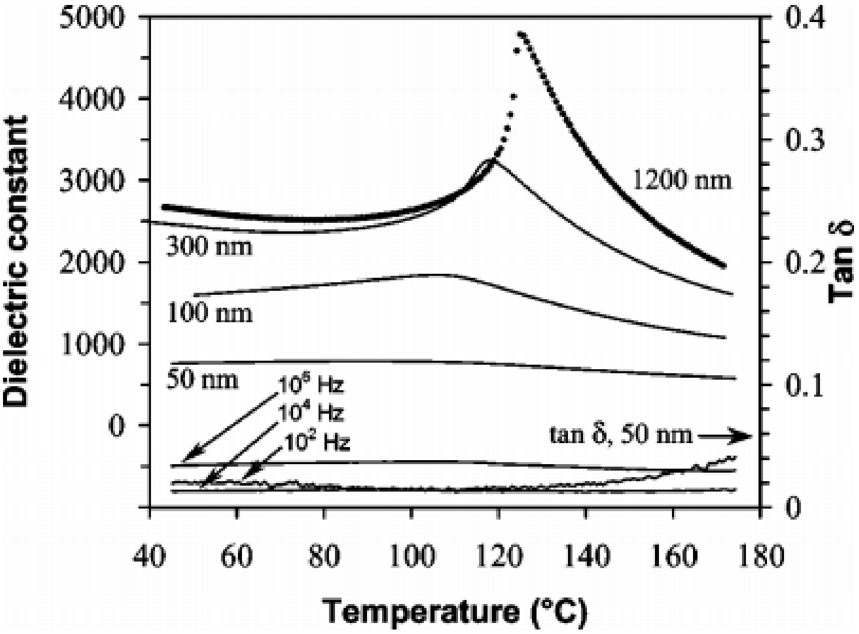

Figure 4. Relative dielectric constant and tan δ at 10^4 Hz as a function of temperature of $BaTiO_3$ using different sizes (50-1200 nm). Reproduced with permission of [61]. Copyright 2004 American Physical Society.

Another factor that influences the dielectric permittivity of $BaTiO_3$ is the porosity. The effect of this parameter on dielectric properties was studied by Hsiang *et al.* [62] In fact, previous models have been reported (*e.g.*, Niesel's equation [63] and Maxwell relationship [64]), assuming that the dielectric constant of a matrix phase ($BaTiO_3$) for porous ceramics to be constant while the effect of pores on dielectric constant can be neglected. Figure 5 exhibits the dielectric constant of $BaTiO_3$ ceramics for different porosities. It was concluded that for porosity below 10 %, the experimental results were consistent with the values obtained from theoretical models. However, when the porosity was greater than 10 %, a deviation between the experimental and theoretical values was found [62].

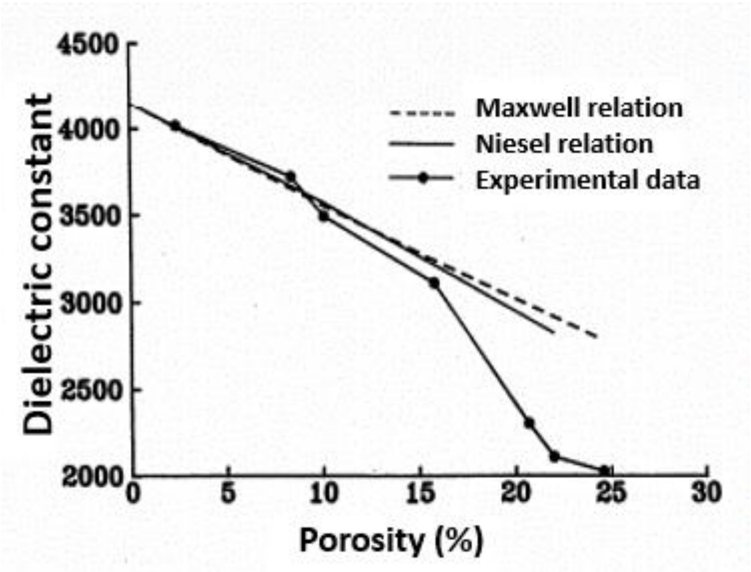

Figure 5. Values of dielectric constant of $BaTiO_3$ at room temperature for different porosities. Reproduced with permission of [62]. Copyright 1995 Japan Society of Applied Physics.

However, when the ceramic filler is added to a polymer matrix, the dielectric permittivity will depend on the dielectric properties of both phases. In fact, various models have been developed to predict the dielectric permittivity of composite material [65–67]. Maxwell-Garnet Equation is valid for a composite system with spherical particles and low filler loading. It can be expressed by equation (3):

$$\varepsilon_{eff} = \left[1 + \frac{3\varphi_f(\varepsilon_{f-}\varepsilon_m)}{\varphi_m(\varepsilon_f - \varepsilon_m) + 3\varepsilon_m}\right] \qquad (3)$$

where ε_{eff} is the effective permittivity of the composite material, ε_f and ε_m correspond to the permittivities of the filler and polymer, respectively, whereas φ_f and φ_m stand for the volume fractions of filler and matrix, respectively. In fact, this model neglects the effect of the interphase between the filler and polymer matrix and this assumption will be valid for a micro-scale composite [67]. However, for nanocomposites materials, the effect of the interphase could not be longer negligible and must be taken into account.

Vo and Shi [68] proposed a model to describe the effect of the interphase region on the dielectric permittivity of the nanocomposite, taking into account the dielectric permittivities and volume fractions of polymer, nanofiller and interphase. The used relationship to model the effective permittivity for nanocomposite materials containing three components (matrix, interphase region, and filler) can be supplied by equation (4):

$$\varepsilon_c = \frac{h+2l}{h-l} \tag{4}$$

where:

$$h = A - 2B - C \tag{5}$$

and

$$l = \frac{\varepsilon_3 - 1}{\varepsilon_3 + 2}\,A - \frac{(2\varepsilon_3 + 1)}{(\varepsilon_3 + 2)(2\varepsilon_3 + \varepsilon_2)}\,m\left(\frac{b^3}{c^3}\right) \tag{6}$$

with:

$$A = 1 + 2\frac{(\varepsilon_3 - \varepsilon_2)(\varepsilon_2 - \varepsilon_1)}{(2\varepsilon_3 + \varepsilon_2)(2\varepsilon_2 + \varepsilon_1)}\left(\frac{a^3}{b^3}\right) \tag{7}$$

$$B = \frac{(\varepsilon_3 - 1)(\varepsilon_3 - \varepsilon_2)}{(\varepsilon_3 + 2)(2\varepsilon_3 + \varepsilon_2)}\left(\frac{b^3}{c^3}\right) \tag{8}$$

$$C = \frac{(\varepsilon_3 - 1)(\varepsilon_3 + 2\varepsilon_2)(\varepsilon_2 - 1)}{(\varepsilon_3 + 2)(2\varepsilon_3 + \varepsilon_2)(2\varepsilon_2 + \varepsilon_1)}\left(\frac{a^3}{c^3}\right) \tag{9}$$

$$m = (\varepsilon_3 - \varepsilon_2)\frac{(\varepsilon_3 + 2\varepsilon_2)(\varepsilon_2 - \varepsilon_1)}{(2\varepsilon_3 + \varepsilon_1)}\left(\frac{a^3}{b^3}\right) \tag{10}$$

$$\frac{a^3}{b^3} = \frac{(1 + k\varphi_F)}{(1 + k)} \tag{11}$$

$$\frac{b^3}{c^3} = \varphi_F\left[1 + k\frac{(1 - \varphi_F)}{(1 + k\varphi_F)}\right] \tag{12}$$

$$\frac{a^3}{c^3} = \varphi_F \tag{13}$$

$\varepsilon_{1,}\ \varepsilon_2\ and\ \varepsilon_3$ stand for the dielectric permittivities of the ceramic nanoparticles, interphase and polymer matrix, respectively. φ_F represents the volume fraction of ceramic nanofillers, while k is the interphase volume constant, that reflects the matrix/filler interaction strength, where a value of zero designates an insignificant filler-matrix interaction, while positive values indicate the presence of strong interactions [68].

I.3. Strategies of the design of core-shell $BaTiO_3$@polymer/Fluorinated polymer nanocomposites

The role of the polymer matrix is to receive the nanoscale reinforcements to provide the strength in the structure, to improve the properties, and to give the desired shape to the nanocomposite. Thus, these polymer shells will have a great effect on the physical properties of the nanocomposites including its dielectric permittivity. The best case is that the polymer shells exhibit high dielectric permittivity and a good compatibility with the nanofiller, resulting in significantly enhanced energy density of the resulting nanocomposites. Actually, the most studied polymer matrices are fluorinated polymers that display dielectric constants of about 10 at 1 kHz (Table 2) [69–72]. Although having many benefits, the final properties of the nanocomposite will not only depend on the constituting materials but also on the processing methods. Actually, different strategies are used to prepare polymer-based $BaTiO_3$ nanocomposite, as shown in Scheme 1.

Generally, there are different synthetic strategies to get such nanocomposites, including hot pressing [73] , spin coating [74] and melt stretching [75,76] (Scheme 1-b). However, before combining the inorganic fillers with the organic polymer matrix, surface functionalization of the ceramic must be conducted in a first place. Actually, this surface modification is a crucial step in the synthesis process by allowing good compatibility and dispersion of ceramic nanofiller into polymer matrix (Scheme 1-a). Thus, the first step aims to chemically modify $BaTiO_3$ surface using the “grafting from”, “grafting onto” or blending process. The first strategy relies on the formation of the nanocomposites by means of controlled radical polymerization or reversible deactivation radical polymerization (RDRP) of monomers on initiator-functionalized nanoparticle surfaces. The second one consists of the formation of nanocomposites by grafting the pre-prepared polymer chains onto the nanoparticles surface via a reaction between the polymer end-groups and the functional groups on the nanoparticle surfaces. The last technique considers the formation of the nanocomposite by a simple casting or blending using the prepared polymer. These processes yield $BaTiO_3$ surface modified with polymer labeled as $BaTiO_3$@polymer.

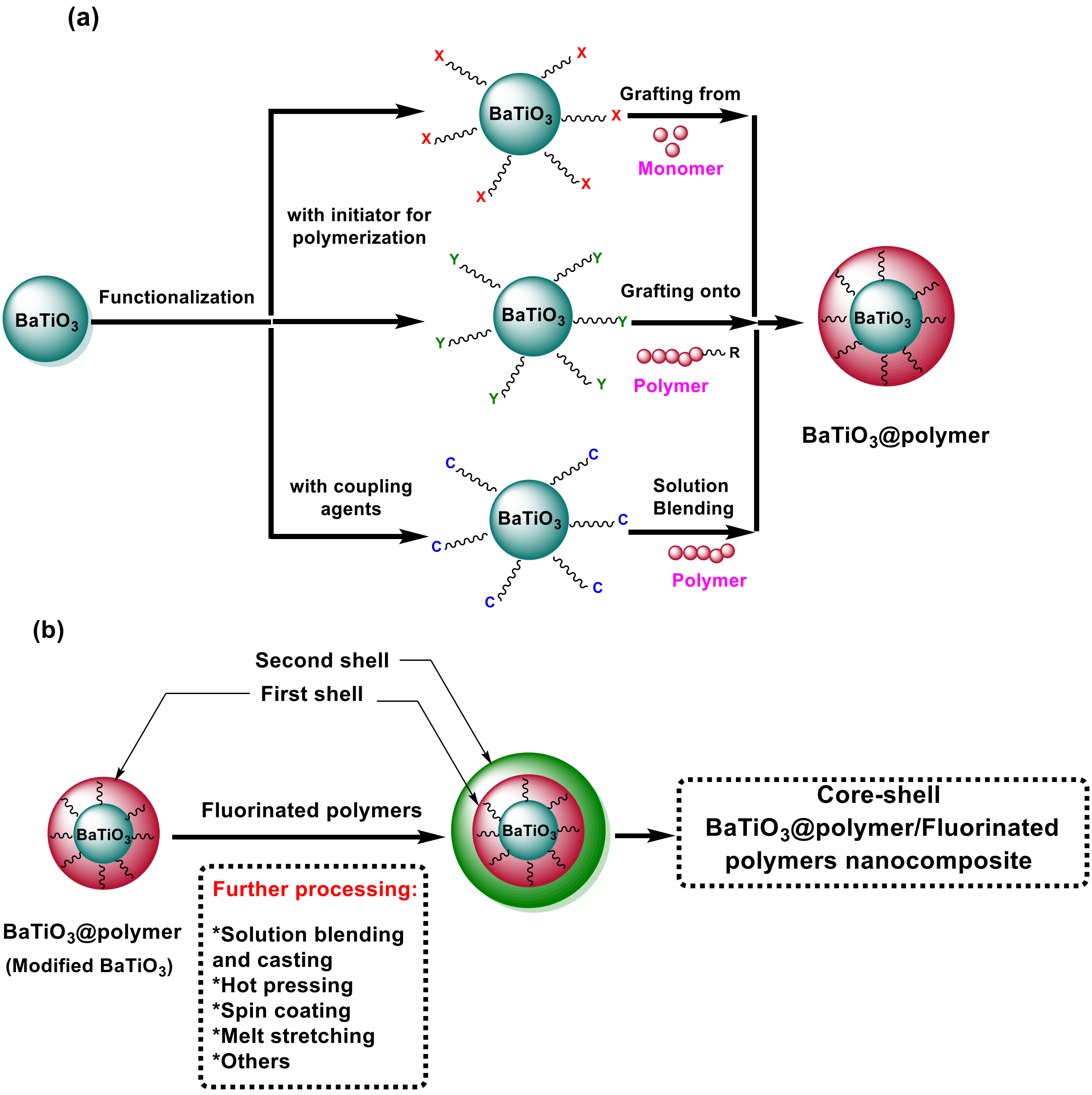

Scheme 1. Schematic illustration of (a) the surface modification of $BaTiO_3$ and (b) the synthesis process of $BaTiO_3$ based polymer nanocomposites, where X stands for -Br (Atom transfer radical polymerization, ATRP); –SC(S)Z (Reversible addition fragmentation chain transfer agent polymerization, RAFT), Y stands for alkyne, R stands for Azide (click chemistry), while C is assigned to coupling agent (*e,g*; silane agent, dopamine, phosphonic acid…) .

In order to further improve the final properties of the prepared nanocomposites, the core-double shell approach could be used. It consists of a simple blending of $BaTiO_3$@polymer with a second polymer shell yielding a nanocomposite labeled as core-double shell system.

The final nanocomposites could be then achieved by further processing such as hot pressing, spin coating and melt stretching (Scheme 1-b).

The most relevant routes reported in the literature for the design of core-shell $BaTiO_3$@polymer/Fluorinated polymers nanocomposites (Scheme 1-b) are solution blending or solution mixing between modified $BaTiO_3$ core ($BaTiO_3$@polymer) and fluorinated polymers as the shell. The materials obtained by casting were molded by hot pressing to prepare the sample films for mechanical, dielectric, and thermal properties.

However, melt-stretching and hot-pressing have also been used for the preparation of core-shell nanocomposites. In fact, Ghallabi *et al.* [77] reported the development of three-phase composites with carbon nanotube (MWCNT) and $BaTiO_3$ nanoparticles embedded into PVDF ($BaTiO_3$@(MWCNT) /PVDF nanocomposites) using Haake blending mixer and pressed by hot-molding technique. Ferri *et al.* [75] also reported the characterization of the nanoscale piezoelectric and ferroelectric behavior of stretched $BaTiO_3$/PVDF nanocomposites by means of the piezoelectric force microscopy (PFM) technique. First, $BaTiO_3$ was functionalized with nitrodopamine (NTD) leading to $BaTiO_3$@NTD modified structures. Then, the nanocomposites with functionalized nanoparticles and PVDF (labelled $BaTiO_3$@NTD/PVDF) were elaborated by blending solution in DMAc solvent. The material obtained by casting was then melt-compounded using a twin-screw micro-extruder and compression molded into a film of 100 μm thickness. The samples were stretched at a draw temperature of 90 °C up to a strain ε=100 % to promote the PVDF polar β crystal phase and thus enabled the polymer to display a piezoelectric response. Indeed, You *et al.* [76] reported another route of nanocomposites preparation by coupling in-*situ* polymerization and hot-stretching techniques. First, the polyaniline (PANI) functionalized barium titanate labelled $BaTiO_3$@PANI nanoparticles were prepared by *in-situ* polymerization of aniline monomer in the presence of $BaTiO_3$. Then, polyarylene Ether Nitrile (PEN)-based nanocomposite films with 40 wt% pure BT and $BaTiO_3$@PANI functionalized nanoparticles were prepared.

Table 2. Dielectric properties of different polymers. Reproduced with permission of [78]. Copyright 2016 American Chemical Society.

Polymers	*Dielectric constant (1 kHz)*	*Loss tangent (1 kHz)*	*Dielectric strength (kV/cm)*
LDPE	2.3	0.003	308.9
high-density polyethylene (HDPE)	2.3	0.0002−0.0007	222.9
BOPP	2.2	0.0002	7500.0
Polystyrene	2.4−2.7	0.008	2000.0
poly(ethylene terephthalate) (PET)	3.6	0.01	2750.0−3000.0
PMMA	4.5	0.05	2500.0
polyvinyl chloride (PVC)	3.4	0.018	400.0
polyetheretherketone (PEEK)	4	0.009 (100 kHz)	
poly(phthalazinone ether ketone)	3.5	0.0063	4700.0
polycarbonate (PC)	3.0	0.0015 (1000 kV/cm)	2520.0
Epoxy	4.5	0.015	250.0−450.0
PVDF	10-12	0.04	1500.0−5000.0
P(VDF-TrFE) [79]	11	0.08	770.0
P(VDF-TrFE-CFE) [79,80]	21-55	0.09-0.1	59.0-660.0
PTFE	2	0.0001	880.0−1760.0
PDMS	2.6	0.01	660.0
Polyimide	3.5	0.04	2380.0
Polyurethane	4.6	0.02	200.0
polyvinyl alcohol	12	0.3	1000.0
Aromatic polyurea(poly(diaminodiphenylmethane diphenylmethane diisocyanate) [p(mda/mdi)]	4.2	0.005	8000.0

I.4. Structure and properties of core-shell $BaTiO_3$@polymer/Fluorinated polymer nanocomposites

I.4.1. Fluoropolymer matrix

Because of their widespread use in many applications, fluoropolymers present a number of interesting properties including high thermal stability, hydrophybicity, improved chemical inertness and low surface tension [81–84]. Recently, many fluorinated polymers and copolymers have been widely used to the synthesis of $BaTiO_3$ based nanocomposites, including PVDF and VDF copolymers (Table 3) [20,27,85–90].

Table 3. Chemical structures of the most used fluoropolymers in dielectric nanocomposites.

Polymer	***Chemical structure***
Poly(vinylidene fluoride): PVDF	$\left(CH_2CF_2\right)_n$
Poly(vinylidene fluoride-*co*-hexafluoropropylene) Poly(VDF-*co*-HFP)	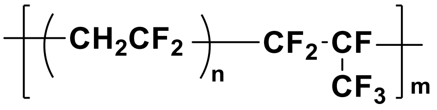 $\left[\left(CH_2CF_2\right)_n-CF_2-\underset{CF_3}{CF}-\right]_m$
Poly(vinylidene fluoride-*ter*-trifluoroethylene-*ter*-chlorotrifluoroethylene): poly(VDF-*ter*-TrFE-*ter*-CTFE)	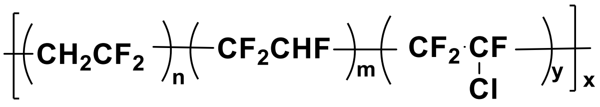 $\left[\left(CH_2CF_2\right)_n\left(CF_2CHF\right)_m\left(CF_2\underset{Cl}{CF}\right)_y\right]_x$

Polyvinylidene fluoride is a semi-crystalline polymer, which contains 59.4 wt % of fluorine and 3 wt % hydrogen atoms [26]. It presents a complex structure that may exist in five different crystalline phases and the most investigated ones are: α, β and γ phases (Figure 6) [91]. Although each phase exhibits various properties, β phase was found to be the most interesting polymorph of PVDF for technological applications thanks to its piezoelectric, pyroelectric and ferroelectric properties that originate from the orientation of the strong dipole in $–CH_2-CF_2$ units along the polymeric chains [26].

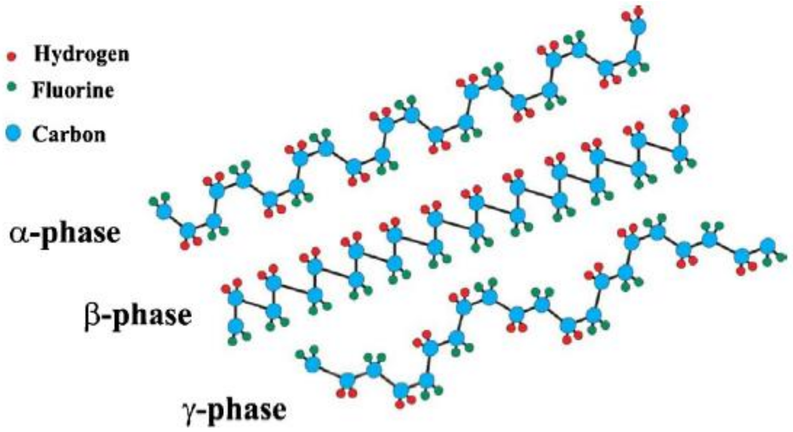

Figure 6. Schematic illustration of three crystalline phases of PVDF. Reproduced with permission of [91]. Copyright 2014 Elsevier.

In order to improve the properties of PVDF and expand its field of applications, several works have been reported on the use of VDF copolymers [26,72,92] or even mixed with ceramics to form nanocomposite systems [93,94]. For example, poly(vinylidene fluoride-co-hexafluoropropene) poly(VDF-*co*-HFP), has been mostly used in Li-ion batteries as polymer electrolyte or even in production of membranes [95–97]. This interest arises from the fact that this copolymer is chemically inert and exhibits a lower crystallinity compared to PVDF [98]. Claude *et al*. [18] prepared poly(VDF-*ter*-TrFE-*ter*-CTFE) terpolymer from the radical copolymerization of VDF and CTFE followed by the reductive dechlorination of CTFE units. Table 4 shows that the introduction of 3.9 mol % of TrFE and 22.5 mol % of CTFE into the PVDF matrix decreases the crystallinity and melting temperature from 50-70% and 155-198 °C for PVDF to 14.4 % and 38 for poly(VDF-*ter*-TrFE-*ter*-CTFE) terpolymer.

Table 4. Structural Characteristics of the prepared VDF- based ferroelectric co- and terpolymers. Reproduced with permission of [18]. Copyright 2008 American Chemical Society.

	Composition (mol %)					
Polymer	***VDF***	***TrFE***	***CTFE***	χ_c ***(%)***	T_m ***(°C)***	ε_r
1	73.6	0	26.4	7.2		14.1
2	73.6	3.9	22.5	14.4	37.8	16.4
3	73.6	9.2	17.2	17.1	72.5	24.1
4	73.6	11.9	14.5	18.0	86.7	24.0
5	73.6	18.3	8.1	24.2	121.0	14.7
6	73.6	19.3	7.1	28.6	127.0	14.2
7	73.6	26.4	0	35.4	163.0	10.4

χ_c, T_m *and* ε_r *stand for crystallinity, melting temperature and relative permittivity, respectively.*

Moreover, the highest permittivities were found in polymers 3 and 4 (Table 4) which indicate the effect and also the importance of molecular composition of terpolymers on the final properties of the system. Soulestin *et al.* [92] reviewed the synthesis and properties of poly(VDF-*ter*-TrFE-*ter*-Monomer) terpolymers. The influence of polymerization strategies and types of termonomers used on the final properties were also discussed. It was concluded that CTFE and CFE are among the most used comonomers since they affect efficiently the crystalline lattice of poly(VDF-*co*-TrFE) terpolymers. Moreover, this terpolymer is considered to be one of the most promising materials thanks to its higher polarization, which is one of the most important features of ferroelectric polymers. Cho *et al.* [99] reported the formation of the β-phase in a poly(VDF-*ter*-TrFE-*ter*-CTFE) film (PVDF:TrFE:CTFE =

62:31:7 in mol%) by solution annealing process at room temperature, by crystallizing the polymer below the curie temperature (Figure 7). This method led to polymeric films with enhanced ferroelectricity compared to a thermally annealed one.

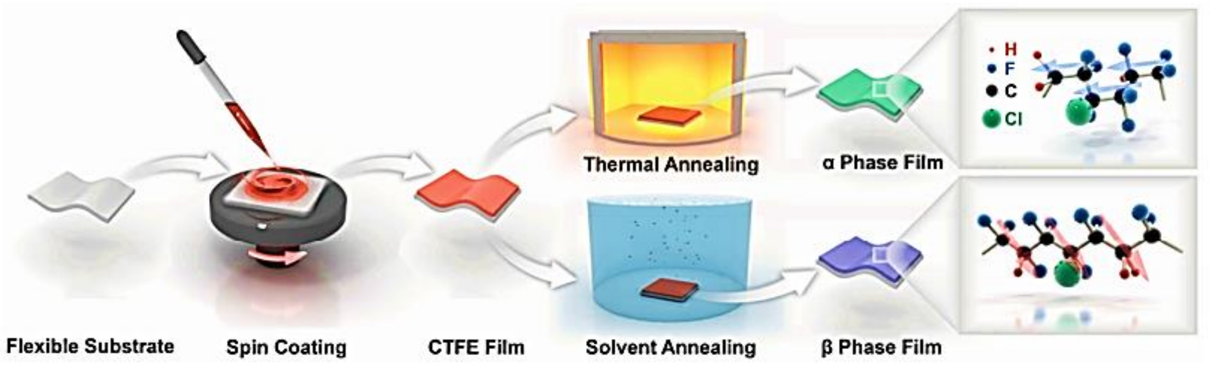

Figure 7. Illustration of the formation of the α and β phases formed using thermal and solvent annealing, respectively. Annealing at a temperature below the curie temperature, using solvent annealing, forms a β-phase dominant film whereas a thermal annealing above the phase transition temperature forms an α-phase dominant film. Reproduced with permission of [99]. Copyright 2016 Wiley.

I.4.2. Surface modification of $BaTiO_3$

Barium titanate nanoparticles are often used as ceramic fillers for polymer matrix composites because they are one of the most commercially available high dielectric constant-materials. However, since untreated $BaTiO_3$ nanoparticles tend to form agglomerates, the good dispersion of the nanoparticle fillers into the polymer matrix and the compatibility between them are always the important factors conditioning the performances of the nanocomposites. Thereby, the surface functionalization is a crucial feature.

I.4.2.1. Modification of $BaTiO_3$ with fluorinated agent

So far, several strategies have been proposed to prevent aggregation of $BaTiO_3$ nanoparticles inserted into the polymer matrix, including surface hydroxylation [100], phosphonic acid [74,101], dopamine [102,103] and coupling agents [104–106]. In order to highlight the importance of the hydroxylation step, Zhou *et al.* [100] reported a comparison between the dielectric properties of a nanocomposite based on a PVDF polymer matrix and raw (c-BT) or hydroxylated (h-BT) $BaTiO_3$ nanoparticles. The results showed that nanocomposites made by hydroxylated nanoparticles display a low temperature and frequency dependence. This suggests that the strong interactions between h-BT fillers and PVDF matrix is the main reason for improving dielectric properties. Dalle Vacche *et al*. [106] studied the effect of surface modification of $BaTiO_3$ with (3-aminopropyl) triethoxysilane (APTES) as a silane coupling agent on properties of poly(VDF-*co*-TrFE)/$BaTiO_3$ composites. The modified particles were well-dispersed in the polymer matrix than that of the unmodified ones leading to reduced aggregate and enhancing the compatibility with the poly(VDF-*co*-TrFE) matrix. In another work, Kim *et al*. [107] reported that surface modification of $BaTiO_3$ with phosphonic acid formed well-ordered nanoparticles into poly(VDF-*co*-HFP) matrix leading to high dielectric constant ($\varepsilon = 43$) and high breakdown strength (210 V μm^{-1}).

However, in order to get better interfacial interactions between the nanofiller and the fluoropolymer, fluorinated modifiers are more preferred as they contain fluorine atoms in their end chains. To study the influence on the compatibility with fluorine polymers, Ehrhardt *et al*. [108] used n-octyl phosphonic acid (OPA) and pentafluorobenzylphosphonic acid (PFBPA) to modify the surface of $BaTiO_3$. The phosphonic acid coated $BaTiO_3$ were then dispersed in solutions of poly(VDF-*co*-HFP) copolymer to form nanocomposites by spin coating technique. Results show that the phosphonic acid with a fluorinated organic host gives rise to a slightly increased of relative permittivity of the resulting composite materials compared to the one containing n-octyl phosphonic acid (Figure 8). This suggests that pentafluorobenzylphosphonic acid provides a better chemical compatibility with poly(VDF-*co*-HFP).

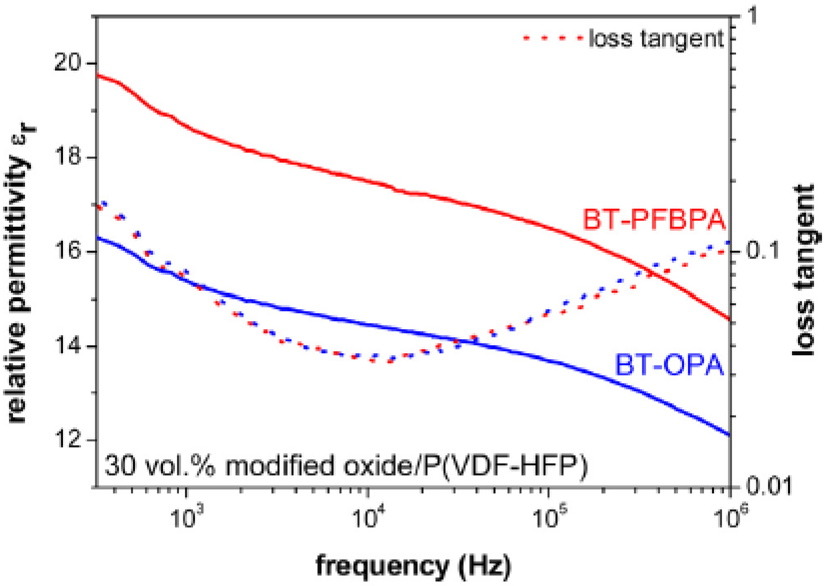

Figure 8. Relative permittivity of BT/Poly(VDF-*co*-HFP) composite films prepared with 30 vol.% $BaTiO_3$ coated with pentafluorobenzyl phosphonic acid (BT-PFBPA) and

octylphosphonic acid (BT-OPA). Reproduced with permission of [108]. Copyright 2013 Elsevier.

PFBPA was used in another survey to modify $BaTiO_3$ surface. For example, Kim *et al*. [74] utilized pentafluorobenzylphosphonic acid (PFBPA) to functionalize $BaTiO_3$ surface before adding poly(VDF-*co*-HFP), to form nanocomposite by spin coating the dispersions on aluminum coated glass substrate (Figure 9).

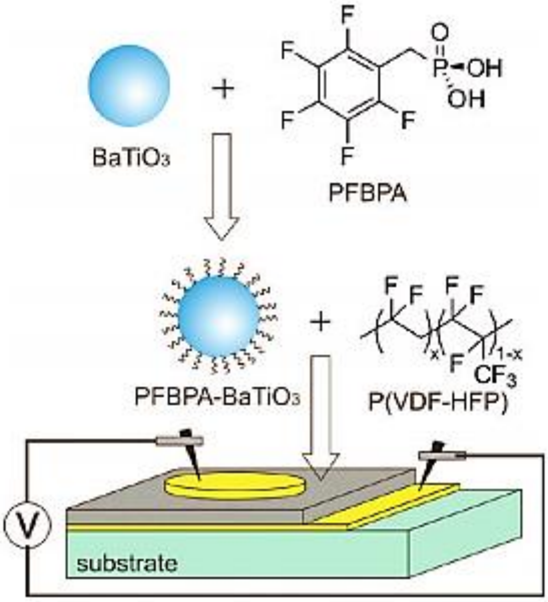

Figure 9. Illustration of surface modification of $BaTiO_3$ with PFBPA. Reproduced with permission of [74]. Copyright 2009 American Chemical Society.

Authors reported the surface modification of $BaTiO_3$ with PFBPA formed homogenous dispersion into the polymeric matrix and therefore uniform nanocomposite thin films.

Zhang *et al*. [109] used (1H,1H,2H,2H-perfluorooctyltrimethoxysilane) to introduce a short perfluoroalkyl chain onto the surface of $BaTiO_3$ nanofibers by chemical reaction between the HO- groups of the oxydized surface of BT and methoxy groups of the fluorinated silane. Then, the modified nanoparticles were incorporated into PVDF by solution blending (Scheme 2). The results indicate that the fluorosilane modified $BaTiO_3$ nanofiber results in a strong interchain interaction with PVDF matrix and improved the interface compatibility between the functionalized filler and the fluoropolymer.

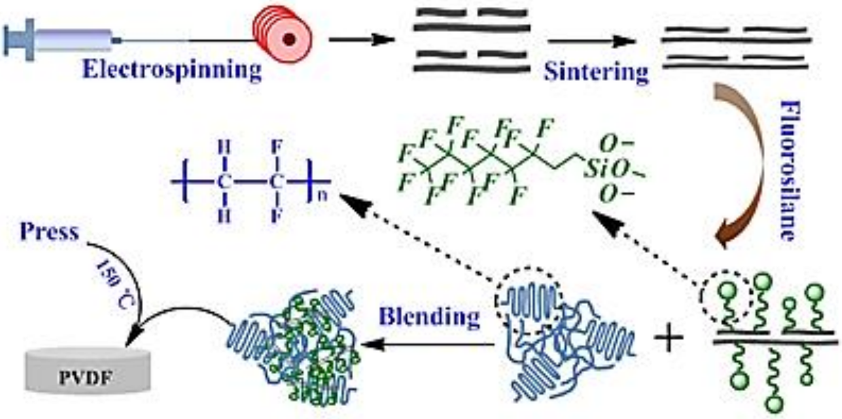

Scheme 2. Schematic illustration of the preparation of PVDF/BT nanocomposite. Reproduced with permission of [109]. Copyright 2014 Elsevier

In another work, Yu *et al.* [110] reported the preparation of PVDF/BT nanocomposites. The nanoparticles were firstly modified with tetrafluorophtalic acid, then incorporated into PVDF matrix by a solution casting method. Figure 10 displays the surface modification process of BT with tetrafluorophtalic acid and the effects on the modification on the PVDF/BT nanocomposite. The fluorinated acid reacts with the hydroxyl groups already present onto the surface of BT using its alkoxy chains. Thanks to its fluorinated aryl groups, the modified BT exhibits good compatibility with PVDF, improves the dispersion of BT and introduces more space charges in the polymer which results in generation of passivation layers, and thereby enhancing the breakdown strength of the nanocomposite.

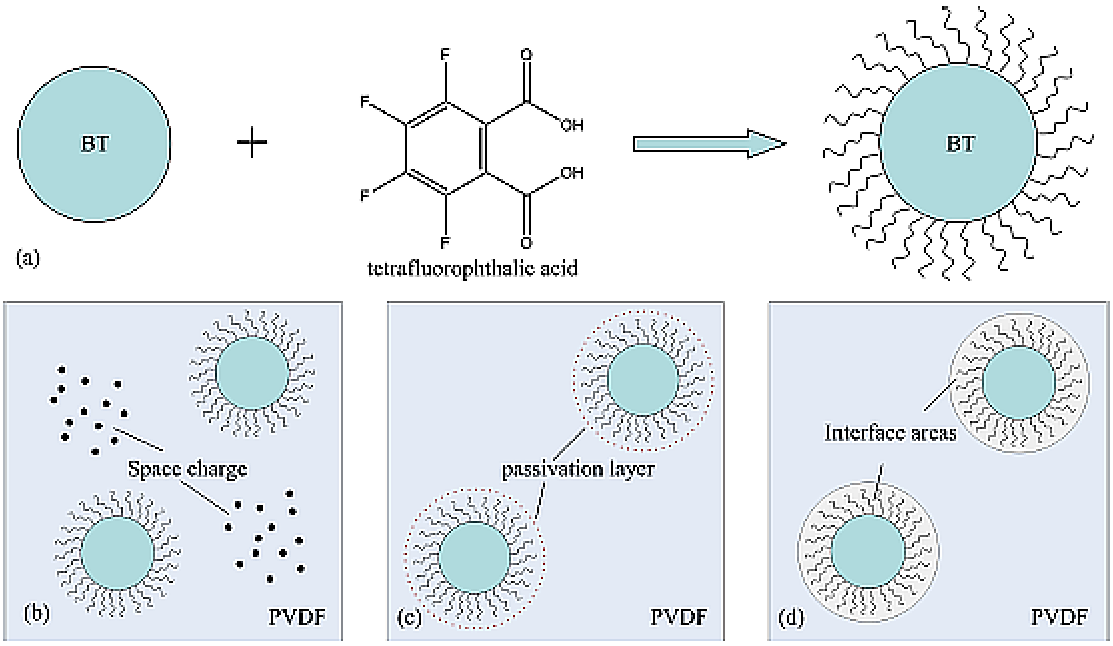

Figure 10. Schematic of surface modification processing of BT nanoparticles (a) and the effects of surface modified BT nanoparticles in BT/PVDF nanocomposites (b), (c), and (d). Reproduced with permission of [110]. Copyright 2013 American Institute of Physics.

Wang *et al*. [111] prepared BT/poly(VDF-*co*-HFP) nanocomposites by a solution casting method. The $BaTiO_3$ nanoparticles were first functionalized with fluoro-polydopamine via a spontaneous self-polymerization upon the surface of $BaTiO_3$ nanowires (Figure 11), then, a desired amount of modified BT was inserted into poly(VDF-*co*-HFP) matrix. It was found that by anchoring a long fluorinated chain upon the dopamine, the resulting fluoro-dopamine modified BT presented homogenous distribution in the polymer matrix, suggesting an excellent compatibility with the fluoropolymer matrix. Moreover, the fluoro-dopamine shell layers improved the dispersion of nanowires and thus increases the affinity with the polymer matrix, resulting in enhanced dielectric permittivity and breakdown strength.

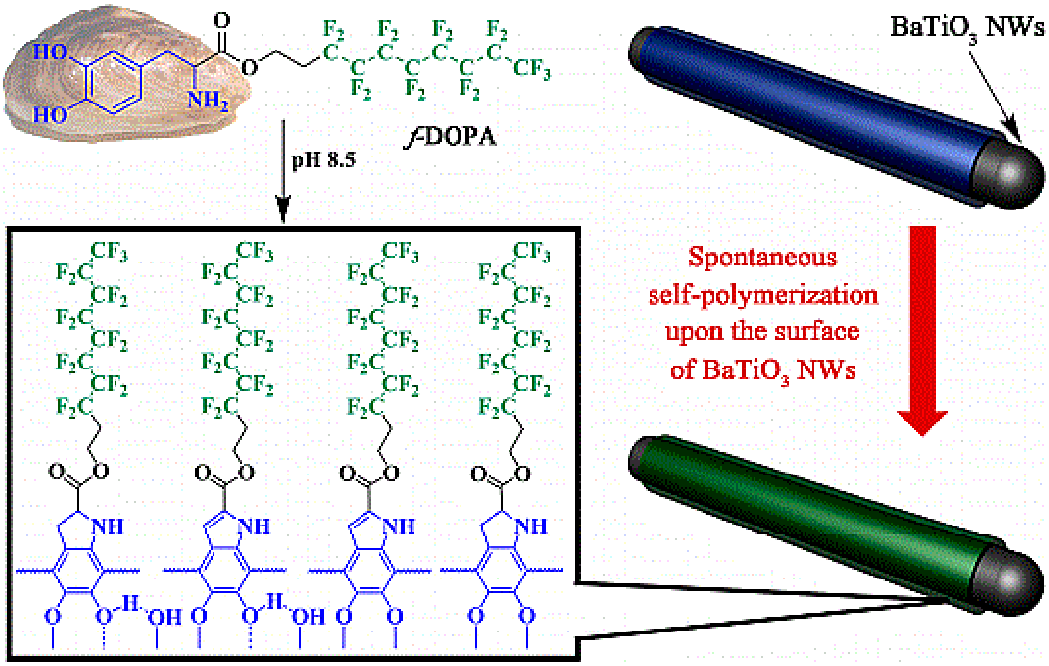

Figure 11. Schematic illustration of the preparation process for fluorinated-DOPA@BaTiO$_3$ NWs. Inset is a photograph of a mussel. Reproduced with permission of [111]. Copyright 2017 American Chemical Society.

I.4.2.2. Modification of BaTiO3 with polymer prepared by "Grafting from" route

I.4.2.2.1. PMMA@BT

Wang *et al.* proceeded to BaTiO$_3$ functionalization with PMMA using ATRP polymerization [112]. The nanoparticles were first coated with tetrameric metallophthalocyanine (TMPc), from which PMMA brushes are grafted. In order to make a comparison, composites without the TMPc interfacial layer were also synthesized. The particle size and size distribution of the resulting nanocomposite were studied (Figure 12). It was found that by increasing the feed ratio of MMA from 5.2 to 18 wt %, the hydrodynamic diameter (Dh) for BTO@TMPc-PMMA particles increased from 109 nm to 186 nm, proving the succefull grafting of PMMA onto coated BaTiO$_3$.

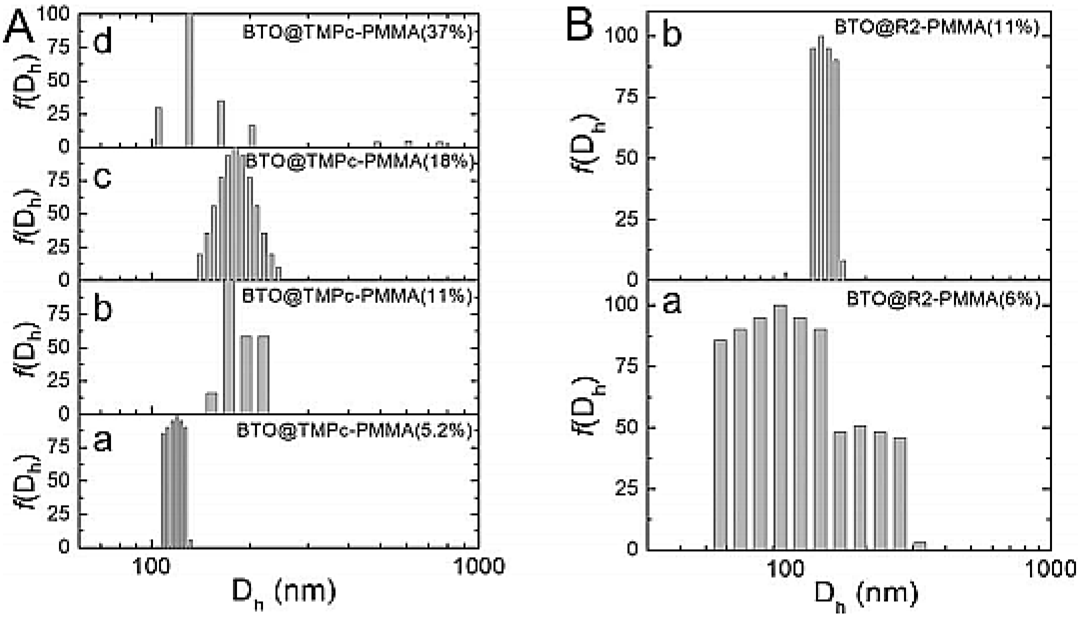

Figure 12. DLS hydrodynamic diameter (D_h) distribution for (A) BTO@TMPc-PMMA and (B) BTO@R2c-PMMA nanoparticles in DMF. The maximum light scattering intensity is normalized to 100%. Reproduced with permission of [112]. Copyright 2014 Wiley.

I.4.2.2.2. PTFEMA or PMMA@BT

Zhang *et al.* [113] prepared a core shell structured nanocomposites with different shell composition and shell thickness by grafting the polymer onto BT surface using ATRP polymerization. Methyl methacrylate (MMA) and 2,2,2-trifluoroethyl methacrylate (TFEMA) were used and two different amounts of these monomers were adopted (Table 5).

Table 5. Summary of grafted polymer contents measured by TGA under nitrogen atmosphere. Reproduced with permission of [113]. Copyright 2017 Elsevier.

Samples	***Feed ratio of monomer to BT-Br (w/w)***	***Weight loss of grafted polymer (%)***
BT-Br	--	1.5
BT@PMMA1	1:1	7.0
BT@PMMA2	2:1	9.5
BT@PTFEMA1	1:1	3.0
BT@PTFEMA2	2:1	3.5

The different analyses performed on the nanocomposites evidenced the successful grafting of both PMMA and PTFEMA onto BT surface. TGA results showed that by increasing monomer feed ratio, the grafted mass of the two polymers increased, which indicate that the grafted polymer content can be controlled by varying the monomer: initiator molar ratio (for example, by increasing the feed ratio of monomer: initiator from 1:1 to 2:1, the weight loss of PMMA increases from 5.5 % to 8.0 %). Moreover, Figure 13 exhibits the shell thickness of the polymer covering BT surface increases by increasing the monomer feed ratios from 7 nm to 12 nm for PMMA and from 4.5 nm to 5.5 nm for PTFEMA.

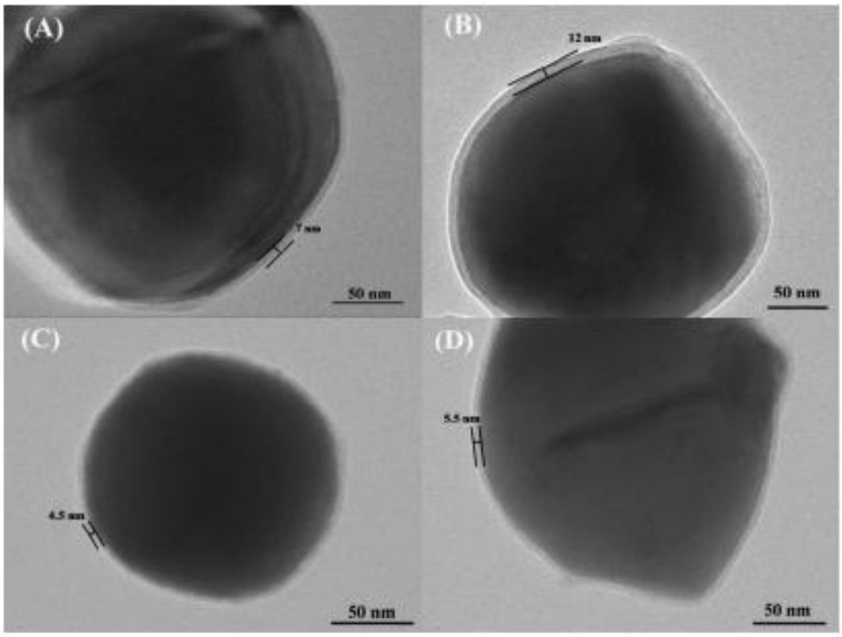

Figure 13. TEM images of the BT@polymer nanoparticles: (A) BT@PMMA1, (B) BT@PMMA2, (C) BT@PTFEMA1 and (D) BT@PTFEMA2. Reproduced with permission of [113]. Copyright 2017 Elsevier.

I.4.2.2.3. PPFOMA@BT

Zhang *et al*. [114] prepared a core shell nanocomposite by grafting 1H,1H,2H,2H-perfluorooctyl methacrylate (PPFOMA) onto BT using ATRP polymerization. First, nanoparticles were treated by hydroxylation, silylation and amidation to anchor the ATRP initiator, then PPFOMA polymer chain was grafted from the initiating sites (Scheme 3). At high PPFOMA feed ratios, the nanoparticles could be suspended in the solvent overnight without precipitation. This suggests that the functionalization of BT nanoparticles with PPFOMA polymer chains leads to a better dispersion of the composite particles. In addition, the dielectric properties of nanocomposites were studied. The dielectric constant (ε) increased significantly by increasing the $BaTiO_3$ fraction in the nanocomposite and reached 7.4 (for a fraction of 71 wt% in $BaTiO_3$), which is 3 times higher than that of PPFOMA (ε=2.6).

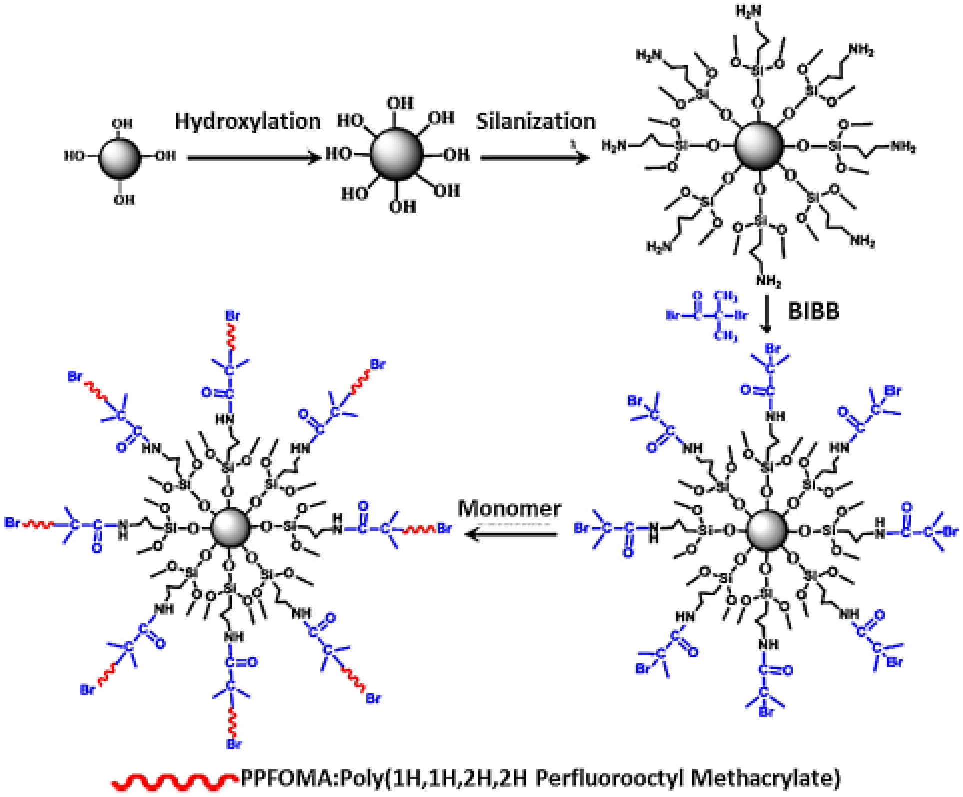

Scheme 3. Preparation of PPFOMA@BaTiO$_3$ by SI-ATRP of 1H,1H,2H,2H-perfluorooctyl methacrylate (PPFOMA). Reproduced with permission of [114]. Copyright 2013 Elsevier.

I.4.2.2.4. PtBA@BT

Du *et al.* [115] used poly(*tert*-butyl acrylate) (P*t*BA) to functionalize BT surface by ATRP polymerization (Figure 14). The first step dealt with the hydroxylation of BT surface by hydrogen peroxide in order to create –OH groups on their surface. The second and third steps consisted of the grafting of silane and bromine agents to obtain ATRP initiating sites, respectively. The last step was the polymerization of *t*BA from functionalized nanoparticles. Theses authors reported that the P*t*BA functionalized nanoparticles reduce the surface energy of the nanoparticles and avoid aggregation leading to a better dispersion and homogenous nanocomposites.

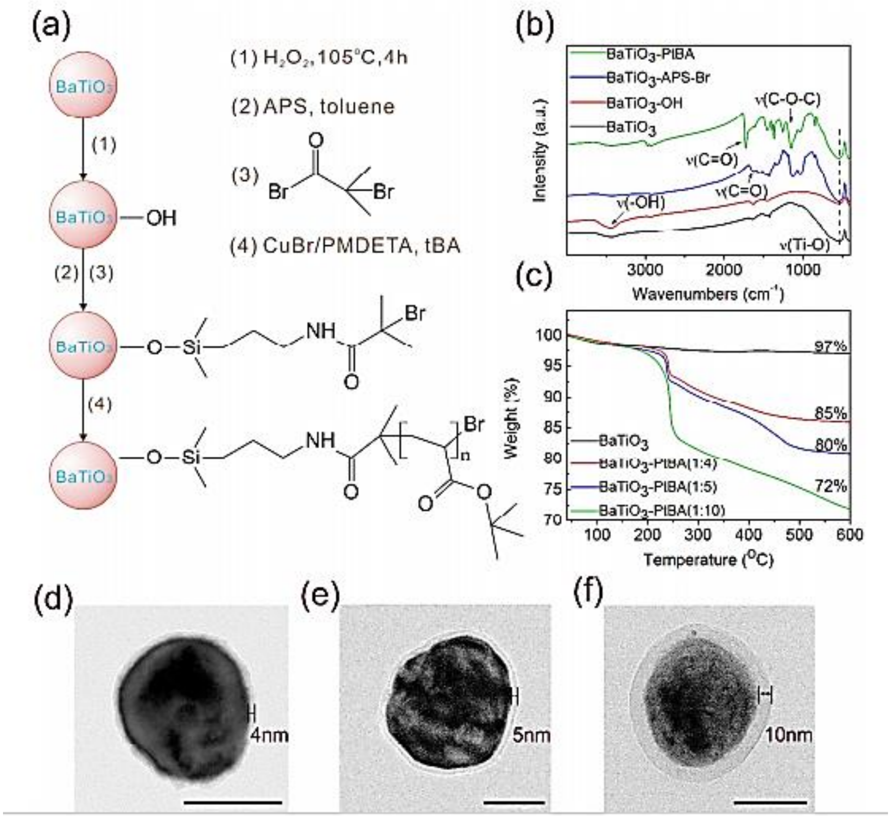

Figure 14. Preparation process and characterizations of the nanoparticles with core-shell structure. a) Schematic diagram illustrating the preparation process of the $BaTiO_3$-P*t*BA by ATRP of *tert*-butyl acrylate. b) FT-IR spectra of the $BaTiO_3$ at various stages of treatment. c) TGA thermogramms for pure $BaTiO_3$ and $BaTiO_3$-PtBA with different polymer shell thicknesses. d-f) TEM images of the core-shell structured $BaTiO_3$-PtBA nanoparticles (scale bar 50 nm). Reproduced with permission of [115]. Copyright 2018 American Chemical Society.

I.4.2.2.5. PGMA@BT

Ejaz *et al.* [25] prepared core-shell nanocomposites via ATRP polymerization through two steps: i) immobilization of initiator sites onto $BaTiO_3$ surface and ii) ATRP polymerization of glycidyl methacrylate (GMA). The dielectric permittivity of PGMA and PGMA@BT nanocomposite decreases as the frequency increases from 100 Hz to 1 MHz (Figure 15). At room temperature, the nanocomposite displays a very high permittivity (54 at 1 kHz) which is 10 times higher than that of PGMA (5.3 at 1 kHz). This enhanced permittivity is related to the good dispersion of the ceramic fillers into the polymer matrix.

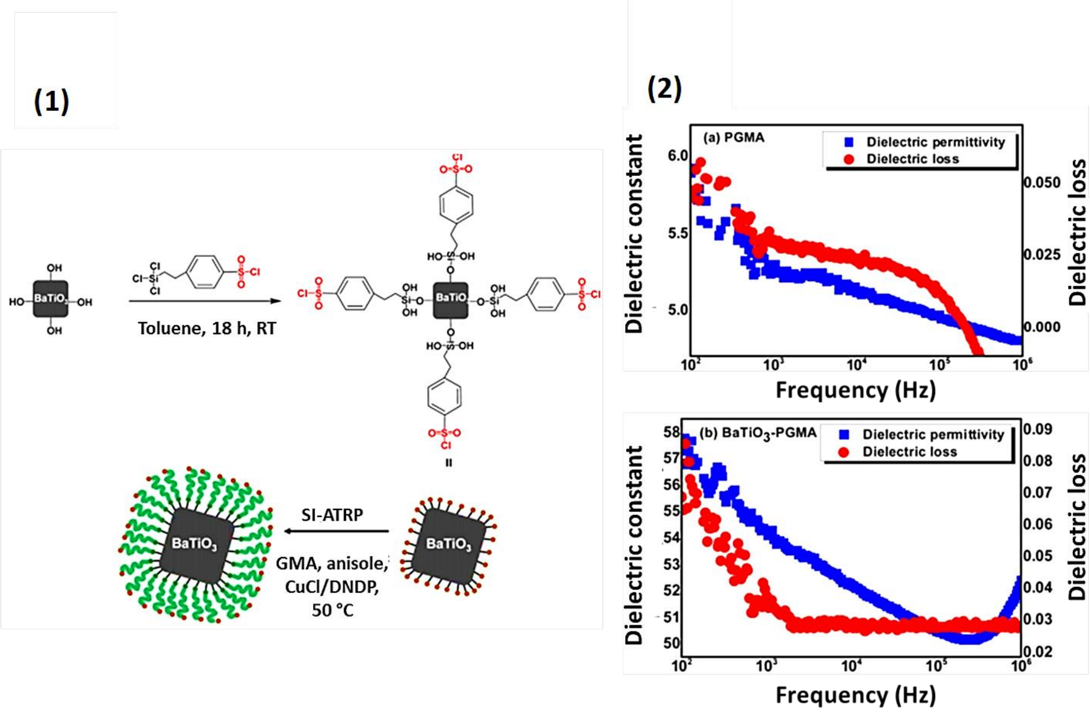

Figure 15. (1) Synthesis of $BaTiO_3$-PGMA core-shell nanocomposites by SI-ATRP of glycidyl methacrylate (GMA) from $BaTiO_3$ nanoparticles. (2) Frequency dependent dielectric properties at 100 -1 MHz: (a) PGMA and (b) $BaTiO_3$-PGMA nanocomposite. Reproduced with permission of [25]. Copyright 2015 Wiley.

I.4.2.2.6. PHEMA-b-PHEMA@BT or PHEMA-b-PANa@BT

Huang *et al*. [116] prepared a well- defined core@shell structured nanocomposites by ATRP polymerization of (meth)acrylates. Since the resulting polymer in ATRP is still “living” after polymerization, it can reinitiate the polymerization of a second monomer to further yield block copolymers. Thus, a double shell polymer was grafted onto the first core@shell (Scheme 4). Three types of (meth)acrylate monomers were used: poly(methyl methacrylate) (PMMA), poly(2-hydroxyethylmethacrylate) (PHEMA) and poly(sodium acrylate) (PANa).

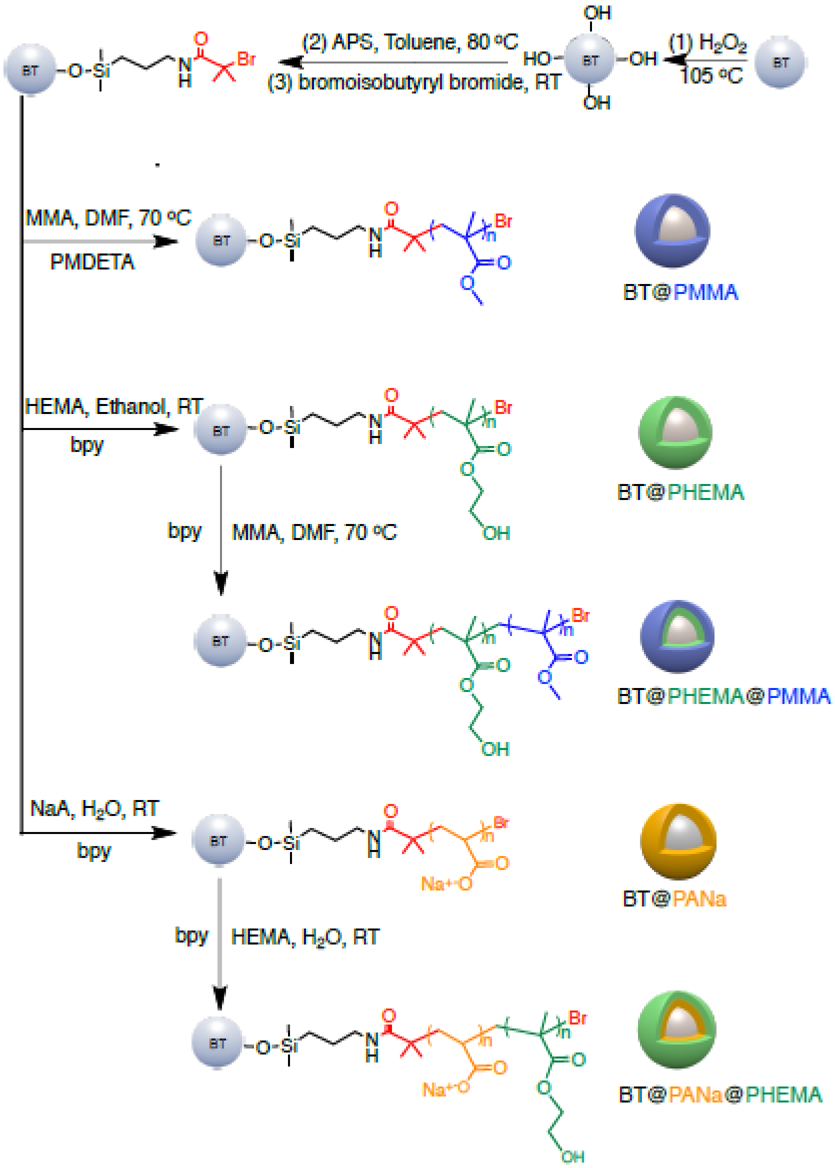

Scheme 4. Diagram illustrating the preparation processes of BT@shell structured nanocomposites. Reproduced with permission of [116]. Copyright 2016 American Chemical Society.

The first shell was chosen to display both high dielectric permittivity and electrical conductivity to provide high polarization, while the second one was selected to be more insulating to maintain a large resistivity and low loss. Figure 16 exhibits the measured DC conductivity of neat polymers and core@shell structured BT nanocomposites. It can be clearly seen that the PHEMA exhibits a higher conductivity than that of PMMA. This high value comes from the fact that PHEMA presents highly polar –OH groups making it more sensible to impurities like water or ions, which increase its conductivity. Indeed, BT@PHEMA@PMMA is close to that of BT@PMMA, while that of PMMA/PHEMA mixture presents a conductivity close to that of PHEMA. This could indicate the successful grafting of the polymer shell, and the more conductive PHEMA shell being well-isolated by the less conductive PMMA.

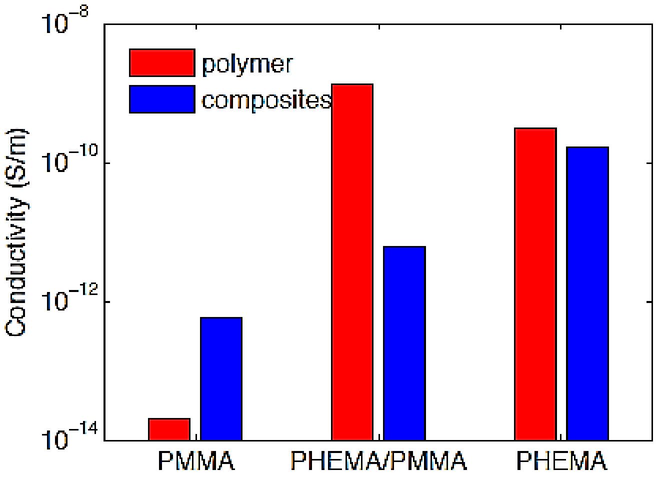

Figure 16. The measured dc conductivity of neat polymers and BT@shell structured nanocomposites under a dc voltage of 10 V. Reproduced with permission of [116]. Copyright 2016 American Chemical Society.

I.4.2.2.7. PMMA@BT/ PGMA@BT/PHEMA@BT

Zhu *et al.* [73] prepared three kinds of polymer nanocomposites using core@shell structured polymer@BT nanoparticles. $BaTiO_3$ nanofillers were functionalized with PMMA, PGMA and PHEMA by RAFT polymerization, where the polymer shells were controlled (reaction time) to have the same shell thickness (Scheme 5).

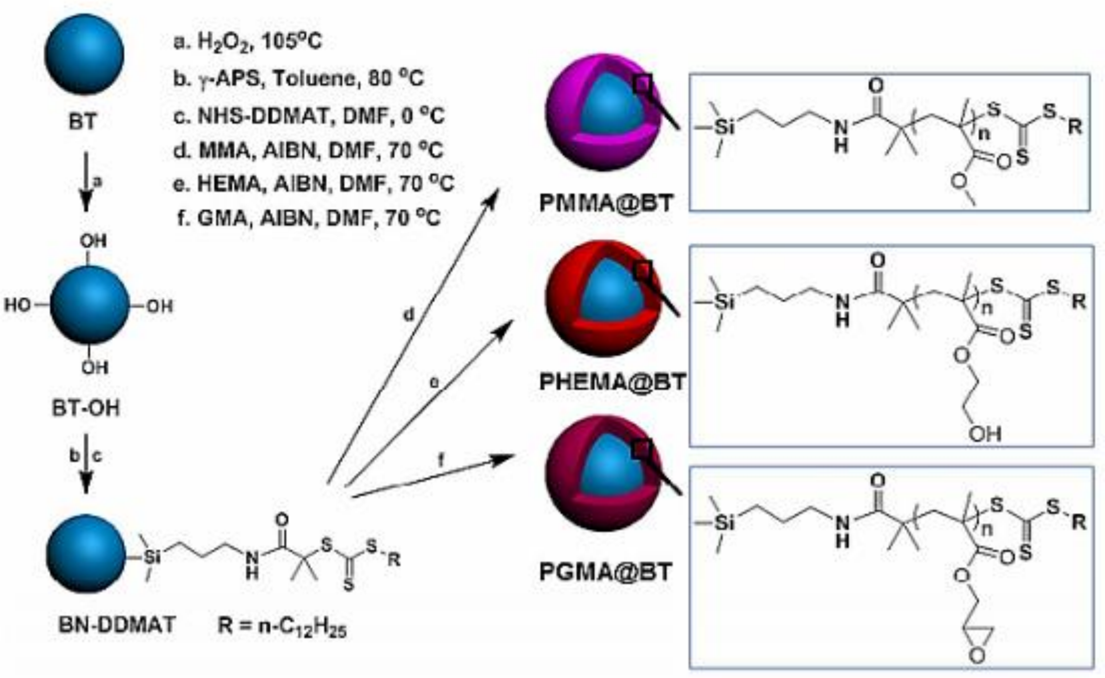

Scheme 5. Preparation process of the polymer@BT nanoparticles by surface initiated RAFT polymerization of various monomer (methyl methacrylate, glycidyl methacrylate and 2-hydroxyethyl methacrylate). Reproduced with permission of [73]. Copyright 2014 American Chemical Society.

Figure 17 exhibits the TEM images of the polymer functionalized nanoparticles. The BT nanofillers are homogenously encapsulated by a thin layer of polymer, the thickness of which varies from 2-3 nm.

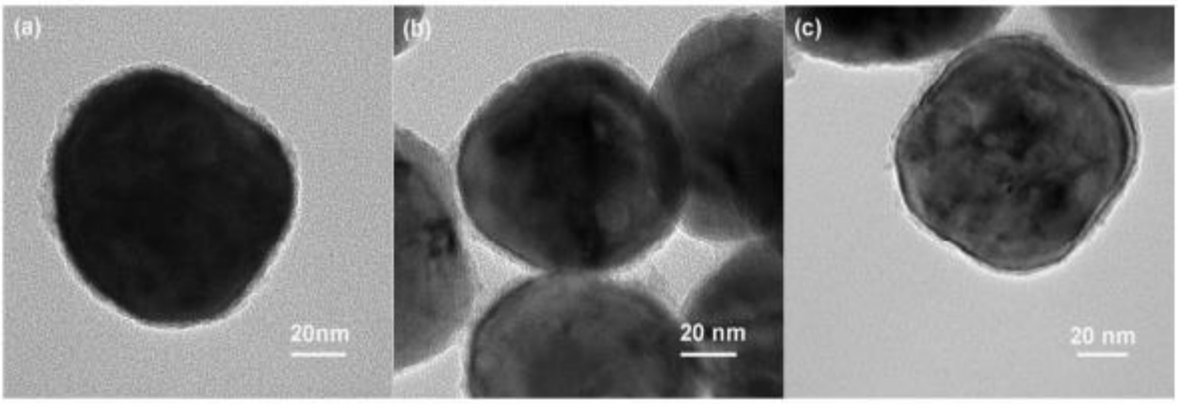

Figure 17. TEM images of the synthesized of poly(methacrylate)@BT nanocomposites using different polymer shells by RAFT polymerization (a) PMMA, (b) PHEMA and (c) PGMA. Reproduced with permission of [73]. Copyright 2014 American Chemical Society.

I.4.2.2.8. PHFDA@BT and PTFEA@BT

Yang *et al.* [27] used two types of fluoroalkyl acrylates, 1H,1H,2H,2-Heptadecafluorodecyl acrylate (HFDA) and 2,2,2-trifluoroethyl acrylate (TFEMA) to functionalize BT surface by RAFT polymerization. These monomers were used to reduce the surface energy of BT nanoparticles and improved their compatibility with the polymer host matrix. The different analyses performed on the functionalized nanoparticles indicate the successful grafting of the two fluopolymers and the higher grafting density of PTFEMA@BT (0.031 chains/nm^2) compared to that of PHFDA@BT (0.021 chains/nm^2) (Table 6). This could be explained by the fact that the long fluoroalkyl groups of PHFDA leading to more larger steric hindrance.

Table 6. Characteristics of the Fluoro-Polymer@BaTiO$_3$ Hybrid Nanoparticles. Reproduced with permission of [27]. Copyright 2013 American Chemical Society.

Sample	*BT-PHFDA1*	*BT-PHFDA2*	*BT-PTFEA1*	*BT-PTFEA2*
Weight loss of nanopartilces (%) [a]	3.45	6.69	3.83	7.09
Mn *of grafting polymer (g/mol)* [b]	4.1×10^3	7.5×10^3	3.4×10^3	5.9×10^3
Mw/Mn *of grafting polymer* [b]	1.23	1.18	1.21	1.16
Grafting density (chains/nm^2) [c]	0.021	0.014	0.031	0.026

[a] *Calculated from TGA results based on the weight loss of BT-EDMAT nanoparticles.* [b] *Obtained from GPC results.* [c] *Considering each particle with d=100 nm and density of 6.02 g/cm^3.*

I.4.2.2.9. PTFMPCS@BT

Chen *et al.* [86] prepared core shell structured BaTiO$_3$@rigid-fluoropolymer nanoparticles from the RAFT polymerization of 2,5-bis{[4-trifluoro(methoxyphenyl)oxycarbonyl]styrene}. By varying the monomer: BT feed ratios, the resulting nanocomposites were denoted as BT-3F1, BT-3F2, and BT-3F3, in which BT-3F1 and BT-3F3 had the thinnest and the thickest polymer shells, respectively. Figure 18 exhibits the TEM images of the functionalized nanoparticles where BT-3F0 refers to unmodified BT. After grafting the polymer from the functionalized nanoparticles, a stable and dense polymer shell was covering the surface of the nanoparticles. The shell thickness varied from 4 to 12 nm (Figure 18), suggesting the successful modification of nanoparticles.

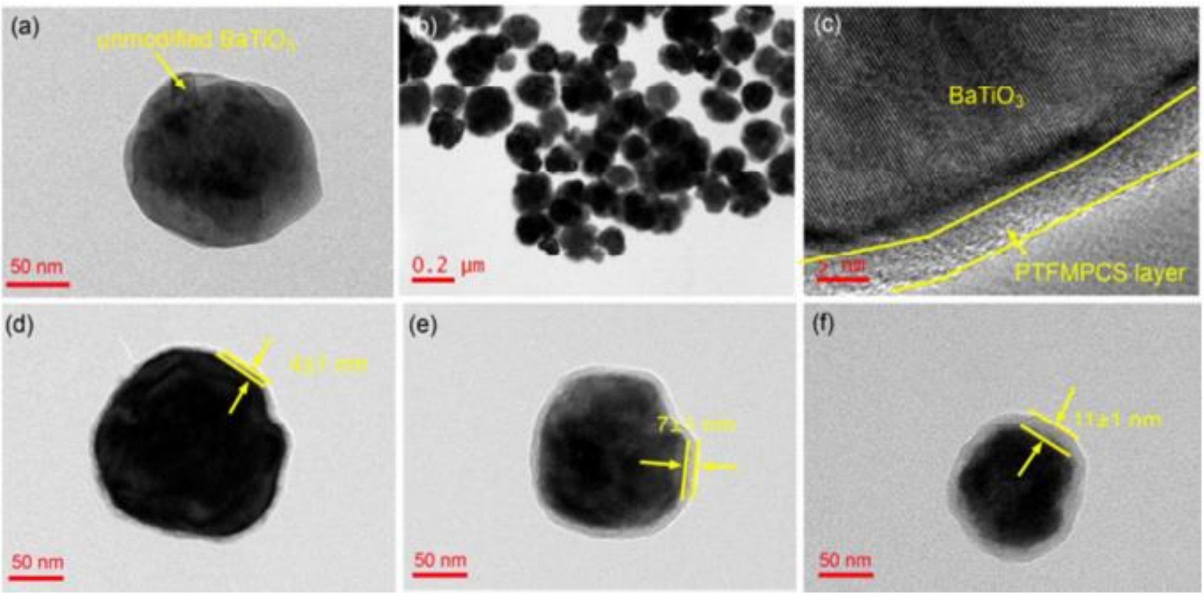

Figure 18. TEM images of (a) BT-3F0, (b) (c) (d) BT-3F1, (e) BT-3F2, and (f) BT-3F3 functionalized BT nanoparticles via RAFT polymerization of 2,5-bis{[4-trifluoro(methoxyphenyl)oxycarbonyl]styrene}. Reproduced with permission of [86]. Copyright 2018 Royal Society of Chemistry.

I.4.2.2.10. P3F, P5F or P7F@BT

Qian *et al.* [117] prepared three kinds of nanocomposites consisting of BT as nanofiller and fluorinated polymers as a matrix using RAFT polymerization (Scheme 6). The three monomers were first synthesized and denoted as poly{2,5-bis[(4-trifluoro(methoxyphenyl)oxycarbonyl]styrene} (P-3F), poly{2,5-bis[(2,3,4,5,6-pentafluoro) oxycarbonyl]styrene} (P-5F), and poly{2,5-bis[(2,3,5,6-tetrafluoro-4-trifluoromethyl)oxycarbonyl]styrene} (P-7F).

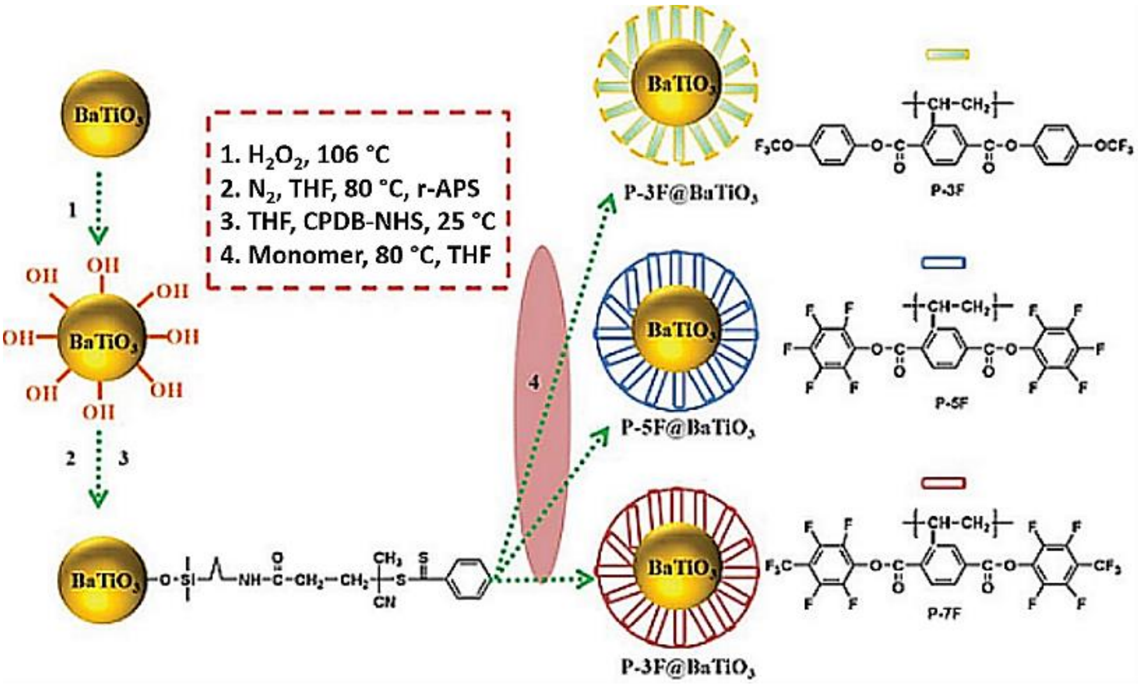

Scheme 6. Synthesis process of fluoropolymer@BaTiO$_3$ nanoparticles starting from BaTiO$_3$ surface functionalization then RAFT polymerization of three kinds of aromatic fluoromonomers. Reproduced with permission of [117]. Copyright 2018 Royal Society of Chemistry.

The functionalized nanoparticles were characterized to evidence the successful surface modification. Figure 19-A exhibits the TEM images recorded for the nanocomposites and it clearly evidences the dense polymer shell covering the nanoparticles, where the thickness of which was around 7 nm. A mapping pattern images were also achieved on P-3F@BT nanocomposites where the different colors are attributed to Ba, Ti, O and F elements, which indicate that the fluoropolymers were successfully introduced onto the BT surface (Figure 19-B).

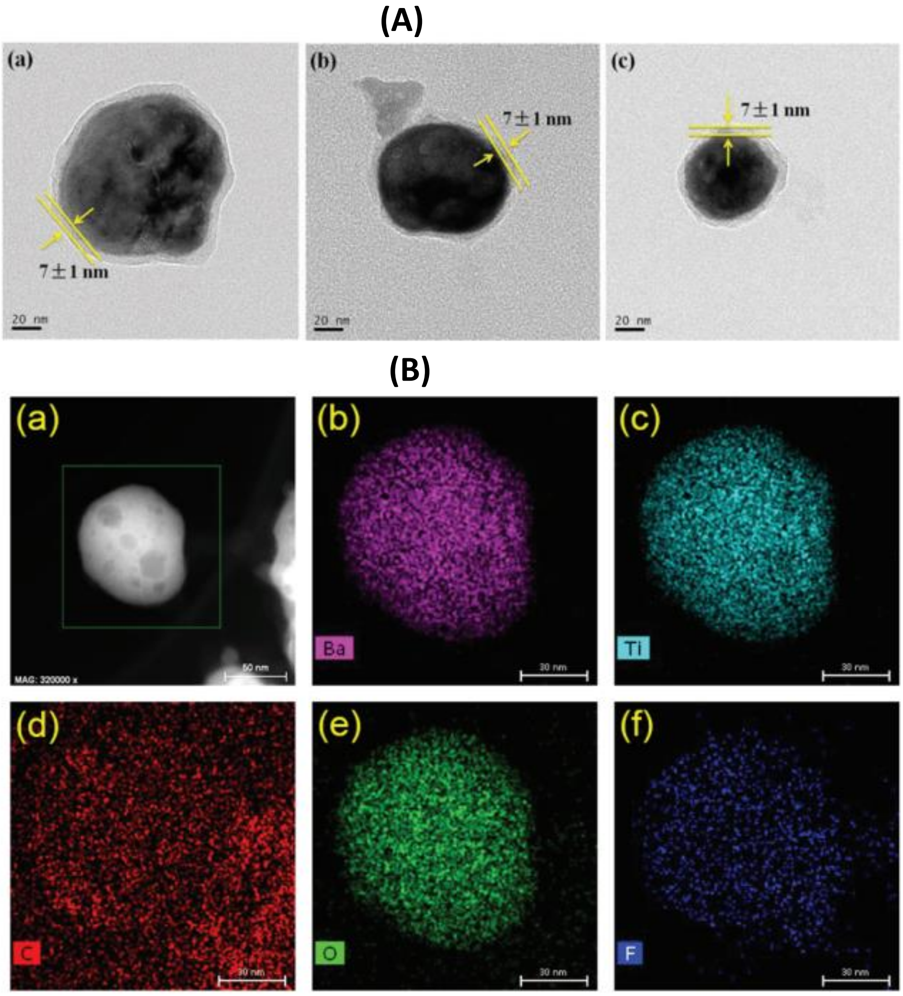

Figure 19. (A) TEM images of (a) P-3F@ $BaTiO_3$, (b) P-5F@ $BaTiO_3$, and (c) P-7F@$BaTiO_3$ nanoparticles and (B) mapping pattern images of BT nanoparticles modified by P-3F. Reproduced with permission of [117]. Copyright 2018 Royal Society of Chemistry.

I.4.2.2.11. PM7F@BT

Lv *et al.* [118] functionalized BT platelets with a fluoropolymer to improve their dispersion and compatibility in the nanocomposite. The fluoro-monomer (2,5-bis[(2,3,5,6-tetra fluoro-4-trifluoromethyl)oxycarbonyl]styrene, M7F) was first synthesized (Scheme 7) then grafted onto BT platelets surface by RAFT polymerization.

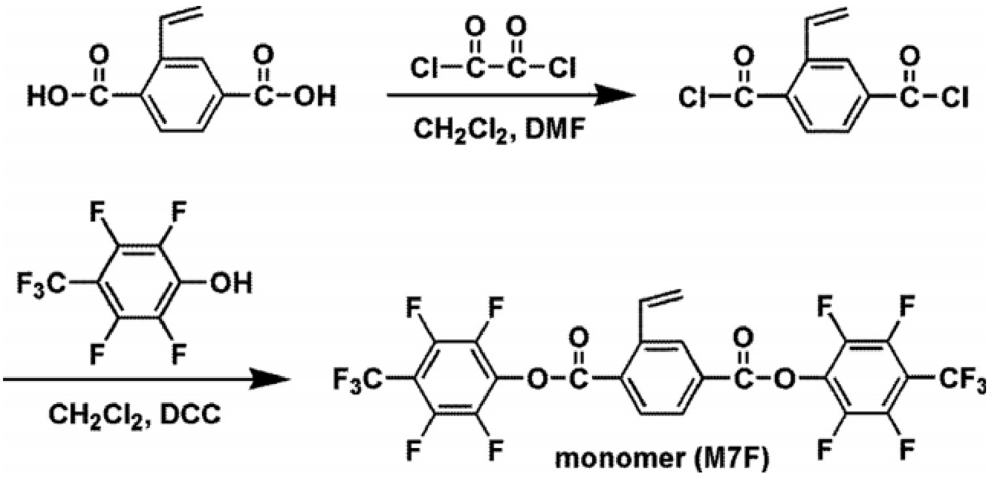

Scheme 7. Synthetic route to M7F styrene. Reproduced with permission of [118]. Copyright 2018 Elsevier.

It was found that the resulting platelets present a uniform morphology and the average thickness was about 1 µm. After immobilization of PM7F onto the functionalized platelets, different characterizations were performed and the results prove the successful grafting of this fluoropolymer onto the functionalized BT. Figure 20 exhibits TEM image of PM7F@BT nanocomposite, where the polymer layer can be clearly seen and covering BT platelets with a thickness of 12.7 nm. Moreover, the structural unit in the molecular chain of this fluoropolymer contains 14 fluorine atoms, resulting in a decreased surface energy of BT platelets.

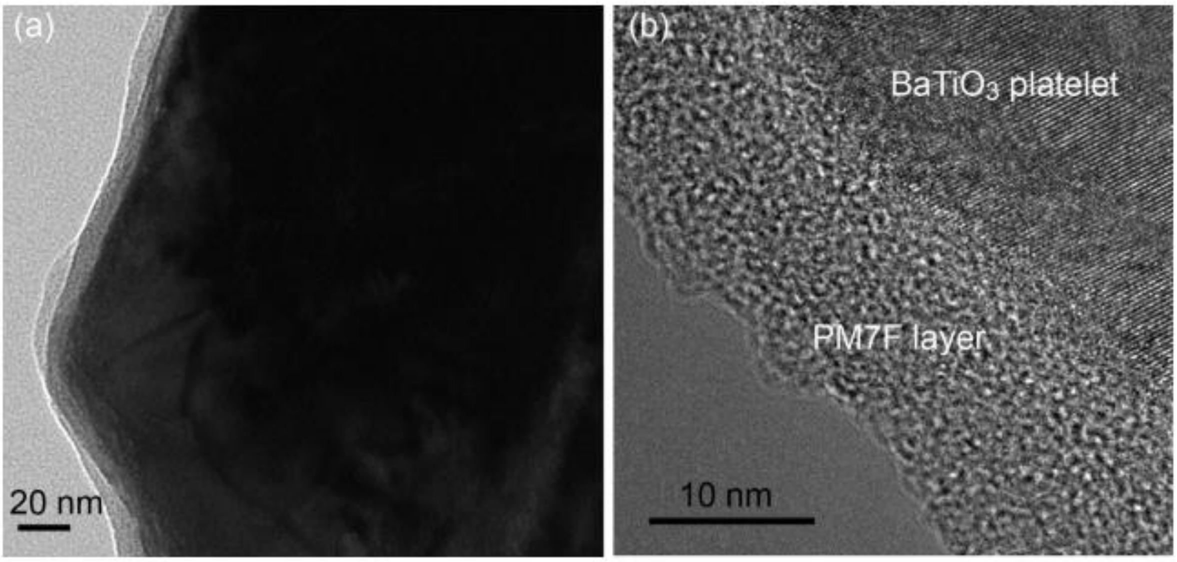

Figure 20. (a) TEM image and (b) high-resolution TEM image of $BaTiO_3$-PM7F. Reproduced with permission of [118]. Copyright 2018 Elsevier.

I.4.2.3. Modification of $BaTiO_3$ with polymer to prepared by "Grafting onto" route

I.4.2.3.1. PS or PMMA@BT

Using the "grafting onto" technique, Yang *et al.* [119] reported another approach to functionalize BT nanoparticles with polymer in order to prepare nanocomposites made by either PS or PMMA. In a first step, RAFT polymerization enabled to synthesize thiol-terminated PS and PMMA. Then, three nanocomposites were obtained with different molecular weights by means of thiol-ene click reaction between the functionalized nanoparticles by alkyl methacrylates and ω-thiol polymers (Figure 21). Dielectric measurements revealed that the dielectric constant of the synthesized nanocomposites was significantly enhanced in comparison to the pure polymers (3.69 for PMMA and 2.74 for PS at 1 kHz).

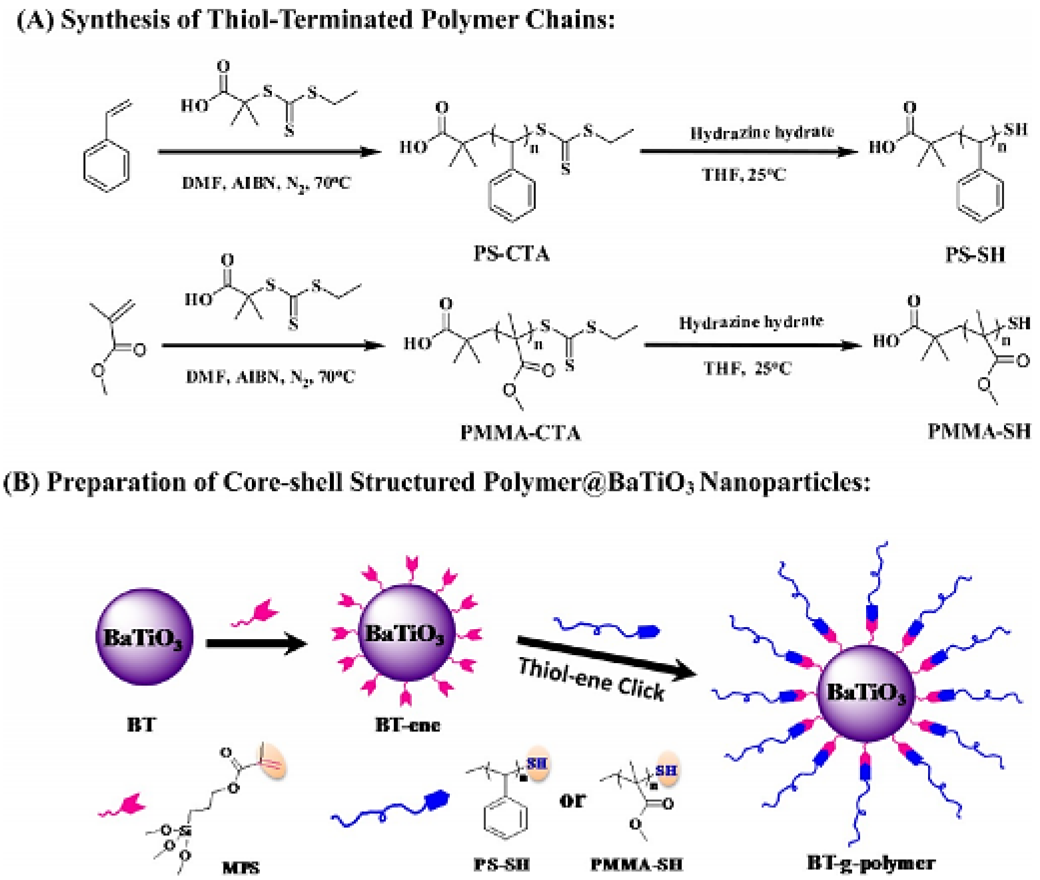

Figure 21. Schematic Illustration for (A) Synthesis of thiol-terminated Polymer Chains via RAFT polymerization and (B) Preparation of Core−Shell Structured Polymer@$BaTiO_3$ Nanocomposites by Thiol−Ene Click Reaction with modified $BaTiO_3$. Reproduced with permission of [119]. Copyright 2014 American Chemical Society.

I.4.2.3.2. PS or PVDF@BT

Ma *et al.* [85] used thiol-terminated PVDF (PVDF-SH) and polystyrene (PS-SH) to functionalize BT surface. PVDF-SH and PS-SH were synthesized in a two steps process, starting from a RAFT polymerization, followed by the aminolysis as depicted by in Figure 22-a. The as prepared polymers were used to functionalize BT-ene nanoparticles using thiol-ene click reaction (Figure 22-b).

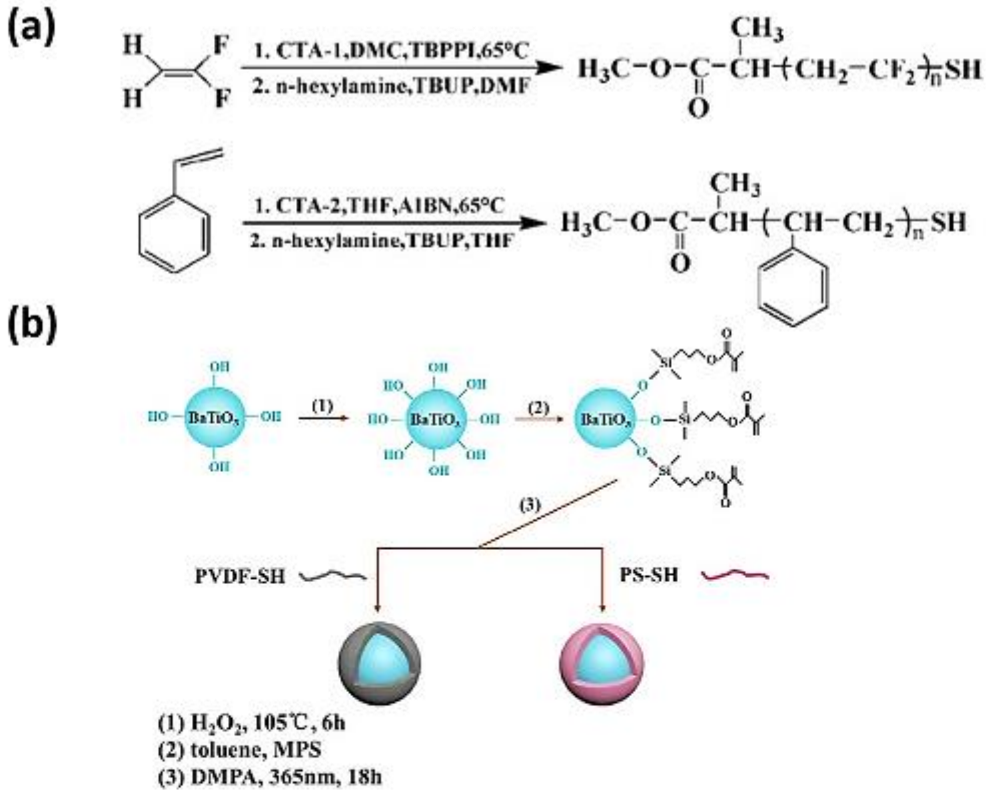

Figure 22. (a) Synthesis process for the preparation of thiol-terminated polymers (CTA-1 refers to O-Ethyl-S-(1-methoxycarbonyl)ethyldithiocarbonate and CTA-2 stands for 2-([(Dodecylsulfanyl)carbonothioyl]sulfanyl)-propanoic acid) and (b) Schematic diagram of the modification process of hybrid nanoparticles. Reproduced with permission of [85]. Copyright 2019 Elsevier.

The functionalized nanoparticles and the synthesized nanocomposites were fully characterized to give evidences on the successful surface modification and grafting of polymers. In addition, the TEM images of PS@BT and PVDF@BT nanocomposites highlight the nanoparticles surrounding by a thin polymer shell with a thickness of ~ 6 nm (Figure 23).

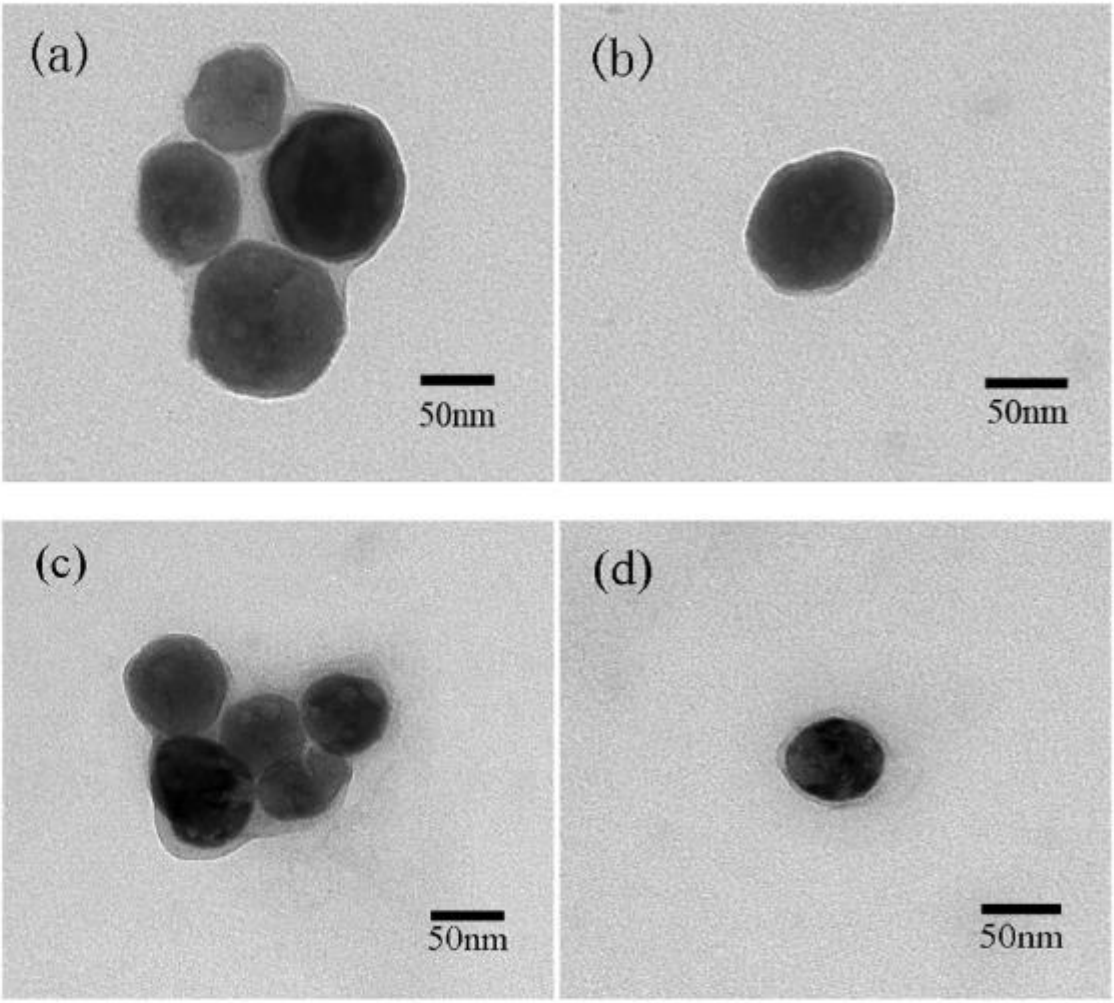

Figure 23. TEM images of PVDF@BT (a, b) and PS@BT (c, d) nanocomposites synthesized by thiol-ene click reaction. Reproduced with permission of [85]. Copyright 2019 Elsevier.

I.4.2.3.3. P(VDF-HFP-GMA)@BT

Xie *et al.* [88] modified BT surface using commercially available poly(VDF-*co*-HFP) functionalized with PGMA by ATRP polymerization. BT nanoparticles were first modified by amino-terminated silane molecules, then, the nanocomposites were prepared by a solution blending method leading to a covalent bonding between the epoxy groups of GMA and amino groups at the surface of modified BT nanoparticles.

To prove the successful grafting of the polymer chains onto the nanoparticles surfaces, the as prepared nanocomposites were re-dissolved in DMF and washed several times in order to remove the free polymer chains. After purification, TEM analysis evidences that BT nanoparticles were coated by a polymer layer, ensuring the successful grafting of PVDF-HFP-GMA onto BT surface (Figure 24).

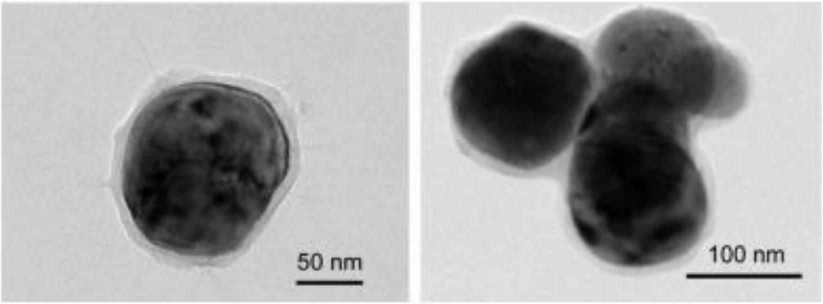

Figure 24. TEM images of the washed PVDF-HFP-GMA grafted BT nanoparticles showing a PVDF-HFP-GMA layer of about 10 nm. Reproduced with permission of [88]. Copyright 2014 Royal Society of Chemistry.

I.4.3. Design of core-shell $BaTiO_3$@polymer/Fluorinated polymer nanocomposites

Recent reviews have summarized the synthesis of $BaTiO_3$ and its surface modification, and their introduction into polymer matrix to get dielectric nanocomposites [120,121]. A detailed review on ferroelectric polymers was also reported by Prateek *et al.* [78]; especially the use of PVDF and its VDF-based copolymer blends in dielectric composites materials for high energy capacitor applications. Regarding the importance of these fluoropolymers and their role in enhancing the final properties of the nanocomposite, further studies are moving toward the elaboration of nanocomposites consisting of a single core and a polymer double shell to get better properties. Herein, we discuss the system based on $BaTiO_3$ nanocomposites modified with a second shell based on a fluorinated polymer according to Scheme 1-b.

I.4.3.1. PMMA@BT/poly(VDF-*co*-HFP)

Wang *et al.* [112] prepared three phase poly(VDF-*co*-HFP)/BTO@TMPc-PMMA nanocomposite films. First, BT nanoparticles were modified by ATRP polymerization of MMA (See section I.4.2.2.1). Then, poly(VDF-*co*-HFP)/BTO@TMPc-PMMA nanocomposites were obtained by a simple mixing of poly(VDF-*co*-HFP) copolymer with the functionalized nanoparticles (Figure 25).

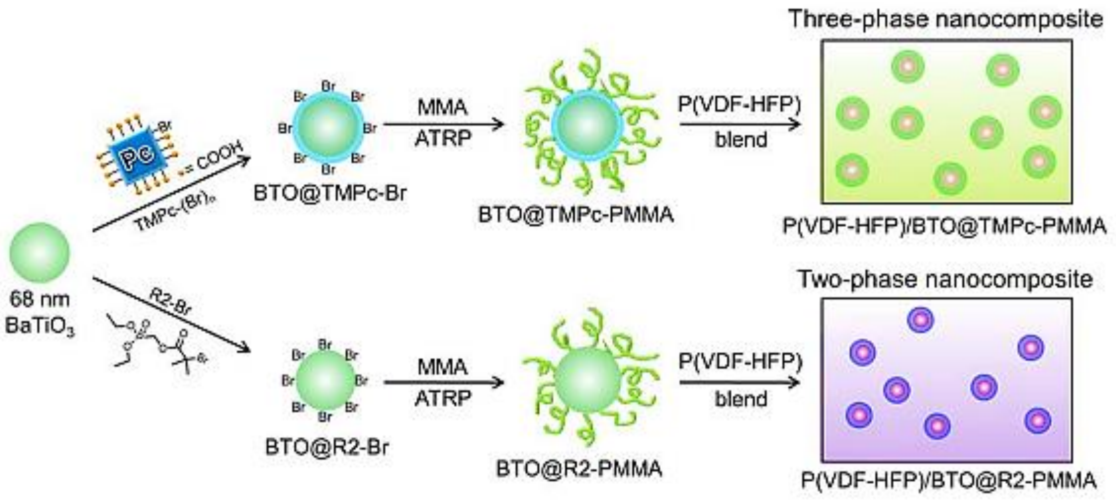

Figure 25. Schematic illustration of the preparation of three- and two-phase poly(VDF-*co*-HFP)/BaTiO$_3$ nanocomposites, respectively. Reproduced with permission of [112]. Copyright 2014 Wiley.

Dielectric measurements on the synthesized nanocomposites indicated that the dielectric constant (ε_r) slightly decreased when the frequency increased (Figure 26). In the case of the three-phase composite films, the introduction of the highly polarizable TMPc improved the permittivity significantly, in comparison with the two phase-composite films. Moreover, the dielectric loss (tan δ) was found to be relatively low (tan δ = 0.02 below 2 kHz) and overlapped with that of the neat poly(VDF-*co*-HFP) copolymer, which indicates that BT nanoparticles did not add additional loss to the system. However, the increase of tan δ at around 10^7 MHz could be attributed to the relaxation phenomenon of the amorphous poly(VDF-*co*-HFP).

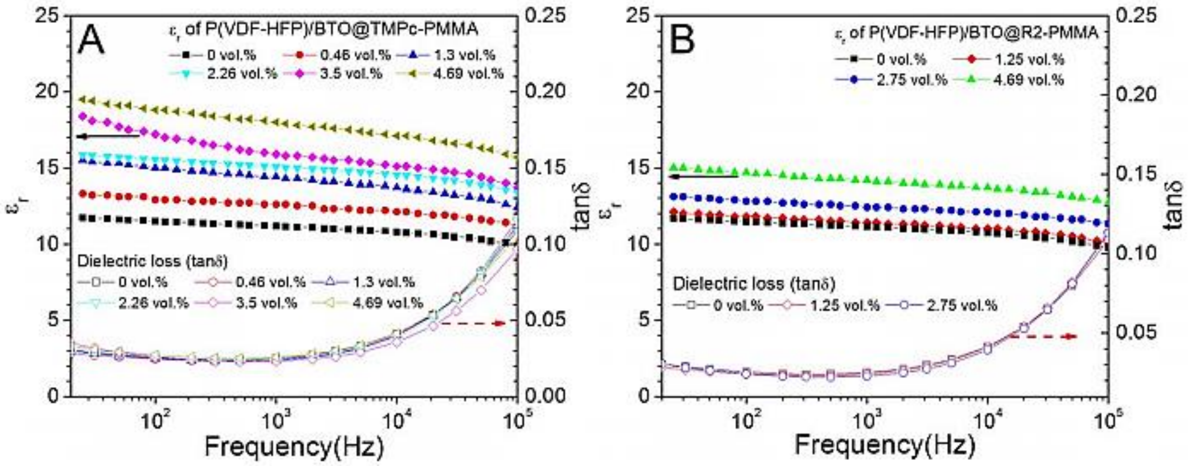

Figure 26. Relative dielectric constant (ε_r) and dielectric loss (tan δ) as a function of frequency for (A) uniaxially stretched poly(VDF-*co*-HFP)/BTO@TMPc-PMMA and (B) uniaxially stretched poly(VDF-*co*-HFP)/BTO@R2-PMMA nanocomposite films, respectively. Reproduced with permission of [112]. Copyright 2014 Wiley.

I.4.3.2. PTFEMA@BT or PMMA@BT/PVDF

Zhang *et al.* [113] prepared core shell structured BT nanoparticles with two different shell compositions and thicknesses (7 and 12 nm for PMMA@BT and 4.5 and 5.5 nm for PTFEMA@BT) by grafting PMMA and PTFEMA via ATRP polymerization (Section I.4.2.2.2). Then, the resulting nanocomposites were incorporated into PVDF matrix by solution blending (Scheme 8).

Authors reported that higher dielectric constant and lower dielectric loss were achieved for both systems in comparison to those of pure PVDF. For example, after adding 80 wt % of PMMA@BT in the PVDF matrix, the dielectric permittivity increased from 6 to 30 at 100 Hz. Moreover, nanocomposites obtained by modification of BT with the fluorinated polymer (PTFEMA) led to lower dielectric loss (0.025 at 100 kHz) and high dielectric constant in comparison to those modified with PMMA (0.022 at 100 kHz), explained by the strong interchain forces between the two fluorinated shells matrix.

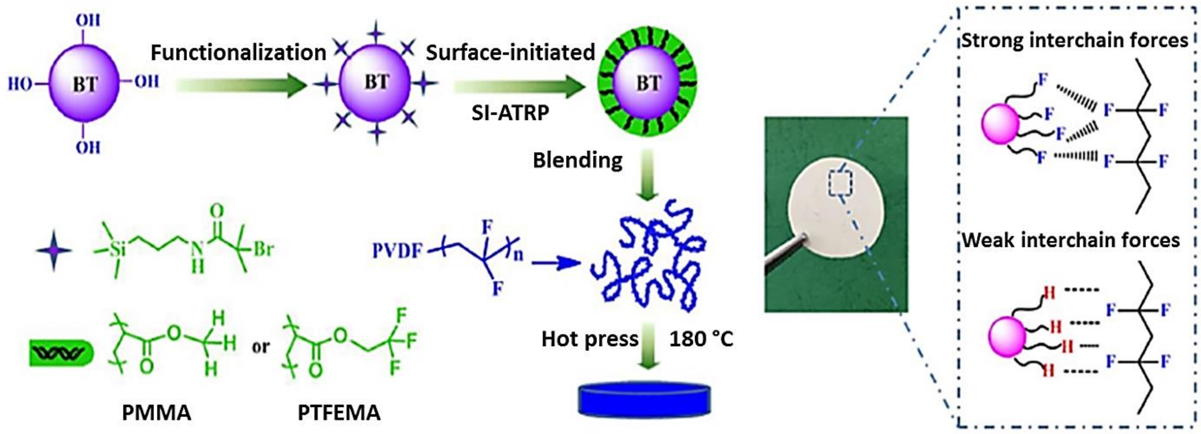

Scheme 8. Illustration for the preparation of BT@polymer/PVDF nanocomposite films. Reproduced with permission of [113]. Copyright 2017 Elsevier.

I.4.3.3. Poly(*tert*-butyl-methacrylate) @BT/PVDF

Du *et al.* [115] used P*t*BA to functionalize BT surface by ATRP polymerization (See section I.4.2.2.4). Then, the modified nanoparticles were mixed into a PVDF matrix. Results showed that the dielectric constant of the nanocomposites increased by increasing the P*t*BA@BT content from 8.5 for the pure PVDF to 15 for nanocomposite with 30 wt % of functionalized nanoparticles (Figure 27).

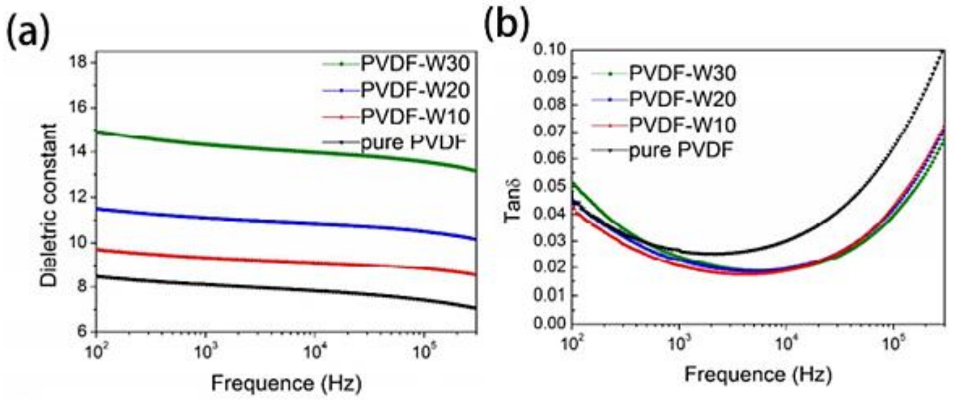

Figure 27. Frequency dependence of room temperature a) dielectric constant and b) loss tangent for PVDF-based films. Reproduced with permission of [115]. Copyright 2018 American Chemical Society.

In order to be able to see the effect of P*t*BA polymer, films of PVDF based on non-functionalized BT were prepared. The dielectric measurements of PVDF/BT nanocomposites show low dielectric permittivities in comparison to those of P*t*BA@BT/PVDF (The dielectric constant at 100 Hz was 14.5 for PVDF/BT and was enhanced to 15 for PVDF-W30)

(Figure 28). This can be attributed to the fact that the non-treated nanoparticles tend to form aggregations and leads to poor dispersion in the polymer matrix which results in decreased performances.

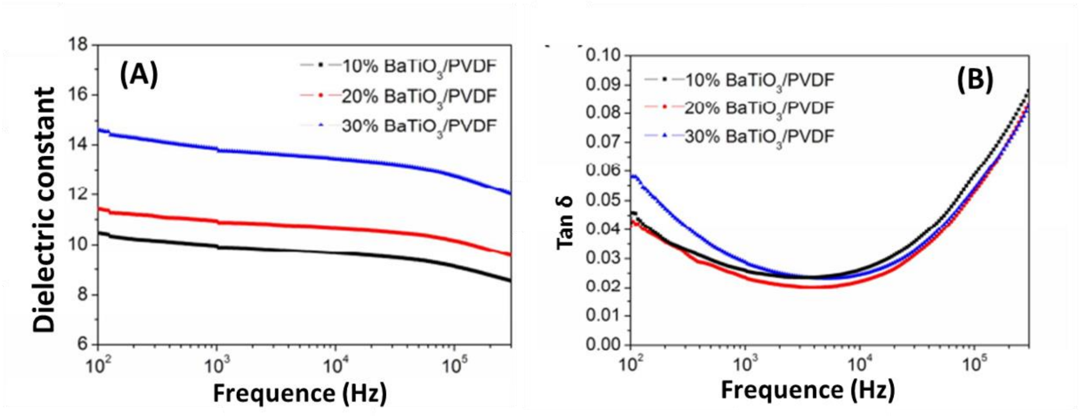

Figure 28. Frequency dependence of room temperature (a) dielectric constant and (b) loss tangent for $BaTiO_3$/PVDF films. Reproduced with permission of [115]. Copyright 2018 American Chemical Society.

Moreover, the functionalization of BT nanofillers with P*t*BA not only avoids aggregation of the nanoparticles inside the PVDF matrix, but also preserves excellent mechanical properties of the polymer, which leads to good flexibility and integrated surface micromorphology.

I.4.3.4. (PMMA or PHEMA or PGMA)@BT/PVDF

Zhu *et al.* [73] prepared three kinds of polymer nanocomposites using core shell structured polymer@BT nanoparticles as filler and PVDF as the polymer matrix.

The first core shell nanocomposite was synthesized using RAFT polymerizations of MMA, GMA and HEMA from functionalized nanoparticles (See section I.4.2.2.7). Then, a second shell of PVDF was introduced by a simple blending and hot pressing of the nanocomposite. Dielectric measurements revealed that, compared with the PVDF matrix, all the nanocomposites displayed enhanced dielectric constant and follows the order PHEMA@BT/PVDF (~21 at 10^2 Hz) > PGMA@BT/PVDF (~18 at 10^2 Hz) > PMMA@BT/PVDF (~16 at 10^2 Hz) (Figure 29). This indicates that, at the same BT content, the dielectric constant of the resulting nanocomposite is determined by the dielectric constant of the interfacial region. Thus, nanocomposite processed from BT functionalized with PHEMA exhibits the highest permittivity due the large dipole moment of the pendant hydroxyethyl groups.

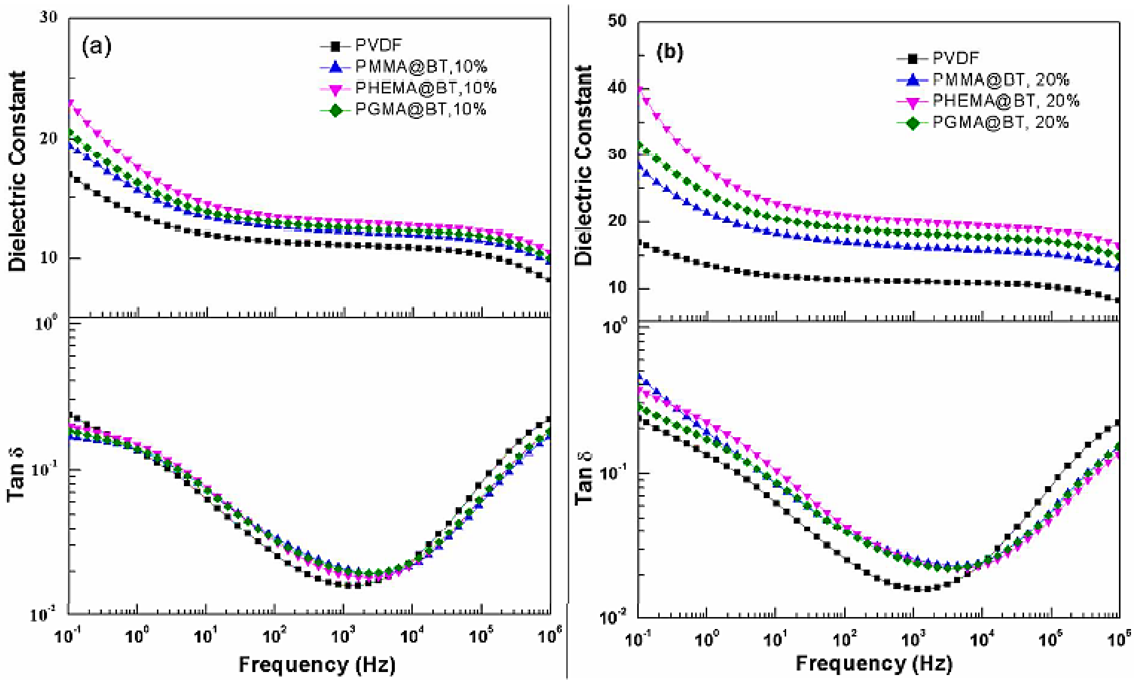

Figure 29. Frequency dependence of dielectric constant and dielectric loss tangent of the polymer@BT based PVDF nanocomposites (a) 10 vol % BT and (b) 20 vol % BT. Reproduced with permission of [73]. Copyright 2014 American Chemical Society.

I.4.3.5. PHFDA@BT or PTFEA@BT /poly(VDF-*co*-HFP)

Yang *et al.* [27] used two types of poly(fluoroacrylate) to functionalize BT surface by RAFT polymerization (See section I.4.2.2.8) before introducing them into poly(VDF-*co*-HFP) polymer matrix using a solution blending method (Scheme 9).

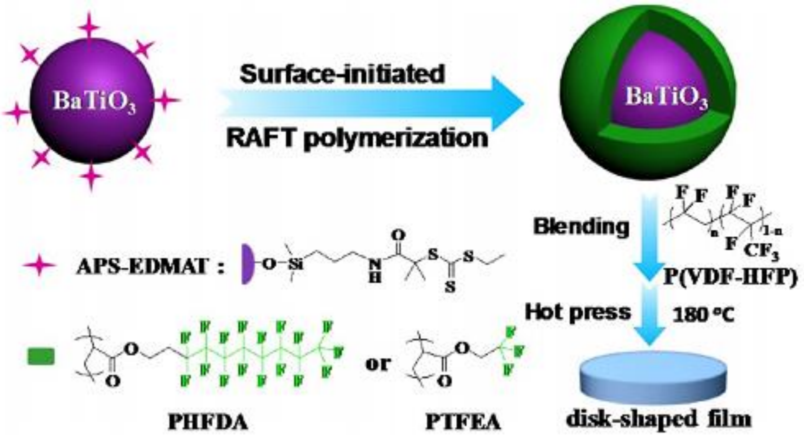

Scheme 9. Preparation of fluoro-polymer@BaTiO$_3$ nanoparticles and poly(VDF-*co*-HFP) nanocomposite films. Reproduced with permission of [27]. Copyright 2013 American chemical Society.

Actually, the functionalization of BT with poly(fluoroacrylate) not only led to enhanced energy storage capability of poly(VDF-*co*-HFP)/Fluoropolymer@BT nanocomposite in comparison with the pure copolymer, but also improved the dielectric properties. For instance, the energy density of the prepared nanocomposites was 5 times higher than that of the pure poly(VDF-*co*-HFP) under an electric field of 20 kV mm^{-1} , while the theoretical maximum energy density was 6.23 J cm^{-3}, which is 50% higher than that of the pure poly(VDF-*co*-HFP) (~4.10 J cm^{-3}).

I.4.3.6. PTFMPCS@BT / poly(VDF-*ter*-TrFE- *ter*-CTFE)

Chen *et al*. [86] used a rigid poly(fluorostyrene) to functionalize BT surface by RAFT polymerization of 2,5-bis{(4-trifluoromethoxyphenyl)oxycarbonyl}styrene with three different shell thicknesses (where BT-3F0 stand for pristine BT and BT-3F1, BT-3F2 and BT-3F3 nanocomposites present shell thicknesses of 4, 7 and 11 nm, respectively) (See Section I.4.2.2.9). The as prepared core shell structured nanoparticles were then incorporated into poly(VDF-*ter*-TrFE-*ter*-CTFE) *ter*-polymer matrix by varying their amount from 5 to 30 vol%. Morphological analysis showed the absence of pore and defects in the prepared nanocomposite films, which indicate that the functionalization of BT with fluoropolymer provides a strong interchain forces with the poly(VDF-*ter*-TrFE-*ter*-CTFE) host matrix. Figure 30 exhibits the dielectric permittivity and dielectric loss of the BT@Fluoropolymer/poly(VDF-t*er*-TrFE-*ter*-CTFE) nanocomposites films. For instance, the dielectric permittivity of poly(VDF-*ter*-TrFE-*ter*-CTFE) matrix was ~ 40 (at 1 kHz) and after introducing 30 vol% of BT-3F1 into poly(VDF-*ter*-TrFE-*ter*-CTFE) matrix, the dielectric permittivity increased from 40 to 80.6 (at 1 kHz). Moreover, by increasing the shell thickness of the nanoparticles (BT-3F3), and for the same filler loading, the dielectric permittivity decreased to ~ 60 (at 1 kHz). The results highlight that the dielectric behavior was significantly affected by the shell thickness and the permittivity of the nanocomposites films increased with the increase of BT@Fluoropolymer nanoparticles content.

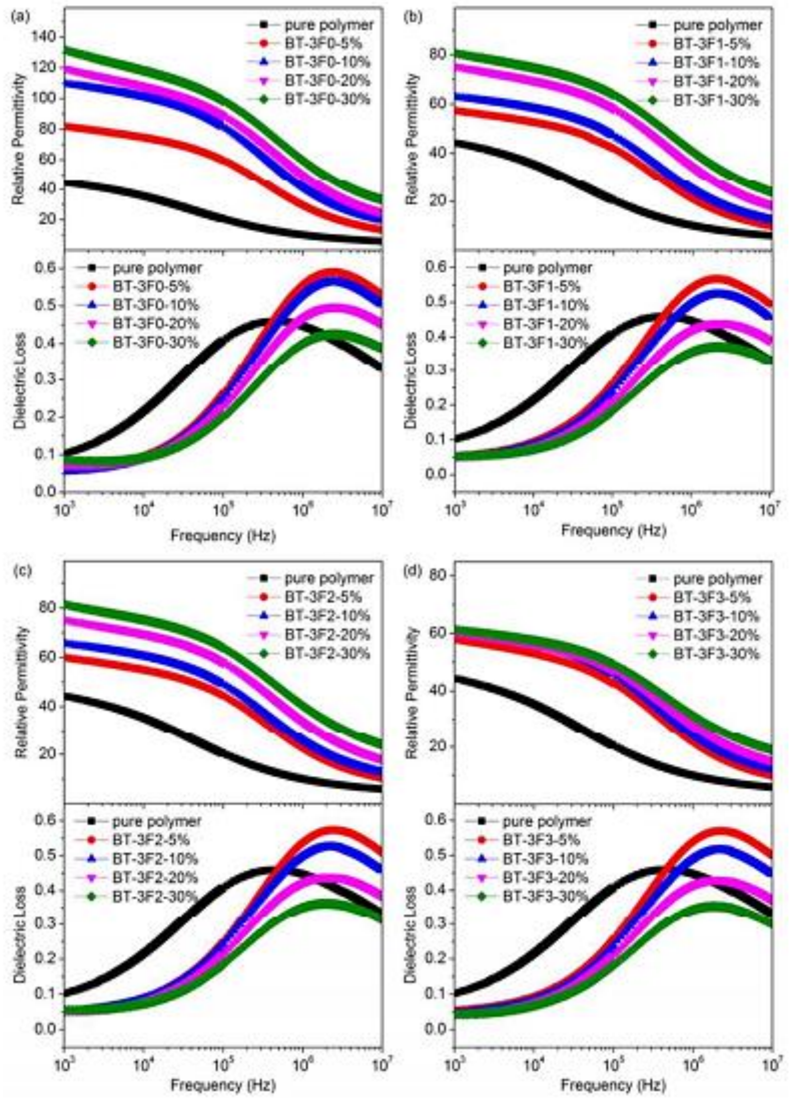

Figure 30. Frequency dependence of permittivity and dielectric loss of the $BaTiO_3$@rigid-fluoro-polymer/poly(VDF-*ter*-TrFE-*ter*-CTFE) nanocomposites films with (a) BT-3F0, (b) BT-3F1, (c) BT-3F2, and (d) BT-3F3. Reproduced with permission of [86]. Copyright 2018 Royal Society of Chemistry.

I.4.3.7. PM7F@BT/ poly(VDF-*ter*-TrFE- *ter*-CTFE)

Lv *et al*. [118] modified BT surface using a fluoropolymer that contains 14 fluorine atoms by RAFT polymerization of {2,5-bis[(2,3,5,6-tetra fluoro-4-

trifluoromethyl)oxycarbonyl]styrene} (Section I.4.2.2.11). Then, the functionalized nanoparticles were introduced into poly(VDF-*ter*-TrFE-*ter*-CTFE) host matrix (Scheme 10).

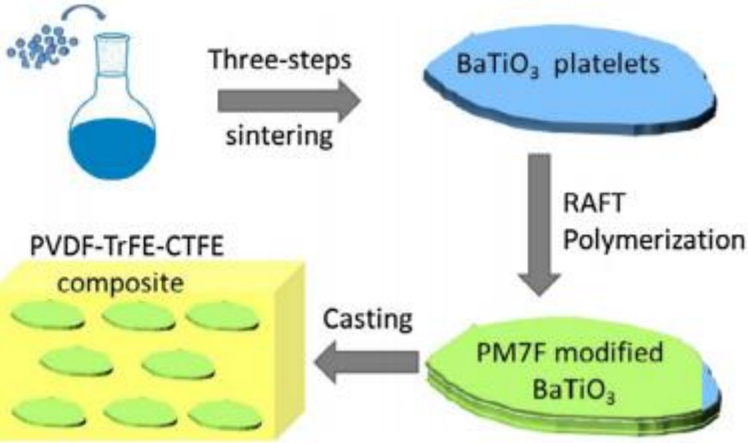

Scheme 10. Schematic illustration of BaTiO$_3$-PM7F/poly(VDF-*ter*-TrFE-*ter*-CTFE) nanocomposite films. Reproduced with permission of [118]. Copyright 2018 Elsevier.

Dielectric measurements revealed that the relative permittivity increased by increasing BT platelets volume fraction with a relatively small loading (Figure 31). At 1 kHz, the permittivity of nanocomposite with only 5 vol% of modified platelets was ~ 70 in comparison to the pure polymer that presents 45 and the enhancement in permittivity is more significant with increasing BT platelets volume fraction.

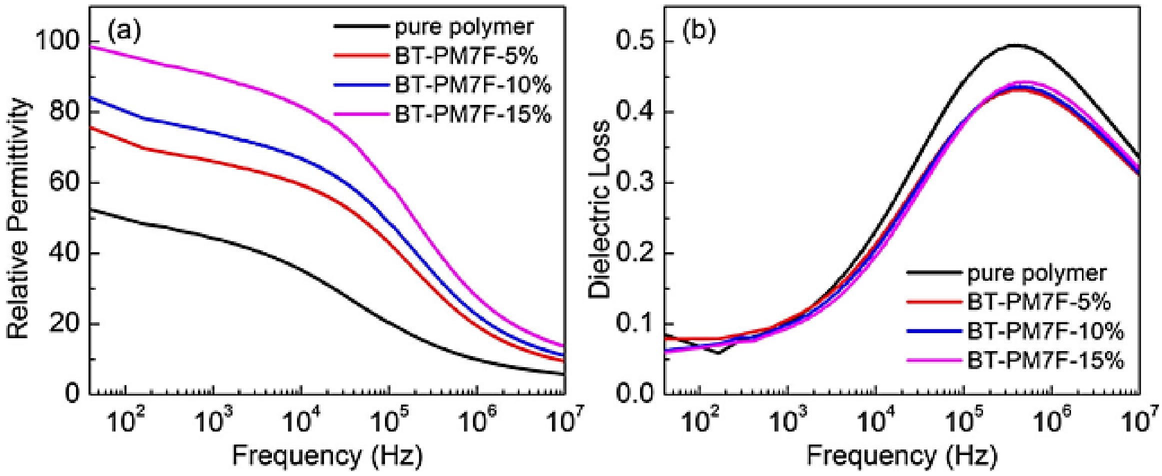

Figure 31. Frequency dependence of (a) permittivities and (b) dielectric loss for BaTiO$_3$-PM7F/poly(VDF-*ter*-TrFE-*ter*-CTFE) nanocomposites. Reproduced with permission of [118]. Copyright 2018 Elsevier.

I.4.3.8. P3F@BT or P5F@BT/ poly(VDF-*ter*-TrFE- *ter*-CTFE)

Qian *et al*. [117] prepared three kinds of nanocomposites consisting on BT nanoparticles and poly(VDF-*ter*-TrFE-*ter*-CTFE) polymer matrix. These nanoparticles were first modified with three types of fluoropolymers denoted as P-nF (n = 3, 5 or 7, is the number of terminal fluorinated groups), (Section I.4.2.2.10). Figure 32 exhibits the frequency dependence of permittivity of the poly(VDF-*ter*-TrFE-*ter*-CTFE)-based nanocomposites with different loading of functionalized BT nanoparticles. It can be seen that the permittivity of the nanocomposites increased by increasing the volume fraction of modified BT nanoparticles. For instance, in the case of P-3F@$BaTiO_3$/poly(VDF-*ter*-TrFE-*ter*-CTFE) nanocomposites, the permittivity increased from 55.4 to 88.5 at 1 kHz when the volume fraction of the modified BT nanoparticles was changed from 5 % to 30 %. On the other hand, when the BT surface was modified with P-7F polymers, the resulting nanocomposites exhibited the lowest permittivities (~ 67 at 30 % of modified BT). This was explained by the good dispersion of BT nanoparticles and the increase of interfacial adhesion between the modified nanoparticles and the polymer matrix, leading to limitation in the movement of molecular dipoles of the polymer matrix.

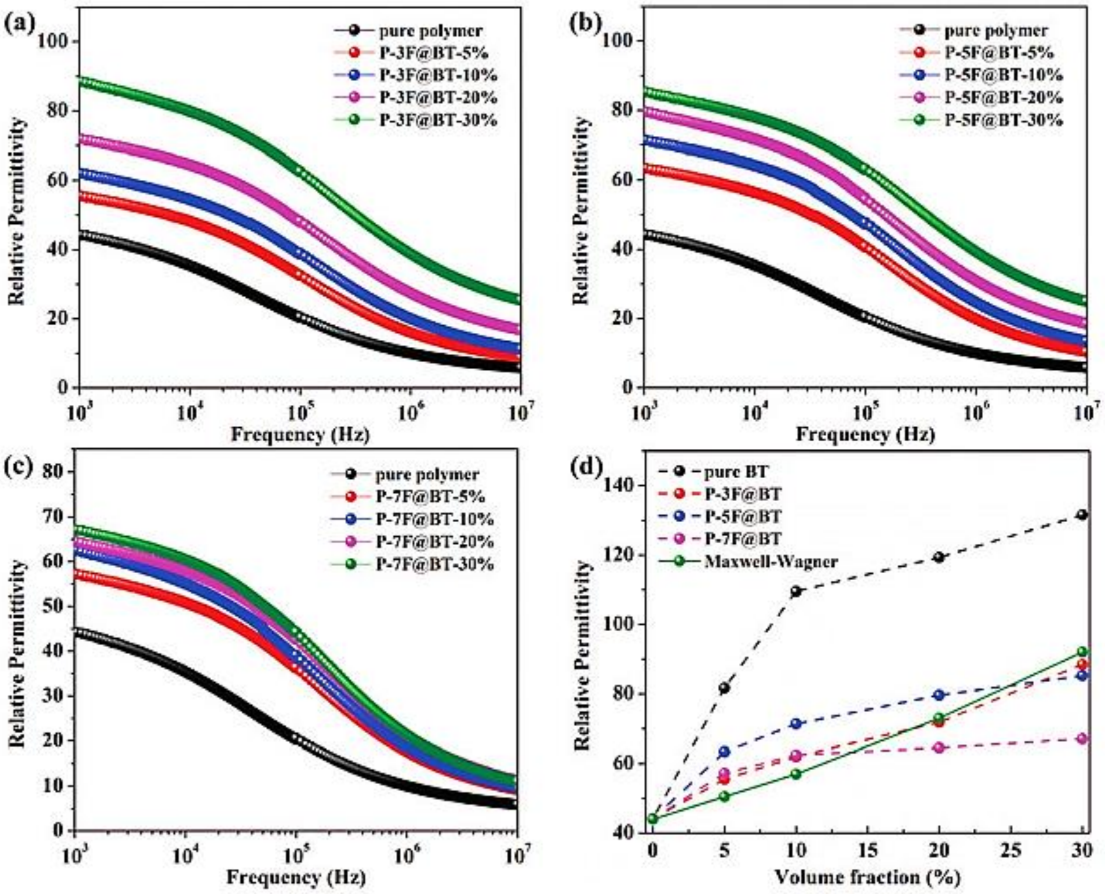

Figure 32. Frequency dependence of permittivity of the P-nF@BT/P (VDF-TrFE-CTFE) nanocomposite films with (a) P-3F@BaTiO$_3$, (b) P-5F@BaTiO$_3$, and (c) P-7F@BaTiO$_3$. (d) Comparison of the relative permittivity (at 1 kHz) of the nanocomposite with the Maxwell–Wagner model. The permittivity of 100 nm BaTiO$_3$ particles is around 1700. Reproduced with permission of [117]. Copyright 2018 Royal Society of Chemistry.

I.4.3.9. PVDF@BT or PS@BT/PVDF

Ma *et al.* [85] reported two kinds of polymer@BT nanoparticles used as composite fillers in PVDF matrix (Scheme 11). First, PS@BT and PVDF@BT were synthesized by thiol-ene reaction (Section I.4.2.3.2). Then, a second shell of PVDF was introduced by simple casting and hot pressing. The dielectric properties and the electric breakdown strength of both PVDF@BT/PVDF and PS@BT/PVDF nanocomposites exhibit an enhancement compared to the pure polymer. For example, the permittivity of PS@BT/PVDF nanocomposites increased from 9.2 for the pure PVDF to 23.6 for nanocomposites filled with 30 vol% of PS@BT. Moreover, the authors revealed that PVDF@BT had a better interfacial interaction with PVDF matrix than that of PS@BT fillers, and this is due to the fact that the shell of the fillers has the same structure as that of the polymer matrix.

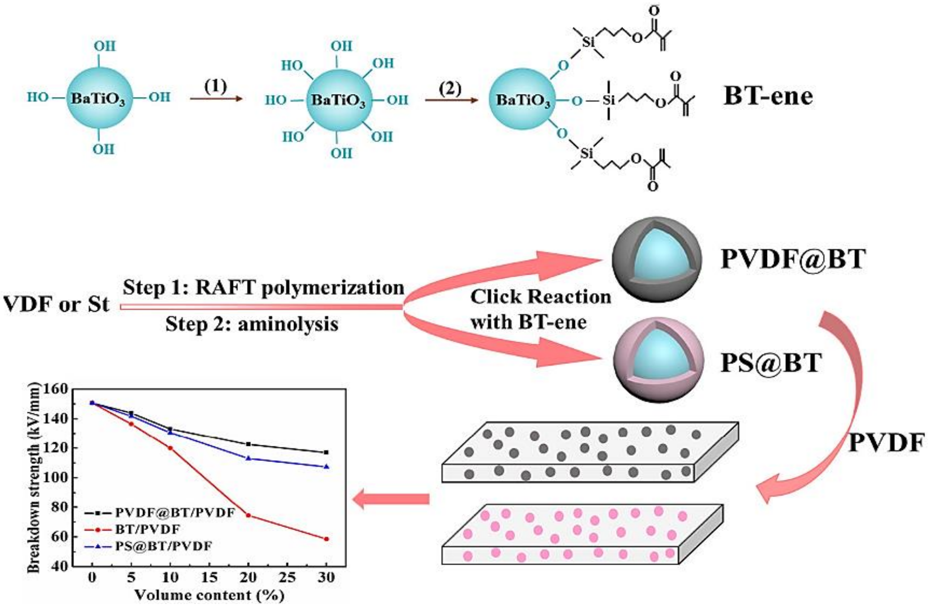

Scheme 11. Schematic illustration of the synthetic process of the core@double shell nanocomposites (PS@BT/PVDF or PVDF@BT/PVDF). Reproduced with permission of [85]. Copyright 2019 Elsevier.

I.4.3.10. HBP@BT/poly(VDF-*ter*-TrFE-*ter*-CFE)

Xie *et al.* [122] used hyperbranched aromatic polyamide (HBP) to decorate BT surface using a polycondensation of 3,5-diaminobenzoic acid (Scheme 12), then, poly(VDF-*ter*-TrFE-*ter*-CFE) was introduced via a solution blending method.

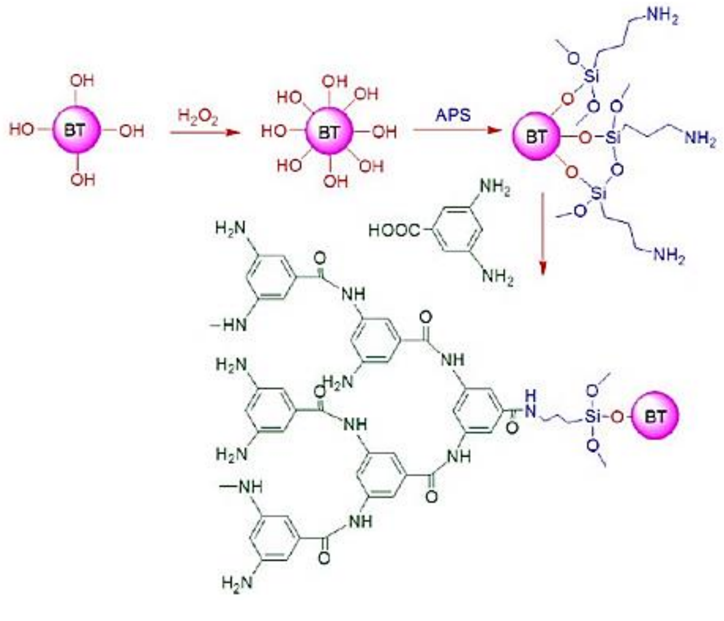

Scheme 12. Schematic Diagram Illustrating the Preparing Process of BT-HBP. Reproduced with permission of [122] . Copyright American Chemical Society 2013.

Results show that the as prepared nanocomposites exhibit enhanced dielectric permittivity compared to the pure polymer. Moreover, by increasing the loading of functionalized nanoparticles, high values were reached. As shown in Figure 33, at 1 kHz and with a loading of 40 vol% of HBP@BT, a high dielectric constant of 1485.5 was achieved for the nanocomposites compared to poly(VDF-*ter*-TrFE-*ter*-CFE) that exhibit only 206.3.

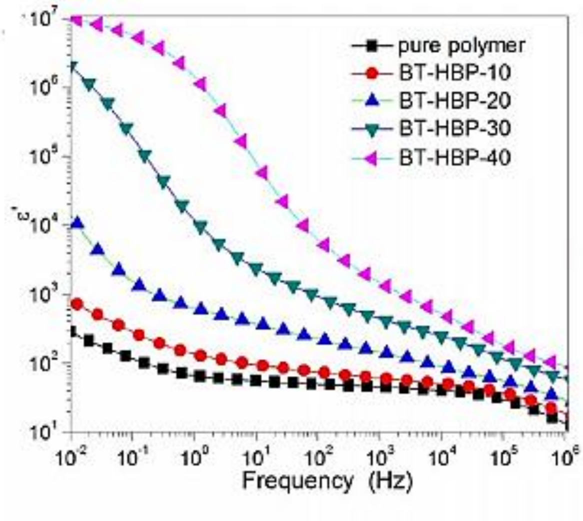

Figure 33. Frequency dependence of dielectric constant for HBP@BT/ poly(VDF-*ter*-TrFE-*ter*-CFE) nanocomposites for different loading of functionalized nanoparticles. Reproduced with permission of [122] . Copyright American Chemical Society 2013.

Table 7 summarizes the permittivities obtained for core-shell systems discussed above. It can be seen that nanocomposites containing more fluorinated polymers exhibit high dielectric constants. For instance, in reference 85, when PVDF is used instead of PS, for the same filler loading, the dielectric permittivity increased from 23.6 to 27.9 at 1 kHz. Indeed, we can not increase the permittivity of fluorinated polymers compared to that of pure $BaTiO_3$, even when using high nanoparticle loading [123]. In fact, by adding higher concentration of ceramic nanoparticles inevitably induces aggregation and inhomogeneity in the fluorinated polymer shell giving rise to electron conduction with a high dielectric loss, very low breakdown strength and undesirable porosity and voids, resulting in deteriorated electrical properties in polymer nanocomposites (*i. e.* permittivity of the resulting nanocomposites). Thus, an appropriate surface modification and choice of the polymer shell would lead to the desired properties.

Table 7. Summary of permittivities obtained for core-shell $BaTiO_3$@polymer/Fluorinated polymer nanocomposites.

Core-shell Polymer@BT/Fluorinated polymer nanocomposites	*Dielectric permittivity (at a given frequency and fillers loading)*	*References*
PTFEA@BT/P(VDF-HFP)	42.5 (1 kHz, 50 %wt)	27
PS@BT/PVDF	23.6 (1 kHz, 30 vol%)	85
PVDF@BT/PVDF	27.9 (1 kHz, 30 vol%)	85
PTFMPCS@BT/poly(VDF-*ter*-TrFE- *ter*-CTFE)	80.6 (1 kHz, 30 vol%)	86
PMMA@BT/PVDF	30 (100 Hz, 80 wt%)	113
PTFEMA@BT/PVDF	36 (100 Hz, 80 wt%)	113
PtBA@BT/PVDF	15 (100 Hz, 30 wt%)	115
PHEMA@BT/PVDF	21 (100 Hz, 20 wt%)	73
PGMA@BT/PVDF	18 (100 Hz, 20 wt%)	73
PM7F@BT/P(VDF-ter-TrFE- ter-CTFE)	70 (1 kHz, 5 vol%)	118

I.5. Applications

Polymer nanocomposites present unique physicochemical properties that cannot be obtained with one component. Thus, the improvement in the properties of polymer nanocomposites have resulted in major interest for versatile fields including medicine, coatings and energy storage [124]. In medical applications, damaged tissues are often replaced with synthetic materials such as ceramics or metals, which are used for engineering hard tissues (*e,g,*. bones and teeth), or even polymers that can be used to manufacture a wide range of both hard and soft tissues, and in some cases, their composites could be also used [125–127]. Gopalakrishnan *et al.* [128] introduced silver nanoparticles into PMMA polymer matrix to reinforce its structure for dental prosthetic materials. The addition of silver nanoparticles was found to enhance the mechanical properties of the polymer and also retarded crack propagation and fracture behavior, and thus improved the durability of the denture base.

Another promising field of use of polymer nanocomposite materials is energy storage applications [71,129–133]. Kumar *et al.* [129] used nanocomposite materials consisting on BT nanoparticles and poly(VDF-*co*-HFP) polymer matrix to prepare a composite solid polymer electrolyte (CSPE) for Li-ion batteries. Since the ionic conductivity of the pure polymer poly(VDF-*co*-HFP) is not enough to be used as SPE, lithium triflate salt was added and the nanocomposites were synthesized by solution casting technique. Figure 34-a exhibits the ionic conductivity of the CSPE with 10 wt% in lithium triflate salt for different BT loading. The ionic conductivity of the CSPE increases to reach 8.89×10^{-6} S cm^{-1} as the maximum value for 4 wt% of BT and decreases by further addition of BT. Figure 36-b gives a comparison of conductivity (σ_{DC}) of pure polymer, SPE loaded with 10 wt% of lithium triflate and 4 wt% of BT. It can be observed that after introduction of BT into the system, the ionic conductivity increased by four orders of magnitude.

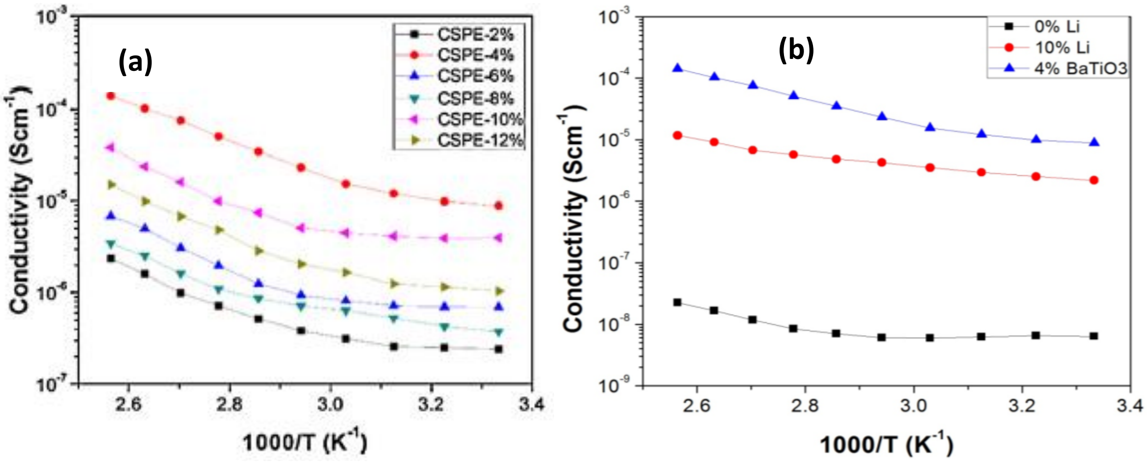

Figure 34. (a) Direct current (DC) conductivity (σ_{DC}) of the CSPEs calculated from complex impedance plots and (b) DC ionic conductivity of pure polymer, SPE loaded with 10 wt. % lithium triflate salt and CSPE loaded with 10 wt. % lithium triflate salt and 4 wt. % $BaTiO_3$. Reproduced with permission of [129]. Copyright 2016 Elsevier.

A similar strategy for the same application was also reported by Sasikumar *et al.* [130] who prepared CSPE using BT, PVAc/poly(VDF-*co*-HFP) and lithium bis-trifluoromethanesulfonylimide (LiTFSI) as the salt (Figure 35). Results show that compared with ceramic free SPE, the conductivity was increased to reach a value of 2 x 10^{-3} Scm^{-1} at ambient temperature. Moreover, it was found that in the case of CSPE made by 7 wt% of BT, an enhancement in discharge capacity of 132 mAh g^{-1} at 0.1 C, cycling performance up to 40 cycles and 99 % Coulombic efficiency were noted.

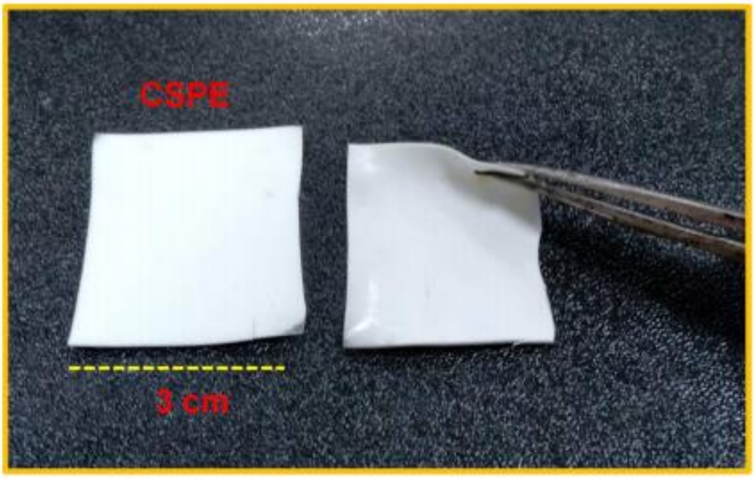

Figure 35. Photograph of free-standing and flexible CSPE. Reproduced with permission of [130] Copyright 2018 American Chemical Society.

In addition to their application in Li-ion batteries, BT based fluoropolymer nanocomposites are also used in capacitors. For example, Tang *et al.* [71] prepared high energy density nanocomposite capacitors using BT nanowires and poly(VDF-*ter*-TrFE-*ter*-CFE) polymer (63/29/8 % mole ratio). Dielectric measurements revealed that the obtained nanocomposites exhibit increased dielectric permittivity at low volume fraction of the fillers and high electric field for energy storage (Figure 36-a). Moreover, BT/poly(VDF-TrFE-CFE) nanocomposites showed an increase in energy density of 10.48 J/cc, which is higher than that of the neat poly(VDF-*ter*-TrFE-*ter*-CFE) polymer (7.21 J/cc) at 300 MV/m electric field (Figure 36-b). This value is more than seven times larger than a high performance commercial polypropylene capacitor.

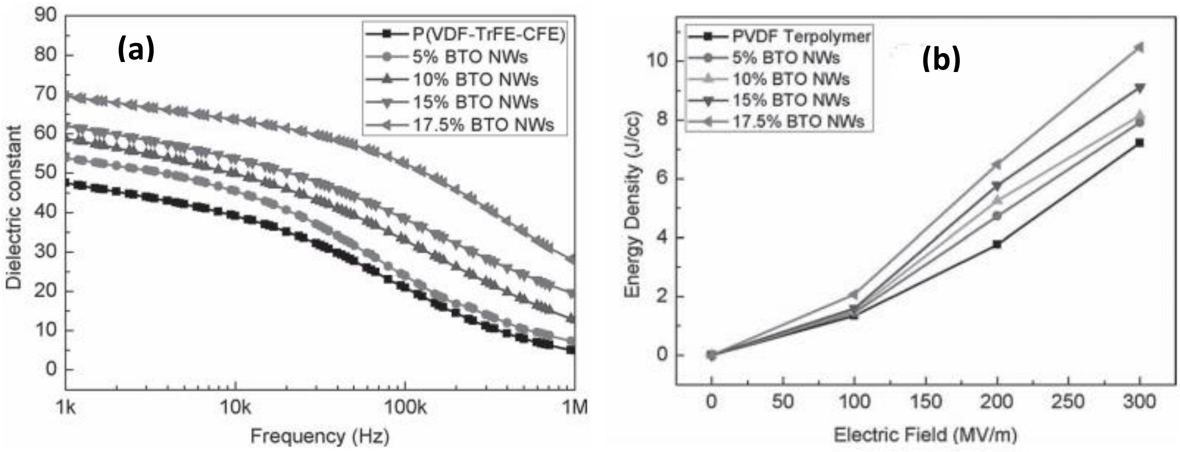

Figure 36. (a) Dielectric permittivity constants of different BT NWs volume fractions in P(VDF-*ter*-TrFE-*ter*-CFE) from 1 kHz to 1 MHz and (b) Energy density of BT/ P(VDF-*ter*-

TrFE-*ter*-CFE) nanocomposite with different volume fractions of BT as a function of the electric field. Reproduced with permission of [71] . Copyright 2013 Wiley.

Hao *et al*. [134] designed a parallel plate capacitance device. The multilayer nanocomposite film consists on a central layer composed of high volume fraction of BT, while the outer layers were predominately PVDF, with a small loading of BT nanoparticles. The obtained films (1.2-1.5 µm) were found to be mechanically flexible and could be removed from the substrate (Figure 37). Moreover, a maximum breakdown strength as high as 495 KV/mm which is 50 % higher than that of the pure PVDF, and a discharge energy density of 19.37 J/cm^3 were obtained, leading to high energy density nanocomposites.

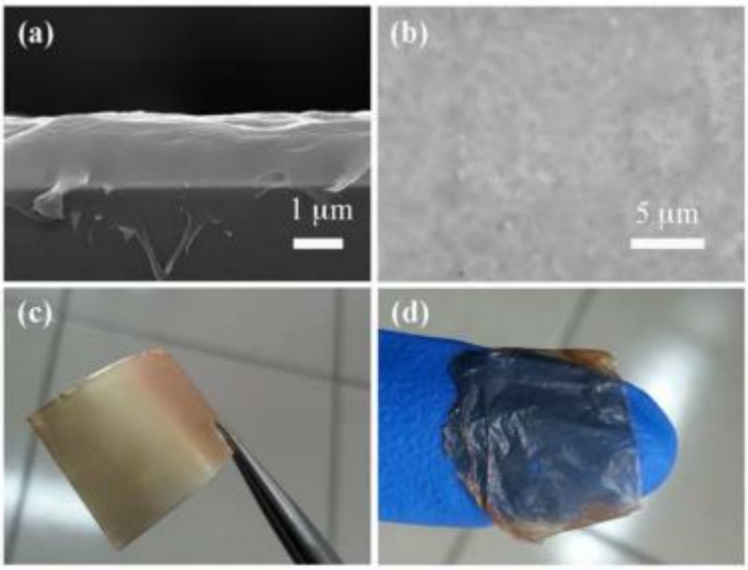

Figure 37. (a) Cross-sectional and (b) Surface SEM image of the BTO/PVDF nanocomposite film, showing a rough interface between the transparent top PVDF layer and the bottom nanocomposite layer. (c) Photograph of the nanocomposite on a flexible aluminum foil substrate, and (d) delaminated from the substrate, showing its continuous polymer nature. Reproduced with permission of [134]. Copyright 2015 Royal Society of Chemistry.

Another promising application of polymer nanocomposites is piezoelectric nanogenerators (PNGs), which aims to convert the mechanical energy available in our daily life like vehicle motion or even in human body (artificial muscle actuators). In fact, PVDF and its copolymers are considered to be the most used polymeric materials in PNGs [135]. Dudem *et al*. [136] designed a PNGs using barium titanate nanoparticles embedded into PVDF. The nanoparticles were first dispersed with Ag nanowires; the resulted mixture was introduced into PVDF matrix. In order to fabricate the PNGs, the nanocomposite film was sandwiched between two

Aluminum substrate and then sealed with a Kapton tape. The prepared PNGs were then tested to harvest the mechanical energy from bicycle, motorcycle, car and human hand. Figure 38 exhibits the piezoelectric potential curves generated by the PNGs device at bending positions and on human hand. The results revealed that the resulting device is flexible enough to generate the electrical output under various bending conditions, and exhibits a hight output voltage of ~4.8 V under large bending conditions.

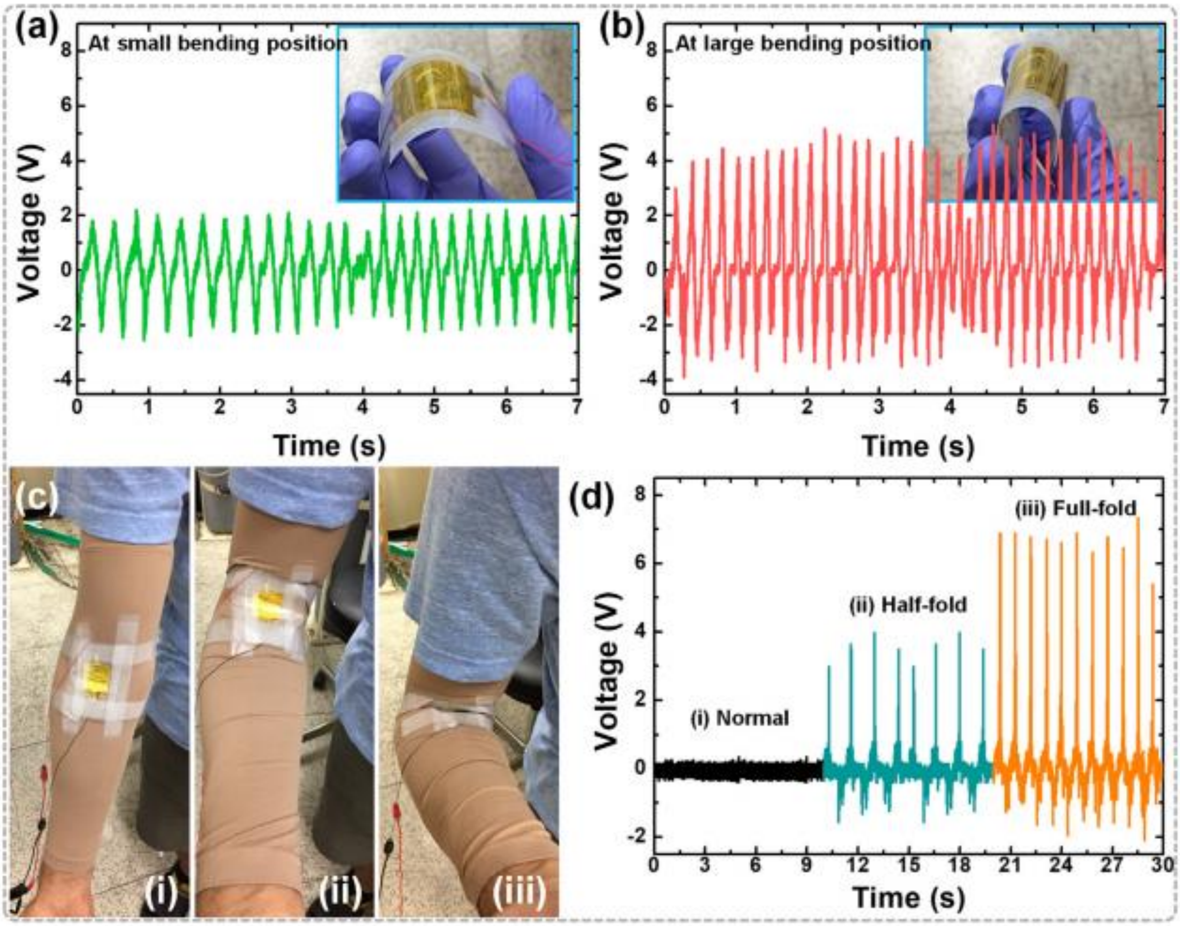

Figure 38. Demonstration for the high-flexibility of the Ag/BTO-PNG device. Piezoelectric potential (i.e., VOC) generated by the Ag/BTO-PNG at (a) small and (b) large bending positions/conditions. Insets of (a) and (b) also depict the photographic images of Ag/BT O-PNG at the small and large bending conditions, respectively. (c) Photographic images and (d) piezoelectric potentials of the Ag/BTO-PNG device located on a human hand (i.e., in front part of the elbow) at (i) normal, (ii) half-, and (iii) full-fold conditions, respectively. Reproduced with permission of [136]. Copyright 2018 Elsevier.

I.6. Conclusion

Nanocomposites depicted in this review are composed of a barium titanate core embedded in a fluorinated polymeric shell. BT is as a ferroelectric ceramic mostly used in dielectric material due to its high dielectric constant. However, this ceramic suffer from low breakdown strength and processing difficulties. In the other hand, polymers generally exhibit high breakdown strength and low permittivities. Thus, by combining the advantages of both components, high dielectric constant materials could be achieved. Various fluoropolymers could be used as shells such as poly(fluoroolefins), poly[fluoro(meth)acrylates] of various fluoroalkyl lengths, PVDF and VDF-containing-copolymers. In certain cases, core-shell $BaTiO_3$@polymer/Fluorinated polymer nanocomposites have also been reported, in order to take advantages from the inner and outer polymer shell.

In fact, these nanocomposite materials could be obtained by different strategies ranging from “grafting from”, “grafting onto” or blending. The first route requires to modify the BT surface by either a macroinitiator (for ATRP method) or macro chain transfer agent (xanthates or trithiocarbonates for RAFT technique), while the third strategy consists on a simple mixing of the pre-prepared polymer with the functionalized nanoparticles. Actually, the first two routes are efficient since they create covalent and thus strong bonds between the core and the shell. The blending technique has been possible when BT@PMMA has been prepared, followed by mixing it with PVDF, taking into account that PVDF and PMMA are miscible.

In the last decade, a growing interest from such nanocomposites has been highlighted by the wide range of applications, focusing on energy storage devices or piezoelectric systems and it can be expected that designing further materials with various sizes and efficiency for the searched applications will still be challenging and will attract the interest of many researchers.

I.7. References

[1] Raman N, Sudharsan S, Pothiraj K. Synthesis and structural reactivity of inorganic–organic hybrid nanocomposites – A review. J Saudi Chem Soc 2012;16:339–52. doi:10.1016/j.jscs.2011.01.012.
[2] Fu S-Y, Sun Z, Huang P, Li Y-Q, Hu N. Some basic aspects of polymer nanocomposites: A critical review. Nano Mater Sci 2019;1:2–30. doi:10.1016/j.nanoms.2019.02.006.
[3] Huang T-C, Yeh J-M, Lai C-Y. Polymer nanocomposite coatings. Adv. Polym. Nanocomposites, Elsevier; 2012, p. 605–38. doi:10.1533/9780857096241.3.605.

[4] Dang Z-M, Yuan J-K, Yao S-H, Liao R-J. Flexible Nanodielectric Materials with High Permittivity for Power Energy Storage. Adv Mater 2013;25:6334–65. doi:10.1002/adma.201301752.

[5] Chen Q, Shen Y, Zhang S, Zhang QM. Polymer-Based Dielectrics with High Energy Storage Density. Annu Rev Mater Res 2015;45:433–58. doi:10.1146/annurev-matsci-070214-021017.

[6] Chu B, Xin Z, Kailiang R, Bret N, Minren L, Qing W, et al. A Dielectric Polymer with High Electric Energy Density and Fast Discharge Speed. Science (80-) 2006;313:334–6. doi:10.1126/science.1127798.

[7] Huang X, Jiang P. Core-Shell Structured High-k Polymer Nanocomposites for Energy Storage and Dielectric Applications. Adv Mater 2015;27:546–54. doi:10.1002/adma.201401310.

[8] Terzić I, Meereboer NL, Mellema HH, Loos K. Polymer-based multiferroic nanocomposites via directed block copolymer self-assembly. J Mater Chem C 2019;7:968–76. doi:10.1039/C8TC05017A.

[9] Villa SM, Mazzola VM, Santaniello T, Locatelli E, Maturi M, Migliorini L, et al. Soft Piezoionic/Piezoelectric Nanocomposites Based on Ionogel/BaTiO3 Nanoparticles for Low Frequency and Directional Discriminative Pressure Sensing. ACS Macro Lett 2019;8:414–20. doi:10.1021/acsmacrolett.8b01011.

[10] Wang G, Huang X, Jiang P. Tailoring Dielectric Properties and Energy Density of Ferroelectric Polymer Nanocomposites by High-k Nanowires. ACS Appl Mater Interfaces 2015;7:18017–27. doi:10.1021/acsami.5b06480.

[11] Zhang X, Shen Y, Xu B, Zhang Q, Gu L, Jiang J, et al. Giant Energy Density and Improved Discharge Efficiency of Solution-Processed Polymer Nanocomposites for Dielectric Energy Storage. Adv Mater 2016;28:2055–61. doi:10.1002/adma.201503881.

[12] Qiao Y, Islam MS, Wang L, Yan Y, Zhang J, Benicewicz BC, et al. Thiophene Polymer-Grafted Barium Titanate Nanoparticles toward Nanodielectric Composites. Chem Mater 2014;26:5319–26. doi:10.1021/cm502341n.

[13] Li J, Seok S Il, Chu B, Dogan F, Zhang Q, Wang Q. Nanocomposites of Ferroelectric Polymers with TiO2 Nanoparticles Exhibiting Significantly Enhanced Electrical Energy Density. Adv Mater 2009;21:217–21. doi:10.1002/adma.200801106.

[14] Xu N, Hu L, Zhang Q, Xiao X, Yang H, Yu E. Significantly Enhanced Dielectric Performance of Poly(vinylidene fluoride-co-hexafluoropylene)-based Composites Filled with Hierarchical Flower-like TiO2 Particles. ACS Appl Mater Interfaces 2015;7:27373–81. doi:10.1021/acsami.5b08987.

[15] Guo R, Roscow J, Bowen C, Luo H, Huang Y, Ma Y, et al. Significantly enhanced permittivity and energy density in dielectric composites with aligned BaTiO3 lamellar structures. J Mater Chem A 2020. doi:10.1039/C9TA11360F.

[16] Bai Y, Cheng Z-Y, Bharti V, Xu HS, Zhang QM. High-dielectric-constant ceramic-powder polymer composites. Appl Phys Lett 2000;76:3804–6. doi:10.1063/1.126787.

[17] Li W, Meng Q, Zheng Y, Zhang Z, Xia W, Zhuo X. Electric energy storage properties of poly(vinylidene fluoride). Appl Phys Lett 2010;96:192905. doi:10.1063/1.3428656.

[18] Claude J, Lu Y, Li K, Wang Q. Electrical Storage in Poly(vinylidene fluoride) based Ferroelectric Polymers: Correlating Polymer Structure to Electrical Breakdown Strength. Chem Mater 2008;20:2078–80. doi:10.1021/cm800160r.

[19] Yu K, Wang H, Zhou Y, Bai Y, Niu Y, Yu K, et al. Enhanced dielectric properties of BaTiO3 / poly (vinylidene fluoride) nanocomposites for energy storage applications. J Appl Phys 2013;113:34105. doi:10.1063/1.4776740.

[20] Bouharras FE, Raihane M, Silly G, Totee C, Ameduri B. Core shell structured Poly(Vinylidene Fluoride) -grafted- BaTiO3 nanocomposites prepared via Reversible

Addition fragmentation chain transfer (RAFT) polymerization of VDF for high energy storage capacitors. Polym Chem 2019;10:891–904. doi:10.1039/C8PY01706A.

[21] Dang Z-M, Wang H-Y, Peng B, Nan C-W. Effect of BaTiO3 size on dielectric property of BaTiO3/PVDF composites. J Electroceramics 2008;21:381–4. doi:10.1007/s10832-007-9201-8.

[22] Li J, Claude J, Norena-Franco LE, Seok S Il, Wang Q. Electrical Energy Storage in Ferroelectric Polymer Nanocomposites Containing Surface-Functionalized BaTiO3 Nanoparticles. Chem Mater 2008;20:6304–6. doi:10.1021/cm8021648.

[23] Dai Z-H, Han J-R, Gao Y, Xu J, He J, Guo B-H. Increased dielectric permittivity of poly(vinylidene fluoride-co-chlorotrifluoroethylene) nanocomposites by coating BaTiO3 with functional groups owning high bond dipole moment. Colloids Surfaces A Physicochem Eng Asp 2017;529:560–70. doi:10.1016/J.COLSURFA.2017.05.065.

[24] Xie L, Huang X, Wu C, Jiang P. Core-shell structured poly(methyl methacrylate)/BaTiO3 nanocomposites prepared by in situ atom transfer radical polymerization: a route to high dielectric constant materials with the inherent low loss of the base polymer. J Mater Chem 2011;21:5897. doi:10.1039/c0jm04574h.

[25] Ejaz M, Puli VS, Elupula R, Adireddy S, Riggs BC, Chrisey DB, et al. Core-shell structured poly(glycidyl methacrylate)/BaTiO3 nanocomposites prepared by surface-initiated atom transfer radical polymerization: A novel material for high energy density dielectric storage. J Polym Sci Part A Polym Chem 2015;53:719–28. doi:10.1002/pola.27485.

[26] Ameduri B. From Vinylidene Fluoride (VDF) to the Applications of VDF-Containing Polymers and Copolymers: Recent Developments and Future Trends. Chem Rev 2009;109:6632–86. doi:10.1021/cr800187m.

[27] Yang K, Huang X, Huang Y, Xie L, Jiang P. Fluoro-Polymer@BaTiO3 Hybrid Nanoparticles Prepared via RAFT Polymerization: Toward Ferroelectric Polymer Nanocomposites with High Dielectric Constant and Low Dielectric Loss for Energy Storage Application. Chem Mater 2013;25:2327–38. doi:10.1021/cm4010486.

[28] Xie L, Huang X, Yang K, Li S, Jiang P. “Grafting to” route to PVDF-HFP-GMA/BaTiO3 nanocomposites with high dielectric constant and high thermal conductivity for energy storage and thermal management applications. J Mater Chem A 2014;2:5244. doi:10.1039/c3ta15156e.

[29] Barber P, Balasubramanian S, Anguchamy Y, Gong S, Wibowo A, Gao H, et al. Polymer Composite and Nanocomposite Dielectric Materials for Pulse Power Energy Storage. Materials (Basel) 2009;2:1697–733. doi:10.3390/ma2041697.

[30] Todd MG, Shi FG. Complex permittivity of composite systems: a comprehensive interphase approach. IEEE Trans Dielectr Electr Insul 2005;12:601–11. doi:10.1109/TDEI.2005.1453466.

[31] Tanaka T, Kozako M, Fuse N, Ohki Y. Proposal of a multi-core model for polymer nanocomposite dielectrics. IEEE Trans Dielectr Electr Insul 2005;12:669–81. doi:10.1109/TDEI.2005.1511092.

[32] Smith MB, Page K, Siegrist T, Redmond PL, Walter EC, Seshadri R, et al. Crystal Structure and the Paraelectric-to-Ferroelectric Phase Transition of Nanoscale BaTiO3. J Am Chem Soc 2008;130:6955–63. doi:10.1021/ja0758436.

[33] Huang K-C, Huang T-C, Hsieh W-F. Morphology-Controlled Synthesis of Barium Titanate Nanostructures. Inorg Chem 2009;48:9180–4. doi:10.1021/ic900854x.

[34] Helen DM. Crystal Structure of Barium Titanate. Nature 1945;155:484–5. doi:10.1038/155484b0.

[35] Vijatovic MM, Bobic JD, Stojanovic BD. History and challenges of barium titanate: Part I. Sci Sinter 2008;40:155–65. doi:10.2298/SOS0802155V.

[36] Kwei GH, Lawson AC, Billinge SJL, Cheong SW. Structures of the ferroelectric

phases of barium titanate. J Phys Chem 1993;97:2368–77. doi:10.1021/j100112a043.

[37] Pan M-J, Randall CA. A brief introduction to ceramic capacitors. IEEE Electr Insul Mag 2010;26:44–50. doi:10.1109/MEI.2010.5482787.

[38] Neagu AM, Curecheriu LP, Cazacu A, Mitoseriu L. Impedance analysis and tunability of BaTiO3–chitosan composites: Towards active dielectrics for flexible electronics. Compos Part B Eng 2014;66:109–16. doi:10.1016/J.COMPOSITESB.2014.04.020.

[39] Hirose N, West AR. Impedance Spectroscopy of Undoped BaTiO3 Ceramics. J Am Ceram Soc 1996;79:1633–41. doi:10.1111/j.1151-2916.1996.tb08775.x.

[40] Tian Z, Wang X, Shu L, Wang T, Song T-H, Gui Z, et al. Preparation of Nano BaTiO3-Based Ceramics for Multilayer Ceramic Capacitor Application by Chemical Coating Method. J Am Ceram Soc 2009;92:830–3. doi:10.1111/j.1551-2916.2009.02979.x.

[41] Feteira A, Sinclair DC, Reaney IM, Somiya Y, Lanagan MT. BaTiO3-Based Ceramics for Tunable Microwave Applications. J Am Ceram Soc 2004;87:1082–7. doi:10.1111/j.1551-2916.2004.01082.x.

[42] Dutta PK, Gregg JR. Hydrothermal synthesis of tetragonal barium titanate (BaTiO3). Chem Mater 1992;4:843–6. doi:10.1021/cm00022a019.

[43] Eckert JO, Hung-Houston CC, Gersten BL, Lencka MM, Riman RE. Kinetics and Mechanisms of Hydrothermal Synthesis of Barium Titanate. J Am Ceram Soc 1996;79:2929–39. doi:10.1111/j.1151-2916.1996.tb08728.x.

[44] Bouloo M, Guillemetfritsch S, Mathieu F, Durand B, Lebey T, Bley V. Hydrothermal synthesis of nanosized BaTiO3 powders and dielectric properties of corresponding ceramics. Solid State Ionics 2005;176:1301–9. doi:10.1016/j.ssi.2005.02.024.

[45] Hao Y, Wang X, Zhang H, Shen Z, Li L. Investigation on the synthesis procedure of ultrafine monodispersed BaTiO3 powders by solvothermal method. J Ceram Soc Japan 2013;121:506–11. doi:10.2109/jcersj2.121.506.

[46] Buscaglia MT, Bassoli M, Buscaglia V, Vormberg R. Solid-State Synthesis of Nanocrystalline BaTiO3 Reaction Kinetics and Powder Properties. J Am Ceram Soc 2008;91:2862–9. doi:10.1111/j.1551-2916.2008.02576.x.

[47] Ashiri R. On the solid-state formation of BaTiO3 nanocrystals from mechanically activated BaCO3 and TiO2 powders: innovative mechanochemical processing, the mechanism involved, and phase and nanostructure evolutions. RSC Adv 2016;6:17138–50. doi:10.1039/C5RA22942A.

[48] Simon-Seveyrat L, Hajjaji A, Emziane Y, Guiffard B, Guyomar D. Re-investigation of synthesis of BaTiO3 by conventional solid-state reaction and oxalate coprecipitation route for piezoelectric applications. Ceram Int 2007;33:35–40. doi:10.1016/J.CERAMINT.2005.07.019.

[49] Miot C, Proust C, Husson E. Dense ceramics of BaTiO3 produced from powders prepared by a chemical process. J Eur Ceram Soc 1995;15:1163–70. doi:10.1016/0955-2219(95)00090-9.

[50] Stockenhuber M, Mayer H, Lercher JA. Preparation of Barium Titanates from Oxalates. J Am Ceram Soc 1993;76:1185–90. doi:10.1111/j.1151-2916.1993.tb03738.x.

[51] Veith M, Mathur S, Lecerf N, Huch V, Decker T. Sol-Gel Synthesis of Nano-Scaled BaTiO3, BaZrO3 and BaTi0.5Zr0.5O3 Oxides via Single-Source Alkoxide Precursors and Semi-Alkoxide Routes. J Sol-Gel Sci Technol 2000;15:145–58.

[52] Ritter JJ, Roth RS, Blendell JE. Alkoxide Precursor Synthesis and Characterization of Phases in the Barium-Titanium Oxide System. J Am Ceram Soc 1986;69:155–62. doi:10.1111/j.1151-2916.1986.tb04721.x.

[53] Lemoine C, Gilbert B, Michaux B, Pirard J-P, Lecloux A. Synthesis of barium titanate by the sol-gel process. J Non Cryst Solids 1994;175:1–13. doi:10.1016/0022-3093(94)90309-3.

[54] Cernea M. Sol-gel synthesis and characterization of BaTiO3 powder. J Opt Adv Mater 2005;7;3015-3022. doi:10.1.1.551.789&rep=rep1&type=pdf.

[55] K. S. Mazdiyasni. Fine particle perovskite processing. Am Ceram SOC Bull 1984;63:591–4.

[56] Flaschen SS. An Aqueous Synthesis of Barium Titanate. J Am Chem Soc 1955;77:6194–6194. doi:10.1021/ja01628a030.

[57] Phule PP, Risbud SH. Sol-Gel Synthesis of Barium Titanate Powders Using Barium Acetate and Titanium(IV) Isopropoxide. Adv Ceram Mater 1988;3:183–5. doi:10.1111/j.1551-2916.1988.tb00197.x.

[58] Buscaglia MT, Buscaglia V, Viviani M, Petzelt J, Savinov M, Mitoseriu L, et al. Ferroelectric properties of dense nanocrystalline BaTiO3 ceramics. Nanotechnology 2004;15:1113–7. doi:10.1088/0957-4484/15/9/001.

[59] Li B, Wang X, Li L, Zhou H, Liu X, Han X, et al. Dielectric properties of fine-grained BaTiO3 prepared by spark-plasma-sintering. Mater Chem Phys 2004;83:23–8. doi:10.1016/j.matchemphys.2003.08.009.

[60] Luan W, Gao L, Kawaoka H, Sekino T, Niihara K. Fabrication and characteristics of fine-grained BaTiO3 ceramics by spark plasma sintering. Ceram Int 2004;30:405–10. doi:10.1016/S0272-8842(03)00124-X.

[61] Zhao Z, Buscaglia V, Viviani M, Buscaglia MT, Mitoseriu L, Testino A, et al. Grain-size effects on the ferroelectric behavior of dense nanocrystalline BaTiO 3 ceramics. Phys Rev B 2004;70:24107. doi:10.1103/PhysRevB.70.024107.

[62] Hsiang H-I, Yen F-S, Huang C-Y. Effects of Porosity on Dielectric Properties of BaTiO3 Ceramics. Jpn J Appl Phys 1995;34:1922–5. doi:10.1143/JJAP.34.1922.

[63] Fang T-T, Hsieh H-L, Shiau F-S. Effects of Pore Morphology and Grain Size on the Dielectric Properties and Tetragonal-Cubic Phase Transition of High-Purity Barium Titanate. J Am Ceram Soc 1993;76:1205–11. doi:10.1111/j.1151-2916.1993.tb03742.x.

[64] Kingery WD, Bowen HK, Uhlmann DR. Introduction to ceramics. Wiley. New York: 1976.

[65] Murugaraj P, Mainwaring D, Mora-Huertas N. Dielectric enhancement in polymer-nanoparticle composites through interphase polarizability. J Appl Phys 2005;98:54304. doi:10.1063/1.2034654.

[66] Tuncer E, Serdyuk YV, Gubanski SM. Dielectric mixtures: electrical properties and modeling. IEEE Trans Dielectr Electr Insul 2002;9:809–28. doi:10.1109/TDEI.2002.1038664.

[67] Yoon D-H, Zhang J, Lee BI. Dielectric constant and mixing model of BaTiO3 composite thick films. Mater Res Bull 2003;38:765–72. doi:10.1016/S0025-5408(03)00075-8.

[68] Vo HT, Todd M, Shi FG, Shapiro AA, Edwards M. Towards model-based engineering of underfill materials: CTE modeling. Microelectronics J 2001;32:331–8. doi:10.1016/S0026-2692(00)00152-X.

[69] Wang Q, Zhu L. Polymer nanocomposites for electrical energy storage. J Polym Sci Part B Polym Phys 2011;49:1421–9. doi:10.1002/polb.22337.

[70] Zhu L, Wang Q. Novel Ferroelectric Polymers for High Energy Density and Low Loss Dielectrics. Macromolecules 2012;45:2937–54. doi:10.1021/ma2024057.

[71] Tang H, Lin Y, Sodano HA. Synthesis of High Aspect Ratio BaTiO3 Nanowires for High Energy Density Nanocomposite Capacitors. Adv Energy Mater 2013;3:451–6. doi:10.1002/aenm.201200808.

[72] Soulestin T, Marcelino Dos Santos Filho P, Ladmiral V, Lannuzel T, Domingues Dos Santos F, Améduri B. Ferroelectric fluorinated copolymers with improved adhesion properties. Polym Chem 2017;8:1017–27. doi:10.1039/C6PY02063A.

[73] Zhu M, Huang X, Yang K, Zhai X, Zhang J, He J, et al. Energy Storage in

Ferroelectric Polymer Nanocomposites Filled with Core–Shell Structured Polymer@BaTiO3 Nanoparticles: Understanding the Role of Polymer Shells in the Interfacial Regions. ACS Appl Mater Interfaces 2014;6:19644–54. doi:10.1021/am504428u.

[74] Kim P, Doss NM, Tillotson JP, Hotchkiss PJ, Pan M-J, Marder SR, et al. High Energy Density Nanocomposites Based on Surface-Modified BaTiO3 and a Ferroelectric Polymer. ACS Nano 2009;3:2581–92. doi:10.1021/nn9006412.

[75] Ferri A, Barrau S, Bourez R, Da Costa A, Chambrier MH, Marin A, et al. Probing the local piezoelectric behavior in stretched barium titanate/poly(vinylidene fluoride) nanocomposites. Compos Sci Technol 2020;186. doi:10.1016/j.compscitech.2019.107914.

[76] You Y, Tu L, Wang Y, Tong L, Wei R, Li X. Achieving secondary dispersion of modified nanoparticles by hot-stretching to enhance dielectric and mechanical properties of polyarylene ether nitrile composites. Nanomaterials 2019;9. doi:10.3390/nano9071006.

[77] Ghallabi Z, Samet M, Arous M, Kallel A, Boiteux G, Royaud I, et al. Giant Permittivity and Low Dielectric Loss in Three Phases BaTiO3/Carbon Nanotube/Polyvinylidene Fluoride Composites. J Adv Phys 2014;3:87–91. doi:10.1166/jap.2014.1108.

[78] Prateek, Thakur VK, Gupta RK. Recent Progress on Ferroelectric Polymer-Based Nanocomposites for High Energy Density Capacitors: Synthesis, Dielectric Properties, and Future Aspects. Chem Rev 2016;116:4260–317. doi:10.1021/acs.chemrev.5b00495.

[79] Ullah A, ur Rahman A, Won Ahn C, Rahman M, Ullah A, Rehman Z, et al. Enhancement of dielectric and energy density properties in the PVDF-based copolymer/terpolymer blends. Polym Eng Sci 2015;55:1396–402. doi:10.1002/pen.24083.

[80] Capsal J-F, Galineau J, Lallart M, Cottinet P-J, Guyomar D. Plasticized relaxor ferroelectric terpolymer: Toward giant electrostriction, high mechanical energy and low electric field actuators. Sensors Actuators A Phys 2014;207:25–31. doi:10.1016/J.SNA.2013.12.008.

[81] Park IJ, Lee S-B, Choi CK. Surface properties for poly(perfluoroalkylethyl methacrylate)/poly(n-alkyl methacrylate)s mixtures. J Appl Polym Sci 1994;54:1449–54. doi:10.1002/app.1994.070541008.

[82] Liu M, Chen Y, Zhang C, Bo Z. Stable superhydrophobic fluorine containing polyfluorenes. Chinese J Polym Sci 2012;30:308–15. doi:10.1007/s10118-012-1127-1.

[83] Fu GD, Kang ET, Neoh KG, Lin CC, Liaw DJ. Rigid Fluorinated Polyimides with Well-Defined Polystyrene/Poly(pentafluorostyrene) Side Chains from Atom Transfer Radical Polymerization. Macromolecules 2005;38:7593–600. doi:10.1021/ma0506435.

[84] Ameduri B. Fluoropolymers: The Right Material for the Right Applications. Chem - A Eur J 2018;24:18830–41. doi:10.1002/chem.201802708.

[85] Ma J, Azhar U, Zong C, Zhang Y, Xu A, Zhai C, et al. Core-shell structured PVDF@BT nanoparticles for dielectric materials: A novel composite to prove the dependence of dielectric properties on ferroelectric shell. Mater Des 2019;164:107556. doi:10.1016/J.MATDES.2018.107556.

[86] Chen S, Lv X, Han X, Luo H, Bowen CR, Zhang D. Significantly improved energy density of BaTiO3 nanocomposites by accurate interfacial tailoring using a novel rigid-fluoro-polymer. Polym Chem 2018;9:548–57. doi:10.1039/C7PY01914A.

[87] Toor A, So H, Pisano AP. Improved Dielectric Properties of Polyvinylidene Fluoride Nanocomposite Embedded with Poly(vinylpyrrolidone)-Coated Gold Nanoparticles. ACS Appl Mater Interfaces 2017;9:6369–75. doi:10.1021/acsami.6b13900.

[88] Xie L, Huang X, Yang K, Li S, Jiang P. “Grafting to” route to PVDF-HFP-GMA/BaTiO3 nanocomposites with high dielectric constant and high thermal conductivity for energy storage and thermal management applications. J Mater Chem A 2014;2:5244. doi:10.1039/c3ta15156e.

[89] Capsal J-F, Dantras E, Dandurand J, Lacabanne C. Physical structure of P(VDF-TrFE)/barium titanate submicron composites. J Non Cryst Solids 2012;358:794–8. doi:10.1016/j.jnoncrysol.2011.12.028.

[90] Kim Y, Kim KH, Lee A, Kim M-S, Yoo B, Lee J-K. Highly Fluorinated Polymer-Inorganic Nanoparticle Composites Processable with Fluorous Solvents. J Nanosci Nanotechnol 2017;17:5510–4. doi:10.1166/jnn.2017.14179.

[91] Martins P, Lopes AC, Lanceros-Mendez S. Electroactive phases of poly(vinylidene fluoride): Determination, processing and applications. Prog Polym Sci 2014;39:683–706. doi:10.1016/J.PROGPOLYMSCI.2013.07.006.

[92] Soulestin T, Ladmiral V, Dos Santos FD, Améduri B. Vinylidene fluoride- and trifluoroethylene-containing fluorinated electroactive copolymers. How does chemistry impact properties? Prog Polym Sci 2017;72:16–60. doi:10.1016/j.progpolymsci.2017.04.004.

[93] Costa CM, Firmino Mendes S, Sencadas V, Ferreira A, Gregorio R, Gómez Ribelles JL, et al. Influence of processing parameters on the polymer phase, microstructure and macroscopic properties of poly(vinilidene fluoride)/Pb(Zr0.53Ti0.47)O3 composites. J Non Cryst Solids 2010;356:2127–33. doi:10.1016/J.JNONCRYSOL.2010.07.037.

[94] Jiang B, Pang X, Li B, Lin Z. Organic–Inorganic Nanocomposites via Placing Monodisperse Ferroelectric Nanocrystals in Direct and Permanent Contact with Ferroelectric Polymers. J Am Chem Soc 2015;137:11760–7. doi:10.1021/jacs.5b06736.

[95] Qiao S, Mingxin Y, Xiao Z, Yushun Y, Chunrong W. Structure and performance of porous polymer electrolytes based P(VDF-HFP) for lithium ion batteries. J Power Sources 2002;103:286–92. doi:https://doi.org/10.1016/S0378-7753(01)00868-0.

[96] Li GC, Zhang P, Zhang HP, Yang LC, Wu YP. A porous polymer electrolyte based on P(VDF-HFP) prepared by a simple phase separation process. Electrochem Commun 2008;10:1883–5. doi:10.1016/j.elecom.2008.09.035.

[97] Soresi B, Quartarone E, Mustarelli P, Magistris A, Chiodelli G. PVDF and P(VDF-HFP)-based proton exchange membranes. Solid State Ionics 2004;166:383–9. doi:10.1016/J.SSI.2003.11.027.

[98] Neese B, Wang Y, Chu B, Ren K, Liu S, Zhang QM, et al. Piezoelectric responses in poly(vinylidene fluoride/hexafluoropropylene) copolymers. Appl Phys Lett 2007;90:242917. doi:10.1063/1.2748076.

[99] Cho Y, Ahn D, Park JB, Pak S, Lee S, Jun BO, et al. Enhanced Ferroelectric Property of P(VDF-TrFE-CTFE) Film Using Room-Temperature Crystallization for High-Performance Ferroelectric Device Applications. Adv Electron Mater 2016;2:1600225. doi:10.1002/aelm.201600225.

[100] Zhou T, Zha J-W, Cui R-Y, Fan B-H, Yuan J-K, Dang Z-M. Improving Dielectric Properties of BaTiO3/Ferroelectric Polymer Composites by Employing Surface Hydroxylated BaTiO3 Nanoparticles. ACS Appl Mater Interfaces 2011;3:2184–8. doi:10.1021/am200492q.

[101] Kim BP, Jones SC, Hotchkiss PJ, Haddock JN, Kippelen B, Marder SR, et al. Phosphonic Acid-Modified Barium Titanate Polymer Nanocomposites with High Permittivity and Dielectric Strength. Adv Mater 2007;19:1001–5. doi:10.1002/adma.200602422.

[102] Song Y, Shen Y, Liu H, Lin Y, Li M, Nan C-W. Improving the dielectric constants and breakdown strength of polymer composites: effects of the shape of the BaTiO3 nanoinclusions, surface modification and polymer matrix. J Mater Chem 2012;22:16491. doi:10.1039/c2jm32579a.

[103] Defebvin J, Barrau S, Lyskawa J, Woisel P, Lefebvre J-M. Influence of nitrodopamine-functionalized barium titanate content on the piezoelectric response of poly(vinylidene fluoride) based polymer-ceramic composites. Compos Sci Technol 2017;147:16–21. doi:10.1016/j.compscitech.2017.05.001.

[104] Guo C, Fuji M. Effect of silicone coupling agent on dielectric properties of barium

titanate/silicone elastomer composites. Adv Powder Technol 2016;27:1162–72. doi:10.1016/J.APT.2016.03.028.

[105] Liu S, Xue S, Zhang W, Zhai J. Enhanced dielectric and energy storage density induced by surface-modified BaTiO3 nanofibers in poly(vinylidene fluoride) nanocomposites. Ceram Int 2014;40:15633–40. doi:10.1016/J.CERAMINT.2014.07.083.

[106] Dalle Vacche S, Oliveira F, Leterrier Y, Michaud V, Damjanovic D, Månson J-AE. Effect of silane coupling agent on the morphology, structure, and properties of poly(vinylidene fluoride–trifluoroethylene)/BaTiO3 composites. J Mater Sci 2014;49:4552–64. doi:10.1007/s10853-014-8155-x.

[107] Kim P, Jones SC, Hotchkiss PJ, Haddock JN, Kippelen B, Marder SR, et al. Phosphonic Acid-Modified Barium Titanate Polymer Nanocomposites with High Permittivity and Dielectric Strength. Adv Mater 2007;19:1001–5. doi:10.1002/adma.200602422.

[108] Ehrhardt C, Fettkenhauer C, Glenneberg J, Münchgesang W, Pientschke C, Großmann T, et al. BaTiO3–P(VDF-HFP) nanocomposite dielectrics—Influence of surface modification and dispersion additives. Mater Sci Eng B 2013;178:881–8. doi:10.1016/j.mseb.2013.04.013.

[109] Zhang X, Ma Y, Zhao C, Yang W. High dielectric constant and low dielectric loss hybrid nanocomposites fabricated with ferroelectric polymer matrix and BaTiO3 nanofibers modified with perfluoroalkylsilane. Appl Surf Sci 2014;305:531–8. doi:10.1016/J.APSUSC.2014.03.131.

[110] Yu K, Niu Y, Xiang F, Zhou Y, Bai Y, Wang H. Enhanced electric breakdown strength and high energy density of barium titanate filled polymer nanocomposites. J Appl Phys 2013;114:174107. doi:10.1063/1.4829671.

[111] Wang G, Huang X, Jiang P. Bio-Inspired Fluoro-polydopamine Meets Barium Titanate Nanowires: A Perfect Combination to Enhance Energy Storage Capability of Polymer Nanocomposites. ACS Appl Mater Interfaces 2017;9:7547–55. doi:10.1021/acsami.6b14454.

[112] Wang J, Guan F, Cui L, Pan J, Wang Q, Zhu L. Achieving high electric energy storage in a polymer nanocomposite at low filling ratios using a highly polarizable phthalocyanine interphase. J Polym Sci Part B Polym Phys 2014;52:1669–80. doi:10.1002/polb.23554.

[113] Zhang X, Zhao S, Wang F, Ma Y, Wang L, Chen D, et al. Improving dielectric properties of BaTiO3/poly(vinylidene fluoride) composites by employing core-shell structured BaTiO3@Poly(methylmethacrylate) and BaTiO3@Poly(trifluoroethyl methacrylate) nanoparticles. Appl Surf Sci 2017;403:71–9. doi:10.1016/j.apsusc.2017.01.121.

[114] Zhang X, Chen H, Ma Y, Zhao C, Yang W. Preparation and dielectric properties of core–shell structural composites of poly(1H,1H,2H,2H-perfluorooctyl methacrylate)@BaTiO3 nanoparticles. Appl Surf Sci 2013;277:121–7. doi:10.1016/J.APSUSC.2013.03.178.

[115] Du X, Liu Y, Wang J, Niu H, Yuan Z, Zhao S, et al. Improved Triboelectric Nanogenerator Output Performance through Polymer Nanocomposites Filled with Core–shell-Structured Particles. ACS Appl Mater Interfaces 2018;10:25683–8. doi:10.1021/acsami.8b05966.

[116] Huang Y, Huang X, Schadler LS, He J, Jiang P. Core@Double-Shell Structured Nanocomposites: A Route to High Dielectric Constant and Low Loss Material. ACS Appl Mater Interfaces 2016;8:25496–507. doi:10.1021/acsami.6b06650.

[117] Qian K, Lv X, Chen S, Luo H, Zhang D. Interfacial engineering tailoring the dielectric behavior and energy density of BaTiO3/P(VDF-TrFE-CTFE) nanocomposites by regulating a liquid-crystalline polymer modifier structure. Dalt Trans 2018;47:12759–68. doi:10.1039/C8DT02626B.

[118] Lv X, Luo H, Chen S, Han X, Ma C, Zhou X, et al. BaTiO3 platelets and poly(vinylidene fluoride-trifluoroethylene-chlorofluoroethylene) hybrid composites for

energy storage application. Mech Syst Signal Process 2018;108:48–57. doi:10.1016/j.ymssp.2018.02.011.

[119] Yang K, Huang X, Zhu M, Xie L, Tanaka T, Jiang P. Combining RAFT Polymerization and Thiol–Ene Click Reaction for Core–Shell Structured Polymer@BaTiO3 Nanodielectrics with High Dielectric Constant, Low Dielectric Loss, and High Energy Storage Capability. ACS Appl Mater Interfaces 2014;6:1812–22. doi:10.1021/am4048267.

[120] Su J, Zhang J. Recent development on modification of synthesized barium titanate (BaTiO3) and polymer/BaTiO3 dielectric composites. J Mater Sci Mater Electron 2018;30:1–19. doi:10.1007/s10854-018-0494-y.

[121] Niu Y, Wang H. Dielectric Nanomaterials for Power Energy Storage: Surface Modification and Characterization. ACS Appl Nano Mater 2019;2:627–42. doi:10.1021/acsanm.8b01846.

[122] Xie L, Huang X, Huang Y, Yang K, Jiang P. Core-shell Structured Hyperbranched Aromatic Polyamide/BaTiO3 Hybrid Filler for Poly(vinylidene fluoride-trifluoroethylene-chlorofluoroethylene) Nanocomposites with the Dielectric Constant Comparable to That of Percolative Composites. ACS Appl Mater Interfaces 2013;5:1747–56. doi:10.1021/am302959n.

[123] Guo N, DiBenedetto SA, Tewari P, Lanagan MT, Ratner MA, Marks TJ. Nanoparticle, Size, Shape, and Interfacial Effects on Leakage Current Density, Permittivity, and Breakdown Strength of Metal Oxide−Polyolefin Nanocomposites: Experiment and Theory. Chem Mater 2010;22:1567–78. doi:10.1021/cm902852h.

[124] Luo H, Zhou X, Ellingford C, Zhang Y, Chen S, Zhou K, et al. Interface design for high energy density polymer nanocomposites. Chem Soc Rev 2019;48:4424–65. doi:10.1039/c9cs00043g.

[125] Dasgupta Q, Madras G, Chatterjee K. Biodegradable polyol-based polymers for biomedical applications. Int Mater Rev 2019;64:288–309. doi:10.1080/09506608.2018.1505066.

[126] Liu T, Huang K, Li L, Gu Z, Liu X, Peng X, et al. High performance high-density polyethylene/hydroxyapatite nanocomposites for load-bearing bone substitute: fabrication, in vitro and in vivo biocompatibility evaluation. Compos Sci Technol 2019;175:100–10. doi:10.1016/j.compscitech.2019.03.012.

[127] Salari M, Mohseni Taromsari S, Bagheri R, Faghihi Sani MA. Improved wear, mechanical, and biological behavior of UHMWPE-HAp-zirconia hybrid nanocomposites with a prospective application in total hip joint replacement. J Mater Sci 2019;54:4259–76. doi:10.1007/s10853-018-3146-y.

[128] Gopalakrishnan S, Raj I, Mathew T. A, Abraham J, Maria HJ, Mozetič M, et al. Development of oral-fluid-impervious and fracture-resistant silver–poly(methyl methacrylate) nanoformulations for intra-oral/extra-oral rehabilitation. J Appl Polym Sci 2019;136:47669. doi:10.1002/app.47669.

[129] Kumar A, Sharma R, Das MK, Gajbhiye P, Kar KK. Impacts of ceramic filler and the crystallite size of polymer matrix on the ionic transport properties of lithium triflate/poly (vinylidene fluoride-co-hexafluoropropene) based polymer electrolytes. Electrochim Acta 2016;215:1–11. doi:10.1016/J.ELECTACTA.2016.08.087.

[130] Sasikumar M, Raja M, Krishna RH, Jagadeesan A, Sivakumar P, Rajendran S. Influence of Hydrothermally Synthesized Cubic-Structured BaTiO3 Ceramic Fillers on Ionic Conductivity, Mechanical Integrity, and Thermal Behavior of P(VDF–HFP)/PVAc-Based Composite Solid Polymer Electrolytes for Lithium-Ion Batteries. J Phys Chem C 2018;122:25741–52. doi:10.1021/acs.jpcc.8b03952.

[131] Prabakaran P, Manimuthu RP, Gurusamy S. Influence of barium titanate nanofiller on PEO/PVdF-HFP blend-based polymer electrolyte membrane for Li-battery applications. J

Solid State Electrochem 2017;21:1273–85. doi:10.1007/s10008-016-3477-z.
[132] Chen J, Xiong X, Shui L, Zhang Q, Yang H, Zhang F. Enhanced dielectric constant and hydrophobicity of P(VDF–TrFE)-based composites. J Mater Sci Mater Electron 2018;29:17612–21. doi:10.1007/s10854-018-9864-8.
[133] Wang Y, Wang L, Yuan Q, Chen J, Niu Y, Xu X, et al. Ultrahigh energy density and greatly enhanced discharged efficiency of sandwich-structured polymer nanocomposites with optimized spatial organization. Nano Energy 2018;44:364–70. doi:10.1016/j.nanoen.2017.12.018.
[134] Hao YN, Wang XH, O'Brien S, Lombardi J, Li LT. Flexible BaTiO3/PVDF gradated multilayer nanocomposite film with enhanced dielectric strength and high energy density. J Mater Chem C 2015;3:9740–7. doi:10.1039/C5TC01903F.
[135] Shepelin NA, Glushenkov AM, Lussini VC, Fox PJ, Dicinoski GW, Shapter JG, et al. New developments in composites, copolymer technologies and processing techniques for flexible fluoropolymer piezoelectric generators for efficient energy harvesting. Energy Environ Sci 2019;12:1143–76. doi:10.1039/C8EE03006E.
[136] Dudem B, Kim DH, Bharat LK, Yu JS. Highly-flexible piezoelectric nanogenerators with silver nanowires and barium titanate embedded composite films for mechanical energy harvesting. Appl Energy 2018;230:865–74. doi:10.1016/j.apenergy.2018.09.009.

Chapter II: Materials, methods and characterizations

II.1. Introduction

This chapter presents the description of the protocols and methods used to functionalize barium titanate surface and the polymerization reactions used to obtain polymer-*g*-$BaTiO_3$ nanocomposites. A brief description of the different instrumental techniques used to characterize, analyze and study the different materials prepared is also presented.

II.2. Materials

Various products have been used in this work, especially barium titanate. This commercial ceramic nanoparticle, supplied by Sigma Aldrich is 100 nm in size. The different characteristics of the reagents used in this study are listed in Table 1.

Table 1: List of chemicals used during this thesis.

Products	***Chemical formula***	***Molar mass (g/mol)***	***Boiling point (°C)***	***Density (g/ml)***
Barium titanate	$BaTiO_3$	233.19	-	6.080
(3-Aminopropyl)	$C_9H_{23}O_3SiN$	221.37	217	0.946
triethoxysilane	H_2O_2	34.01	107	1.110
Hydrogen peroxide				
(3-chloropropyl)	$C_9H_{21}O_3SiCl$	240.80	100	1.000
triethoxysilane				
Potassium ethyl xanthogenate	$C_3H_5OS_2K$	160.30		1.263
Triethylamine	$C_6H_{15}N$	101.19	88.8	0.726
Tert-Butyl peroxypivalate	$C_9H_{18}O_3$	174.24	245.22	0.854
Lithium manganese oxide	$LiMn_2O_4$	180.80	-	4.290
Poly(vinylidene Fluoride)	CH_2CF_2	~1000000	-	1.78
Toluene	C_7H_8	92.14	110-111	0.865
Dichloromethane	CH_2Cl_2	84.93	39.8-40	1.325
Acetone	C_3H_6O	58.08	56	0.791
Tetrahydrofurane	C_4H_8O	72.11	65-67	0.889
Dimethylformamide	C_3H_7ON	73.09	153	0.944
Ethanol	C_2H_6O	46.07	78	0.789
Dimethyl carbonate	$C_3H_6O_2$	90.08	90	1.069
N-Methylpyroolidone	C_5H_9NO	99.13	202	1.028

II.3. Synthesis procedures

As mentioned in the previous chapter, the synthesis procedure of a nanocomposite material based on organic polymer and inorganic filler should start from the functionalization of the ceramic surface to offer a good compatibility and dispersion of ceramic nanofiller into polymer matrix.

II.3.1. Oxidation of $BaTiO_3$

Using a literature procedure for the surface hydroxylation of $BaTiO_3$ nanoparticles [1,2], 10.02 g of $BaTiO_3$ nanoparticles and 60 ml of aqueous solution of H_2O_2 (30 wt%) were combined in a round bottomed flask. The mixture was sonicated for 30 min and then was refluxed at 105 °C for 4 h. The nanoparticles were recovered by centrifugation at 12 500 rpm for 5 min and were washed with deionized water twice. The obtained BT-OH nanoparticles as a white powder were dried under vacuum at 80 °C until a constant weight of 9.58 g (Yield: 98 %).

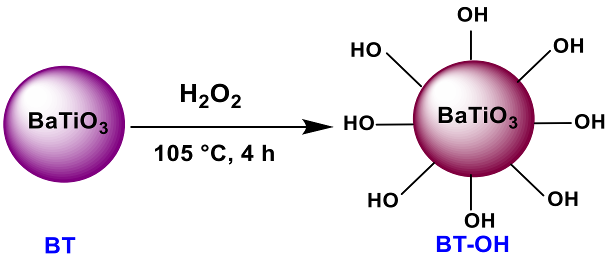

Scheme 1. Oxidation reaction of $BaTiO_3$ nanoparticles in presence of hydrogen peroxide.

II.3.2. Modification of $BaTiO_3$-OH (BT-OH) with (3-chloropropyl) triethoxysilane (CPTS)

6.03 g of BT-OH nanoparticles and 60 ml of toluene were combined in a beaker and the mixture was sonicated for 20 minutes for a better dispersion.

In a 250 ml bicol flask equipped with a magnetic stirrer, the sonicated mixture was introduced, and the system was bubbled for 10 min with nitrogen. 10.03 g (10 ml) of CPTS were added. Then, the mixture was degased for 5 minutes to remove the oxygen from the solution. This mixture was then stirred at 80 °C for 12 under nitrogen. The particles (BT-CPTS) were recovered by centrifugation at 12 500 rpm for 5 min and washed twice with toluene [3,4]. The resulting BT-CPTS particles as a white powder were dried at 80 °C until a constant weight of 5.84 g (Yield: 97 %).

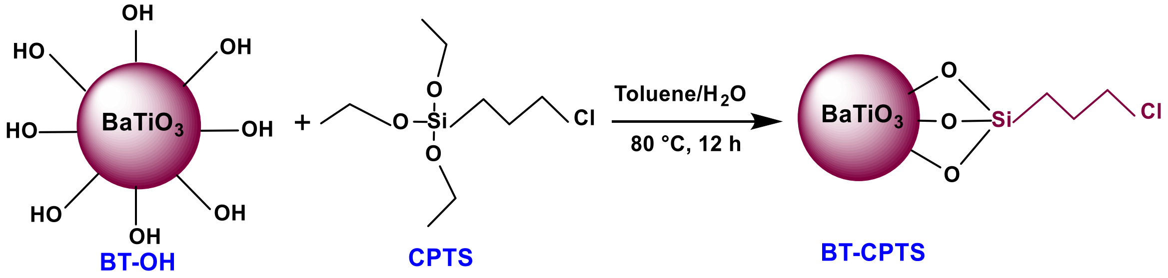

Scheme 2. Modification of oxidized nanoparticles with (3-chloropropyl) triethoxysilane (CPTS).

II.3.3. Modification of BT-CPTS with Potassium ethyl xanthogenate

5.02 g of BT-CPTS and 120 ml of absolute ethanol were placed in a beaker. The mixture was sonicated for 20 minutes for better dispersion. In a 250 ml two necked-round bottom flask equipped with a magnetic stirrer, the sonicated mixture was introduced and the system was saturated for 10 min with nitrogen. Then, 3.57 g of the RAFT agent were added. The mixture was then bubbled for 5 minutes to remove the oxygen from the solution. This mixture was stirred at 80 °C for 12 hours under nitrogen [5]. The particles (BT-XA) were recovered by centrifugation at 12 500 rpm for 5 min and washed several times with ethanol, the resulting BT-XA particles as a white powder were dried at 80 °C until a constant weight of 4.49 g (Yield: 98 %).

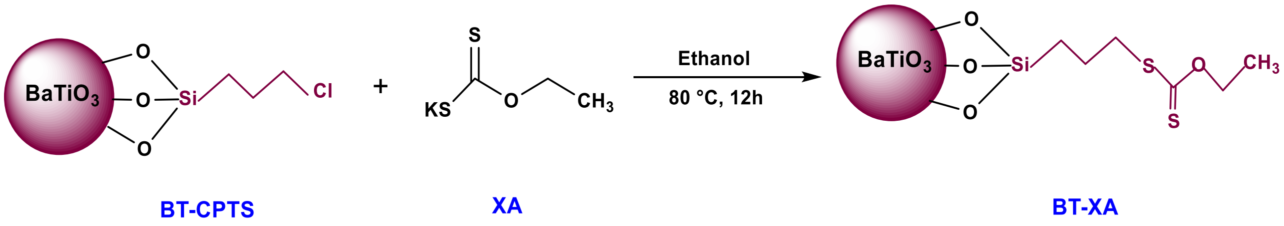

Scheme 3. Functionalization of BT-CPTS with RAFT agent.

The overall yield of the synthesis of BT-XA from pristine BT is 93%

II.3.4. Preparation of PVDF-*g*-$BaTiO_3$ nanocomposites via RAFT Polymerization

A thick 8 mL Carius tube containing BT-XA (30-200 mg), the solvent (7 mL of DMC) and the initiator (0.054 g of TBPPi) was sonicated for 25 min. Then, the tube was degassed by performing at least three freeze-pump-thaw cycles. VDF gaseous monomer (1.5 g) was transferred into the Carius tube cooled at liquid nitrogen temperature using a custom-made manifold that enables accurate measurement of quantities of gas (using a "pressure drop *vs* mass of monomer" calibration curve). The tube was then sealed under dynamic vacuum at the temperature of liquid nitrogen, before being placed horizontally in a shaking water bath thermostated at 64 °C (Figure 1).

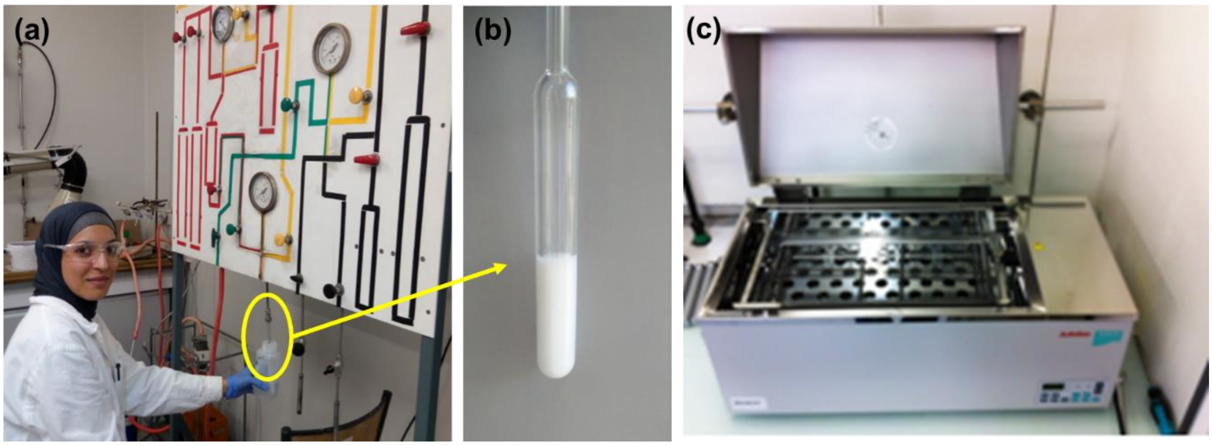

Figure 1. Experimental device used for RAFT polymerization of VDF: (a) Gas injection panel (b) Carius tube and (c) heating shaking bath.

After 15 hours, the tube was frozen into liquid nitrogen, opened, and the solvent was evaporated at 40 °C. Then, the mixture was precipitated from cold pentane. The PVDF-*g*-$BaTiO_3$ nanocomposite was recovered by centrifugation at 5000 rpm for 4 min. All the resulting nanocomposites as white powders were dried under vacuum at 60 °C until constant weight.

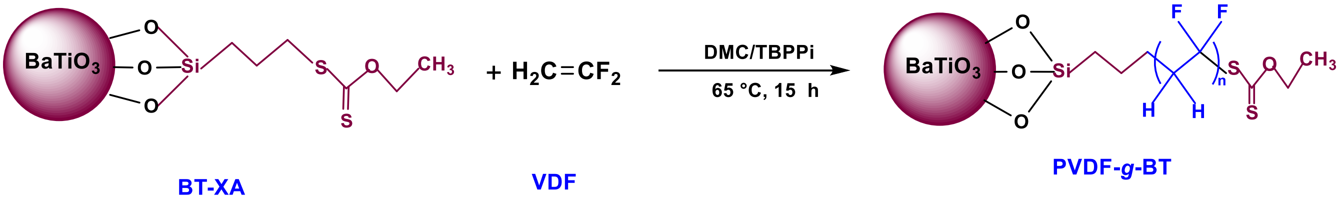

Scheme 4. Preparation of PVDF-g-$BaTiO_3$ nanocomposite using the RAFT polymerization of VDF initiated by *tert*-butyl peroxypivalate (TBPPi) in dimethyl carbonate (DMC).

To be able to compare the effect of the addition of BT nanofiller onto the PVDF polymer matrix, PVDF was also synthesized by RAFT polymerization of VDF in the presence of potassium ethyl xanthate and initiated by *tert*-butyl peroxypivalate.

In order to separate the physisorbed PVDF chains from PVDF-*g*-$BaTiO_3$ nanocomposites, several washing treatments with acetone were performed. An amount of $BaTiO_3$/PVDF nanocomposites obtained after RAFT polymerization was dispersed in acetone, and the mixture was stirred at 35 °C for 16 hours. Then, PVDF-*g*-$BaTiO_3$ nanocomposites were recovered by centrifugation at 5000 rpm for 5 min. The solvent of the supernatant containing the free PVDF chains was evaporated in order to estimate the quantity of such fluorinated polymers.

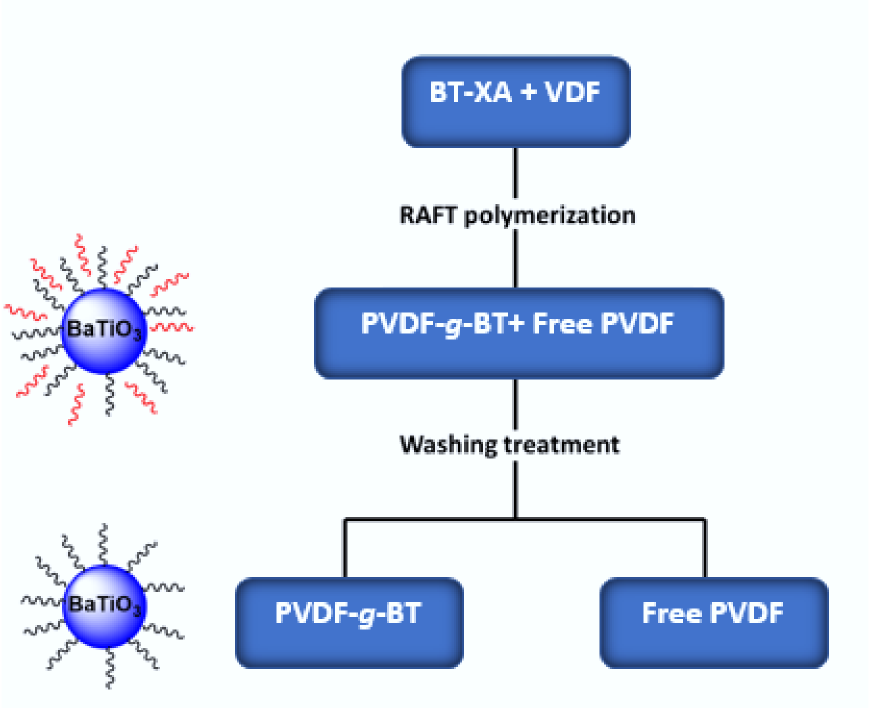

Scheme 5. Illustrative diagram of the treatment carried out after the RAFT polymerization of vinylidene fluoride (VDF) controlled by BT-XA chain transfer agent

II.3.5. Preparation of PVDF-*g*-BT/poly(VDF-*co*-HFP) nanocomposite films by a solution blending method

The synthesis of a core double shell system consisting on PVDF-*g*-BT nanocomposites synthesized previously embedded within poly(VDF-*co*-HFP) copolymer matrix was achieved by using a solution blending method.

First, an amount of PVDF-*g*-BT was dispersed in DMF for 4 h under ultrasonication. At the same time, an amount of the copolymer P(VDF-*co*-HFP) was dissolved in DMF for 4 h at room temperature before adding the nanocomposite slowly. The resulting mixture was stirred vigorously at room temperature. After 20 h, the mixture was poured into Teflon® substrate and then dried 120 ° C for 24 hours (Scheme 6).

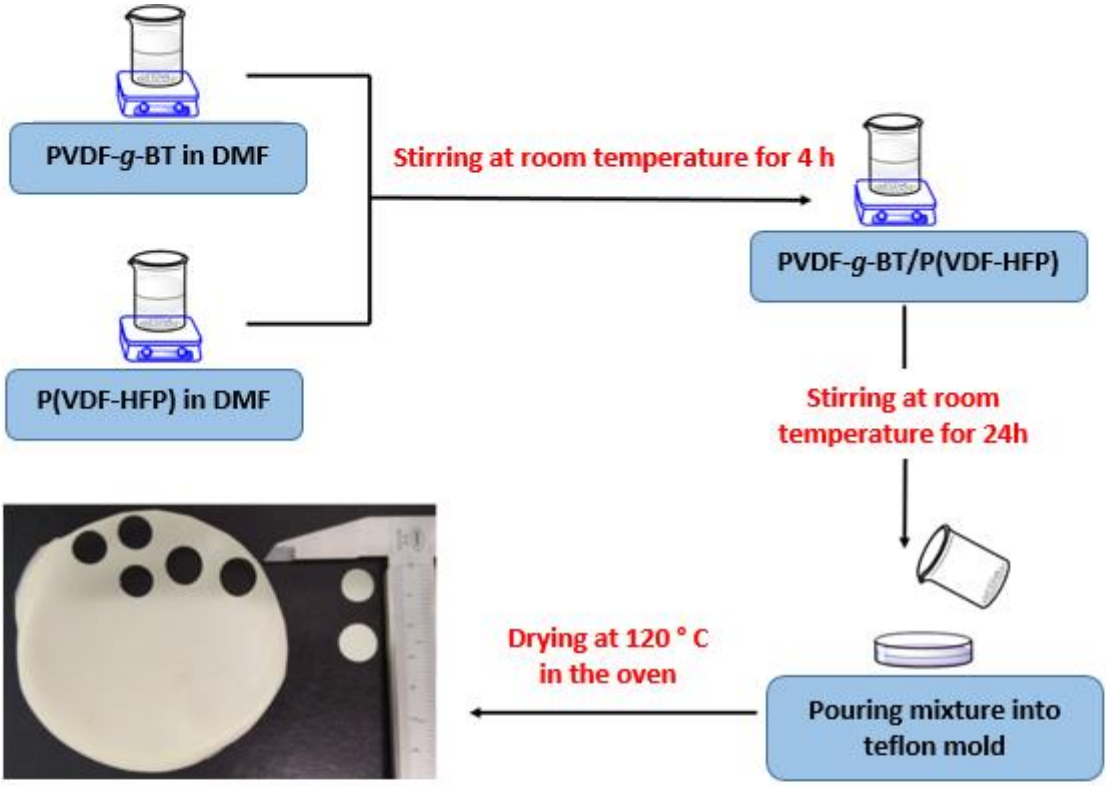

Scheme 6. Sketch illustrating the preparation method of PVDF-*g*-BT / poly(VDF-*co*-HFP) nanocomposite films.

II.4. Characterizations

II.4.1. Spectroscopy and chromatography analysis

II.4.1.1. Fourier transform infrared spectroscopy (FTIR)

One of the most common applications of FTIR spectroscopy is the identification of organic and inorganic compounds of given molecules. This technique consists in applying an infrared radiation on a sample and determining what fraction of the incident radiation is absorbed in a particular energy and that energy corresponds to the frequency of a vibration of a part of a sample molecule [6]. In the present study, FTIR analyses were performed using a "Perkin Elmer Spectrum 1000" (Figure 2) in ATR mode by accumulating 32 scans, over a wavelength range of 400 to 4000 cm^{-1}, with an accuracy of ± 2 cm^{-1} .

Figure 2. Picture of FTIR device used to analyze the functionalized nanoparticles and synthesized nanocomposites.

II.4.1.2. High resolution magic angle spinning nuclear magnetic resonance (HRMAS NMR) spectroscopy

This technique consists in placing the sample in a rotor which is placed in a magnet giving a field B_0. The rotation of the sample is then performed by rotating it at a speed of several kHz on itself at an angle of 54.74 ° to the main magnetic field [7,8] (Scheme 6).

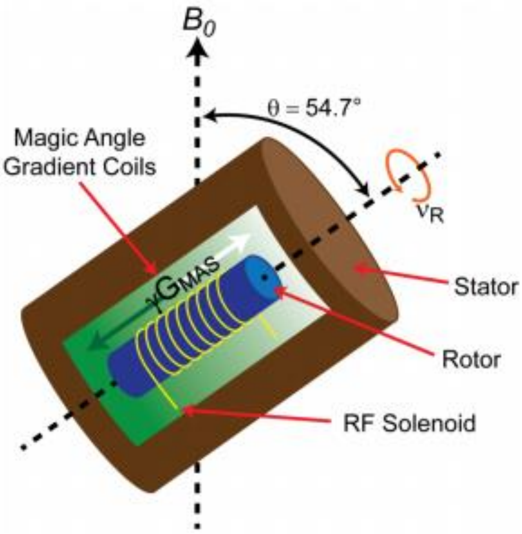

Scheme 7. Schematic representation of a HR-MAS stator with a magic angle gradient along the rotational axis of the rotor [9].

HRMAS NMR spectroscopy was used to qualitatively characterize the surface grafting. High Resolution-MAS NMR experiments were carried out on a Varian VNMRS 600 MHz spectrometer (Figure 3) equipped a wide bore magnet (B_0=14.1T), 2D lock and Z gradients together with a broadband 15N-31P 2 channels 4 mm Fast Nano probe optimized for ^{19}F. Prior to HR-MAS NMR experiments, the PVDF-*g*-$BaTiO_3$ powder nanocomposite samples were inserted into a quartz 4 mm zirconia HRMAS rotor insert and drops of DMSO (used as deuterium solvent for lock and sample surface-or PVDF- impregnation) were added. The as-prepared sample was then inserted into to a 4 mm zirconia HRMAS rotor. Experiments were performed at room temperature. The sample spinning rate was 4 kHz for ^{1}H and 6.5 KHz for ^{19}F. A single pulse sequence was used with pulse durations of 12 μs corresponding to flip angle of 90 °. A recycling delay of 1 s was used and 646 transients were co-added.

Figure 3. Picture of HRMAS NMR spectroscope used to analyze functionalized $BaTiO_3$ and PVDF-*g*-BT nanocomposites.

II.4.1.3. Size exclusion chromatography (SEC)

This technique consists in introducing the polymer solution into a column filled with porous beads and recovering the fractions as a function of the elution time in the column (elution time). Depending on their size, macromolecules will be eluted after a longer or shorter time [10].

SEC analyses were carried out on a Polymer Laboratories "PL-GPC 50 Plus" instrument (Figure 4) using 2 PL gel Mixed-C 5 µm columns (range of molecular weight from 200 to 2.10^6 g/mol) thermostated at 35 °C equipped with a refractive index detector. Dimethylformamide (DMF) with 1% LiBr was used as the eluent (1.0 mL/min). Calibration was performed using Varian polymethylmethacrylate (PMMA) narrow standards and toluene as a flow marker.

Figure 4. GPC device used to characterize the free PVDF chains extracted from the nanocomposites.

II.4.2. Thermal analysis

II.4.2.1. Thermogravimetric analysis (TGA)

TGA is a technique that allows measurement of the mass variation of a given sample when subjected to controlled atmosphere temperature programming. Thermogravimetric measurements were performed using a TA Instrument Q50 apparatus (Figure 5). Samples were heated under air [*i.e.* a mixed atmosphere of nitrogen and oxygen (60 mL/min and 40 mL/min, respectively)] with a heating rate of 10 °C/min from room temperature to 800 °C.

Figure 5. TGA device used to characterize the different samples.

II.4.2.2. Differential scanning calorimetry (DSC)

DSC analysis is used to determine the variation of heat flux emitted or received by a sample when subjected to controlled atmosphere temperature programming. In the present work, DSC measurements were performed on 10-15 mg samples on a Netzsch DSC 200 F3 instrument (Figure 6) using the following heating/cooling cycle: first heating from 20 °C to 250 °C at 20 °C/min, cooling from 250 to -100 °C at 20 °C/min, isotherm plateau at -100 °C for 10 min, second heating from -100 °C to 250 °C at 10 °C/min and last cooling from 250 °C to 20 °C at 40 °C/min. Calibration of the instrument was performed with noble metals and checked before analysis with an indium sample (T_m = 156.6 °C).

Melting temperatures and melting enthalpies (ΔH_m) were determined from the lowest point of the valley with the highest depth and the area of enthalpy peak, respectively. The degrees of crystallinity of the graft PVDF were determined using equation 1:

$$\text{Degree of cristallinity } (\chi) = \frac{\Delta \mathrm{H_m}}{\Delta \mathrm{H_c}} \times 100 \qquad (1)$$

where ΔH_c (104.5 J g^{-1}, 104.7 J g^{-1}) corresponds to the melting enthalpy of a 100 % crystalline α phase PVDF [11,12] and 100 % crystalline P(VDF-*co*-HFP) [13,14], respectively. While ΔH_m is the heat of fusion of the sample under consideration (determined by DSC in J g^{-1}).

Figure 6. DSC device used to characterize the different samples.

II.4.3. Morphological analysis

II.4.3.1. Scanning electronic microscopy (SEM)

The microstructure of PVDF-*g*-$BaTiO_3$ was observed by Scanning Electron Microscope (SEM, TESCAN-VEGA 3) equipped with Energy Dispersive Spectrometer (EDS, EDAX Team). All samples were deposited on a carbon conductive adhesive tape, then coated with carbon to improve the conductivity. While the microstructure of PVDF-*g*-BT@ P(VDF-*co*-HFP) nanocomposite films was observed using a scanning electron microscope (SEM, Zeiss HD15) equipped with an energy dispersive mapping (EDS, Oxford X-MAX). All samples were deposited on a carbon conductive adhesive tape and then coated with platinum to improve the conductivity.

II.4.3.2. Transmission electronic microscopy (TEM)

A drop (7 µL) of the sample solution (particles dispersed in ethanol) was placed on a perforated carbon film-coated copper grid for 50 s, blotted with filter paper and dried with a vacuum pump. The sample was transferred in a single axis tilt sample holder and observed at 100 kV acceleration voltage in a JEOL 1200 EXII transmission electron microscopy at 25 °C (Figure 7).

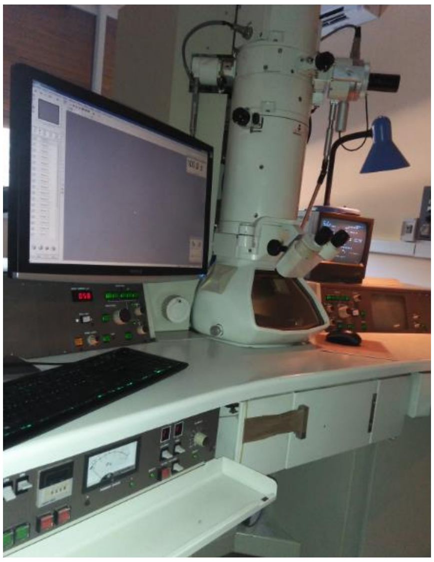

Figure 7. Transmission electronic microscope used to characterize the different samples.

II.4.3.3. X-ray diffraction (DRX)

X-ray diffraction is used to identify the nature and structure of crystalline phase products. It is a non-destructive method used for the qualitative and quantitative analysis of polycrystalline samples. In this work, X-ray diffraction (DRX) measurements were performed using Bragg–Brentano geometry on a Bruker D8 Advance diffractometer (Figure 8), using Cu K_α radiation (λ=1.5418 Å) with 30 KV and 10 mA, Soller slits of 0.02 rad on incident and diffracted beams; divergence slit of 0.5°; antiscatter slit of 1°; receiving slit of 0.1 mm; with sample spinner, and a Lynxeye detector type with a maximum global count rat >1000.000.000 cps. The pattern was scanned through steps of 0.010142° (2θ), between 10 and 80° (2θ) with a fixed-time counting of 0.8 seconds/step.

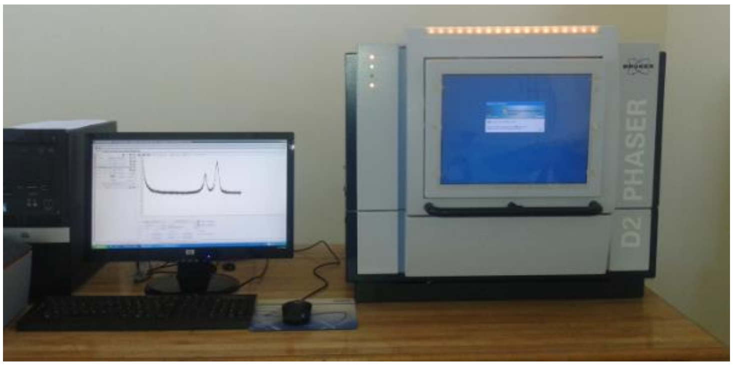

Figure 8. Picture of XRD device used to analyze the different samples.

II.4.4. Dielectric measurements

Broadband Dielectric Spectroscopy (BDS) was used to investigate the effect of $BaTiO_3$ loading on the dielectric properties of PVDF-*g*-BT nanocomposites. An Alpha Analyzer spectrometer by Novocontrol technologies GmbH & Co. equipped with a Novocontrol Quatro nitrogen gas flow cryostat was employed (Figure 9). The prepared pellets (10 mm diameter, about 50 μm thickness), capped between two thin layers of Pb, were placed in the BDS measurement cell. The temperature range was from -100 to 125°C with a heating rate of 5 or 10°C/min and the measured frequency range was from 1.7×10^{-2} Hz to 10^{7} Hz. Amplitude of the applied sinusoidal voltage was 1.5 V.

Figure 9. Broadband dielectric spectroscope.

II.4.5. Mechanical analysis

Uniaxial tensile tests on specimens were performed at a crosshead speed of 2.5 mm/min using a 5566 INSTRON tensile machine equipped with a 2-kN load cell. The stiffness (using four rectangular specimens of each sample, where the thickness of the films vary from 0.16 to 0.26 mm) was calculated in the linear region of stress– strain curves using trendlines within the strain region 0-2% (Figure 10).

Figure 10. Tensile machine used to analyze the mechanical properties of nanocomposite films.

II.4.6. Electrochemical characterizations

II.4.6.1.Electrode preparation

The cathode films were prepared using 70 wt% $LiMn_2O_4$ as active material, 18 wt% of Carbon black (C65) as conductive agent, 12 wt% of the binder (PVDF or PVDF-*g*-BT nanocomposite or both) and N-methylpyrrolidone (NMP) as solvent. Whatman glass microfiber filters (grade GF/D) used as separators, Li metal foil was used as the anode material, and 1M LiPF6 dissolved in a solution of ethylene carbonate/dimethyl carbonate (1:1 vol %) as the electrolyte.

To form the slurry, the precursors were homogenized in an agate pestle. After several minutes of blending with a mortar, the mixture was transferred to an agate ball-milling jar (with four balls) (Figure 11-a) and NMP was added. The mixture was then ball-milled softly at 500 rpm for 30 min. The obtained slurry was spread uniformly on aluminum metal grade foil (0.018 mm, Goodfellow) casted by a four sided film applicator (150 µm) from Elcometer (Figure 11-b). After 48 h of drying at room temperature, the casted films were further dried under dynamic vacuum at 80 °C and - 0.850 bar relative pressure in an XFL020 drying oven, France Etuves. In order to enhance the dispersity of the precursors, the dried films were calendered at 50 °C at 5 rotations per minute, where the thickness was fixed at 30 µm (Figure 11-c), then punched to discs with 12.7 mm in diameter.

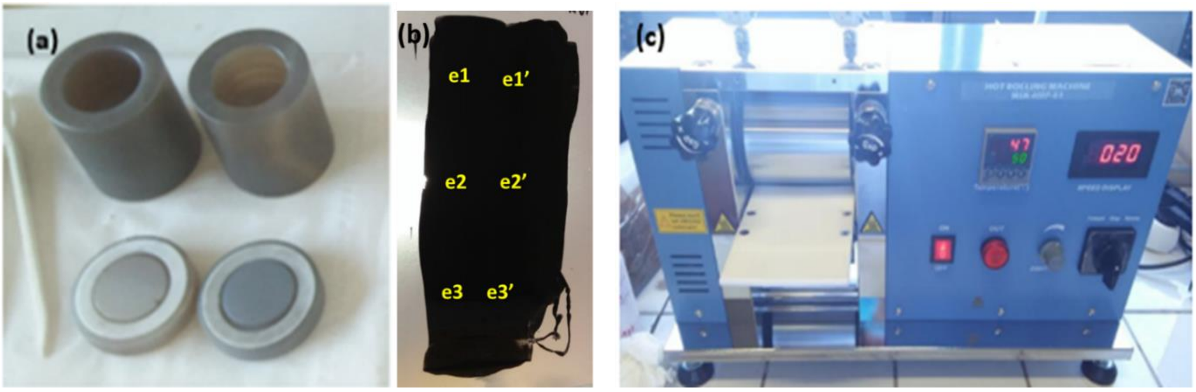

Figure 11. Electrodes preparation: (a) homogenization of precursors (b) casting of the slurry on aluminum foil and (c) Electrodes calendering.

II.4.6.2. Half coin cell assembly

316 L stainless steel 2032 coin–cells were used to characterize the positive electrode material under argon atmosphere in a glovebox. To assemble the coin-cell, the spring was placed on the small lid first in order to maintain battery pressure, then lithium foil, which was punched to discs with 14 mm in diameter and already positioned on a thick spacer that plays the role of current collector from the anode side was sited. The electrolyte was dropped on the separator (16 mm) and the prepared electrode was then placed with its aluminum surface in contact with the coin cell big lid. In the last step, the coin cell big lid was fixed on the top and the cell was sealed by a crimping machine.

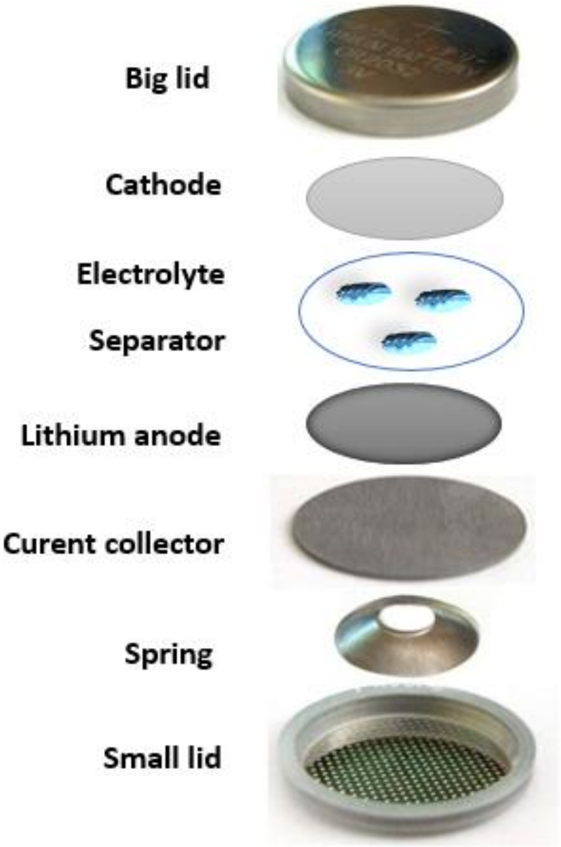

Scheme 8. Schematic illustration of half coin-cell component.

II.4.6.3. Cyclic voltammetry

The cyclic voltammetry is a popular experiment in chemical research, since it can provide useful information about redox reactions in a form of which is easily obtained and interpreted [15]. This technique consists on varying the applied potential at a working electrode in both forward and reverse directions, at a given scan rate, while observing the current [16]. In the present work, a VSP-3000 instrument was used from 3.2 V to 4.5 V at a scan rate of 0.5 mV/s to characterize cells made with active material and from 0 V to 3.5 V for cells made without active material.

II.4.6.4. Galvanostatic cycling

This technique is considered as the most standard tool for studying the behavior of batteries upon cycling [17]. The battery performances are determined as a function of its charge and discharge conditions. During Galvanostatic cycling of the battery, the charge and discharge cure=rent are often expressed as a C-rate, calculated from the battery capacity. A C-rate is a measure of which a battery is charged or discharged relatively to its maximum capacity. For example, a 1 C-rate means that the discharge current will discharge the entire battery in 1 hour.

The prepared cells were characterized using a BCS-805 battery cycler from BioLogic // BTS 4000 battery testing system from Neware (Figure 12) offering 8 independent channels with a maximum current of ±150 mA per channel. The cells were charged and discharged for 55 cycles from 2.5 V to 4.5 V and from 3.4 V to 4.3 V at various current densities, and the current rate was increased from 1 C to 10 C. The theoretical specific capacity C of $LiMn_2O_4$ was considered equal to 148 mA h g^{-1}, for a 1-e^- process. All current densities were calculated as C×n for a charge/discharge with n lithium ions (de)inserted in 1 h.

Figure 12. BCS-805 device used to perform the cycling performances of the prepared cells.

II.5. References

[1] X. Zhang, S. Zhao, F. Wang, Y. Ma, L. Wang, D. Chen, C. Zhao, W. Yang, Improving dielectric properties of BaTiO3/poly(vinylidene fluoride) composites by employing core-shell structured BaTiO3@Poly(methylmethacrylate) and BaTiO3@Poly(trifluoroethyl methacrylate) nanoparticles, Appl. Surf. Sci. 403 (2017) 71–79. doi:10.1016/j.apsusc.2017.01.121.

[2] L. Xie, X. Huang, C. Wu, P. Jiang, Core-shell structured poly(methyl methacrylate)/BaTiO3 nanocomposites prepared by in situ atom transfer radical polymerization: a route to high dielectric constant materials with the inherent low loss of the base polymer, J. Mater. Chem. 21 (2011) 5897. doi:10.1039/c0jm04574h.

[3] S. Jafarzadeh, V. Haddadi-Asl, H. Roghani-Mamaqani, Nanofibers of poly (hydroxyethyl methacrylate)-grafted halloysite nanotubes and polycaprolactone by combination of RAFT polymerization and electrospinning, J. Polym. Res. 22 (2015) 123. doi:10.1007/s10965-015-0773-8.

[4] X.T. Cao, A.M. Showkat, K.L.N. Thi, S.-S. Hong, K.T. Lim, Synthesis and Properties of Poly(N-vinylcarbazole) Covalently Functionalized Zinc Oxide Nanocomposites, Mol. Cryst. Liq. Cryst. 618 (2015) 95–102. doi:10.1080/15421406.2015.1076298.

[5] M.R. Islam, L.G. Bach, K.T. Lim, Poly(2-hydroxyethyl methacrylate) grafted halloysite nanotubes as a molecular host matrix for luminescent ions prepared by surface-initiated RAFT polymerization and coordination chemistry, Appl. Surf. Sci. 276 (2013) 298–305. doi:10.1016/J.APSUSC.2013.03.086.

[6] B. Stuart, Infrared Spectroscopy, in: Kirk-Othmer Encycl. Chem. Technol., John Wiley & Sons, Inc., Hoboken, NJ, USA, 2015: pp. 1–18. doi:10.1002/0471238961.0914061810151405.a01.pub3.

[7] W.P. Power, High-Resolution Magic Angle Spinning-Enabling Applications of NMR Spectroscopy to Semi-Solid Phases, 2011. doi:10.1016/B978-0-12-385857-3.00003-7.

[8] A.D.C. Santos, F.A. Fonseca, L.M. Lião, G.B. Alcantara, A. Barison, High-resolution magic angle spinning nuclear magnetic resonance in foodstuff analysis, TrAC - Trends Anal. Chem. 73 (2015) 10–18. doi:10.1016/j.trac.2015.05.003.

[9] T. M.Alam, J. E.Jenkins, HR-MAS NMR Spectroscopy in Material Science, in: Adv. Asp. Spectrosc., InTech, 2012. doi:10.5772/48340.

[10] S. Mukherjee, Isolation and Purification of Industrial Enzymes: Advances in Enzyme Technology, in: Adv. Enzym. Technol., Elsevier, 2019: pp. 41–70. doi:10.1016/b978-0-444-64114-4.00002-9.

[11] K. Nakagawa, Y. Ishida, Annealing effects in poly(vinylidene fluoride) as revealed by specific volume measurements, differential scanning calorimetry, and electron microscopy, J. Polym. Sci. Part A-2 Polym. Phys. 11 (1973) 2153–2171. doi:10.1002/pol.1973.180111107.

[12] K. Nakagawa, Y. Ishida, Estimation of amorphous specific volume of poly(vinylidene fluoride) as a function of temperature, Kolloid-Zeitschrift Und Zeitschrift Für Polym. 251 (1973) 103–107. doi:10.1007/BF01498933.

[13] Z. He, Q. Cao, B. Jing, X. Wang, Y. Deng, Gel electrolytes based on poly(vinylidenefluoride-co-hexafluoropropylene)/thermoplastic polyurethane/poly(methyl methacrylate) with in situ SiO2 for polymer lithium batteries, RSC Adv. 7 (2017) 3240–3248. doi:10.1039/C6RA25062A.

[14] A.L. Ahmad, U.R. Farooqui, N.A. Hamid, Effect of graphene oxide (GO) on Poly(vinylidene fluoride-hexafluoropropylene) (PVDF- HFP) polymer electrolyte membrane, Polymer (Guildf). 142 (2018) 330–336. doi:10.1016/J.POLYMER.2018.03.052.

[15] D.H. Evans, K.M. O'Connell, R.A. Petersen, M.J. Kelly, Cyclic voltammetry, J. Chem. Educ. 60 (1983) 290–293. doi:10.1021/ed060p290.

[16] Joshi PS, Sutrave DS, A Brief Study of Cyclic Voltammetry and Electrochemical Analysis, Int. J. ChemTech Res. 11 (2018) 77–88. doi:10.20902/IJCTR.2018.110911.

[17] A. Balducci, D. Belanger, T. Brousse, J.W. Long, W. Sugimoto, A guideline for reporting performance metrics with electrochemical capacitors: From electrode materials to full devices, J. Electrochem. Soc. 164 (2017) A1487–A1488. doi:10.1149/2.0851707jes.

Chapter III: Core shell structured Poly(Vinylidene Fluoride) *-grafted-* $BaTiO_3$ nanocomposites prepared via Reversible Addition-fragmentation chain transfer (RAFT) polymerization of VDF for high energy storage capacitors (2)

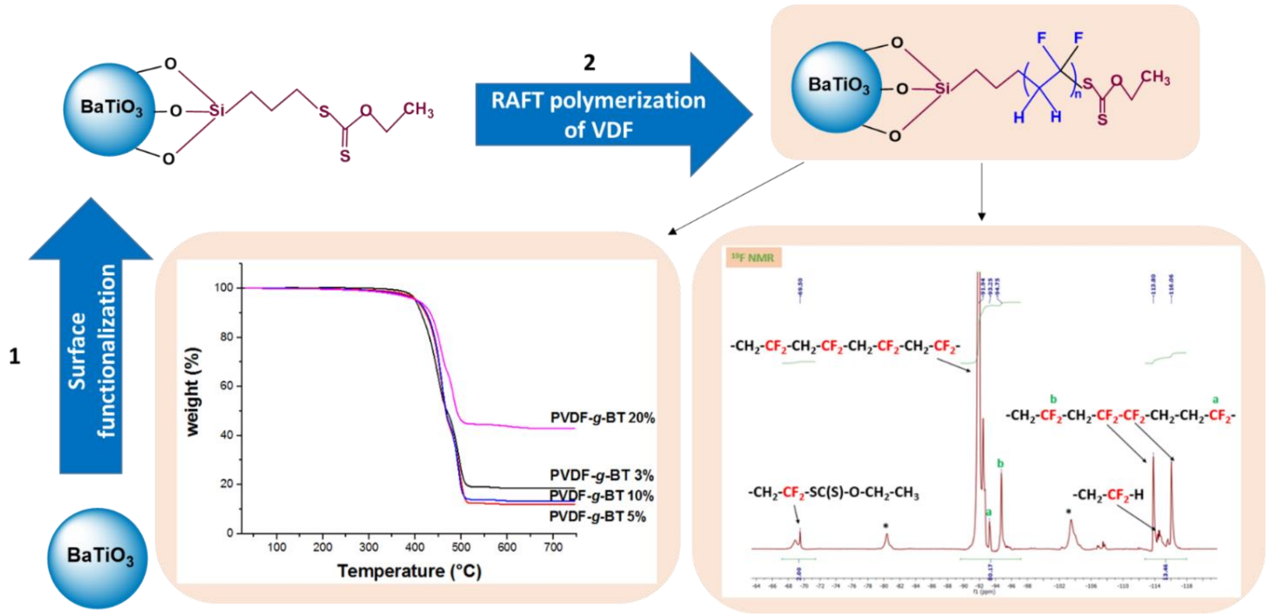

---

[2] This chapter has been published in **Polymer Chemistry** Journal:

***Bouharras et al., Polym. Chem.**, 2019,10, 891-904*

III.1 Introduction

High dielectric constant (high-k) ceramic/polymer nanocomposites represent an emerging material platform for advanced energy-storage technologies and dielectric applications because the efficient properties and giant dielectric constants of ceramics, such as $BaTiO_3$, with the flexibility, the low cost and easy processing of polymers [1]. Polar polymers such as PVDF and VDF-based copolymers serve as the best selected (co)polymers for high energy density applications. Chapter 1 provided an update of various studies to design core-Shell $BaTiO_3$/ fluoropolymer based on poly[fluoroalkyl meth(acrylate)]s, PVDF and its co- and terpolymers nanocomposites, to study their properties and performances and to supply their applications. Core-shell nano-architecture strategies are versatile and powerful tools for the design and synthesis of advanced high-k polymer nanocomposites. A special focus emphasizes their advantages over conventional melt-mixing and solution-mixing methods that lead to aggregation and poor dielectric properties.

In contrast of the above strategies for the preparation of $BaTiO_3$/PVDF nanocomposites using solution mixing as the technique, this work reports the first synthesis of homogeneous core-shell modified PVDF-*grafted*-$BaTiO_3$ nanocomposites. The ceramic fillers were surface modified with xanthate to allow the RAFT *in-situ* VDF polymerization (Grafting from), ensuring a chemical bond of PVDF with the $BaTiO_3$ surface. This technique has the advantages of compatibility with a wide range of functionalities in monomer types, and no metallic ion complexes are needed in contrast to ATRP (actually, residual copper salt may lead to high leakage current under high electric field and undesirable of dielectric properties [2]). The effect of $BaTiO_3$ percentage on the properties of these nanocomposites was studied. To the best of our knowledge, it is the first time that this approach has been used to fabricate bonded PVDF onto nanoparticle surfaces. The resulting nanocomposites were fully characterized by FT-IR, ^{19}F and ^{1}H HRMAS NMR spectroscopies, SEC, XRD, MEB, TEM, DSC and TGA.

III.2 Results and discussion

Previously, Yang *et al.* [3] and Zhu *et al.* [4] reported the functionalization of the $BaTiO_3$ by RAFT agent (trithiocarbonate) in four steps: (i) preparation of S-1-dodecyl (or S-1-ethyl)-S′-(α,α′-dimethyl-α″-acetic acid) trithiocarbonate (DDMAT), (ii) activation of DDMAT by N-hydroxysuccinimide (NHS-DDMAT), (iii) preparation of amino-functionalized $BaTiO_3$

($BaTiO_3$-NH_2) by reaction of hydroxylated $BaTiO_3$ and γ-aminopropyl triethoxysilane, and (iv) preparation of DDMAT anchored $BaTiO_3$ nanoparticles by reaction between NHS-DDMAT and $BaTiO_3$-NH_2.

In contrast to their procedure, our strategy was to use xanthate functionalized BT, since xanthates are efficient chain transfer agents to control the RAFT (co)polymerization of VDF[5–9] . Scheme 2 represents the general procedure for the preparation of functionalized $BaTiO_3$ by RAFT agent which was used in the last step to synthesis the PVDF-*g*-$BaTiO_3$ nanocomposites.

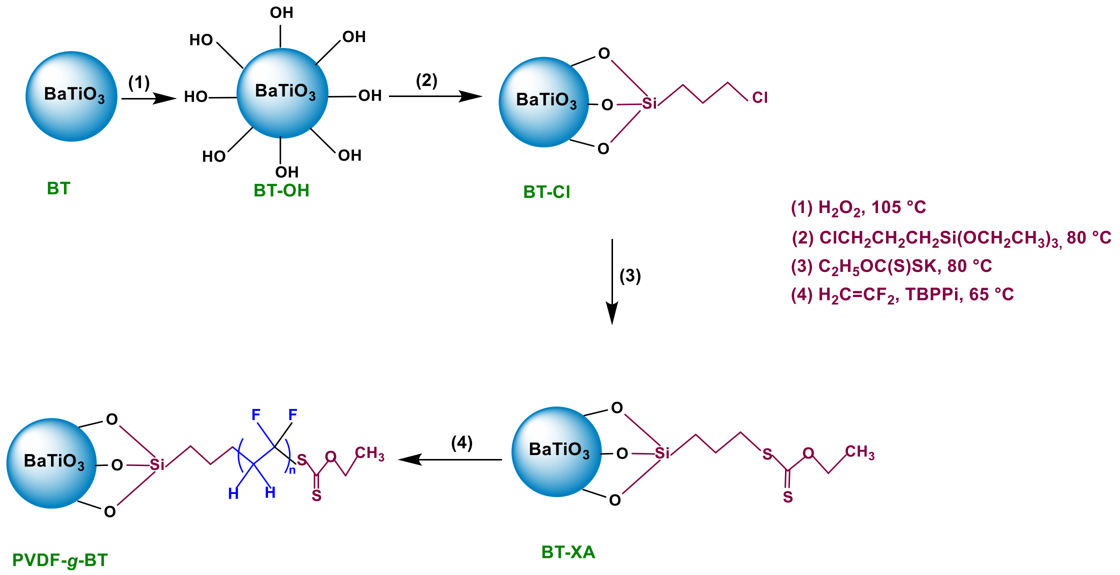

Scheme 1. Sketch illustrating the synthesis process of PVDF-*g*-$BaTiO_3$ nanocomposites by RAFT polymerization of VDF in the presence of Xanthates (from the modification of $BaTiO_3$ nanoparticles) where TBPPi stands for *tert*-butyl peroxypivalate.

The commercially available $BaTiO_3$ nanoparticles possess too few -OH groups on their surface that are less active and thus are difficult to efficiently manipulate their surface chemistry [2]. Almadhoun *et al.*[10] prepared nanocomposites generated from surface-hydroxylated $BaTiO_3$ nanoparticles as a filler and poly(VDF-TrFE) copolymer as a matrix. The results show that the surface modification results in better dispersion of the nanoparticles in the polymer matrix, yielding in a higher degree of particle-matrix interaction whereas the untreated $BaTiO_3$ is likely to forming agglomerates which lead to a higher inhomogeneity when it is incorporated into a polymer matrix. Inspired by this study, the first step of Scheme 1 is the hydroxylation of pristine $BaTiO_3$. These hydroxylated $BaTiO_3$ (BT-OH) were functionalized by RAFT agent (Xanthate) in two steps (Reactions 2 and 3, Scheme 1). Initially, the surface of BT-OH nanoparticles was modified by the condensation reaction of 3-

chloropropyltriethoxysilane (BT-CPTS), and it was subsequently reacted in the second step with potassium xanthogenate to produce nanoparticles bearing RAFT xanthate (BT-XA). All steps led to high yields.

In the last step of Scheme 1, the PVDF-*g*-$BaTiO_3$ core-shell nanocomposites were prepared by RAFT polymerization of VDF in the presence of BT-XA using *tert*-butyl peroxypivalate (TBPPi) as the initiator and the reaction mechanism is depicted in scheme 2. At this temperature, the initiator has a half-life of 2 hours and the generated radicals enable to initiate the polymerization of VDF[5,6,9]. As previously reported, RAFT polymerization is a versatile technique that can easily tune the shell thickness of the core-shell nanostructured nanocomposites by varying the monomer feed ratios [11]'[3]. In fact, Chen *et al.*[12] reported that the shell thickness can be designed by the polymerization degree via RAFT polymerization. In this work, four weight $[BaTiO_3\text{-}XA]_0$:$[VDF]_0$ ratios were chosen (*i.e.* 3, 5, 10 and 20 %). The resulting materials were characterized by different spectroscopic and thermal analyses.

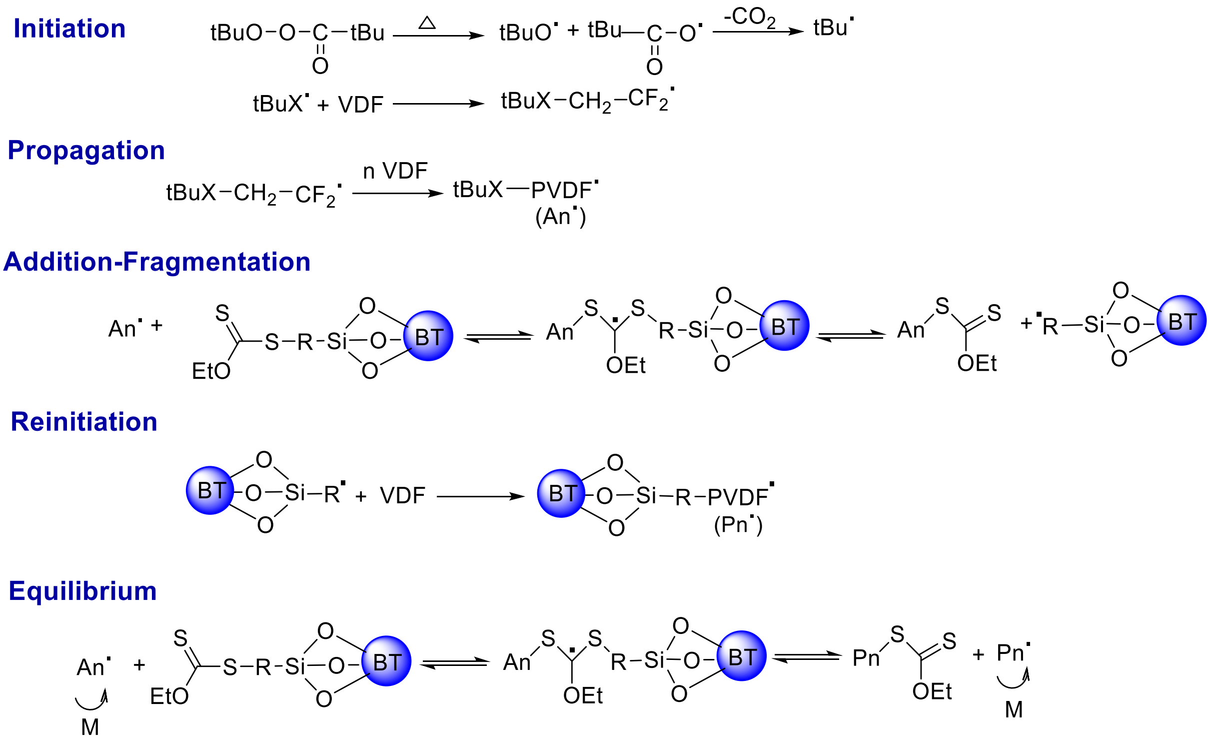

Scheme 2. Mechanism of Reversible Addition-Fragmentation Chain-Transfer Polymerization (RAFT) of VDF.

III.3. Spectroscopy Characterizations

III.3.1 FT-IR spectroscopy

FT-IR spectroscopy was employed to reveal the anchoring of xanthate onto the $BaTiO_3$ and PVDF-*g*-$BaTiO_3$ nanocomposites (Scheme 1). Figure 1a exhibits the FT-IR spectra of the $BaTiO_3$, before and after modification ($BaTiO_3$-OH, $BaTiO_3$-CPTS and $BaTiO_3$-XA). The IR spectrum of the as-received $BaTiO_3$ nanoparticles presents absorption bands at 580 and 1435 cm^{-1} assigned to the stretching vibration of CO_3^{2-} from the residual $BaCO_3$ in the $BaTiO_3$ and the vibration mode of a metal-dioxo bridge, respectively[13]. Another absorption band at 1633 cm^{-1} is characteristic for the bending mode of -O-H resulting from the physically adsorbed water on $BaTiO_3$ nanoparticles [14] and also confirmed by absorption bands (stretching) observed between 3000-3600 cm^{-1}.

After treatment of $BaTiO_3$ nanoparticles with hydrogen peroxide, purification and drying, the absorption bands in FT-IR spectrum of hydroxylated $BaTiO_3$ are similar to those of the pristine $BaTiO_3$ with a slight increase in the intensity of the broad -OH absorption band at 3452 cm^{-1} (Figure 1a).

Upon incorporation of the silane coupling agent having chloride functionality and compared with $BaTiO_3$-OH, new absorption bands at 1041-1094 and 2935 cm^{-1} were observed in BT-CPTS attributed to Si–O–Si and CH_2, respectively. These results indicate the successful introduction of silane coupling agent [15]'[10]. After immobilization of xanthate onto $BaTiO_3$, the $BaTiO_3$-XA was suggested to be formed via covalent bonding as indicated by three characteristic absorption bands at 1002 (C=S), 1130 (C-O), and 2927 cm^{-1} (C-H) confirming previous reports [16–18] (Figure 1a).

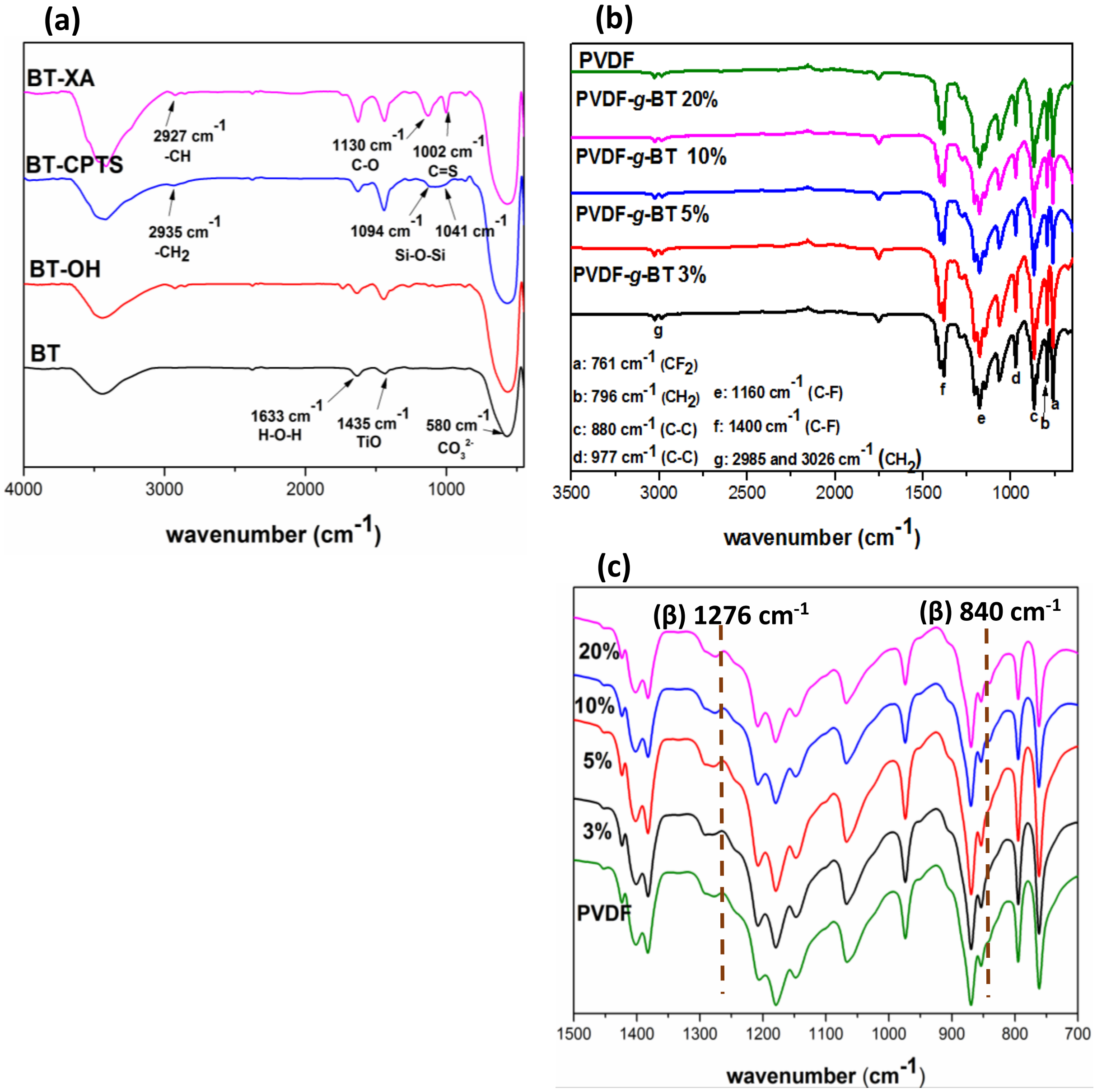

Figure 1. FT-IR spectra of (a) the as-received $BaTiO_3$ (BT), BT-OH, BT-CPTS and BT-XA, (b) FT-IR spectra of PVDF and PVDF-*g*-$BaTiO_3$ nanocomposites starting from 3, 5, 10 and 20 wt % of $BaTiO_3$, (c) Expansion of the 700-1500 cm^{-1} zone in the FT-IR spectra.

After purification, the core-shell PVDF-*g*-$BaTiO_3$ nanocomposites were characterized by FT-IR (Figure 1b). Additional absorption bands at 1160, 1400 cm^{-1} corresponding to C-F stretching were observed. In addition, the absorption band at 2985 and 3026 cm^{-1} (stretching of $-CH_2$ of VDF units) became stronger than that of BT-XA (Figure 1a). PVDF is ferroelectric polymer which exhibits crystalline phases (α, β and γ) affecting its electric properties [19,20]. Therefore, it is of interest to know the effects of $BaTiO_3$ nanoparticles on the grafted structure of PVDF. FT-IR spectrum (Figure 1c) shows frequencies at 761, 796, 880 and 977 cm^{-1}, characteristic of the α-phase of PVDF [19,21–24]. In addition, no absorption bands at 1276 and 840 cm^{-1} of the β phase of PVDF were observed in the spectra of PVDF-*g*-$BaTiO_3$ nanocomposites [19,25]. The FT-IR results confirm the successful grafting of PVDF onto the modified surface of $BaTiO_3$ and indicate that PVDF exhibits α crystalline phase only.

III.3.2 High Resolution Magic Angle Spinning (HR MAS)

More evidences of the successful modification and the grafting of PVDF from BT surface are supplied by high resolution magic angle spinning (HR MAS) spectroscopy. Figure 2 displays the HR MAS ^1H spectrum of pristine $BaTiO_3$ (BT), modified with hydrogen peroxide (BT-OH), with silane agent (BT-Cl) and with chain transfer agent (BT-XA). It is noted the decrease of signal at 10.15 ppm, assigned to OH groups, confirming their consumption during the fixation of silane agent [26].

The signals at 0.70, 1.73, 3.57 and 1.40 ppm evidences the presence of –Si-O-$\mathbf{CH_2}$-CH_2-CH_2-Cl, –Si-O-CH_2-$\mathbf{CH_2}$-CH_2-Cl, –Si-O-CH_2-CH_2-$\mathbf{CH_2}$-Cl for BT-Cl, and the –SC(S)O$CH_2$$\mathbf{CH_3}$ in BT-XA, respectively, suggesting that the silane agent and the chain transfer agent were successfully grafted on $BaTiO_3$ [27,28].

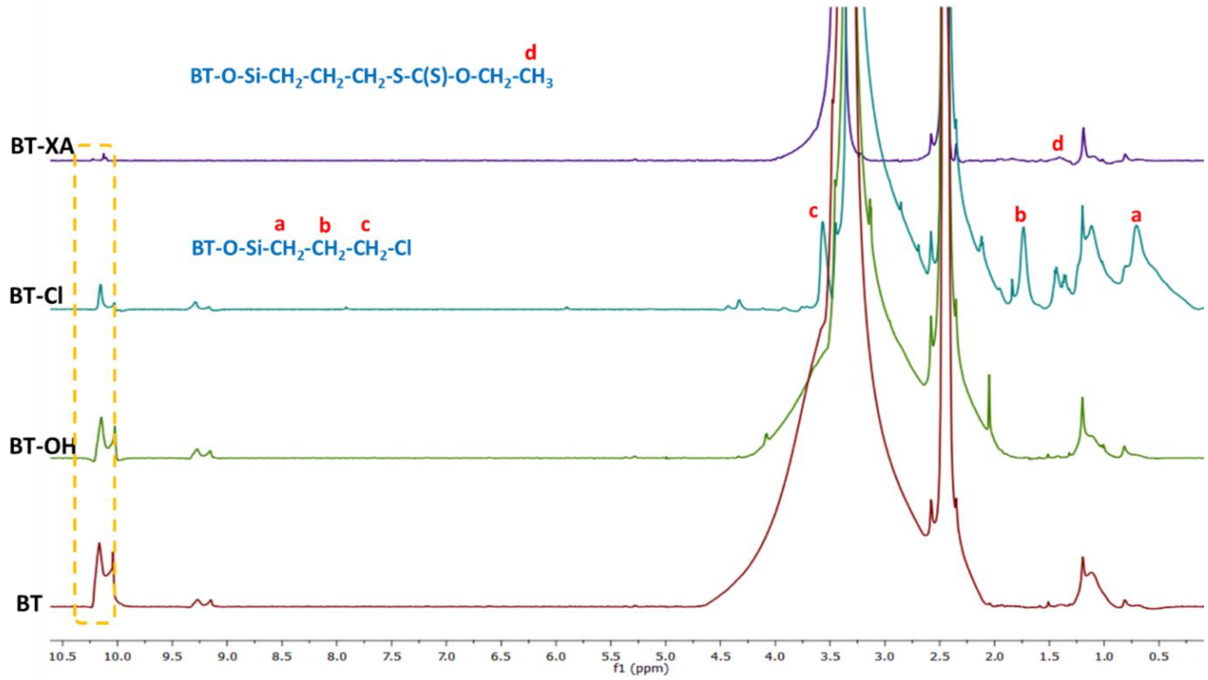

Figure 2. Expansion of the 0.5 to 10.5 ppm region of the ^{1}H HRMAS spectrum in DMSO of pristine BaTiO$_3$ (BT), modified with hydrogen peroxide (BT-OH), with silane agent (BT-Cl) and with chain transfer agent (BT-XA).

The HR MAS NMR spectra of PVDF-*g*-BaTiO$_3$ nanocomposite in DMSO-d$_6$ provide more detailed evidence of the successful grafted PVDF onto the surface of BaTiO$_3$ nanoparticles. Figures 3 and 4 display the ^{19}F and ^{1}H HRMAS NMR spectra of nanocomposite filled with 3 wt% of BaTiO$_3$, respectively. To the best of our knowledge, the ^{19}F HRMAS NMR spectra of nanocomposite has never been reported to characterize the fluorinated polymer grafted onto the nanofillers.

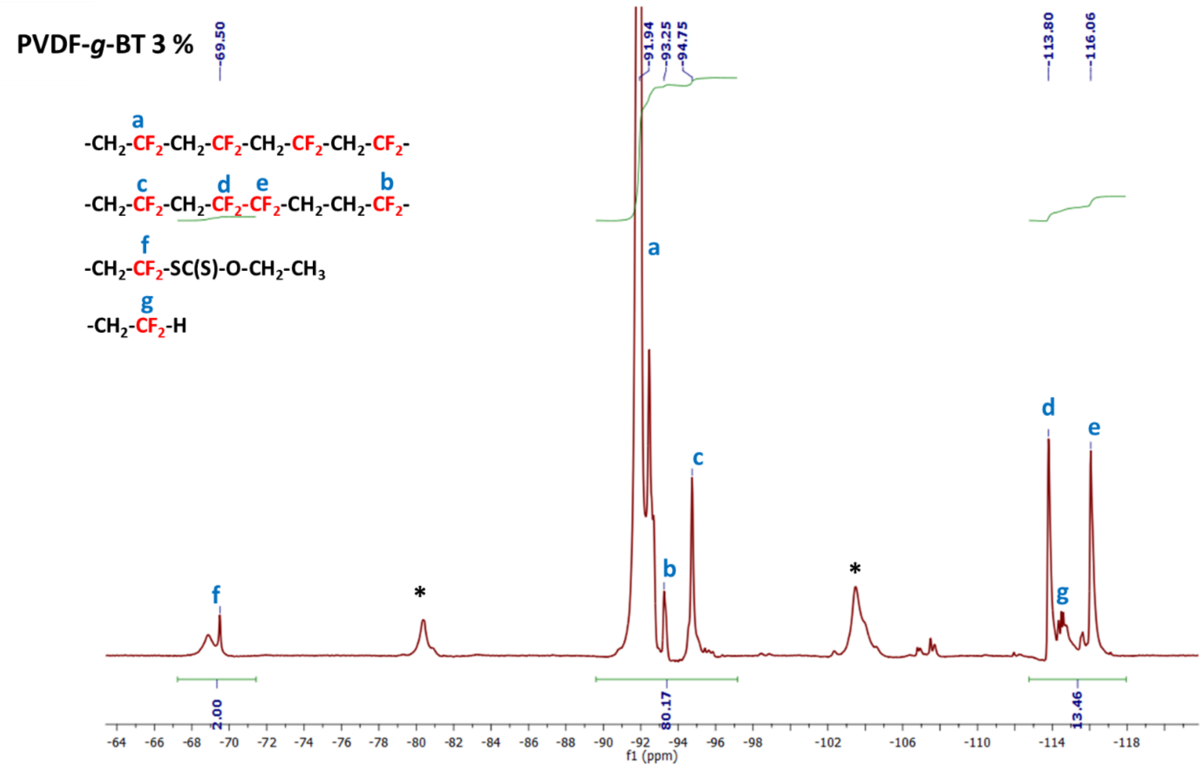

Figure 3. Expansion of the -64 to -120 ppm region of the ^{19}F HRMAS spectrum recorded in d$_6$-DMSO of PVDF-*g*-BaTiO$_3$ nanocomposite filled with 3 wt % of BaTiO$_3$ (* stands for the spinning bands).

Deuterated DMSO enables to swell PVDF located at the BaTiO$_3$ surface. Figure 3 exhibits an intense signal at -92 ppm, characteristic of head-to-tail (HT) addition of VDF (-CH$_2$$\mathbf{CF_2}$-CH$_2$$\mathbf{CF_2}$-CH$_2$$\mathbf{CF_2}$-CH$_2$$\mathbf{CF_2}$-) [6–9]. Signals at -114 ppm and -116 ppm are assigned to chain defects caused by head-to-head VDF reverse additions (-CH$_2$CF$_2$-CH$_2$$\mathbf{CF_2}$-CF$_2CH_2$-CH$_2CF_2$-) and (-CH$_2CF_2$-CH$_2CF_2$-$\mathbf{CF_2}CH_2$-CH$_2CF_2$-), respectively [29]. A signal at -70 ppm is relative to difluoromethylene adjacent to the xanthate group -CH$_2$-$\mathbf{CF_2}$-SCS-O-CH$_3$ [6–8].

^{19}F HRMAS spectrum also enables to calculate the degree of polymerization ($\overline{DP_n}$) from the integrals of the signals assigned above, according to equation 1.

$$\overline{DP_n} = \frac{(\int_{-92.0}^{-94.8} CF_2\,(HT) + \int_{-114.0}^{-116.3} CF_2(HH))/2}{(\int_{-69.0}^{-70.2} CF_2(end\ group))/2} + 1 \qquad (1)$$

where $\int_{-i}^{-j} CF_x$ stands for the integral of the signal ranging from -i to -j ppm assigned to CF$_x$ group.

The ^{19}F HRMAS NMR spectra of the nanocomposites containing 5, 10 and 20 wt% of BT-XA are also supplied in the Apendix I (Figures A1-A3).

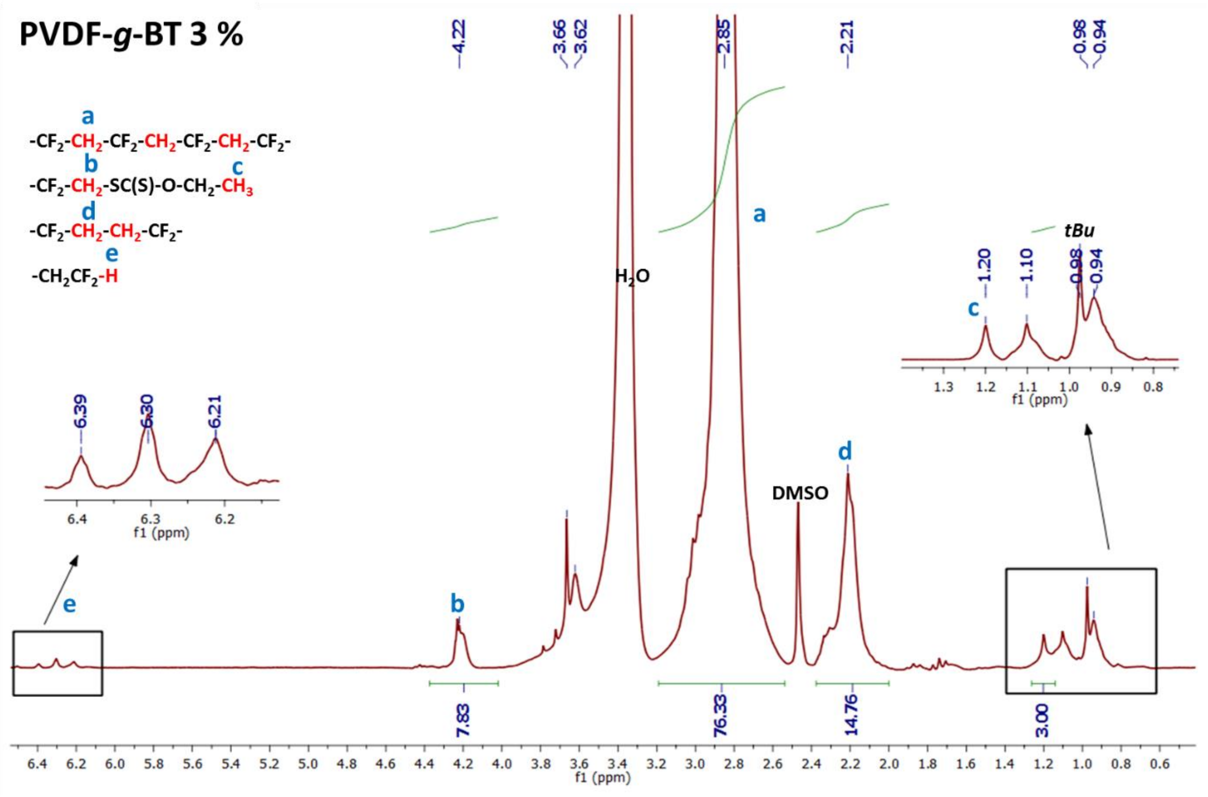

Figure 4. Expansion of the 0.6 to 6.4 ppm region of the ^{1}H HRMAS NMR spectrum recorded in d$_6$-DMSO of PVDF-*g*-BaTiO$_3$ nanocomposite filled with 3 wt % of BaTiO$_3$.

The ^{1}H HRMAS NMR spectrum (Figure 4) exhibits an intense signal centered at 2.8 ppm corresponding to the methylene of the regular head-to-tail (HT) addition of VDF (- CF$_2$**CH$_2$**-CF$_2$**CH$_2$**-CF$_2$**CH$_2$**-CF$_2$-). Signal at 2.2 ppm is characteristic of the tail-to-tail (TT) addition of VDF (-CF$_2$**CH$_2$-CH$_2$**CF$_2$-) while that at 4.2 ppm is assigned to methylene terminal VDF units (CF$_2$-CF$_2$**CH$_2$-** SC(S)-O-CH$_2$-CH$_3$). Moreover, signal at 1.2 ppm is attributed to CH$_3$ in Z group of Xanthate (-CF$_2$-CH$_2$-SC(S)-O-CH$_2$-**CH$_3$**) [8]. The triplet of triplets centered at 6.3 ppm is attributed to the proton end group in -CH$_2$CF$_2$-H from the transfer to dimethylcarbonate. The resulting CH$_3$OC(O)OCH$_2^{\bullet}$ radical is able to initiate another PVDF chain giving rise to a singlet at 3.7 ppm corresponding to the methyl end group. In addition, the singlet at 0.95 ppm is assigned to the *tert*butyl end group (Scheme 2) from the fragment of radical initiator [30].

The degree of polymerization can be also calculated from ^{1}H HRMAS NMR using the integrals of the signals assigned to CH$_2$ group of regular VDF additions, CH$_2$ groups of reverse additions of VDF, CH_2 of terminal units of VDF and Z group of Xanthate, according to equation (2).

$$\overline{DP_n} = \frac{(\int_{2.6}^{3.2} CH_2\,(HT) + \int_{2.0}^{2.4} CH_2(TT) + \int_{4.1}^{4.3} CH_2(end-group))}{\frac{2}{3} \times (\int_{1.15}^{1.3} CH_3(Z-CTA))} \qquad (2)$$

The Appendix gives the ^{1}H HRMAS NMR spectra of the nanocomposites containing 5, 10 and 20 wt% of BT-XA (Appendix I: Figures A4-A6).

Table 1 summarizes the degrees of polymerization obtained from ^{1}H and ^{19}F HRMAS NMR spectroscopy for the prepared nanocomposites with different loadings of $BaTiO_3$ starting from 3, 5, 10 and 20 wt%. This table shows a good agreement of the degrees of polymerization from both NMR techniques.

Table 1. DP_n and molar masses obtained from ^{19}F and ^{1}H HRMAS NMR spectroscopy for the prepared nanocomposites from equations (1, 2 and 4).

BT in feed (%)	**DP_n from ^{1}H NMR**	**$\bar{M}_n$ (^{1}H NMR)**	**DP_n from ^{19}F NMR**	**$\bar{M}_n$ (^{19}F NMR)**	**$\bar{M}_n$ of free polymer**
3	50	3670	48	3540	7500
5	44	3290	44	3290	6800
10	39	2970	41	3100	6400
20	36	2780	39	2970	5600

III.3.4 Molar Masses of PVDF from SEC and HR MAS spectroscopy

After washing treatment, the free PVDF was characterized with SEC in DMF with PMMA standards. Table 2 summarizes PVDF yields, percentages of grafted and ungrafted (or free) PVDF prepared by *in-situ* VDF RAFT polymerization, and the molar masses $\bar{M}_n$, $\bar{M}_w$ and dispersity (*Đ*) values of free PVDF from nanocomposites (Scheme 5, Chapter II) determined by SEC. The PVDF yield was calculated using the equation (3) bellow:

$$Yield\ of\ PVDF = \frac{m_{nanocomposite}}{m_{VDF} + m_{BT-XA}} \qquad (3)$$

where $m_{nanocomposite},\ m_{VDF}\ and\ m_{BT-XA}$ represent the weight of the obtained nanocomposite after polymerization (total product mixture) and the introduced VDF and BT-XA, respectively.

Table 2. In situ RAFT polymerization of VDF, Molar masses $\bar{M}_n$, $\bar{M}_w$ and dispersity values (Đ) of PVDF nanocomposites determined by SEC.

wt % of BT in feed	*PVDF Yield (%)*[a)]	*% of Grafted PVDF* [b)]	*% of Free PVDF* [b)]	$\bar{M}_n$ [c)]	$\bar{M}_w$ [c)]	*Đ* [c)]
0	67	-	-	12 730	22 700	1.8
3	64	55	45	7 500	18 200	2.4
5	94	62	38	6 800	14 900	2.2
10	95	57	43	6 400	13 600	2.1
20	96	42	58	5 600	12 900	2.3

[a)] Yield of PVDF after RAFT polymerization in the presence of $BaTiO_3$-XA (before purification) (65 °C, 15 h)

[b)] % of grafted PVDF (PVDF-*g*- $BaTiO_3$) and physisorbed PVDF (Free PVDF) after watching and centrifugation

[c)] SEC: solvent: Dimethylformamide (DMF), Calibration with PMMA standards.

From all the contents of ceramic nanoparticles of free PVDF from PVDF-*g*-$BaTiO_3$ x wt% nanocomposites, the highest molar mass was obtained with 3 wt% of $BaTiO_3$ while the molar mass of nanocomposites decreases by increasing the $BaTiO_3$ ratio. The lowest one was obtained with 20 wt% of $BaTiO_3$ content (Table 2). Actually, the functionalized nanofiller acted as a chain transfer agent in the radical polymerization of VDF as it was reported in the clay nanocharge/fluorinated methacrylate leading a decreasing order of molar masses with an increasing nanoclay loading [31].

The literature reports that the cleavage of grafted polymers (*e.g.* methacrylates) onto nanofillers was achieved in the presence of HF or HCl [27,32,33]. We conducted different experiments to attempt getting the molar masses of grafted PVDF onto BT-XA.

To cleave the attached PVDF from the functionalized $BaTiO_3$ nanoparticles, an amount of PVDF-*g*-BT was dispersed in a mixture of DMF or DMF/Aliquat according to procedures describe in literature [27,32]. Then Acid (HF or HCl) was added and the mixture was allowed to stir for a certain time and temperature. At the end of the reaction, the mixture was centrifuged, and the supernatant was concentrated then precipitated over cold pentane or methanol.

Table 3. Experiments conducted to enable the acidic cleavage of attached PVDF from functionalized nanoparticles.

Exp N°	**wt $_{PVDF\text{-}g\text{-}BT}$ (% of BT) (mg)**	**wt (Aliquat) (mg)**	**V $_{DMF}$ (ml)**	**V $_{acid}$ (ml)**	**time (T, °C)**
1	50 (10%)	5	3	0.5 (HF)	16 hr (25)
2	50 (10%)	5	3	0.5 (HF)	3 days (25)
3	30 (5%)	5	3	0.5 (HF)	5 days (25)
4	50 20%	0	5	0.5 (HCl)	16 hr (80)
5	40 (3%)	0	4	0.4 (HCl)	16 hr (80)

Even after five days in HF (Exp.3, Table 3), no PVDF was recovered after precipitation of the supernatant from cold pentane or methanol. This surprising behavior may be attributed to the high chemical inertness of PVDF in acid medium. The PVDF shell can be considered as a protective shield which may not enable this cleavage. Hence, the molar masses of grafted PVDF could not be achieved by SEC. In fact, they could be determined by ^{19}F and ^{1}H HRMAS NMR spectroscopies from equations 1, 2 and 4 (Table 1) according to equation previously reported by Guerre *et al*. [8]

$$M_{n,NMR} = M_{n,CTA} + DP(Z - CTA) \times M_{n,VDF} \qquad (4)$$

where $M_{n,CTA}$ = 472 g/mol and $M_{n,VDF}$ = 64 g/mol (CTA stands for the $BaTiO_3$-O_3Si-$(CH_2)_3$-SC(S)-OCH_2CH_3).

Table 1 shows that the molar masses decrease when increasing $BaTiO_3$ loading in the feed. In fact, rising the xanthate functions onto $BaTiO_3$ nanoparticles leads to enhanced transfer onto $PVDF^{\bullet}$ macroradicals resulting in low PVDF molar masses.

III.3.5 Morphology characterizations

III.3.5.1 X-ray diffraction (XRD)

X-ray diffraction (XRD) results have been often also used to determine phases of PVDF [34]. Figure 5 shows the XRD patterns of pristine $BaTiO_3$ nanoparticles, PVDF obtained by RAFT polymerization, and PVDF-*g*-$BaTiO_3$ nanocomposites synthesized from 5 wt% of $BaTiO_3$.

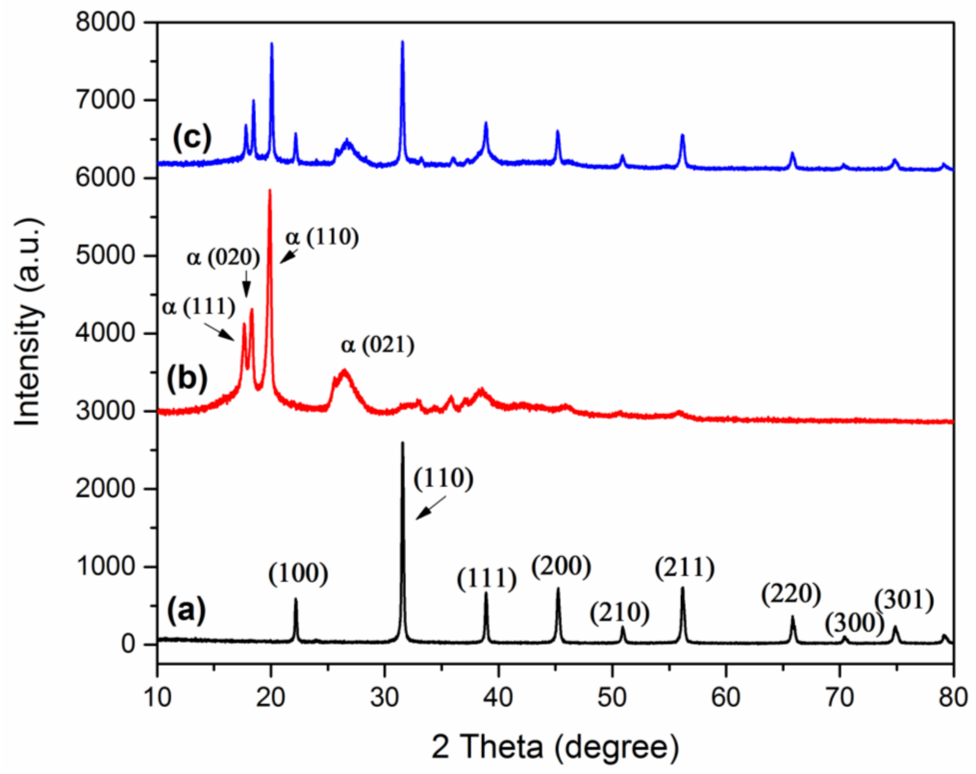

Figure 5. XRD patterns of: (a) the as received $BaTiO_3$ nanoparticles, (b) PVDF and (c) purified nanocomposites PVDF-*g*-$BaTiO_3$ 5 wt %.

As displayed in Figure 5a, the XRD patterns of the as received ceramic $BaTiO_3$ nanoparticles exhibits the characteristic peaks located at 2θ= 22°, 31°, 38°, and 45° assigned to the diffractions planes (100), (110), (111) and (200), respectively, corresponding to cubic phase of $BaTiO_3$ [35]'[36]. The diffraction patterns (Figure 4b) of PVDF display peaks at 2θ= 17°, 18°, 19° and 26° attributed to (100), (020), (110) and (021) diffraction planes, respectively, characteristic to α phase of PVDF [19,34,37]. No characteristic diffraction peak related to β phase of PVDF was observed at 2θ=20.26° (corresponding to diffraction planes (110) and (200)) [19] (Figure 5b). Finally, the XRD patterns of PVDF-*g*-$BaTiO_3$ nanocomposites containing 5 wt% of $BaTiO_3$ (Figure 5c) show both peaks of $BaTiO_3$ ceramic particles and α phase of PVDF. On the other hand, the XRD analyses indicate that PVDF crystallizes in α phase during the *in-situ* RAFT polymerization of VDF in the presence of BT-XA, and confirm the results obtained by FT-IR study. A similar result was obtained in the preparation of PVDF-*g*-$BaTiO_3$ 20% wt nanocomposite during melt process [37].

III.3.5.2 Scanning Electronic Microscopy (SEM)

The resulting nanocomposites were analyzed by electron microscopy (SEM and TEM). First, SEM enabled to evaluate the dispersion of nanofillers within matrix polymers [25],[38]. Figure 6a exhibits a typical SEM image obtained for the PVDF-*g*-$BaTiO_3$ nanocomposites using different $BaTiO_3$ concentrations. In all nanocomposites, $BaTiO_3$ nanoparticles are embedded within the PVDF polymer matrix, and neither agglomeration no pores could be found. These results indicate that the $BaTiO_3$ nanoparticles are well dispersed in the PVDF matrix and that strong chemical bonding exists between the $BaTiO_3$ core and the PVDF shell. Furthermore, the elemental analysis (EDX, Figure 6b) scan of PVDF-*g*-$BaTiO_3$ nanocomposites reveals the characteristic peaks of Ba, Ti, O, C and F, the compositions of which are in suitable agreement with the BT percentages used in the preparation of nanocomposites. These results clearly indicate the successful formation of PVDF-*g*-$BaTiO_3$.

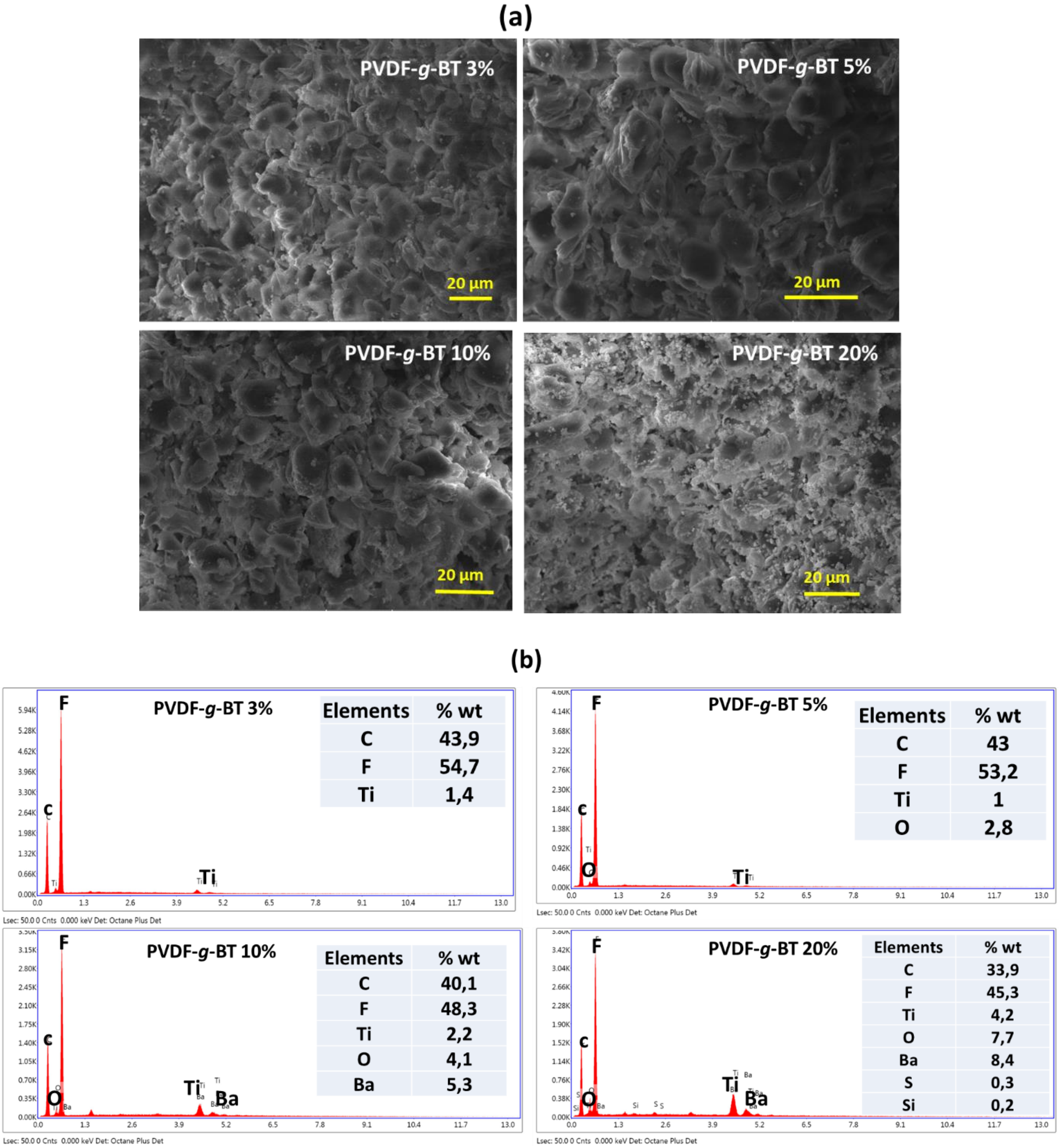

PVDF-*g*-BT 3%

Elements	% wt
C	43,9
F	54,7
Ti	1,4

PVDF-*g*-BT 5%

Elements	% wt
C	43
F	53,2
Ti	1
O	2,8

PVDF-*g*-BT 10%

Elements	% wt
C	40,1
F	48,3
Ti	2,2
O	4,1
Ba	5,3

PVDF-*g*-BT 20%

Elements	% wt
C	33,9
F	45,3
Ti	4,2
O	7,7
Ba	8,4
S	0,3
Si	0,2

Figure 6. (a): SEM micrographs of PVDF-*g*-$BaTiO_3$ nanocomposites from different BT loadings (scan bar: 20 µm), and (b) : their respective elemental analysis (EDX).

III.3.5.3 Transmission Electronic Microscopy (TEM)

TEM was also used to observe the morphology of pristine and organomodified $BaTiO_3$ nanoparticles, and the functionalized $BaTiO_3$ (BT) nanoparticles via RAFT polymerization of VDF. TEM images of BT, BT-OH, BT-CPTS and BT-XA are displayed in Figure 7.

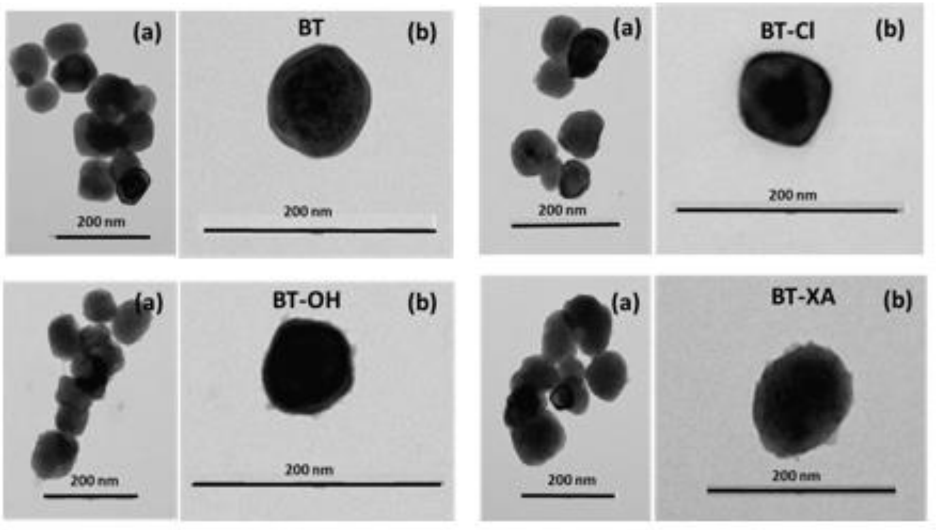

Figure 7. TEM images of the as received and functionalized $BaTiO_3$ particles with (a) (low magnification) and (b) (higher magnification).

After modification of $BaTiO_3$ nanoparticles surface, it is clearly noted the presence of a thin clear layer surrounding the functionalized $BaTiO_3$ core and confirmed the NMR, FT-IR and TGA analyses. Figure 8 displays the TEM images of PVDF-*g*-BT with different $BaTiO_3$ loadings and exhibits a PVDF polymer shell directly coated on the surface of BT. This features the successful grafting of PVDF onto the functionalized nanoparticles. Thus, by increasing the $BaTiO_3$ feed in the system, the average shell thickness decreased from 5.1 nm to 2.2 nm for nanocomposites produced from 5 wt% and 20 wt%, respectively. The thickness of the PVDF shell is similar to those of poly(alkyl methacrylate) [39] and poly(2,2,2-trifluoroethyl methacrylate) layer grafted onto modified $BaTiO_3$ although the authors used higher $BaTiO_3$ feed amount (up to 50 wt%) [40].

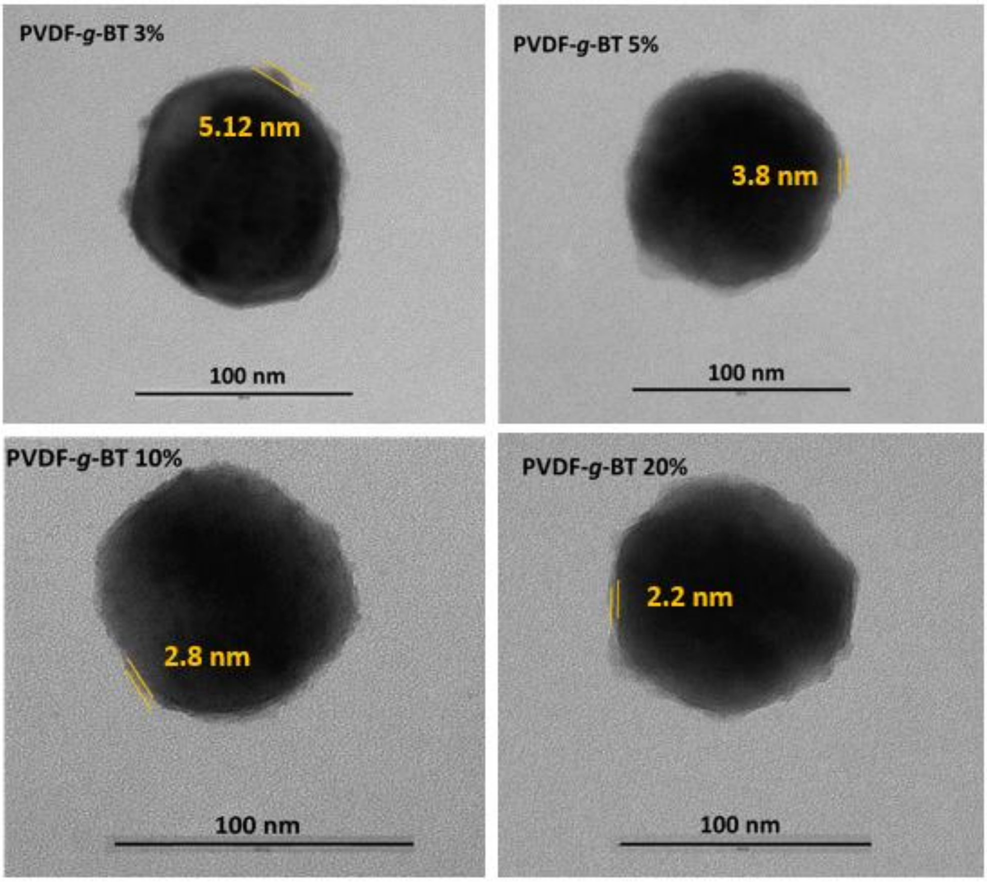

Figure 8. TEM images of PVDF-g-BT nanocomposite with different $BaTiO_3$ amount (3, 5, 10 and 20%).

III.3.6 Thermal properties

III.3.6.1 Thermogravimetric analysis (TGA)

In order to further support the successful modification of $BaTiO_3$ by PVDF polymer, the thermal stabilities of the organomodified $BaTiO_3$ and the PVDF-*g*-$BaTiO_3$ nanocomposites were studied by TGA under air (Figure 9) and differential scanning calorimetry (DSC, Figure 10).

The TGA thermogram of pristine $BaTiO_3$ shows a very high thermostablity with a small weight loss (0.13 % at 150 °C) attributed to the release of absorbed water molecules on the surface, thus confirming the FT-IR analyses.

The $BaTiO_3$ modified with hydrogen peroxide ($BaTiO_3$-OH) preserves its maximum weight before 300 °C since OH degrades. At 600 °C, the maximum weight loss is 1.45 % and confirms that -OH groups were introduced onto $BaTiO_3$ surface (Figure 9a). The BT-CPTS weight loss ws found to be 1.18 % at 600 °C due to the degradation of the silane group. At this temperature, in the case of $BaTiO_3$-XA, the weight loss was estimated to be 0.92 % suggesting that the RAFT agent was also introduced successfully onto $BaTiO_3$ surface (Figure 9a). These findings confirm the FT-IR results.

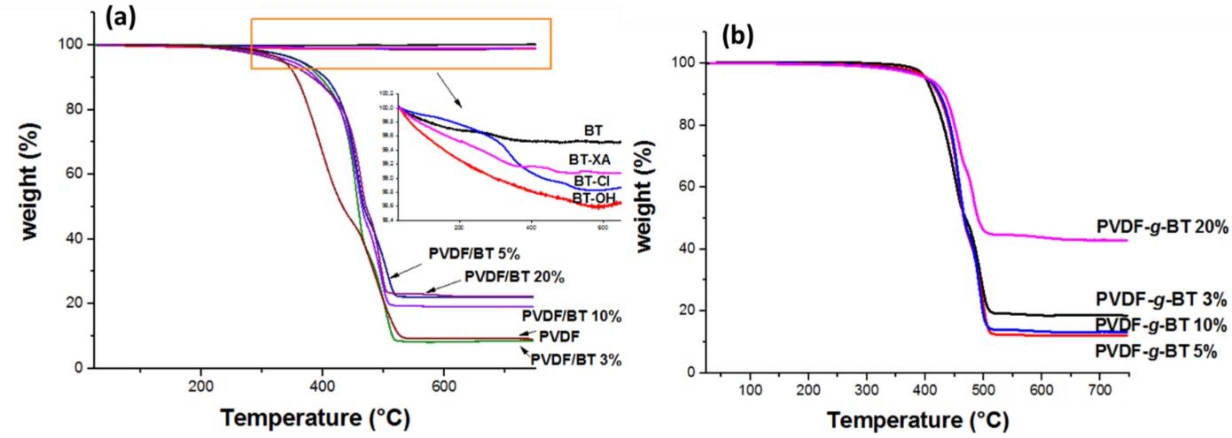

Figure 9. TGA thermograms (under air) of (a) functionalized $BaTiO_3$ nanoparticles and PVDF-*g*-$BaTiO_3$ nanocomposites with different $BaTiO_3$ amount (3, 5, 10 and 20 wt %) after centrifugation but not purified and (b) TGA thermograms of $BaTiO_3$/PVDF nanocomposites after several purification treatments (PVDF-*g*-$BaTiO_3$).

The effect of $BaTiO_3$ composition loading on the thermal degradation of PVDF-*g*-$BaTiO_3$ nanohybrids was examined. Figure 9a shows the TGA thermograms of $BaTiO_3$/PVDF nanocomposites before purification (or washing treatment with acetone) including grafted PVDF onto the surface of $BaTiO_3$ and ungrafted or free PVDF (Scheme 6, Chapter II). Taking into account the starting of degradation, the nanocomposites stability decreases as follows: PVDF-*g*-$BaTiO_3$ 20% > PVDF-*g*-$BaTiO_3$ 10% > PVDF-*g*-$BaTiO_3$ 5% > PVDF-*g*-$BaTiO_3$ 3%. On the other hand, the weight losses recorded at 600 °C indicate the following decreasing thermal stability order: PVDF-*g*-$BaTiO_3$ 20% > PVDF-*g*-$BaTiO_3$ 3% > PVDF-*g*-$BaTiO_3$ 10% > PVDF-*g*-$BaTiO_3$ 5% (Table 4). Durand *et al.*[41] reported the efficiency of PVDF washing by acetone monitored by TGA of radical grafting of 1-iodo tetrafluoroethylene and VDF telomers onto silica bearing vinyl groups. These authors conclude the necessity to wash the modified silica several times after that radical grafting to get rid off the physisorbed fluorinated telomers. In our case, after washing the PVDF-*g*-$BaTiO_3$ nanocomposites according to the procedure described above (Scheme 6, Chapter II) to remove the impurities and free or physisorbed PVDF, the TGA analysis was also performed on the resulting PVDF-*g*-$BaTiO_3$ nanocomposites. Figures 9b displays TGA thermograms of PVDF-*g*-$BaTiO_3$ nanocomposites and their weight losses before and after purification. The characteristic decomposition temperatures, T_d and T'_d, as well as the weight losses at 600 °C are summarized in Table 4.

Table 4. Temperature decompositions, weight loss at 600 °C of PVDF-*g*-$BaTiO_3$ nanocomposites before purification, melting temperature Tm and crystallinity X (%) recorded for PVDF-*g*-$BaTiO_3$ nanocomposites after purification.

wt % of BT in feed	T_d *(°C)* a)	T'_d *(°C)* b)	*Weight loss of PVDF-g-$BaTiO_3$ at 600 °C (%)* c)	*Weight loss of PVDF-g-$BaTiO_3$ at 600 °C (%)* d)	ΔH_m *(J g^{-1})* e)	*Crystallinity X (%)* f)
0	339		91		49	47
3	373	391	92	81	47	45
5	380	404	77	89	51	48
10	384	407	81	86	42	40
20	393	415	78	56	27	21

a) T_d : Starting degradation temperature of PVDF-*g*-$BaTiO_3$ nanocomposites before purification.
b) T'_d : Beginning degradation temperature of PVDF-*g*-$BaTiO_3$ nanocomposites obtained after purification.
c) Weight loss of $BaTiO_3$/PVDF before purification determined by TGA (under air)
d) Weight loss of $BaTiO_3$/PVDF after purification (PVDF-*g*-$BaTiO_3$) determined by TGA
e) Melting enthalpy measured by DSC analysis under nitrogen after second heating
f) Crystallinity X calculated from Equation 1 of Chapter II.

Figure 9b reveals several features: (i) all PVDF-*g*-$BaTiO_3$ nanocomposites exhibit a significantly better thermal stability than that of the pure PVDF, with an increase of 52-76 °C in T'_d compared to that of neat PVDF which starts to decompose at 339 °C. In fact, incorporation of a well-dispersed organomodified $BaTiO_3$ onto PVDF matrix is known to enhance the thermal stability by acting as a mass transport barrier to the volatile products generated during decomposition [42], (ii) the increase of the decomposition temperatures for the nanocomposites with higher $BaTiO_3$ content may be attributed to the good dispersion and the high loading of nanofiller, (iii) compared to Figure 9a, removing the physisorbed PVDF from $BaTiO_3$/PVDF during the washing treatment leads to an improved thermal stability of the resulting PVDF-*g*-$BaTiO_3$ nanohybrids where PVDF is covalently bonded onto $BaTiO_3$.

III.3.6.2 Differential Scanning Calorimetry (DSC)

Differential scanning calorimetry (DSC) was used for the identification of the crystalline phase of PVDF and PVDF-*g*-$BaTiO_3$ nanocomposites, and also the influence of the $BaTiO_3$ concentration on the degree of crystallinity and melting temperature. The melting and cooling DSC thermograms are presented in Figure 10.

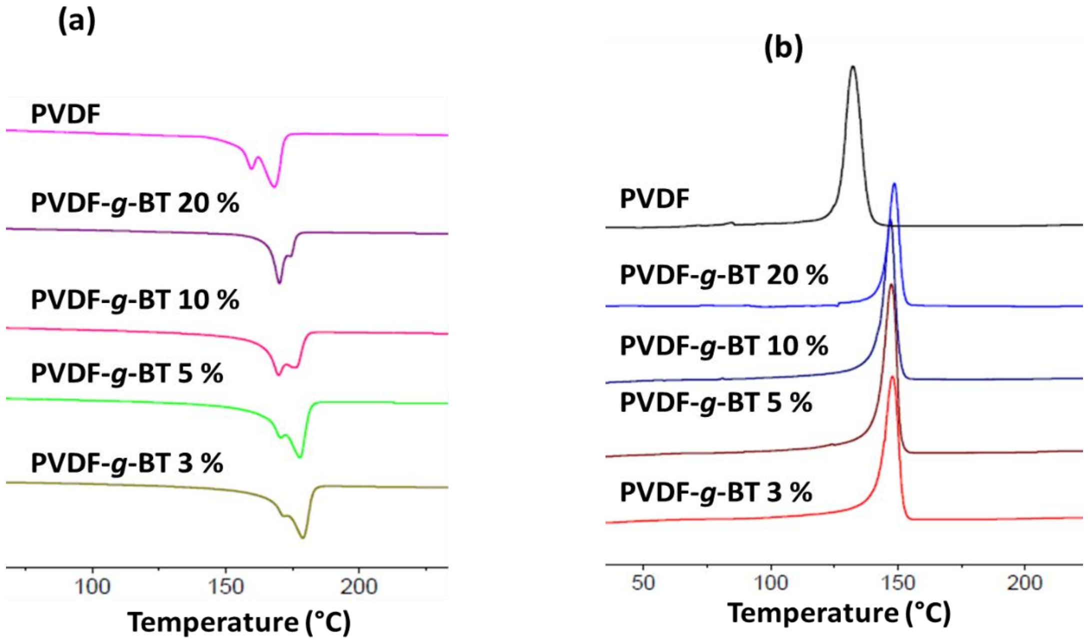

Figure 10. DSC thermograms (second heating and cooling) of PVDF from conventional radical polymerization of VDF initiated by TBPPI and PVDF-*g*-$BaTiO_3$ nanocomposites with different BT fractions: (a) heating process, (b) cooling process.

Figure 10-a displays the melting behaviors of pure PVDF and PVDF-*g*-$BaTiO_3$ nanohybrids. The nanocomposite samples exhibit two endothermic melting temperatures, T_m, in the range 150-183 °C slightly shifted toward high temperatures comparatively to the pure PVDF prepared in the same conditions. The interaction between nanofiller surface and the PVDF dipole should be the main factor [43–45]. Mendes *et al.*[25] reported the effect of the filler concentration on the thermal properties of $BaTiO_3$/PVDF nanocomposites prepared via simple casting with different ceramic contents and the existence of the two endothermic peaks of PVDF physisorbed on the surface of BT, attributed to the coexistence of α and β-phases in the samples confirmed by FT-IR and XRD analyses. In our case, the FT-IR and XRD results of the grafting of PVDF on the surface of BT exhibit only α-phase of PVDF. Therefore, the two endothermic peaks in DSC thermograms (Figure 10-a) are assigned to the α-phase in the nanocomposites. As reported by Costa *et al.*[44] the thermal behavior of α-phase PVDF is more complicated. Its melting point displays two endothermic peaks and its origin can be mainly ascribed to the presence of a “bimodal distribution” of crystal sizes or to the recrystallization and remelting during the DSC heating [44–47]. It is noted also that with pure PVDF and lower percentage of $BaTiO_3$ grafted on the surface of PVDF (3 and 5wt %), the second melting peak is higher than the first one corresponding to lower shoulder. This

behavior is reversed in the thermograms of nanocomposites with higher BT concentration (10 and 20 wt%) where the first peak is more important. It could be in agreement with the existence of the “bimodal distribution” of crystal which one peak is more important than the other one depending on the $BaTiO_3$ percentage [44,47,48].

Figure 10b presents the DSC cooling thermograms of PVDF and PVDF-*g*-$BaTiO_3$ nanocomposites. The crystallization peak temperature of PVDF is 132.4 °C, whereas when 3, 5, 10 and 20 wt % BT are used, this temperature increases up to 142.2, 147.5, 147.1 and 148.7 °C, respectively. These results clearly show that the addition of a small BT amount to the PVDF matrix induced an obvious increase in the crystallization temperature of the PVDF polymer.

The influence of $BaTiO_3$ loading is also obvious in the degree of crystallinity (X) of the polymer, listed in Table 4. It can be observed that these values are smaller than those of the pure PVDF and decrease with increasing BT content. Obviously, the presence and the quality of $BaTiO_3$ dispersion may significantly affect the crystallization behavior of PVDF matrix.

III.7 Conclusion

A series of PVDF-*g*-$BaTiO_3$ nanocomposites with well-defined core shell structure was prepared by unprecedented RAFT polymerization of VDF from the surface of $BaTiO_3$ nanoparticles. The first step aimed to functionalize the surface of the as received ceramic nanoparticles to create xanthate functions and sites for the RAFT polymerization using potassium ethyl xanthate as the chain transfer agent. Then, grafting of PVDF from the surface of modified $BaTiO_3$ was achieved by RAFT polymerization using different $BaTiO_3$ amounts (3-20 wt %) and the effect of such a percentage on the properties of the nanocomposite was studied. The results show the successful surface modification and grafting of PVDF onto $BaTiO_3$ leading to nanocomposites with enhanced thermal stability. The higher the $BaTiO_3$, the better the thermostability of the resulting nanocomposites. Noteworthy, HRMAS spectroscopy well highlighted the presence of PVDF on the $BaTiO_3$ surface, also confirmed by IR and XRD that indicated α phase-PVDF was mainly produced.

The thickness of the shell determined by TEM showed that decreasing the feed of $BaTiO_3$ weight leads to an increase from 2.2 nm to 5.1 nm for nanocomposites produced from 5 wt% and 20 wt%, respectively. In addition, the crystallinity rate decreased when the BT loading increased.

Dielectric nanocomposites incorporating core-shell PVDF-*g*-$BaTiO_3$ nanostructured in term of influence of $BaTiO_3$ concentration on dielectric properties (*e.g.* dielectric permittivity, dielectric loss, loss modulus and conductivity) are discussed in Chapter IV.

III.8 References

[1] L. Gu, T. Li, Y. Xu, C. Sun, Z. Yang, D. Zhu, D. Chen, Effects of the particle size of BaTiO 3 fillers on fabrication and dielectric properties of BaTiO 3 /Polymer/Al films for capacitor energy-storage application, Materials (Basel). 12 (2019). doi:10.3390/ma12030439.

[2] L. Xie, X. Huang, C. Wu, P. Jiang, Core-shell structured poly(methyl methacrylate)/BaTiO3 nanocomposites prepared by in situ atom transfer radical polymerization: a route to high dielectric constant materials with the inherent low loss of the base polymer, J. Mater. Chem. 21 (2011) 5897. doi:10.1039/c0jm04574h.

[3] K. Yang, X. Huang, L. Xie, C. Wu, P. Jiang, T. Tanaka, Core-shell structured polystyrene/BaTiO3 hybrid nanodielectrics prepared by in situ RAFT polymerization: A route to high dielectric constant and low loss materials with weak frequency dependence, Macromol. Rapid Commun. 33 (2012) 1921–1926. doi:10.1002/marc.201200361.

[4] M. Zhu, X. Huang, K. Yang, X. Zhai, J. Zhang, J. He, P. Jiang, Energy Storage in Ferroelectric Polymer Nanocomposites Filled with Core-shell Structured Polymer @ BaTiO3 Nanoparticles : Understanding the Role of Polymer Shells in the Interfacial Regions, ACS Appl. Mater. Interfaces. 6 (2014) 19644–19654. doi:10.1021/am504428u.

[5] G. Kostov, F. Boschet, J. Buller, L. Badache, S. Brandsadter, B. Ameduri, First Amphiphilic Poly(vinylidene fluoride-co-3,3,3-trifluoropropene)-b-oligo(vinyl alcohol) Block Copolymers as Potential Nonpersistent Fluorosurfactants from Radical Polymerization Controlled by Xanthate, Macromolecules. 44 (2011) 1841–1855. doi:10.1021/ma102679f.

[6] E. Girard, J.-D. Marty, B. Ameduri, M. Destarac, Direct Synthesis of Vinylidene Fluoride-Based Amphiphilic Diblock Copolymers by RAFT/MADIX Polymerization, ACS Macro Lett. 1 (2012) 270–274. doi:10.1021/mz2001143.

[7] Y. Patil, B. Ameduri, First RAFT/MADIX radical copolymerization of tert-butyl 2-trifluoromethacrylate with vinylidene fluoride controlled by xanthate, Polym. Chem. 4 (2013) 2783. doi:10.1039/c3py21139h.

[8] M. Guerre, B. Campagne, O. Gimello, K. Parra, B. Ameduri, V. Ladmiral, Deeper Insight into the MADIX Polymerization of Vinylidene Fluoride, Macromolecules. 48 (2015) 7810–7822. doi:10.1021/acs.macromol.5b01528.

[9] S. Banerjee, Y. Patil, O. Gimello, B. Ameduri, Well-defined multiblock poly(vinylidene fluoride) and block copolymers thereof: a missing piece of the architecture puzzle, Chem. Commun. 53 (2017) 10910–10913. doi:10.1039/C7CC06122F.

[10] M.N. Almadhoun, U.S. Bhansali, H.N. Alshareef, Nanocomposites of ferroelectric polymers with surface-hydroxylated BaTiO3 nanoparticles for energy storage applications, J. Mater. Chem. 22 (2012) 11196. doi:10.1039/c2jm30542a.

[11] K. Yang, X. Huang, Y. Huang, L. Xie, P. Jiang, Fluoro-Polymer@BaTiO3 Hybrid Nanoparticles Prepared via RAFT Polymerization: Toward Ferroelectric Polymer

Nanocomposites with High Dielectric Constant and Low Dielectric Loss for Energy Storage Application, Chem. Mater. 25 (2013) 2327–2338. doi:10.1021/cm4010486.

[12] S. Chen, X. Lv, X. Han, H. Luo, C.R. Bowen, D. Zhang, Significantly improved energy density of BaTiO3 nanocomposites by accurate interfacial tailoring using a novel rigid-fluoro-polymer, Polym. Chem. 9 (2018) 548–557. doi:10.1039/C7PY01914A.

[13] S.-J. Chang, W.-S. Liao, C.-J. Ciou, J.-T. Lee, C.-C. Li, An efficient approach to derive hydroxyl groups on the surface of barium titanate nanoparticles to improve its chemical modification ability, J. Colloid Interface Sci. 329 (2009) 300–305. doi:10.1016/J.JCIS.2008.10.011.

[14] T.T.M. Phan, N.C. Chu, V.B. Luu, H. Nguyen Xuan, D.T. Pham, I. Martin, P. Carrière, Enhancement of polarization property of silane-modified BaTiO3 nanoparticles and its effect in increasing dielectric property of epoxy/BaTiO3 nanocomposites, J. Sci. Adv. Mater. Devices. 1 (2016) 90–97. doi:10.1016/J.JSAMD.2016.04.005.

[15] M.R. Islam, L.G. Bach, K.T. Lim, Poly(2-hydroxyethyl methacrylate) grafted halloysite nanotubes as a molecular host matrix for luminescent ions prepared by surface-initiated RAFT polymerization and coordination chemistry, Appl. Surf. Sci. 276 (2013) 298–305. doi:10.1016/J.APSUSC.2013.03.086.

[16] J.O. Leppinen, C.I. Basilio, R.H. Yoon, In-situ FTIR study of ethyl xanthate adsorption on sulfide minerals under conditions of controlled potential, Int. J. Miner. Process. 26 (1989) 259–274. doi:10.1016/0301-7516(89)90032-X.

[17] J.O. Leppinen, FTIR and flotation investigation of the adsorption of ethyl xanthate on activated and non-activated sulfide minerals, Int. J. Miner. Process. 30 (1990) 245–263. doi:10.1016/0301-7516(90)90018-T.

[18] P. Talonen, G. Sundholm, W.-H. Li, S. Floate, R.J. Nichols, A combined in situ infrared spectroscopy and scanning tunnelling microscopy study of ethyl xanthate adsorption on Au(111), Phys. Chem. Chem. Phys. 1 (1999) 3661–3666. doi:10.1039/a902078k.

[19] P. Martins, A.C. Lopes, S. Lanceros-Mendez, Electroactive phases of poly(vinylidene fluoride): Determination, processing and applications, Prog. Polym. Sci. 39 (2014) 683–706. doi:10.1016/J.PROGPOLYMSCI.2013.07.006.

[20] T. Soulestin, P. Marcelino Dos Santos Filho, V. Ladmiral, T. Lannuzel, F. Domingues Dos Santos, B. Améduri, Ferroelectric fluorinated copolymers with improved adhesion properties, Polym. Chem. 8 (2017) 1017–1027. doi:10.1039/C6PY02063A.

[21] R. Gregorio, M. Cestari, F.E. Bernardino, Dielectric behaviour of thin films of β-PVDF/PZT and β-PVDF/BaTiO3 composites, J. Mater. Sci. 31 (1996) 2925–2930. doi:10.1007/BF00356003.

[22] N. Durand, B. Ameduri, B. Boutevin, Synthesis and characterization of functional fluorinated telomers, J. Polym. Sci. Part A Polym. Chem. 49 (2011) 82–92. doi:10.1002/pola.24420.

[23] D. Mandal, K. Henkel, D. Schmeisser, Comment on “Preparation and Characterization of Silver–Poly(vinylidene fluoride) Nanocomposites: Formation of Piezoelectric Polymorph of Poly(vinylidene fluoride),” J. Phys. Chem. B. 115 (2011) 10567–10569. doi:10.1021/jp201335j.

[24] A. Salimi, A.A. Yousefi, Analysis Method: FTIR studies of β-phase crystal formation

in stretched PVDF films, Polym. Test. 22 (2003) 699–704. doi:10.1016/S0142-9418(03)00003-5.

[25] S.F. Mendes, C.M. Costa, C. Caparros, V. Sencadas, S. Lanceros-Méndez, Effect of filler size and concentration on the structure and properties of poly(vinylidene fluoride)/BaTiO3 nanocomposites, J. Mater. Sci. 47 (2012) 1378–1388. doi:10.1007/s10853-011-5916-7.

[26] Y.B. Monakhova, B.W.K. Diehl, Rapid ^{1} H NMR determination of hydrogen peroxide in cosmetic products and chemical reagents, Anal. Methods. 8 (2016) 4632–4639. doi:10.1039/C6AY00936K.

[27] S. Jafarzadeh, V. Haddadi-Asl, H. Roghani-Mamaqani, Nanofibers of poly (hydroxyethyl methacrylate)-grafted halloysite nanotubes and polycaprolactone by combination of RAFT polymerization and electrospinning, J. Polym. Res. 22 (2015) 123. doi:10.1007/s10965-015-0773-8.

[28] M.A. Melo Jr, C.T.G.V.M.T. Pires, C. Airoldi, The influence of the leaving iodine atom on phyllosilicate syntheses and useful application in toxic metal removal with favorable energetic effects, RSC Adv. 4 (2014) 41028–41038. doi:10.1039/C4RA06615D.

[29] A.D. Asandei, O.I. Adebolu, C.P. Simpson, Mild-Temperature Mn (CO)10 -Photomediated Controlled Radical Polymerization of Vinylidene Fluoride and Synthesis of Well-Defined Poly(vinylidene fluoride) Block Copolymers, J. Am. Chem. Soc. 134 (2012) 6080–6083. doi:10.1021/ja300178r.

[30] J. Guiot, A. B. Ameduri, B. Boutevin, Radical Homopolymerization of Vinylidene Fluoride Initiated by tert-Butyl Peroxypivalate. Investigation of the Microstructure by 19F and 1H NMR Spectroscopies and Mechanisms, Macromolecules. 35 (2002) 8694–8707. doi:10.1021/MA0202641.

[31] M. Karamane, M. Raihane, M.A. Tasdelen, T. Uyar, M. Lahcini, M. Ilsouk, Y. Yagci, Preparation of fluorinated methacrylate/clay nanocomposite via in-situ polymerization: Characterization, structure, and properties, J. Polym. Sci. Part A Polym. Chem. 55 (2017) 411–418. doi:10.1002/pola.28403.

[32] L. Xiong, H. Liang, R. Wang, L. Chen, A novel route for the synthesis of poly(2-hydroxyethyl methacrylate-co-methyl methacrylate) grafted titania nanoparticles via ATRP, J. Polym. Res. 18 (2011) 1017–1021. doi:10.1007/s10965-010-9502-5.

[33] W. Ma, H. Otsuka, A. Takahara, Poly(methyl methacrylate) grafted imogolite nanotubes prepared through surface-initiated ARGET ATRP, Chem. Commun. 47 (2011) 5813. doi:10.1039/c1cc10661a.

[34] R. Gregorio, Determination of the α, β, and γ crystalline phases of poly(vinylidene fluoride) films prepared at different conditions, J. Appl. Polym. Sci. 100 (2006) 3272–3279. doi:10.1002/app.23137.

[35] X.H. Zhu, J.M. Zhu, S.H. Zhou, Z.G. Liu, N. Ben Ming, D. Hesse, Microstructural Characterization of BaTiO3 Ceramic Nanoparticles Synthesized by the Hydrothermal Technique, Solid State Phenom. 106 (2005) 41–46. doi:10.4028/www.scientific.net/SSP.106.41.

[36] R. Pązik, R. Andersson, L. Kępiński, J.-M. Nedelec, V.G. Kessler, G.A. Seisenbaeva, Surface Functionalization of the Metal Oxide Nanoparticles with Biologically Active

Molecules Containing Phosphonate Moieties. Case Study of BaTiO3, J. Phys. Chem. C. 115 (2011) 9850–9860. doi:10.1021/jp2000656.

[37] Z. Ghallabi, M. Samet, M. Arous, A. Kallel, G. Boiteux, I. Royaud, G. Seytre, Giant Permittivity and Low Dielectric Loss in Three Phases BaTiO3/Carbon Nanotube/Polyvinylidene Fluoride Composites, J. Adv. Phys. 3 (2014) 87–91. doi:10.1166/jap.2014.1108.

[38] V. Sencadas, M.V. Moreira, S. Lanceros-Méndez, A.S. Pouzada, R. Gregório Filho, α-to β Transformation on PVDF Films Obtained by Uniaxial Stretch, Mater. Sci. Forum. 514–516 (2006) 872–876. doi:10.4028/www.scientific.net/MSF.514-516.872.

[39] M. Zhu, X. Huang, K. Yang, X. Zhai, J. Zhang, J. He, P. Jiang, Energy Storage in Ferroelectric Polymer Nanocomposites Filled with Core–Shell Structured Polymer@BaTiO3 Nanoparticles: Understanding the Role of Polymer Shells in the Interfacial Regions, ACS Appl. Mater. Interfaces. 6 (2014) 19644–19654. doi:10.1021/am504428u.

[40] X. Zhang, S. Zhao, F. Wang, Y. Ma, L. Wang, D. Chen, C. Zhao, W. Yang, Improving dielectric properties of BaTiO3/poly(vinylidene fluoride) composites by employing core-shell structured BaTiO3@Poly(methylmethacrylate) and BaTiO3@Poly(trifluoroethyl methacrylate) nanoparticles, Appl. Surf. Sci. 403 (2017) 71–79. doi:10.1016/j.apsusc.2017.01.121.

[41] N. Durand, P. Gaveau, G. Silly, B. Améduri, B. Boutevin, Radical grafting of tetrafluoroethylene and vinylidene fluoride telomers onto silica bearing vinyl groups, Macromolecules. 44 (2011) 6249–6257. doi:10.1021/ma200921b.

[42] M. Ejaz, V.S. Puli, R. Elupula, S. Adireddy, B.C. Riggs, D.B. Chrisey, S.M. Grayson, Core-shell structured poly(glycidyl methacrylate)/BaTiO3 nanocomposites prepared by surface-initiated atom transfer radical polymerization: A novel material for high energy density dielectric storage, J. Polym. Sci. Part A Polym. Chem. 53 (2015) 719–728. doi:10.1002/pola.27485.

[43] L. Xiong, H. Liang, R. Wang, L. Chen, A novel route for the synthesis of poly(2-hydroxyethyl methacrylate-co-methyl methacrylate) grafted titania nanoparticles via ATRP, J. Polym. Res. 18 (2011) 1017–1021. doi:10.1007/s10965-010-9502-5.

[44] C.M. Costa, S. Firmino Mendes, V. Sencadas, A. Ferreira, R. Gregorio, J.L. Gómez Ribelles, S. Lanceros-Méndez, Influence of processing parameters on the polymer phase, microstructure and macroscopic properties of poly(vinilidene fluoride)/Pb(Zr0.53Ti0.47)O3 composites, J. Non. Cryst. Solids. 356 (2010) 2127–2133. doi:10.1016/J.JNONCRYSOL.2010.07.037.

[45] Q. Jia, X. Huang, G. Wang, J. Diao, P. Jiang, MoS2 Nanosheet Superstructures Based Polymer Composites for High-Dielectric and Electrical Energy Storage Applications, J. Phys. Chem. C. 120 (2016) 10206–10214. doi:10.1021/acs.jpcc.6b02968.

[46] K.K. Jana, B. Ray, D.K. Avasthi, P. Maiti, Conducting nano-channels in an induced piezoelectric polymeric matrix using swift heavy ions and subsequent functionalization, J. Mater. Chem. 22 (2012) 3955. doi:10.1039/c2jm15132d.

[47] C. Marega, A. Marigo, Influence of annealing and chain defects on the melting behaviour of poly(vinylidene fluoride), Eur. Polym. J. 39 (2003) 1713–1720. doi:10.1016/S0014-3057(03)00062-4.

[48] A.A. Minakov, D.A. Mordvintsev, C. Schick, Melting and reorganization of poly(ethylene terephthalate) on fast heating (1000 K/s), Polymer (Guildf). 45 (2004) 3755–3763. doi:10.1016/J.POLYMER.2004.03.072.

Appendix I

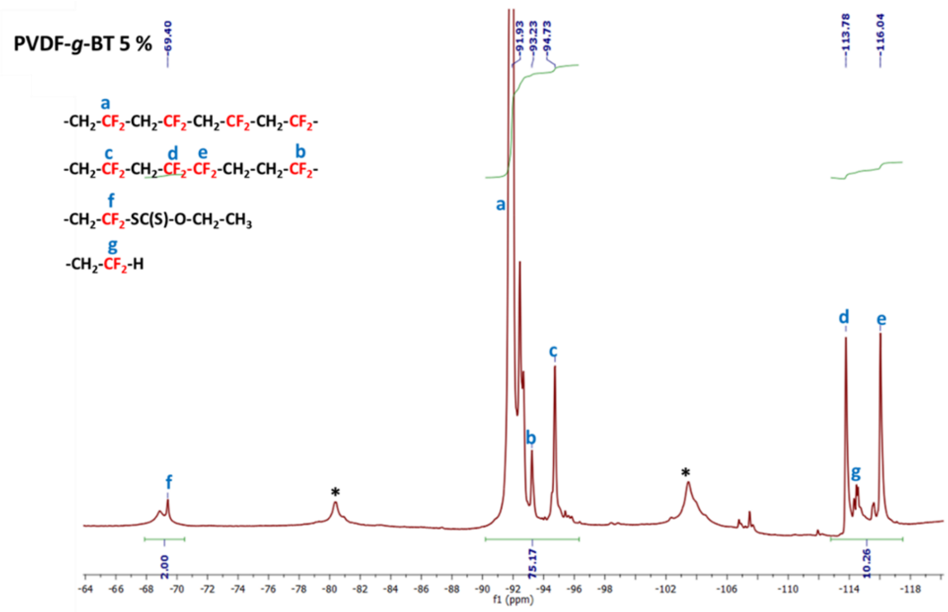

Figure A1. Expansion of the −64 to −120 ppm region of the ^{19}F HRMAS spectrum recorded in d_6-DMSO of PVDF-*g*-BaTiO$_3$ nanocomposite filled with 5 wt % of BaTiO$_3$ (* stands for the spinning bands).

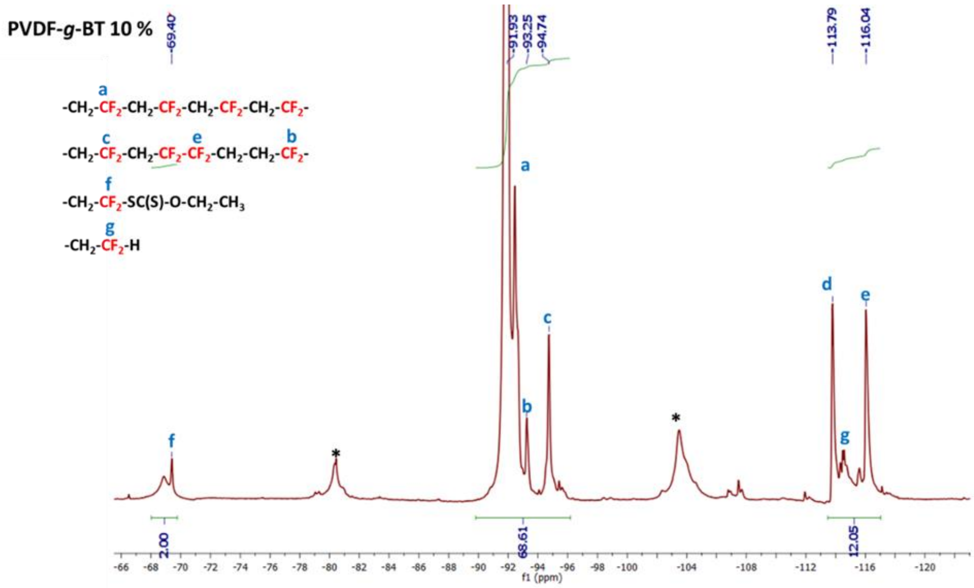

Figure A2. Expansion of the −64 to −120 ppm region of the ^{19}F HRMAS spectrum recorded in d_6-DMSO of PVDF-*g*-BaTiO$_3$ nanocomposite filled with 10 wt % of BaTiO$_3$ (* stands for the spinning bands).

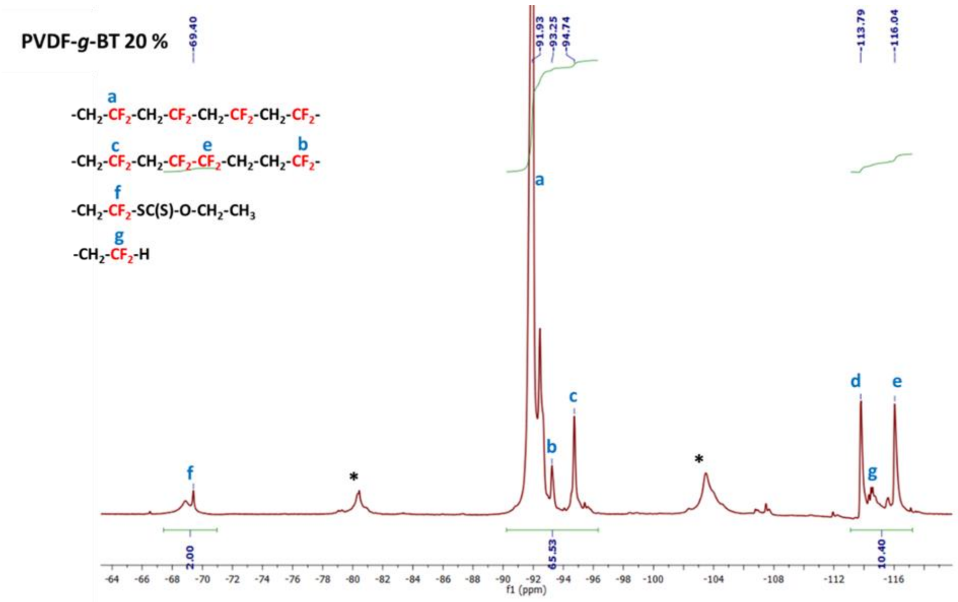

Figure A3. Expansion of the −64 to −120 ppm region of the ^{19}F HRMAS spectrum recorded in d$_6$-DMSO of PVDF-g-BaTiO$_3$ nanocomposite filled with 20 wt % of BaTiO$_3$ (* stands for the spinning bands).

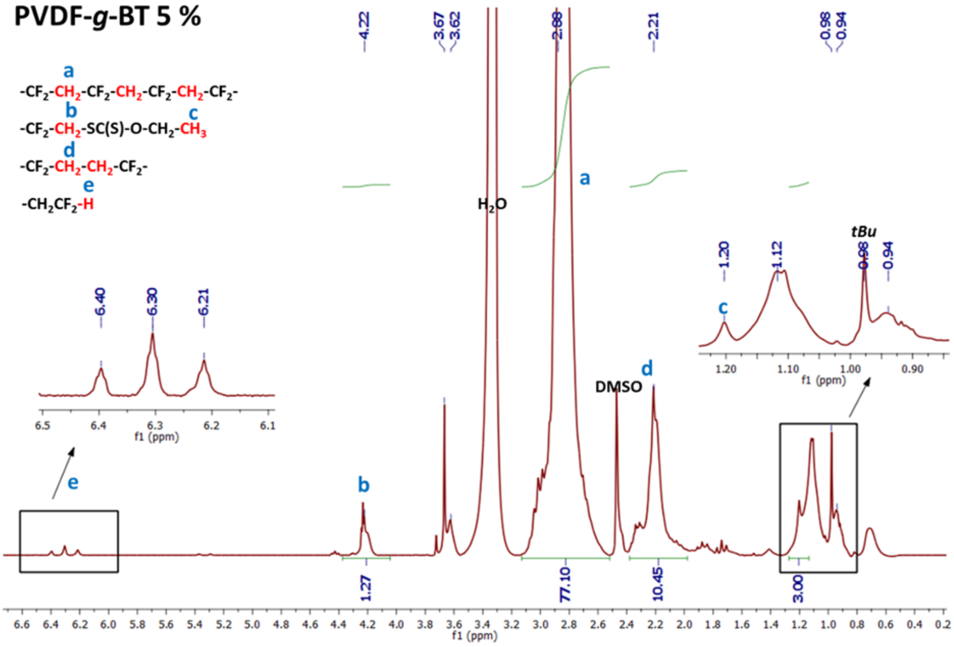

Figure A4. Expansion of the 0.2 to 6.4 ppm region of the ^{1}H HRMAS NMR spectrum in DMSO PVDF-*g*-BT nanocomposites filled with 5 wt % of BaTiO$_3$.

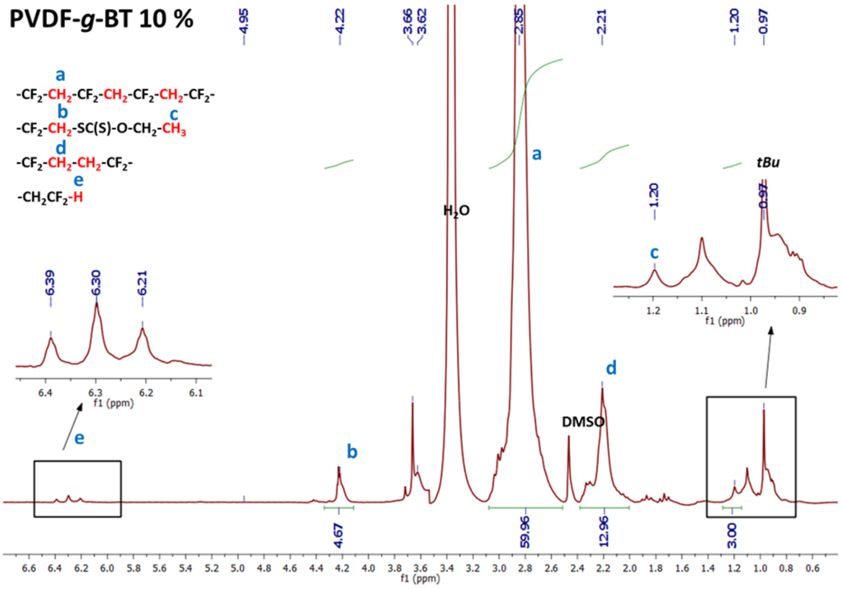

Figure A5. Expansion of the 0.2 to 6.4 ppm region of the ^{1}H HRMAS NMR spectrum in DMSO PVDF-*g*-BT nanocomposites filled with 10 wt % of $BaTiO_3$.

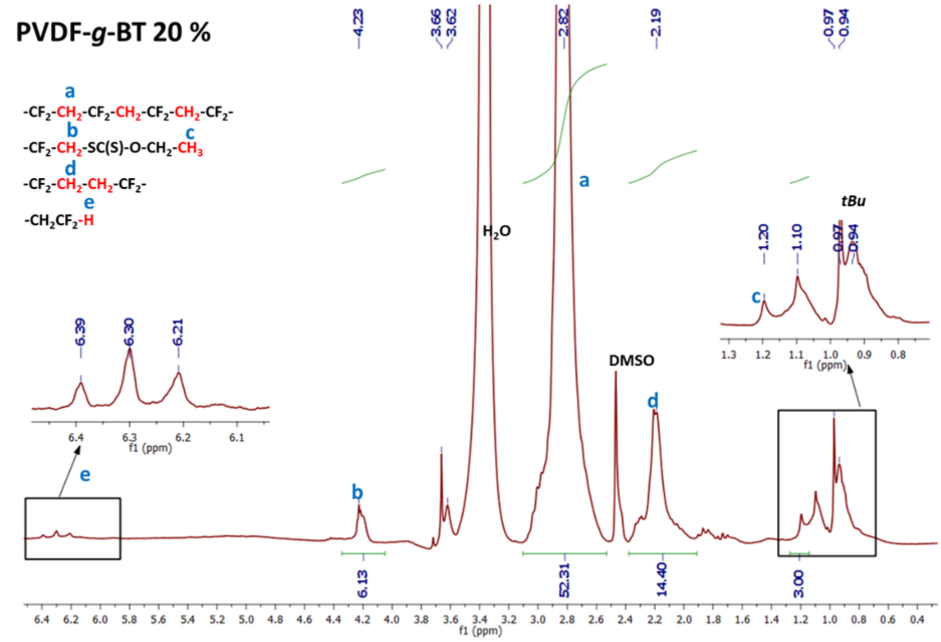

Figure A6. Expansion of the 0.2 to 6.4 ppm region of the ^{1}H HRMAS NMR spectrum in DMSO PVDF-*g*-BT nanocomposites filled with 20 wt % of $BaTiO_3$.

Chapter IV: Dielectric characterization of core-shell structured Poly(Vinylidene Fluoride) -*grafted*- $BaTiO_3$ nanocomposites

IV.1. Introduction

In the recent years, significant developments in energy storage systems have been reported due to their scientific as well as technological importance [1]. Among them, dielectric nanocomposites have drawn great attention because of their wide range of use [2– 4].

At present, the synthesis of a dielectric nanocomposite by the introduction of high dielectric constant inorganic nanoparticles into an organic polymer matrix, is a promising way to obtain high energy density materials. In general, the energy density can be written by the following equation:

$$U = \frac{1}{2}\, \varepsilon_0\, \varepsilon_r\, E^2 \qquad (1)$$

where $\varepsilon_0, \varepsilon_r$ *and* E are the permittivity of the free space (8.854 $\times 10^{-14}$ F/cm), the relative permittivity and E is the electric breakdown strength, respectively. These material properties are of most interest during the preparation of a dielectric nanocomposite. Thus, high energy densities could be reached by either increasing dielectric permittivity and/or electric breakdown strength. Moreover, the nanocomposite structure should have a balance of both nanofillers and polymer properties to lead to an increase in energy storage.

PVDF and its copolymers has been widely reported in the literature due to its attractive ferroelectric properties [5–8]. It is a semi-crystalline polymer that presents glass transition, melting and Curie temperatures in the range of -40 to -30 °C, 155-192 °C and 195-197 °C, respectively [9]. PVDF is a fluorinated hydrocarbon with a repeat unit ($-CH_2CF_2-$) that can exhibit different crystalline phases (named α, β, γ, δ and ε) [10]. The β phase is the one with the highest permittivity, while the α one is the most stable. However, the application of an electric field may lead to phase transitions. The α phase forms from the melt by normal crystallization and progressively forms the δ phase when an electric field of 100-150 MV/m is applied, then transforms to β phase when a high electric field of ~500 MV/m is applied [11]. In addition, β phase could also be reached by applying a mechanical deformation to α phase at stretching ratios of more than 5 at 80 °C to get a maximum of β phase content of 80% [12,13]. This stretching temperature results as the optimum condition, since increasing this value leads to a lower degree of transformation [13]. The dielectric constant of PVDF lies in the range of 6-12 [14]. By introducing high dielectric constant nanofillers into the PVDF matrix, such figure can be improved.

Barium titanate is one of the most explored perovskite ferroelectric materials, thanks to its attractive dielectric and piezoelectric properties, leading to its wide employment in several applications such as in electronic industry [15–20]. $BaTiO_3$ generally exhibits high dielectric permittivity, affected by several factors including the nanoparticles size. Mao *et al.* [21] investigated the size effect on dielectric properties of PVDF/BT nanocomposites. It was found that the highest permittivity of nanocomposites was obtained for nanoparticle sizes around 80-100 nm, reaching a maximum value of 93 (at 1 kHz) for 100 nm size. However, the dielectric permittivity remained nearly constant (~ 65 at 1 kHz) for particle size larger than 250 nm, and decreased with particle size under 50 nm.

Another important factor that affects dielectric permittivity of nanocomposites is the interface between ceramic nanoparticles and polymer matrix [22,23]. Thus, the selection of an appropriate pre-treatment of nanoparticles may be crucial to obtain high-energy storage nanocomposites. Dang *et al.* [24] used a commercial silane agent (KH550: $HN_2(CH_2)_2Si(OC_2H_5)_3$) to functionalize BT surface and improve its compatibility with PVDF matrix. To be able to observe the effect of the modifier agent, different amounts of KH550 were used. An optimum concentration of 1.0 wt % was found to give the highest values of permittivity, that resulted of around 40-50.

In this Chapter, we report on dielectric characterizations performed on nanocomposites prepared by means of Reversible Addition Fragmentation chain Transfer agent polymerization (RAFT) and consisting on $BaTiO_3$ nanoparticles as fillers and PVDF as the polymer matrix. The effect of BT loading on dielectric permittivity is also studied.

IV.2. Sample preparation

PVDF-*g*-BT with different loadings of $BaTiO_3$ were used. Synthesis and characterization of this nanocomposite materials are reported in Chapter II and III, respectively. In brief, the as received $BaTiO_3$ nanoparticles were firstly surface-modified by anchoring xanthates functions to their surface. Then, grafting of PVDF into the functionalized surface was performed using the “Reversible Addition Fragmentation chain Transfer agent (RAFT)” polymerization of VDF.

Table 1 shows the weight losses of the nanocomposites at 700 °C obtained by Thermo-Gravimetric Analysis (TGA). Crystalline fraction of as-prepared samples was obtained by comparing their specific melting enthalpy, measured during the first heating ramp by

Differential Scanning Calorimetry (Table 1), with that of a 100% crystalline PVDF known from the literature [25]. Crystallinity values resulted around 70% or higher for all samples.

Table 1. Weight loss at 700 °C, specific melting enthalpy, and crystalline fraction, for the different PVDF-*g*-BT nanocomposites [26].

wt % of BT in feed	*Weight loss of PVDF-g-$BaTiO_3$ at 700 °C (%)* [a]	*wt % of BT in nano-composite*	*vol % of BT in nano-composite*	*ΔH_m ($J\ g^{-1}$)* [b]	*Crystallinity X (%)*[c]
0	99	1±1	0.3±0.3	49	47
5	87	13±1	4.2±0.3	51	48
10	84	16±1	5.3±0.3	42	40
20	62	38±1	15.3±0.3	27	21

[a] Determined by TGA

[b] Specific melting enthalpy ΔH_m measured by DSC analysis under nitrogen on first heating, referred to the mass of sole PVDF determined after TGA

[c] Crystallinity determined from $\frac{\Delta H_m}{(1-\varphi)\Delta H_c} \times 100$, where ΔH_c (104.5 J g^{-1}) corresponds to the specific melting enthalpy of 100% crystalline α phase PVDF and is the weight fraction of the filler in the nanocomposite.

Pellets were prepared by a manual hydraulic press. The sample (nanocomposite powder) was placed in the compression cylinder. Then, a hydraulic press was used to apply the necessary pressure (1.25 kbar) to the sample through the press piston. Pellets were also prepared for the as-received BT nanoparticles as well as for pure PVDF.

IV.3. Results and discussion

Figure 1-a exhibits the frequency dependence of dielectric permittivity at 20 °C for the nanocomposites filled with different ratios of BT. It can be seen that the dielectric permittivity of the pure PVDF and all nanocomposites decreases by increasing the frequency. This can be explained by the fact that when the frequency increased, the dipoles of fillers and polymers cannot change their orientation fast enough, which results in a decrease of the dielectric permittivity [27–29].

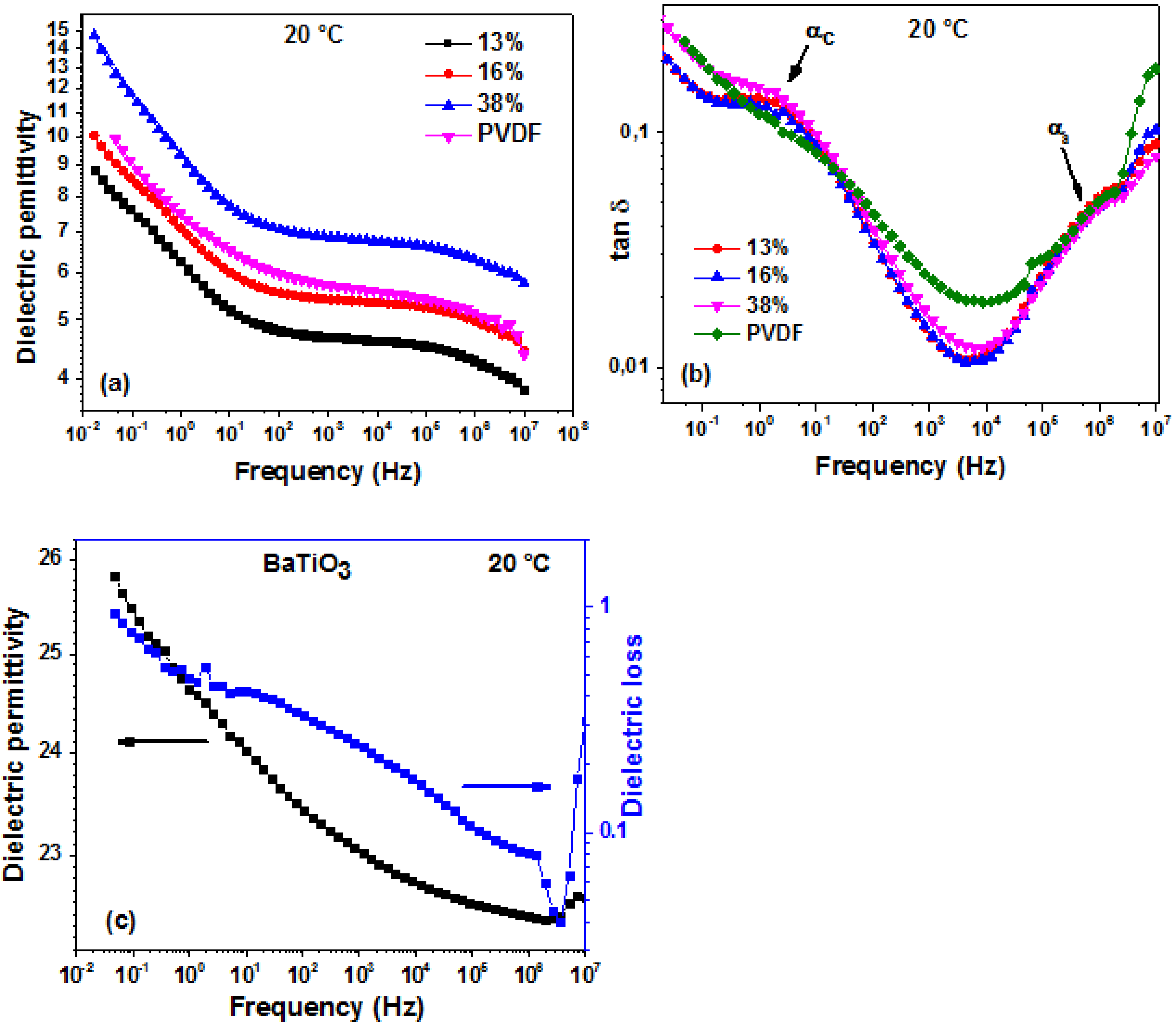

Figure 1. Frequency dependence of (a) dielectric constant and (b) dielectric loss of PVDF and PVDF-*g*-BT nanocomposites at 20 °C. (c) Frequency dependence of dielectric constant and dielectric loss of the as-received $BaTiO_3$ nanoparticles at 20 °C.

The increase of the BT amount in the nanocomposite results in increased dielectric permittivity. The obtained values are in agreement with TGA analysis. Unexpectedly however, values lower than that of the pure PVDF are reached in the case of nanocomposites filled with 13% and 16 wt% of BT. Similar trends were found in Arshad *et al.*'s work [30], who studied dielectric properties of a nanocomposite materials based on PVDF and Magnesium oxide nanofillers. It was found that after adding 1% of MgO in the PVDF matrix, a slight decrease of permittivity was observed for the nanocomposites as compared to the pure polymer. However, with further increasing of MgO content from 3 % to 5 % in PVDF, an increase in dielectric constant was perceived.

It is believed that the introduction of nanoparticles within the polymer matrix tend to create nucleation sites leading to increased crystalline fraction and thus a deceased in the permittivity and this was well seen in 13 % and 16 % samples where the volume fraction of BT were 4.2 % and 5.3 % [30]. However, when the filler amount is high enough, the contribution of the amorphous part becomes less important and the permittivity of the nanocomposite material will be affected more by the one of the nanoparticle.

Figure 1-b presents the frequency dependence of dielectric loss of pure PVDF and PVDF-*g*-BT nanocomposites at 20 °C. The curve exhibits two relaxation peaks at around 10^0 Hz and 10^6 Hz. The first peak is attributed to α_c relaxation peak in PVDF as well as in nanocomposites, and this relaxation was assigned, according to some authors to the non-polar phase of PVDF in the nanocomposite [31,32], while for others, this phenomenon is due to the molecular motions in the crystalline regions of the polymer [33,34], then, the second relaxation is assigned to glass transition temperature of PVDF [31]. In Figure 1-c, the dielectric spectrum of a pellet of as-received BT nanoparticles is shown. It is evident how the apparent dielectric constant of this sample (23.5 – 26, decreasing with frequency) results much lower than the nominal one (150).

The frequency dependence of dielectric permittivity for PVDF-*g*-BT nanocomposite at different temperatures is shown in Figure 2. It can be noted that as the temperature increases, the dielectric permittivity for all nanocomposites increases as well. For example, in the case of nanocomposites filled with 20 wt% of BT, at 10^{-2} Hz, the permittivity is ~15 at 20 °C and reaches ~ 480 at 100 °C.

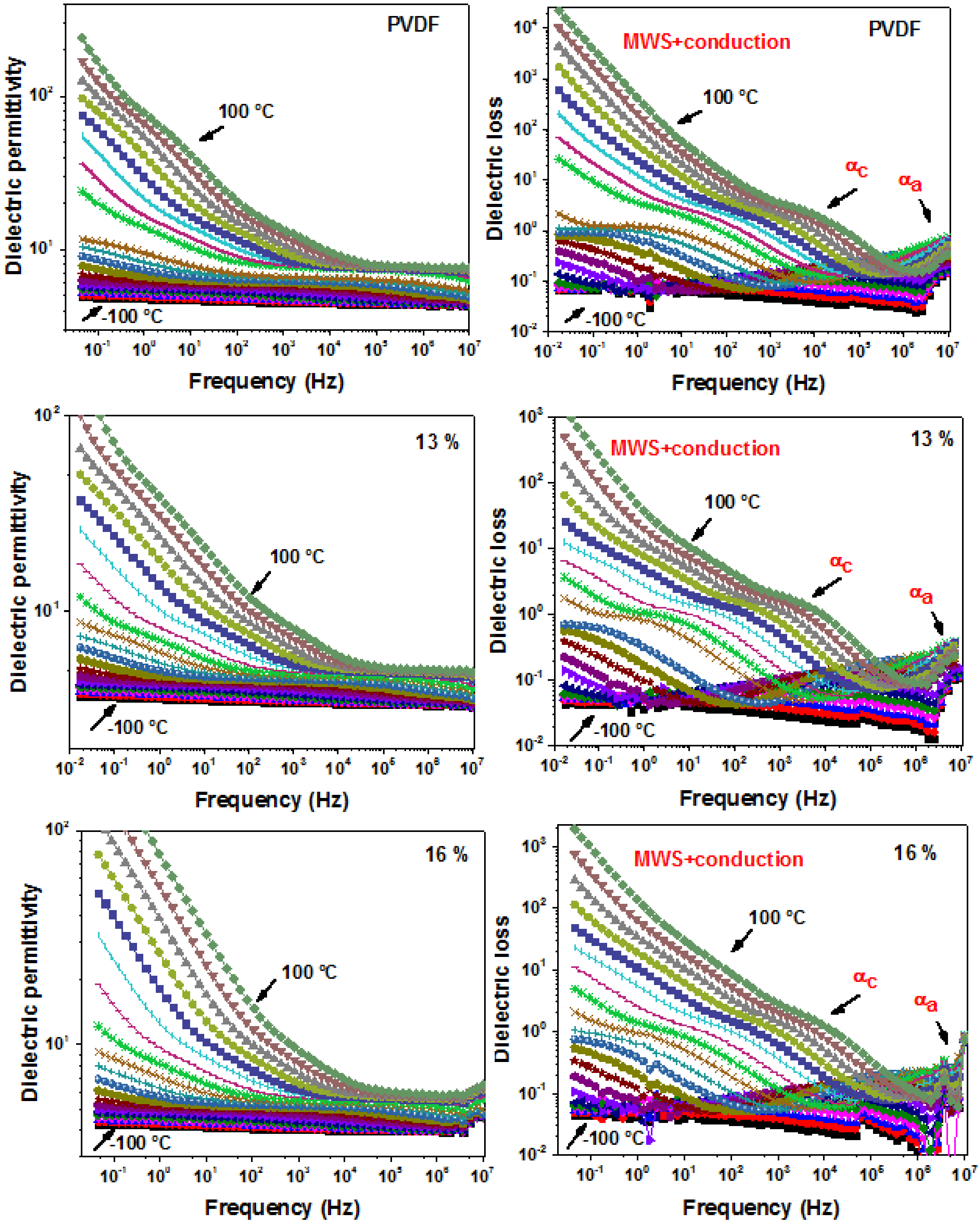
PVDF
Dielectric permittivity
100 °C
-100 °C
Frequency (Hz)
10^{1}
10^{2}
10^{-1} 10^{0} 10^{1} 10^{2} 10^{3} 10^{4} 10^{5} 10^{6} 10^{7}
PVDF
MWS+conduction
Dielectric loss
100 °C
α_c
α_a
-100 °C
Frequency (Hz)
10^{-2} 10^{-1} 10^{0} 10^{1} 10^{2} 10^{3} 10^{4}
10^{-2} 10^{-1} 10^{0} 10^{1} 10^{2} 10^{3} 10^{4} 10^{5} 10^{6} 10^{7}
13 %
Dielectric permittivity
100 °C
-100 °C
Frequency (Hz)
10^{1}
10^{2}
10^{-2} 10^{-1} 10^{0} 10^{1} 10^{2} 10^{3} 10^{4} 10^{5} 10^{6} 10^{7}
13 %
MWS+conduction
Dielectric loss
100 °C
α_c
α_a
-100 °C
Frequency (Hz)
10^{-2} 10^{-1} 10^{0} 10^{1} 10^{2} 10^{3}
10^{-2} 10^{-1} 10^{0} 10^{1} 10^{2} 10^{3} 10^{4} 10^{5} 10^{6} 10^{7}
16 %
Dielectric permittivity
100 °C
-100 °C
Frequency (Hz)
10^{1}
10^{2}
10^{-1} 10^{0} 10^{1} 10^{2} 10^{3} 10^{4} 10^{5} 10^{6} 10^{7}
16 %
MWS+conduction
Dielectric loss
100 °C
α_c
α_a
-100 °C
Frequency (Hz)
10^{-2} 10^{-1} 10^{0} 10^{1} 10^{2} 10^{3}
10^{-1} 10^{0} 10^{1} 10^{2} 10^{3} 10^{4} 10^{5} 10^{6} 10^{7}

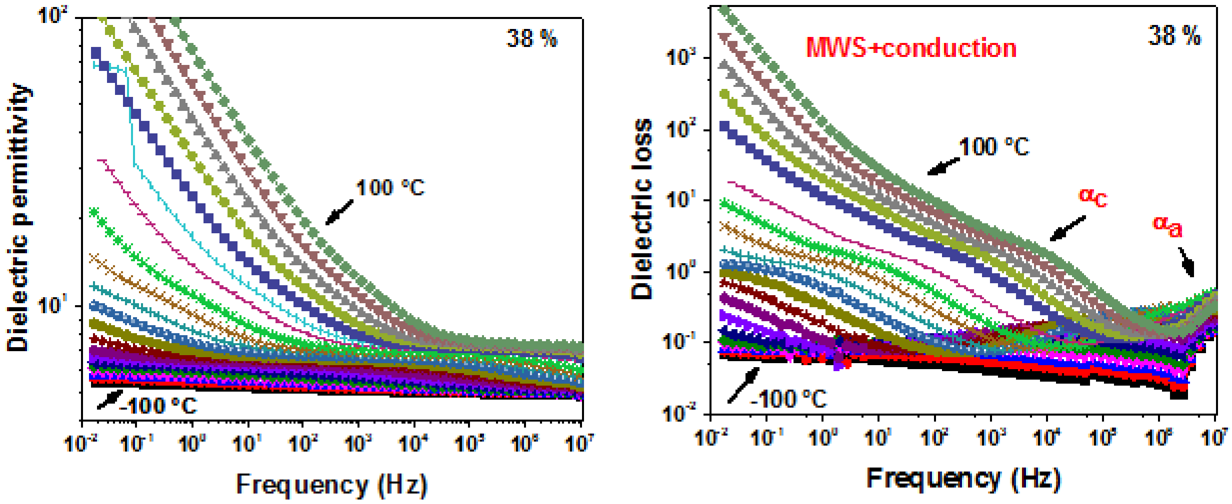

Figure 2. Frequency dependence of dielectric constant and dielectric loss of pure PVDF and PVDF-*g*-BT nanocomposites at various temperatures (From -100 °C to 100 °C by a step of 10°C).

In addition to crystalline relaxation related to PVDF, interfacial or Maxwell-Wagner-Sillars (MWS) polarization can also be seen in nanocomposites [36]. The rapid increase of permittivity at low frequencies is due to the electrode polarization, and the effect of this latter can completely hide the low frequency relaxations [37]. To overcome this issue, McCrum *et al.*[38–41] introduced the electric modulus formalism that suppresses the effect of electrode polarization, which can be expressed by the following equation:

$$M^* = \frac{1}{\varepsilon^*} = M' + jM'' \qquad (2)$$

where

$$M' = \frac{\varepsilon'}{\varepsilon'^2 + \varepsilon''^2} \;, and \;\; M'' = \frac{\varepsilon''}{\varepsilon'^2 + \varepsilon''^2} \qquad (3)$$

Figure 3 exhibits the dielectric loss modulus (M'') of pure PVDF, $BaTiO_3$ and PVDF-*g*-BT nanocomposite versus the frequency and at different temperatures. In contrast to Figure 1-b, which reveals only two crystalline relaxation peaks, Figure 3 reveals three relaxation peaks. In fact, the third relaxation peak that appears (for $T \geq 30$ °C) is attributed to interfacial or MWS polarization. It can be clearly seen that this relaxation is present in PVDF-*g*-BT (MWS_c) nanocomposite system as well as in PVDF (MWS_p) and it originates from the presence of fillers or even impurities that exhibits different permittivity and conductivity values, which result in heterogeneous system [42].

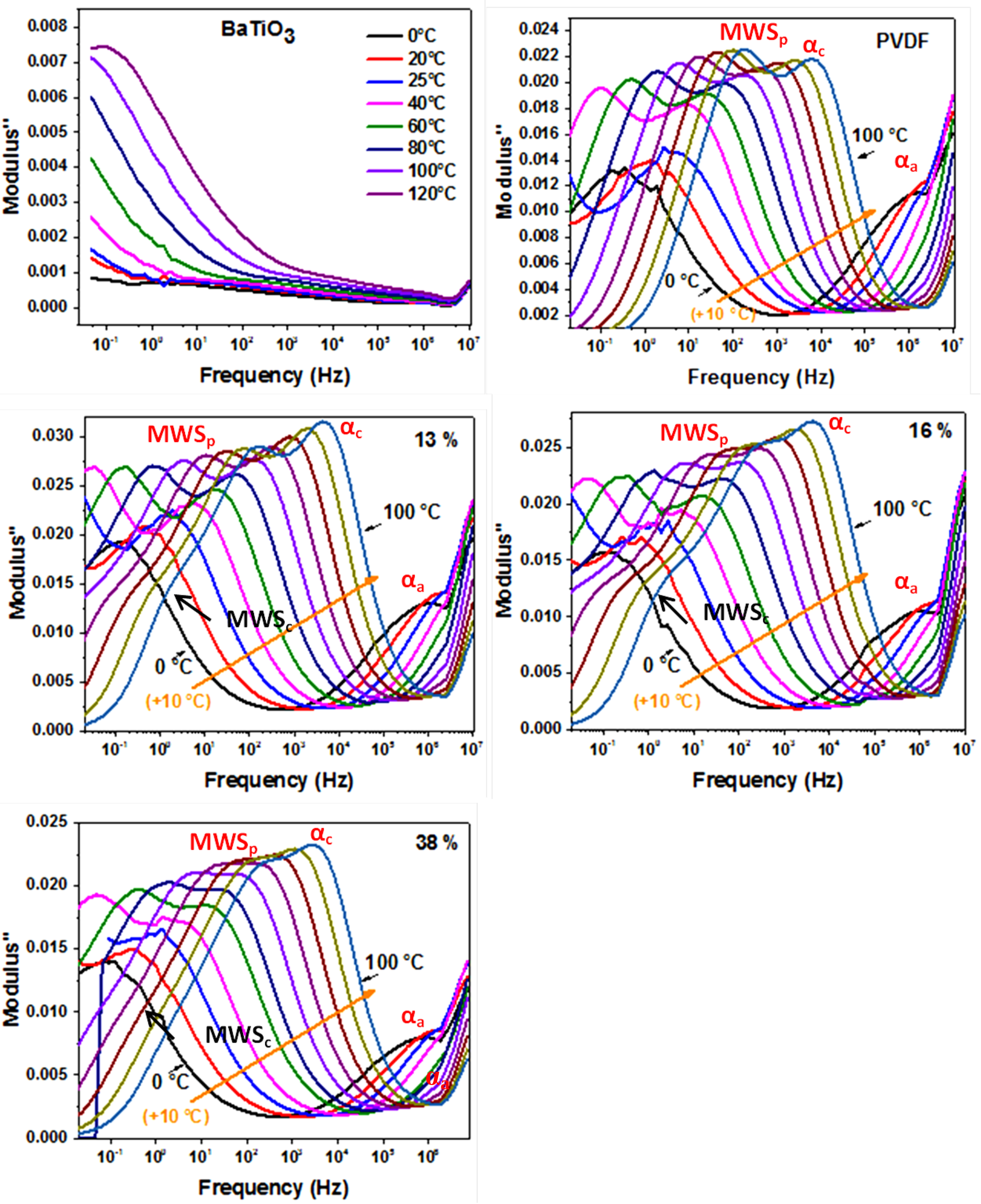

Figure 3. Dielectric loss modulus (M'') as a function of frequency for BaTiO$_3$, PVDF and PVDF-*g*-BT nanocomposites at different temperatures.

Figure 4 exhibits the frequency dependence of real part of electric Modulus (Modulus') for the pure PVDF and for PVDF-*g*-BT nanocomposites filled with 13, 16, and 38 wt % of BT at temperatures varying from 0 to 100 ° C. For all samples, it is noted the existence of two step-like transition from low to high values of the real part of the electric modulus (Modulus') at temperatures higher than 30 °C. The mentioned transitions evidence the presence of two relaxation processes which should be accompanied by two loss peaks in the plot of the imaginary part of electric modulus versus frequency (Figure 3). Indeed, it can be clearly seen from Figure 3 that the loss peaks are clearly formed in the frequency range where both transitions occur.

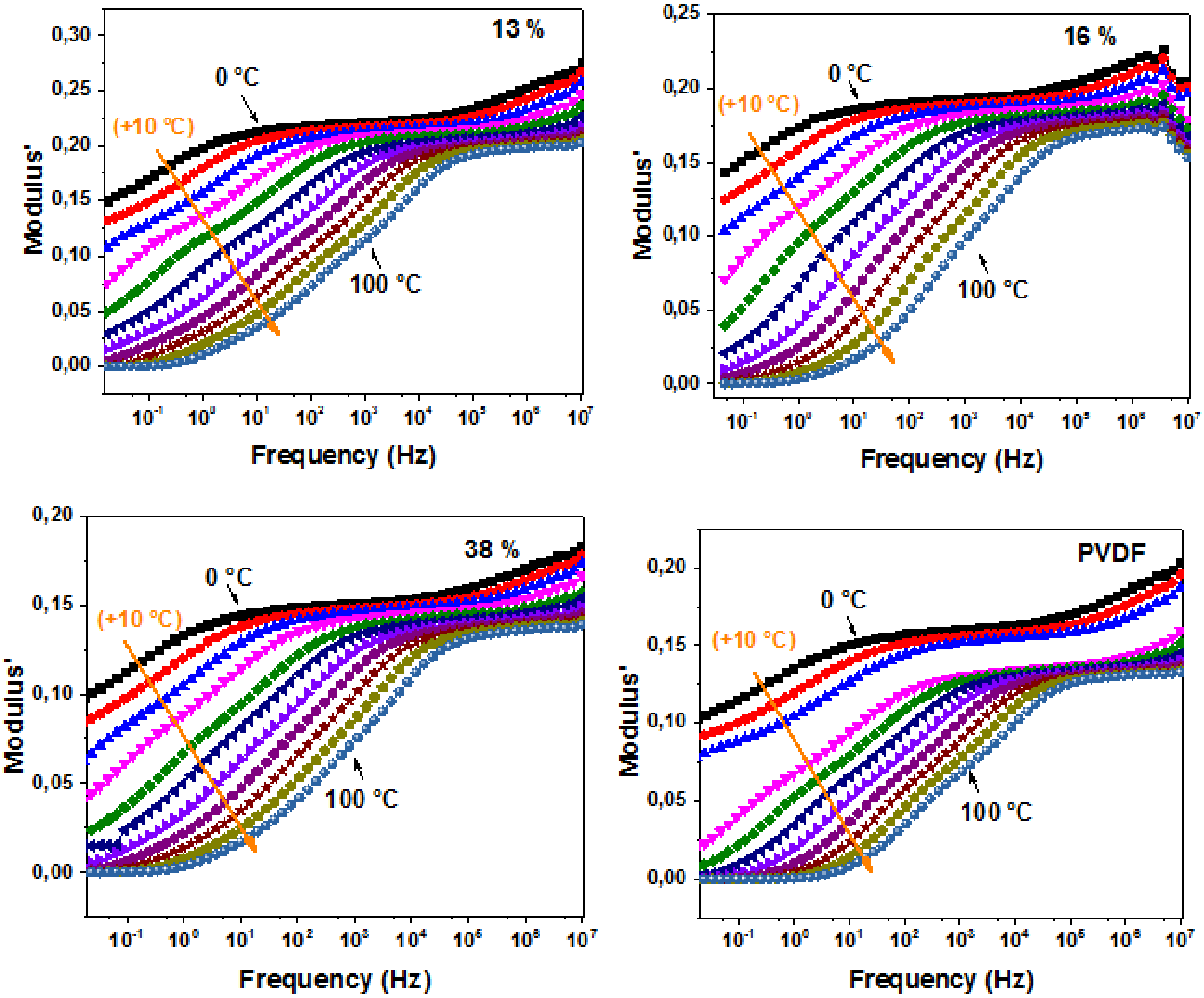

Figure 4. Real part of electric modulus (Modulus') as a function of frequency for PVDF and PVDF-*g*-BT nanocomposites at different $BaTiO_3$ loadings and temperatures.

In order to analyze quantitatively the dielectric relaxations, the Havriliak-Negami (HN) function is used:

$$\varepsilon^*(f) = \Sigma \left[\frac{\Delta\varepsilon}{\left(1 + \left(i\frac{f}{f_0}\right)^{\alpha}\right)^{\beta}} \right] - i\frac{\sigma_0}{\varepsilon_0(2\pi f)^m} \qquad (4)$$

where $\Delta\varepsilon$ is dielectric relaxation strength defined as $\Delta\varepsilon = \varepsilon_s - \varepsilon_\infty$ (ε_s and ε_∞ are the low- and the high-frequency limits of the real part of dielectric permittivity), α and β ($\alpha \geq 0$ and $\beta \leq 1$) are the parameters describing asymmetry and width of distribution of relaxation times, respectively. The added term ($\frac{\sigma_0}{\varepsilon_0(2\pi f)^m}$) stands for conductivity effects, where σ_0 is related to the direct-current conductivity of the samples and ε_0 is the dielectric constant of vacuum. The exponent m characterizes the conduction process [43].

For better evaluation of the β relaxation, we have selected the data acquired at temperatures below 10 °C, while for the α_c relaxation the highest temperatures were used. Figure 5 exhibits the logarithmic frequency (log $f_{\max}$) as a function of inverse of temperature (1000/T). It is observed, for all nanocomposites, that the logarithmic relaxation times of crystalline and β relaxations decrease with increasing temperature and exhibit a linear behavior that is well described by the Arrhenius equation [43]:

$$f = f_\infty \exp\left(-\frac{E_a}{KT}\right) \qquad (5)$$

f_∞, E_a, K and T stand for the relaxation frequency at infinite temperature, the activation energy, the Boltzmann's constant (1.38×10^{-23} J K^{-1}) and the absolute temperature, respectively. Logarithmic relaxation frequency versus inverse temperature is reported in the Arrhenius plot of Figure 5. Fitting results for the relaxation time and activation energy for both processes are reported in Table 2.

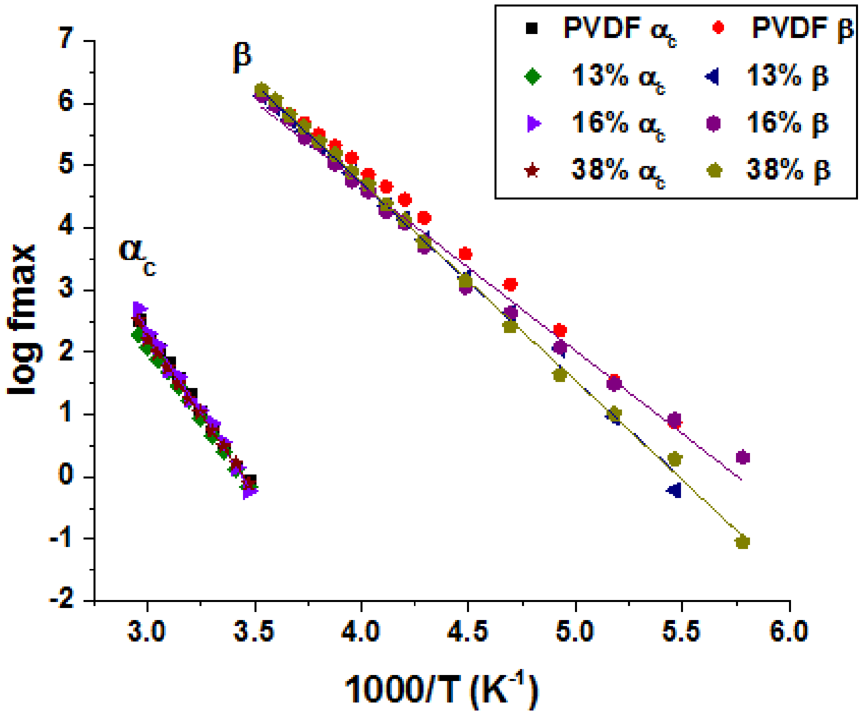

Figure 5. Arrhenius plot of the logarithmic relaxation time versus inverse temperature for PVDF and PVDF-*g*-BT nanocomposites.

Table 2. Relaxation time and activation energy obtained by best fitting for PVDF and PVDF-g-BT nanocomposites.

Samples	***β* relaxation**		***α_c* relaxation**	
	τ_∞ [s]	**E_a [kJ/mol]**	**τ_∞ [s]**	**E_a [kJ/mol]**
PVDF pure	1.31×10^{-17}	53.3	3.03×10^{-19}	99.4
13%	6.38×10^{-19}	60.7	9.16×10^{-20}	103.3
16%	6.95×10^{-17}	54.1	2.09×10^{-19}	100.5
38%	4.52×10^{-19}	61.3	1.66×10^{-18}	95.0

The relaxation time for α_c relaxation of PVDF was 3.05×10^{-19} s and decreases to 9.16×10^{-20} s after adding 13 wt% of $BaTiO_3$, which can be explained by the free charge accumulation at the interface. On the other hand, the activation energy was found to increase from 99.4 kJ/mol for pure PVDF to 103.3 kJ/mol for PVDF-*g*-BT nanocomposites with 13 wt% of $BaTiO_3$. Similar behaviors were found in previous work [31,44,45], and this phenomenon was explained by the fact that the addition of nanofillers into the polymer matrix decreases the mobility of the polymer chains and hinders the orientation of electric field which results in increasing of the activation energy.

To be able to explain the effect of each component on the dielectric properties of the nanocomposite, several models have been developed [46–48]. For a spherical nanoparticle and low filler loading, Maxwell-Garnett Equation could be written as:

$$\varepsilon = \varepsilon_m \left[1 + \frac{3\varphi_f(\varepsilon_{f-}\varepsilon_m)}{\varphi_m(\varepsilon_f - \varepsilon_m) + 3\varepsilon_m}\right] \qquad (6)$$

where ε, ε_f, ε_m, φ_f *and* φ_m are the permittivities of the nanocomposite material, permittivities of the filler and polymer and the volume fractions of filler and matrix, respectively [49,50]. Figure 6 exhibits the predicted and experimental values of dielectric permittivities as a function of frequency at room temperature for the nanocomposites.

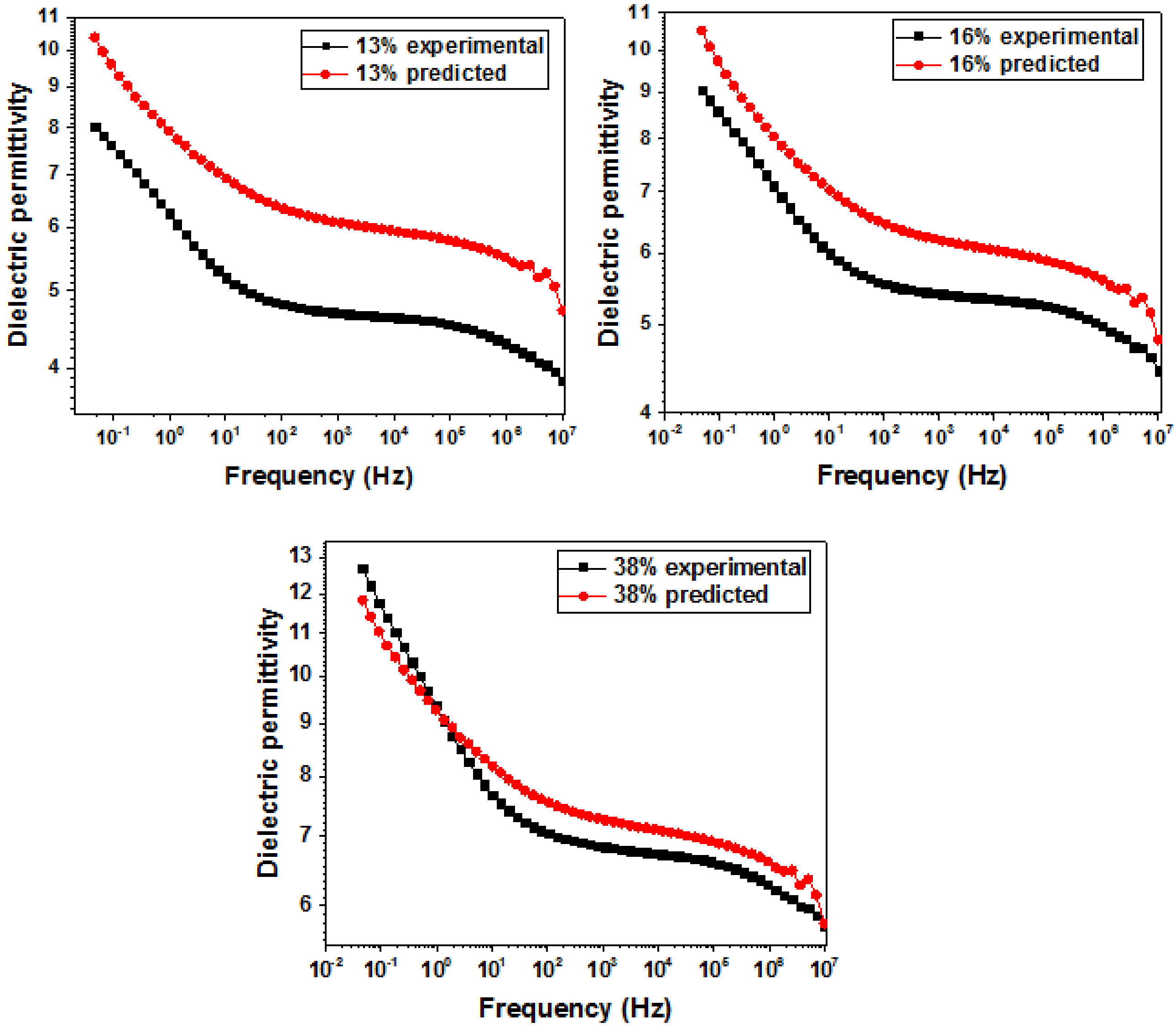

Figure 6. Predicted and experimental values of dielectric permittivity for PVDF-*g*-BT nanocomposites with different loading of BT at room temperature.

It can be seen from Figure 6, that for all nanocomposites, both predicted dielectric permittivities and those obtained from experimental results decrease with increasing frequency. Moreover, the dielectric permittivities obtained from experimental results are smaller than the predicted ones. This can be reconciled by assuming that the interface plays a strong role.

Vo and Shi [51] developed a model to describe the effect of the interphase region on the dielectric permittivity which takes into account the dielectric permittivities and volume fractions of polymer, nanofiller and interphase. The relationship used for modeling the effective permittivity for nanocomposite materials containing three components (the matrix, interphase region, and filler) can be expressed by the following equation:

$$\varepsilon_c = \frac{h+2l}{h-l} \qquad (7)$$

where:

$$h = A - 2B - C \qquad (8)$$

and

$$l = \frac{\varepsilon_3 - 1}{\varepsilon_3 + 2} A - \frac{(2\varepsilon_3 + 1)}{(\varepsilon_3 + 2)(2\varepsilon_3 + \varepsilon_2)}\, m \left(\frac{b^3}{c^3}\right) \qquad (9)$$

with:

$$A = 1 + 2\frac{(\varepsilon_3 - \varepsilon_2)(\varepsilon_2 - \varepsilon_1)}{(2\varepsilon_3 + \varepsilon_2)(2\varepsilon_2 + \varepsilon_1)}\left(\frac{a^3}{b^3}\right) \qquad (10)$$

$$B = \frac{(\varepsilon_3 - 1)(\varepsilon_3 - \varepsilon_2)}{(\varepsilon_3 + 2)(2\varepsilon_3 + \varepsilon_2)}\left(\frac{b^3}{c^3}\right) \qquad (11)$$

$$C = \frac{(\varepsilon_3 - 1)(\varepsilon_3 + 2\varepsilon_2)(\varepsilon_2 - 1)}{(\varepsilon_3 + 2)(2\varepsilon_3 + \varepsilon_2)(2\varepsilon_2 + \varepsilon_1)}\left(\frac{a^3}{c^3}\right) \qquad (12)$$

$$m = (\varepsilon_3 - \varepsilon_2)\frac{(\varepsilon_3 + 2\varepsilon_2)(\varepsilon_2 - \varepsilon_1)}{(2\varepsilon_3 + \varepsilon_1)}\left(\frac{a^3}{b^3}\right) \qquad (13)$$

$$\frac{a^3}{b^3} = \frac{(1 + k\varphi_F)}{(1+k)} \qquad (14)$$

$$\frac{b^3}{c^3} = \varphi_F\left[1 + k\frac{(1-\varphi_F)}{(1+k\varphi_F)}\right] \qquad (15)$$

$$\frac{a^3}{c^3} = \varphi_F \qquad (16)$$

Here, $\varepsilon_{1,}\ \varepsilon_2\ and\ \varepsilon_3$ stands for the dielectric permittivities of the ceramic nanoparticles, interphase and polymer matrix, respectively, and φ_F represents the volume fraction of ceramic nanofillers, while k is the interphase volume constant, that reflects the matrix/filler interaction strength, where a value of zero designates an insignificant filler-matrix interaction, while positive values indicates the presence of strong interactions [51].

Figure 7 exhibits the measured and calculated plots of dielectric permittivity for PVDF-*g*-BT nanocomposites with different volume fractions of BT. By using the interphase approach based on Vo-Shi model, [51] the best fit of calculated values with experimental data is obtained for k = 0.12 and ε_2=33, and this high dielectric constant obtained for the interphase can be attributed to the formation of dipoles with high molecular polarizability [46].

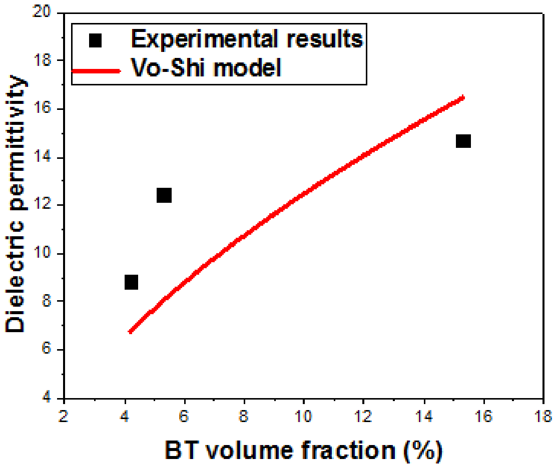

Figure 7. BT volume fraction dependence of dielectric permittivity for PVDF-*g*-BT nanocomposites at 10^{-2} Hz and 20 °C.

Figure 8 exhibits the frequency dependence of conductivity σ for pure PVDF and PVDF-*g*-BT nanocomposites, obtained from the equation (17) [52]:

$$\sigma = \varepsilon'' 2\pi f\, \varepsilon_0 \qquad (17)$$

where ε″ is loss factor, ε_0 is the permittivity of free space and f is the frequency (Hz).

It can be seen that the conductivity increases with the increase of frequency and temperature for all the nanocomposites as well as for the pure PVDF. Moreover, at 20 °C and over the whole frequency range, the conductivity is independent of the volume fraction of the fillers and is close to that of the PVDF, indicating the good insulating properties of the nanocomposites [53].

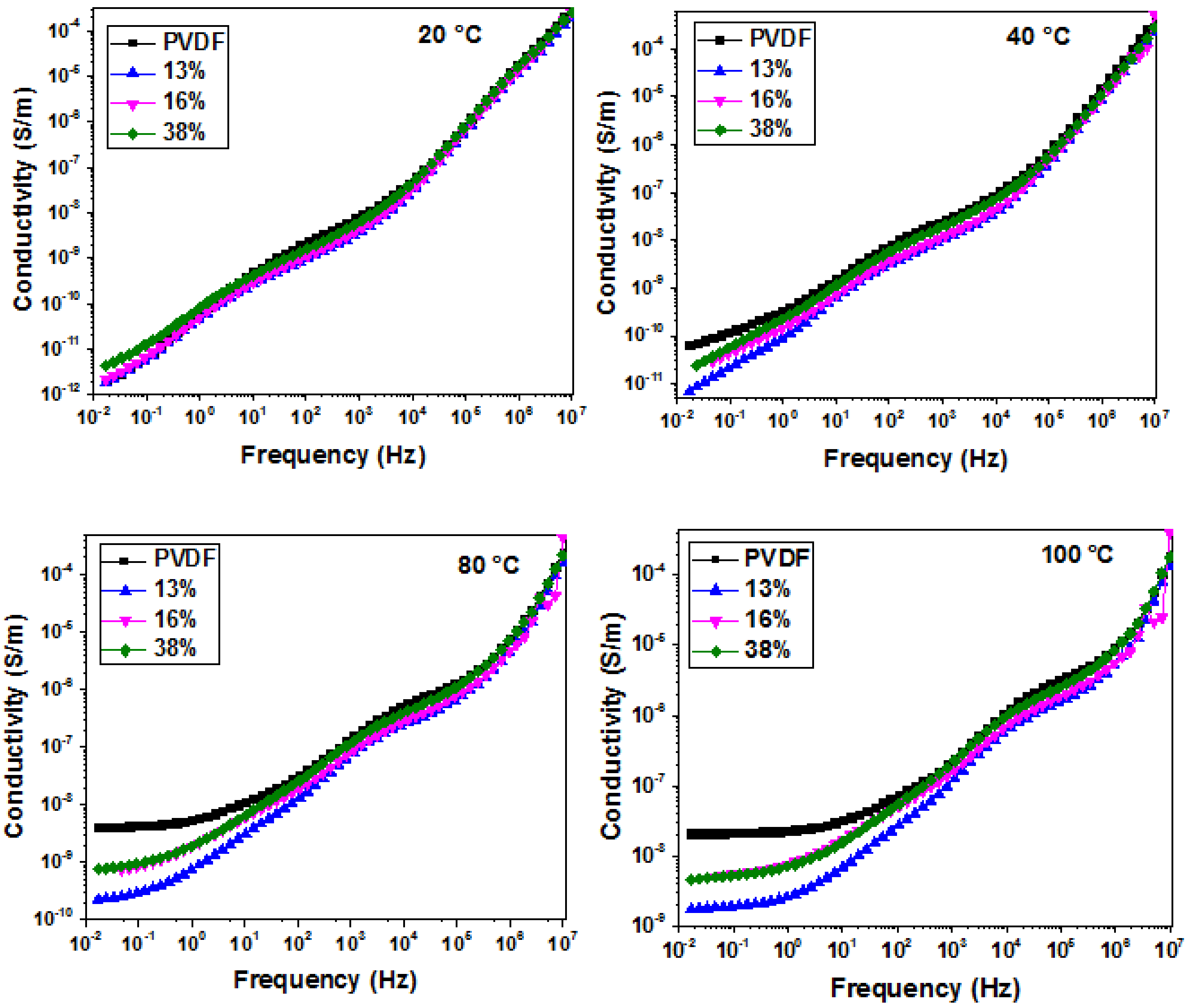

Figure 8. Frequency dependence of conductivity for PVDF and PVDF-*g*-BT nanocomposites at different temperatures.

IV.4. Conclusion

The dielectric properties of core shell structured nanocomposites made by Poly (Vinylidene Fluoride) -*grafted*- $BaTiO_3$ were investigated. The dielectric permittivity of the nanocomposites increased from 9 for the pure PVDF to 13 after adding 38 wt% of $BaTiO_3$ to the polymer matrix. All the samples exhibited two main relaxation processes that fits well the Arrhenius fittings. Moreover, the modulus formalism enables to display a third relaxation process related to interfacial or MWS polarization, which originates from the presence of impurities that exhibits different permittivity values, resulting in heterogeneous systems. Finally, the conductivity measurements revealed an independency of the volume fraction of the $BaTiO_3$, and the values were close to those of the PVDF, indicating the good insulating properties of the resulting nanocomposites.

IV.5. References

[1] Akinyele DO, Rayudu RK. Review of energy storage technologies for sustainable power networks. Sustain Energy Technol Assessments 2014;8:74–91. doi:10.1016/j.seta.2014.07.004.

[2] Wang Q, Zhu L. Polymer Nanocomposites for Electrical Energy Storage 2011:1421–9. doi:10.1002/polb.22337.

[3] Tomer V, Polizos G, Manias E, Randall CA. Epoxy-based nanocomposites for electrical energy storage. I: Effects of montmorillonite and barium titanate nanofillers. J Appl Phys 2010;108:74116. doi:10.1063/1.3487275.

[4] Wang L, Huang X, Zhu Y, Jiang P. Enhancing electrical energy storage capability of dielectric polymer nanocomposites via the room temperature Coulomb blockade effect of ultra-small platinum nanoparticles. Phys Chem Chem Phys 2018;20:5001–11. doi:10.1039/C7CP07990G.

[5] Zhang X, Ma Y, Zhao C, Yang W. High dielectric constant and low dielectric loss hybrid nanocomposites fabricated with ferroelectric polymer matrix and BaTiO3 nanofibers modified with perfluoroalkylsilane. Appl Surf Sci 2014;305:531–8. doi:10.1016/J.APSUSC.2014.03.131.

[6] Liu S, Xue S, Zhang W, Zhai J. Enhanced dielectric and energy storage density induced by surface-modified BaTiO3 nanofibers in poly(vinylidene fluoride) nanocomposites. Ceram Int 2014;40:15633–40. doi:10.1016/J.CERAMINT.2014.07.083.

[7] Gao L, He J, Hu J, Li Y. Large Enhancement in Polarization Response and Energy Storage Properties of Poly(vinylidene fluoride) by Improving the Interface Effect in Nanocomposites. J Phys Chem C 2014;118:831–8. doi:10.1021/jp409474k.

[8] Yu K, Niu Y, Zhou Y, Bai Y, Wang H. Nanocomposites of Surface-Modified BaTiO3 Nanoparticles Filled Ferroelectric Polymer with Enhanced Energy Density. J Am Ceram Soc 2013;96:2519–24. doi:10.1111/jace.12338.

[9] Ameduri B. From Vinylidene Fluoride (VDF) to the Applications of VDF-Containing Polymers and Copolymers: Recent Developments and Future Trends. Chem Rev 2009;109:6632–86. doi:10.1021/cr800187m.

[10] Soulestin T, Ladmiral V, Dos Santos FD, Améduri B. Vinylidene fluoride- and trifluoroethylene-containing fluorinated electroactive copolymers. How does chemistry impact properties? Prog Polym Sci 2017;72:16–60. doi:10.1016/j.progpolymsci.2017.04.004.

[11] Yu Y-J, Mcgaughey AJH. Energy barriers for dipole moment flipping in PVDF-related ferroelectric polymers. J Chem Phys 2016;144:14901. doi:10.1063/1.4939152.

[12] Branciforti MC, Sencadas V, Lanceros-Mendez S, Gregorio R. New technique of processing highly oriented poly(vinylidene fluoride) films exclusively in the β phase. J Polym Sci Part B Polym Phys 2007;45:2793–801. doi:10.1002/polb.21239.

[13] Martins P, Nunes JS, Hungerford G, Miranda D, Ferreira A, Sencadas V, et al. Local variation of the dielectric properties of poly(vinylidene fluoride) during the α- to β-phase transformation. Phys Lett A 2009;373:177–80. doi:10.1016/j.physleta.2008.11.026.

[14] Wan C, Bowen CR. Multiscale-structuring of polyvinylidene fluoride for energy harvesting: the impact of molecular-, micro- and macro-structure. J Mater Chem A 2017;5:3091–128. doi:10.1039/C6TA09590A.

[15] Smith MB, Page K, Siegrist T, Redmond PL, Walter EC, Seshadri R, et al. Crystal Structure and the Paraelectric-to-Ferroelectric Phase Transition of Nanoscale BaTiO3. J Am Chem Soc 2008;130:6955–63. doi:10.1021/ja0758436.

[16] Huang K-C, Huang T-C, Hsieh W-F. Morphology-Controlled Synthesis of Barium Titanate Nanostructures. Inorg Chem 2009;48:9180–4. doi:10.1021/ic900854x.

[17] Neagu AM, Curecheriu LP, Cazacu A, Mitoseriu L. Impedance analysis and tunability of BaTiO3–chitosan composites: Towards active dielectrics for flexible electronics. Compos Part B Eng 2014;66:109–16. doi:10.1016/J.COMPOSITESB.2014.04.020.

[18] Hirose N, West AR. Impedance Spectroscopy of Undoped BaTiO3 Ceramics. J Am Ceram Soc 1996;79:1633–41. doi:10.1111/j.1151-2916.1996.tb08775.x.

[19] Tian Z, Wang X, Shu L, Wang T, Song T-H, Gui Z, et al. Preparation of Nano BaTiO3-Based Ceramics for Multilayer Ceramic Capacitor Application by Chemical Coating Method. J Am Ceram Soc 2009;92:830–3. doi:10.1111/j.1551-2916.2009.02979.x.

[20] Feteira A, Sinclair DC, Reaney IM, Somiya Y, Lanagan MT. BaTiO3-Based Ceramics for Tunable Microwave Applications. J Am Ceram Soc 2004;87:1082–7. doi:10.1111/j.1551-2916.2004.01082.x.

[21] Mao YP, Mao SY, Ye Z-G, Xie ZX, Zheng LS. Size-dependences of the dielectric and ferroelectric properties of BaTiO3/polyvinylidene fluoride nanocomposites. J Appl Phys 2010;108:14102. doi:10.1063/1.3443582.

[22] Todd MG, Shi FG. Complex permittivity of composite systems: a comprehensive interphase approach. IEEE Trans Dielectr Electr Insul 2005;12:601–11. doi:10.1109/TDEI.2005.1453466.

[23] Tanaka T, Kozako M, Fuse N, Ohki Y. Proposal of a multi-core model for polymer nanocomposite dielectrics. IEEE Trans Dielectr Electr Insul 2005;12:669–81. doi:10.1109/TDEI.2005.1511092.

[24] Dang Z-M, Wang H-Y, Xu H-P. Influence of silane coupling agent on morphology and dielectric property in BaTiO3/polyvinylidene fluoride composites. Appl Phys Lett 2006;89:112902. doi:10.1063/1.2338529.

[25] Nakagawa K, Ishida Y. Estimation of amorphous specific volume of poly(vinylidene fluoride) as a function of temperature. Kolloid-Zeitschrift Und Zeitschrift Für Polym 1973;251:103–7. doi:10.1007/BF01498933.

[26] Bouharras FE, Raihane M, Silly G, Totee C, Ameduri B. Core shell structured Poly(Vinylidene Fluoride) -grafted- BaTiO3 nanocomposites prepared via Reversible Addition fragmentation chain transfer (RAFT) polymerization of VDF for high energy storage capacitors. Polym Chem 2019;10:891–904. doi:10.1039/C8PY01706A.

[27] Fu J, Hou Y, Zheng M, Wei Q, Zhu M, Yan H. Improving Dielectric Properties of PVDF Composites by Employing Surface Modified Strong Polarized BaTiO3 Particles

Derived by Molten Salt Method. ACS Appl Mater Interfaces 2015;7:24480–91. doi:10.1021/acsami.5b05344.

[28] Liu S, Xue S, Xiu S, Shen B, Zhai J. Surface-modified Ba(Zr0.3Ti0.7)O3 nanofibers by polyvinylpyrrolidone filler for poly(vinylidene fluoride) composites with enhanced dielectric constant and energy storage density. Sci Rep 2016;6:26198. doi:10.1038/srep26198.

[29] Li J, Claude J, Norena-Franco LE, Seok S Il, Wang Q. Electrical Energy Storage in Ferroelectric Polymer Nanocomposites Containing Surface-Functionalized BaTiO3 Nanoparticles. Chem Mater 2008;20:6304–6. doi:10.1021/cm8021648.

[30] Arshad AN, Wahid MHM, Rusop M, Majid WHA, Subban RHY, Rozana MD. Dielectric and structural properties of poly(vinylidene fluoride) (PVDF) and poly(vinylidene fluoride-trifluoroethylene) (PVDF-TrFE) filled with magnesium oxide nanofillers. J Nanomater 2019;2019. doi:10.1155/2019/5961563.

[31] Chanmal C V., Jog JP. Dielectric relaxations in PVDF/BaTiO3 nanocomposites. eXPRESS Polym Lett 2008;2:294–301. doi:10.3144/expresspolymlett.2008.35.

[32] Kochervinskii V V., Malyshkina IA, Markin G V., Gavrilova ND, Bessonova NP. Dielectric relaxation in vinylidene fluoride–hexafluoropropylene copolymers. J Appl Polym Sci 2007;105:1101–17. doi:10.1002/app.26145.

[33] Yano S. Dielectric relaxation and molecular motion in poly(vinylidene fluoride). J Polym Sci Part A-2 Polym Phys 1970;8:1057–72. doi:10.1002/pol.1970.160080704.

[34] Nakagawa K, Ishida Y. Dielectric relaxations and molecular motions in poly(vinylidene fluoride) with crystal form II. J Polym Sci Part A-2 Polym Phys 1973;11:1503–33. doi:10.1002/pol.1973.180110804.

[35] Kripotou S, Sovatzoglou S, Pandis C, Kuliček J, Mičušík M, Omastova M, et al. Effects of CNT inclusions on structure and dielectric properties of PVDF/CNT nanocomposites. Phase Transitions 2016;89:717–30. doi:10.1080/01411594.2016.1180518.

[36] Mittal V. Characterization Techniques for Polymer Nanocomposites. 2012.

[37] Chanmal C V., Jog JP. Dielectric relaxations in PVDF/BaTiO3 nanocomposites. Express Polym Lett 2008;2:294–301. doi:10.3144/expresspolymlett.2008.35.

[38] Tsangaris GM, Kouloumbi N, Kyvelidis S. Interfacial relaxation phenomena in particulate composites of epoxy resin with copper or iron particles. Mater Chem Phys 1996;44:245–50. doi:10.1016/0254-0584(96)80063-0.

[39] Psarras G., Manolakaki E, Tsangaris G. Electrical relaxations in polymeric particulate composites of epoxy resin and metal particles. Compos Part A Appl Sci Manuf 2002;33:375–84. doi:10.1016/S1359-835X(01)00117-8.

[40] Patsidis AC, Psarras G. Dielectric behaviour and functionality of polymer matrix-ceramic BaTiO3 composites. Polym Lett 2008;2:718–26. doi:10.3144/expresspolymlett.2008.85.

[41] Kontos GA, Soulintzis AL, Karahaliou1 PK, Psarras GC, Georga SN, Krontiras CA, et al. Electrical relaxation dynamics in TiO2 – polymer matrix composites. Polym Lett 2007;1:781–9. doi:10.3144/expresspolymlett.2007.108.

[42] TSANGARIS GM, PSARRAS GC, KOULOUMB N. Electric modulus and interfacial polarization in composite polymeric systems. J Mater Sci 1998;33:2027–37. doi:10.1023/A:1004398514901.

[43] Kochervinskij V V., Malyshkina IA, Bessonova NP, Suljanov SN, Dembo KA. Effect of recrystallization on the molecular mobility of a copolymer of vinylidene fluoride and hexafluoropropylene. J Appl Polym Sci 2011;120:13–20. doi:10.1002/app.32993.

[44] Rekik H, Ghallabi Z, Royaud I, Arous M, Seytre G, Boiteux G, et al. Dielectric relaxation behaviour in semi-crystalline polyvinylidene fluoride (PVDF)/TiO2 nanocomposites. Compos Part B Eng 2013;45:1199–206. doi:10.1016/J.COMPOSITESB.2012.08.002.

[45] Bello A, Laredo E, Grimau M. Distribution of relaxation times from dielectric spectroscopy using Monte Carlo simulated annealing: Application to-PVDF. n.d.

[46] Murugaraj P, Mainwaring D, Mora-Huertas N. Dielectric enhancement in polymer-nanoparticle composites through interphase polarizability. J Appl Phys 2005;98:54304. doi:10.1063/1.2034654.

[47] Tuncer E, Serdyuk YV, Gubanski SM. Dielectric mixtures: electrical properties and modeling. IEEE Trans Dielectr Electr Insul 2002;9:809–28. doi:10.1109/TDEI.2002.1038664.

[48] Yoon D-H, Zhang J, Lee BI. Dielectric constant and mixing model of BaTiO3 composite thick films. Mater Res Bull 2003;38:765–72. doi:10.1016/S0025-5408(03)00075-8.

[49] Prateek, Thakur VK, Gupta RK. Recent Progress on Ferroelectric Polymer-Based Nanocomposites for High Energy Density Capacitors: Synthesis, Dielectric Properties, and Future Aspects. Chem Rev 2016;116:4260–317. doi:10.1021/acs.chemrev.5b00495.

[50] Levy O, Stroud D. Maxwell Garnett theory for mixtures of anisotropic inclusions: Application to conducting polymers. Phys Rev B - Condens Matter Mater Phys 1997;56:8035–46. doi:10.1103/PhysRevB.56.8035.

[51] Vo HT, Todd M, Shi FG, Shapiro AA, Edwards M. Towards model-based engineering of underfill materials: CTE modeling. Microelectronics J 2001;32:331–8. doi:10.1016/S0026-2692(00)00152-X.

[52] Feng Y, Li WL, Hou YF, Yu Y, Cao WP, Zhang TD, et al. Enhanced dielectric properties of PVDF-HFP/BaTiO3-nanowire composites induced by interfacial polarization and wire-shape. J Mater Chem C 2015;3:1250–60. doi:10.1039/c4tc02183e.

[53] Zhou W, Dong L, Sui X, Wang Z, Zuo J, Cai H, et al. High dielectric permittivity and low loss in PVDF filled by core-shell Zn@ZnO particles. J Polym Res 2016;23:45. doi:10.1007/s10965-016-0941-5.

Chapter V: Synthesis and characterizations of core double shell structured nanocomposite based on Polyvinylidene fluoride-*grafted*-$BaTiO_3$/Poly(VDF-*co*-HFP) films

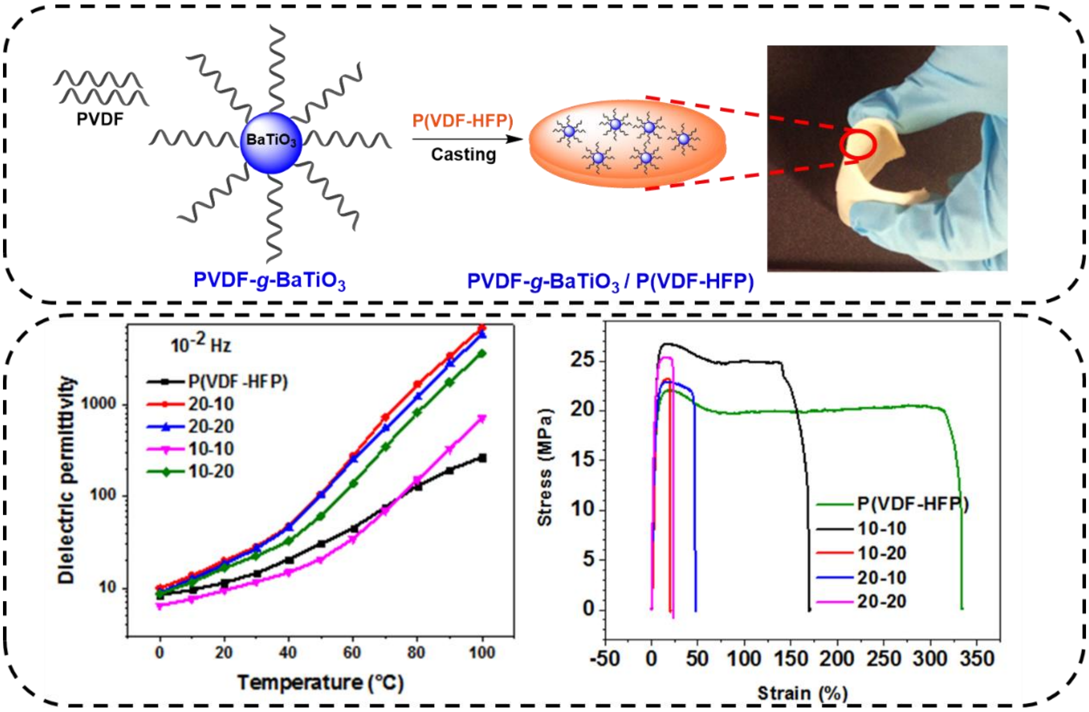

V.1. Introduction

Dielectric nanocomposites have drawn a great attention due to their wide range of applications in energy storage systems, by combining high breakdown strength, flexibility and good processability of polymers with high permittivity of oxides such as $BaTiO_3$ [1–4]. In fact, ferroelectric fluorinated polymers, such as polyvinylidene fluoride (PVDF) and its binary/ ternary copolymers such as poly(vinylidene fluoride-*co*-trifluoroethylene, P(VDF-TrFE), poly(VDF-*co*-chlorofluroethylene), P(VDF-CTFE), poly(VDF-*co*-trifluoroethylene), P(VDF-TFE), poly(VDF-*co*-hexafluoropropylene), P(VDF-HFP), and P(VDF-TrFE-CTFE), have received much attention for high-tech applications due the to the fact that they present the highest dielectric constants among all polymeric materials (ε ~ 10-12 at 1 kHz) [5–11] thanks to the strong C-F dipole moment [12].

Prateek *et al.* [13] comprehensively reviewed the use of ferroelectric PVDF binary/ ternary copolymers and $BaTiO_3$ nanoparticles as potential components in dielectric nanocomposite materials for high energy density capacitor applications.

A high filler loading of supercapacitif $BaTiO_3$ nanoparticules (*e.g.* >50 vol %) is required to achieve satisfactory dielectric constant nanocomposite due to the large permittivity difference between the filler and the polymer. Due to the large contrast of surface energy and electrical properties of nanofillers and PVDF matrix materials, they lead to the aggregation and phase separation of $BaTiO_3$ in the polymer matrix, the uneven distribution of the electrical field near the nanofiller–matrix interfaces and complicated interfacial polarization, resulting in the decrement of the energy density [14–16].

To overcome these issues, obtaining a homogeneous nanoparticle dispersion in the polymer matrix becomes a long-standing challenge in developing excellent dielectric storage materials. This can be achieved by nanoparticle surface modification and functionalization leading to enhanced filler-polymer compatibility. Actually, the surface modification could be performed either by using hydroxylation [17], phosphonic acid [18,19], dopamine [11,20] and coupling agent [21–23]. Another “interfacial modifier engineering” is the employing of flexible polymers by grafting polymers on the surface of $BaTiO_3$ and leading to core-shell nanostructured [24–26]. This step aims to chemically modify $BaTiO_3$ surface using the “grafting from”, “grafting onto” by surface initiated *in situ* controlled radical polymerization (RDRP) such as atom transfer radical polymerization (ATRP) and reversible addition-fragmentation chain transfer (RAFT), and then introducing it into PVDF based polymers as second shell to obtain the so-called core double shell system $BaTiO_3$-*g*-polymers@PVDF polymers [24–28]. Du et *al.* [26] functionalized $BaTiO_3$ surface by poly(*tert*-butyl acrylate) P(*t*BuA) using ATRP, and the obtained core-shell $BaTiO_3$-*gratfed*-P(*t*BuA) were then introduced into a PVDF matrix. The resulting nanocomposites displayed an enhancement in dielectric permittivity compared to those of PVDF films based on non-functionalized $BaTiO_3$. However, a slight enhancement in dielectric permittivity was observed, the calculated effective dielectric constants at 150 MV/m are 26.5 and 20.4 for PVDF with 30% loading of $BaTiO_3$-*g*-P(*t*BuA) and pure PVDF films, respectively. The nanocomposite films with higher than 30% loading of nanoparticles had poor mechanical strength caused by the structural imperfections due to poor interaction forces between PVDF polymers and non-fluorinated modified nanoparticles.

To overcome this disadvantage and obtain better interfacial interactions between the nanofillers and the fluoropolymer matrix, surface functionalization of $BaTiO_3$ nanoparticles with fluorinated polymers (*i.e.*, poly(2,2,2-trifluoroethyl methacrylate) [26], poly(1H,1H,2H,2H-perfluorooctyl methacrylate) [29], poly(2,2,2-trifluoroethyl acrylate) and poly(1H,1H,2H,2H-hepta decafluorodecyl acrylate) [26], poly(2,5-bis[(4-trifluoromethoxyphenyl) oxycarbonyl] styrene) [4,30], and poly(dodecfluoroheptyl methacrylate) [31] has been used to enhance the interface of fluorinated modifiers/PVDF-based polymers using a blending solution. On the other hand, the polymer shells were robust grafted onto the fluorinated surface of the nanoparticles, either providing strong interchain forces with PVDF based polymers. For example, Zhang et *al.* [25] also investigated the effect of the two-fluorinated shell interactions on the final properties of the obtained nanocomposites. The system consists first on grafting either poly(methyl methacrylate) (PMMA) or poly(2,2,2-trifluoroethyl methacrylate) (PTFEMA) onto $BaTiO_3$ using ATRP polymerization, followed by their incorporation into PVDF matrix by a solution blending method. In fact, in both systems, an improvement in dielectric permittivity was observed. However, when the fluorinated polymer (PTFEMA) was used to functionalize the nanoparticles, high dielectric constants and low dielectric losses were obtained as compared to the system where the nanoparticles were modified by PMMA, and this improvement was explained by the strong interaction forces between the two-fluorinated shell matrix. In contrast to core-shell $BaTiO_3$-*grafted*-poly(fluorinated (meth)acrylates) reported before, Ma et *al.* [32] prepared a core double shell nanocomposite using two different polymers. In a first step, $BaTiO_3$ was surface functionalized using either polystyrene or PVDF by a thiol-ene reaction (Grafting onto). Then, a second shell of PVDF was introduced by a simple casting and hot pressing. The results revealed that when $BaTiO_3$ was functionalized with PVDF, it leads to significant positive influence on the improvement of dielectric constant and vanishing of dielectric loss of the resulting nanocomposite compared to those prepared using core-shell $BaTiO_3$-*g*-PS. In fact, 15% increase in dielectric constant is observed in PVDF-*g*- BT/PVDF as compared to PS-*g*- BT/PVDF at 30% filler loading, which is due to the fact that the shell of the fillers has the same structure as that of the host polymer matrix. Recently, our team have recently used the *in-situ* RAFT polymerization of VDF to modify $BaTiO_3$ nanoparticles to improve the interfacial compatibility with fluorinated polymers [33].

More recently, we had published a review related to the core-double shell $BaTIO_3$-*g*-Polymers/PVDF based (co) and (ter) polymers [34]. The most double shell fluoropolymer studied is PVDF. However, PVDF exhibits major disadvantages such as high melting temperatures, which generate energetic costs to enable the processing of this polymer and poor solubility in common organic solvents [12]. To overcome these limitations, copolymerization of VDF is the most general and powerful method to perform effective systematic changes in polymer properties, and is widely used in the production of commercial fluorinated copolymers. We choose to used P(VDF-HFP) ferroelectric copolymer in this study. P(VDF-HFP) is widely used in different applications such as coatings, back sheets of photovoltaics and particularly in Lithium-ion batteries as polymer electrolyte or membrane polymer due to the high crystallinity of the PVDF, the good mechanical stability and the high ionic conductivity of the HFP [5–10]. Its low permittivity (6-8) compared to PVDF and some copolymers and terpolymers limits its application as insulating material. In addition few work was reported in developing core double shell of BT-*g*-fluorinated polymer with P(VDF-HFP) [26].

This work deals with a core double shell system prepared using PVDF-g-$BaTiO_3$ as the filler and P(VDF-HFP) as the polymer matrix. The core-shell structured PVDF-g-$BaTiO_3$ nanocomposites were synthesized via using RAFT polymerization of VDF reported [33]. Then, the resulted nanocomposites were introduced into P(VDF-HFP) copolymer matrix by solution blending method. The merit of this method is that the insulating fluoropolymer shells (PVDF-g-BT) have similar chemical structure and surface energy with P(VDF-HFP) matrix, which not only could enhance the dispersion of BT nanoparticles but also could improve the interfacial adhesion between the nanoparticles and fluoropolymer matrix in comparison to non-fluorinated modified $BaTiO_3$ nanoparticles, and therefore improve the dielectric permittivity of P(VDF-HFP) matrix [25]. In addition, SEC analysis of grafted PVDF in modified BT indicated lower molar masses ($6500<\overline{M_n}<7500$ g. mol^{-1}) [33] with poor film-forming properties (brittle materials). The films obtained by casting with commercially P(VDF-HFP) copolymer in the double core-shell nanocomposites were mechanically stable, such properties are required in developing nanocomposites films by molding technique for energy capacitor devices. The obtained films PVDF-*g*-BaTiO$_3$/P(VDF-HFP) were then fully characterized by FT-IR, TGA, DSC and SEM. The mechanical and the dielectric properties were examined and the effect of the percentage of PVDF-*g*-BaTiO$_3$ nanocomposites on the properties of the films was also investigated.

V.2 Materials

This study deals with a core double shell system prepared using PVDF-*g*-BaTiO$_3$ as the filler and P(VDF-HFP) as the polymer matrix. The PVDF-*g*-BaTiO$_3$ nanocomposites were synthesized using RAFT polymerization of VDF according to Chapter III. Then, the resulted nanocomposites were introduced into commercially available Poly(VDF-*co*-HFP) copolymer matrix by solution blending (Scheme 6, Chapter II). The obtained films were fully characterized by FT-IR, TGA, DSC and SEM. The mechanical and the dielectric properties were examined and the effect of the percentage of PVDF-*g*-BaTiO$_3$ nanocomposites on the properties of the films was also investigated. Table 1 summarizes the nomenclature of the samples.

Table 8. Nomenclature of different core-double shells PVDF-g-BT x% /P(VDF-HFP) (X/Y).

Samples PVDF-*g*-BT x% /P(VDF-HFP) (X/Y)	**Code x-X**	**x= m_{BT}/m_{VDF} weight ratio in core-shell PVDF-*g*-BT x%**[*]	**X/Y weight ratio $m_{PVDF\text{-}g\text{-}BT\ x\%}/m_{P(VDF\text{-}HFP)}$ in Core-double shell**
PVDF-*g*-BT 10% /P(VDF-HFP) (10/90)	10-10	10	10/90
PVDF-*g*-BT 10% /P(VDF-HFP) (20/80)	10-20	10	20/80
PVDF-*g*-BT 20% /P(VDF-HFP) (10/90)	20-10	20	10/90
PVDF-*g*-BT 20% /P(VDF-HFP) (20/80)	20-20	20	20/80

[*] x% = weight ratio used during RAFT polymerization for VDF for the preparation of Core-shell PVDF-*g*-BT x% [33].

V.3. Results and discussion

V.3.1. FT-IR spectra analysis

FT-IR spectra of pristine P(VDF-HFP) copolymer, 10-10, 10-20, 20-10 and 20-20 nanocomposite films are represented in Figure 1. The band around 1062 cm^{-1} corresponds to symmetrical stretching mode of CF_2. The peak shown at 1170 and 1400 cm^{-1} corresponds to -C-F- scissoring and bending vibrations of vinyl group, respectively [5–7,35]. FTIR spectrum (Figure.1b) of P(VDF-HFP) shows also the characteristic peaks at 762, 794 and 972 cm^{-1} corresponding to α phase, while peak at 835 cm^{-1} is assigned to the β phase structure [5–7,35]. The amorphous phase of P(VDF-HFP) is observed at 876 cm^{-1}. After introduction of PVDF-*g*-BT core-shell with lower loading (10-20 wt %) into the P(VDF-HFP) matrix, the detected peaks for α phase structure (762, 794 and 972 cm^{-1}) was suppressed in the composite samples. This indicates that the introduction of fillers into the P(VDF-HFP) matrix induced α phase transformation to β phase. These observations confirm Kumar et *al.*'s study [36], who prepared nanocomposite films based on graphene oxide embedded within P(VDF-HFP) matrix through solution casting method and their FTIR spectra showed also the disappearance of the characteristic peaks of the α phase structure in the nanocomposite. Indeed, P(VDF-HFP) bands 1400, 1170, 1069 and 876 cm^{-1} are shifted slightly to 1402, 1170, 1071 and 875 cm^{-1} in the composite samples. This shifting of peaks in PVDF-*g*-BT/P(VDF-HFP) composite materials also revealed the polymer PVDF- P(VDF-HFP) interaction in composite system.

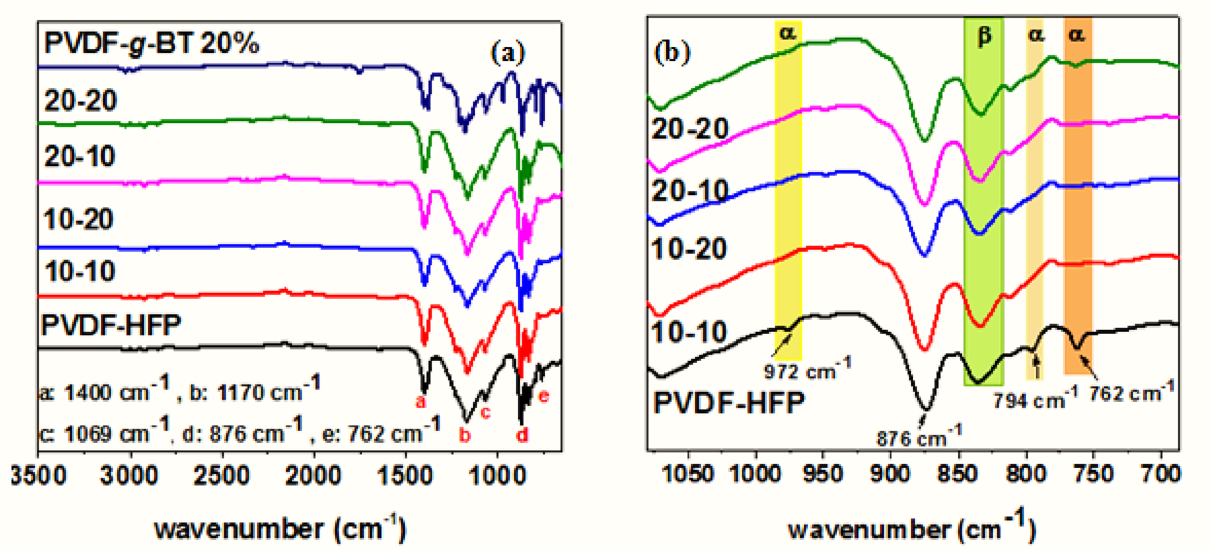

Figure 1. FT-IR spectra of (a) P(VDF-HFP) copolymer and 10-10, 10-20, 20-10 and 20-20 nanocomposite films made by solution blending method and (b) Expansion of the 650-1070 cm^{-1} zone of the FT-IR spectra.

V.3.2. Scanning electron microscopy (SEM)

The morphology of the films was studied using scanning electron microscopy (SEM) and energy dispersive spectroscopy mapping technique. Actually, the morphology of the casted films depends strongly on the drying conditions during the preparation [6,37]. Tian *et al.* [37] prepared a P(VDF-HFP) membrane material by dissolving P(VDF-HFP) pellets in a solvent under two different conditions. The membranes dried at atmosphere exhibit a porous structure, while those dried at 60 °C under vacuum were dense, indicating the huge influence of the drying procedure on the morphology of the membranes. In the present study, the drying procedure was performed at 120 °C under vacuum and the obtained films were dense. Figure 2 displays cross-section morphologies of pristine P(VDF-HFP) copolymer and the corresponding core double shell PVDF-*g*-BT/P(VDF-HFP) nanocomposite films. Numerous nanoparticle fillers are shown in the polymer. For all the samples, it can be clearly observed that the PVDF-*g*-BT nanocomposites are well embedded inside the P(VDF-HFP) copolymer. Moreover, no clear agglomeration or voids and defects could be found in the films, suggesting that the grafted PVDF polymer shell can increase the interface adhesion between the BT nanoparticles and P(VDF-HFP) matrix and excellent dispersion of the PVDF-*g*-BT nanoparticles. Similar results were reported by Qian *et al.* [30], Ma et *al.* [32] and Jiang *et al.*[38], who had studied the morphology of BT-*g*-fluorinated styrenes/P(VDF-TFE-CTFE) nanocomposites, core-double shells PVDF-*g*-BT/PVDF and P(VDF-HFP) composites with core-structured Fe_2O_3@BT nanofillers, respectively.

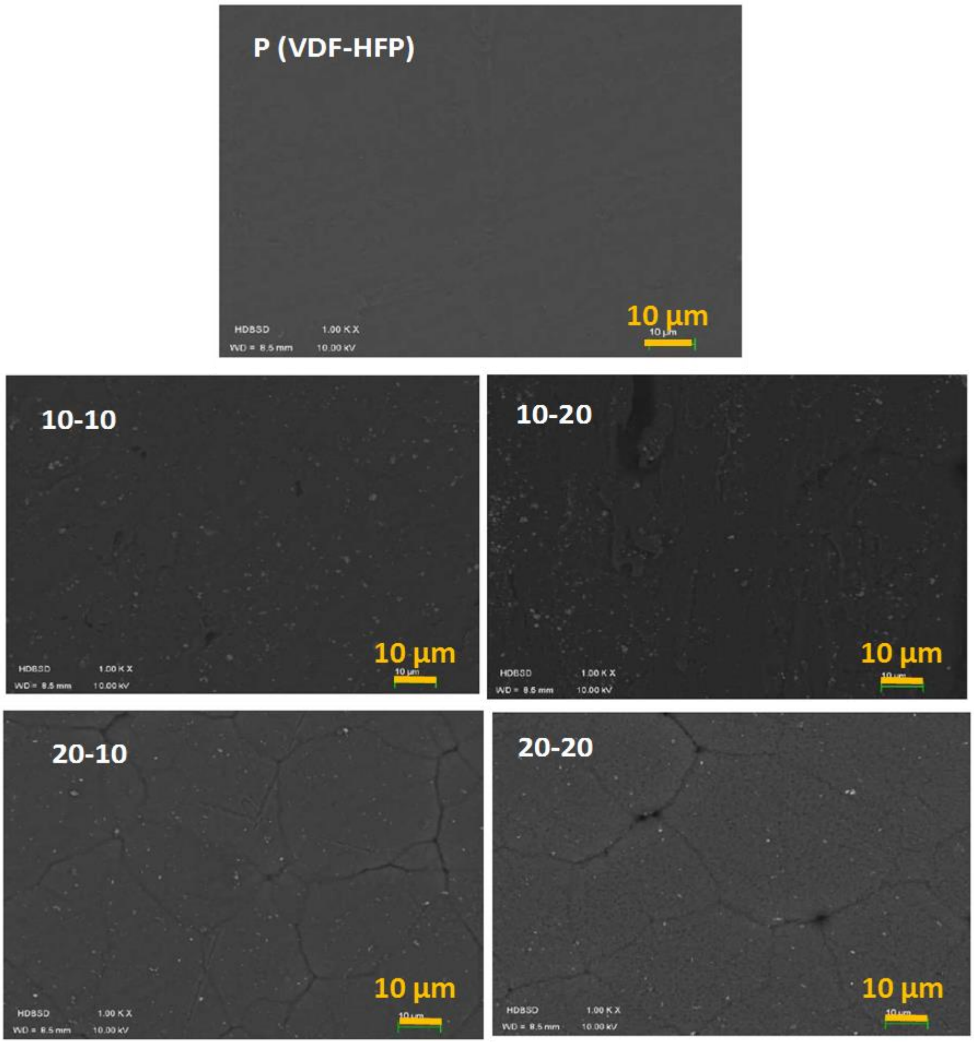

Figure 2. Scanning electronic microscopy of pristine P(VDF-HFP) copolymer and the resulting core double shell nanocomposite films.

Moreover, the spatial distribution of the elements nanoparticles was investigated by energy dispersive mapping technique. Figure 3 shows for example the elemental mapping of the film 10-10 (PVDF-*g*-BT 10% @ P(VDF-HFP) (10/90)). The color in the picture suggested that the sample contained Ba, Ti, C, O and F elements, which are the constituent elements of the core double shell nanocomposite films. In addition, the elements Ba, Ti and O show also the dispersion of BT modified nanoparticles.

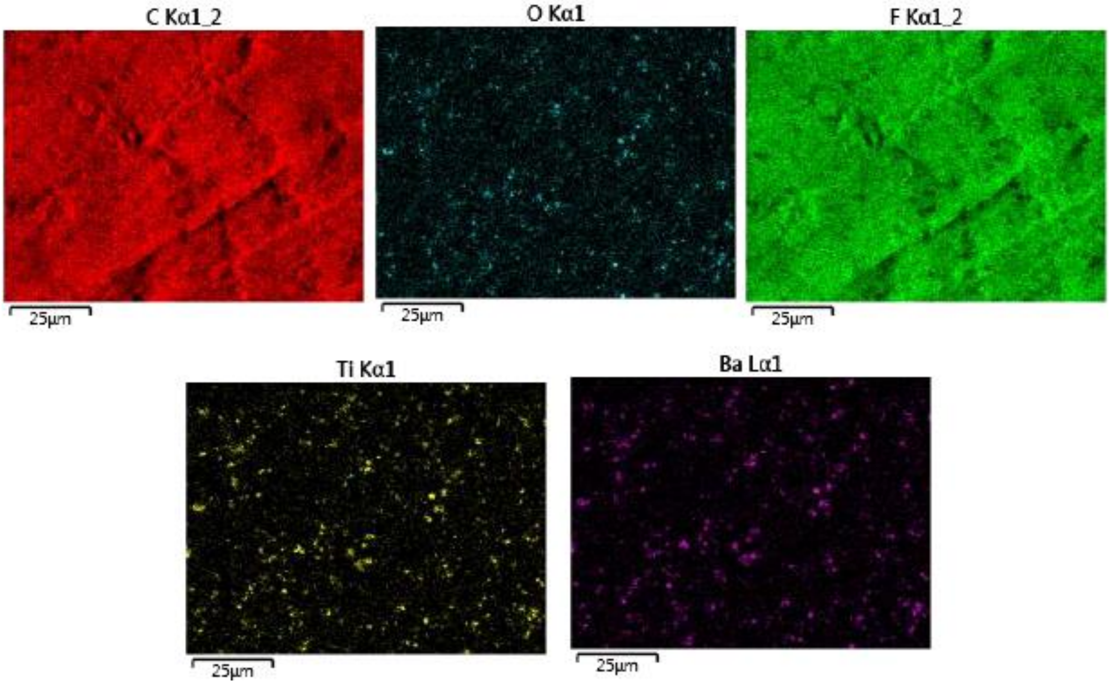

Figure 3. Energy dispersive spectroscopy elemental mapping of core double shell nanocomposite film (10-10: PVDF-*g*-BT 10% @ P(VDF-HFP) (10/90)) for C, O, F, Ti and Ba.

V.3.3. Thermogravimetric analysis (TGA)

The thermal stabilities of pristine P(VDF-HFP) copolymer and nanocomposite films were studied under air by TGA and the resulting thermograms are depicted in Figure 4. Table 2 summarizes the starting degradation temperature (T_d) and the weight losses at 650 °C.

The pristine P(VDF-HFP) copolymer degrades from 446 °C reaching 99.9 % weight loss at 650 °C. Under similar conditions, the starting degradation temperature of the PVDF-*g*-BT/P(VDF-HFP) increased to 459, 460, 462 and 464 °C for the films made from 10-10, 10-20, 20-10 and 20-20 nanocomposites, respectively. The introduction even with a small amount of the PVDF-*g*-BT modified nanoparticles (10 to 20 wt%) was found to enhance the thermal stability of the core-double shell nanocomposites, an improvement of thermal stability, with an increase of 13-18 °C in $T_{d,}$ was observed compared to pristine P(VDF-HFP). On the other hand, introduction of a well-dispersed PVDF-*g*-BT core-shell into P(VDF-HFP) matrix can improve their thermal stability as the dispersed nanoparticles hinder the permeability of volatile degradation products out of the materials, and thus the modified BT generates a barrier effect, which delays the release of thermal degradation products in comparison to the pure polymer. Indeed, with the same percentage of P(VDF-HFP) in the nanocomposites (*e.g.*, 10-10 and 20-10 samples), the increase of the decomposition temperatures was noticed for the PVDF-*g*-BT filled with a higher $BaTiO_3$ content (20 wt%) than those with lower percentage (10 %wt), and may be attributed to the better dispersion and the high loading of nanofiller. As reported by our team [32], the starting degradation temperature, T_d, of PVDF-*g*-BT10% and PVDF-g-BT20% close to 407 and 415 °C, respectively.

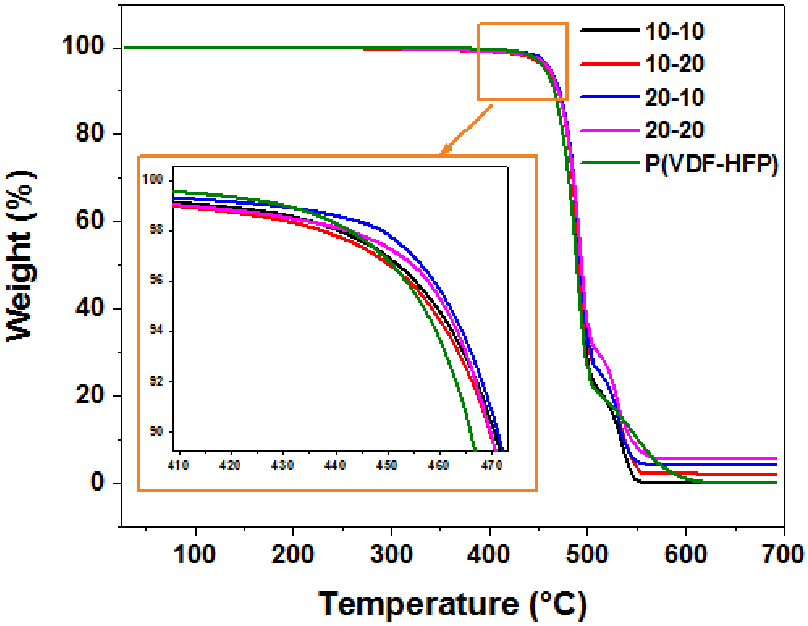

Figure 4. TGA thermograms (under air) of P(VDF-HFP) copolymer and 10-10, 10-20, 20-10 and 20-20 nanocomposite films made by solution blending method.

Table 2. Decomposition temperatures and weight losses at 650 °C of pristine P(VDF-HFP) and the prepared nanocomposite films.

Samples	*T_d (1) (°C)*	*Weight loss (%) at 650 °C*
P(VDF-HFP)	446	99.9
10-10	459	99.9
10-20	460	97.8
20-10	462	95.7
20-20	464	94.4

(1) *T_d: starting degradation temperature.*

V.3.4. Differential Scanning Calorimetry (DSC)

Differential scanning calorimetry (DSC) was used to study the influence of PVDF-*g*-BT nanocomposites concentration on the degree of crystallinity and melting temperature of the prepared nanocomposite films. Figure 5 exhibits the heating and cooling DSC thermograms of the samples, while the enthalpy (ΔH_m), crystallization temperature (T_c), melting temperature (T_m) and crystallinity (χ) of each sample are summarized in Table 2.

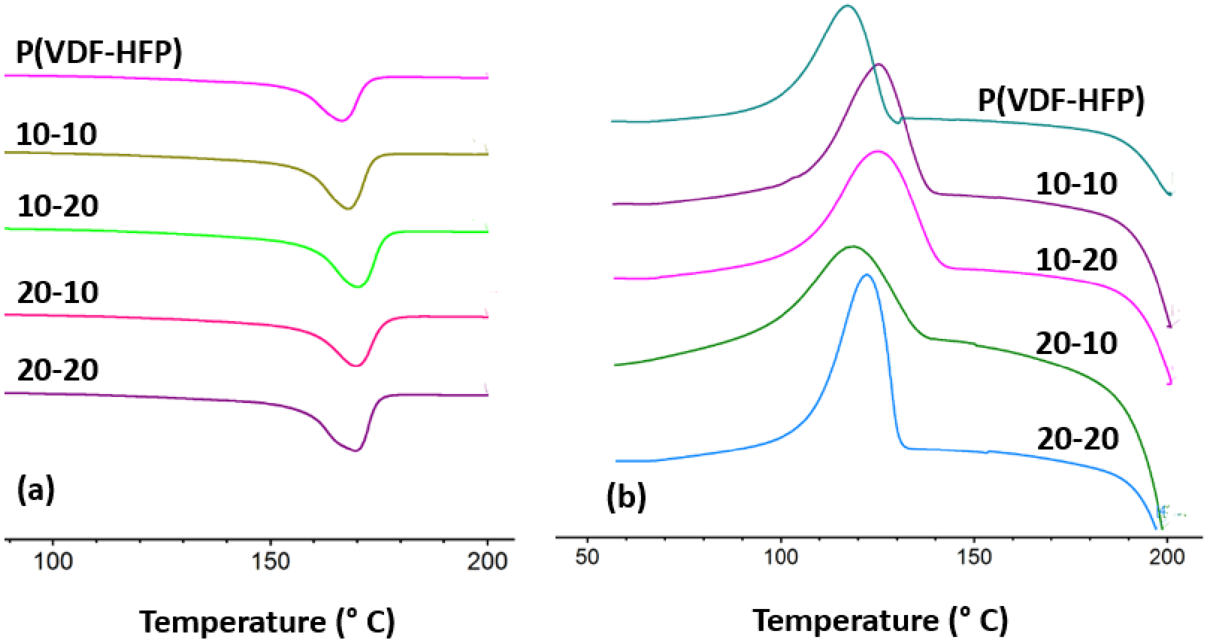

Figure 5. DSC thermograms of pristine P(VDF-HFP) copolymer and 10-10, 10-20, 20-10 and 20-20 nanocomposite films: (a) heating process and (b) cooling process.

From Figure 5a, one endothermic melting peak only is observed for each film. As expected, T_m of pristine P(VDF-HFP) is 167 °C, since the low HFP amount of 3 % mol decreased the melting temperature of the copolymer from 170 °C for PVDF to 167 °C for P(VDF-HFP) [39]. The melting enthalpy was found to increase from 19 J/g for the pristine P(VDF-HFP) copolymer to 22 and 26 J/g after introducing 10 wt % and 20 wt % of PVDF-*g*-BT filled with 20 wt % of $BaTiO_3$, respectively. On the other hand, the crystallization temperature of the P(VDF-HFP) was found to be 117 °C (Figure 5b) and increased to 125 °C after introducing 10-10 nanocomposite. This indicates that the introduction of PVDF-*g*-BT organomodified nanofillers to P(VDF-HFP) matrix induced an increase in crystallization temperature. Moreover, the crystallinity of the films increased from 18 % for the pristine copolymer and reaches 25 % after adding 20 wt % of PVDF-*g*-BT filled with 20 wt % of $BaTiO_3$, suggesting that the PVDF-*g*-BT core-shell nanofiller offers plenty of heterogeneous nucleation sites to P(VDF-HFP) matrix leading to an increased crystallinity [40]. In fact, the increase of melting and crystallization temperatures after introducing fillers into P(VDF-HFP) matrix has been seen in previous works [27,40,41]. For instance, Zhang *et al.*[40] prepared core shell structured $BaTiO_3$@polyalinine nanoparticles embedded into P(VDF-HFP) matrix, and observed an increase in T_c. They explain that behavior by two factors: (i) the introduction of nanofillers into P(VDF-HFP) matrix offers several nucleation sites, and (ii) the fillers could also hinder the movement of P(VDF-HFP) chains and thus retarding the crystallization process.

Table 3. Enthalpy (ΔH_m), crystallization temperature (Tc), melting temperature (Tm) and crystallinity (χ) of P(VDF-HFP) copolymer and its nanocomposite films.

Samples	***P(VDF-HFP)***	***10-10***	***10-20***	***20-10***	***20-20***
ΔH_m ***(J/g)***	19	23	24	22	26
T_c ***(° C)***	117	125	125	119	122
T_m ***(° C)***	167	168	170	170	170
χ ***(%)***	18	22	23	21	25

V.3.5. Dielectric properties

The molecular dynamics of P(VDF-HFP) copolymer matrix and its nanocomposites core-double shell prepared by a solution blending of PVDF-*g*-BT (10 or 20 wt % of BT) nanofillers and P(VDF-HFP) copolymer matrix have been investigated by broadband dielectric spectroscopy (BDS) as a function of temperature and frequencies. The measured of the resulting impedance gives access to dielectric permittivity, dielectric loss, electrical modulus and electrical conductivity values [42].

V.3.5.1. Dielectric properties of P(VDF-HFP) matrix

The relaxation behavior of P(VDF-HFP) is shown in Fig. 6 in which the dielectric permittivity (ε') and dissipation factor (tan δ) as a function of temperature and frequency were reported.

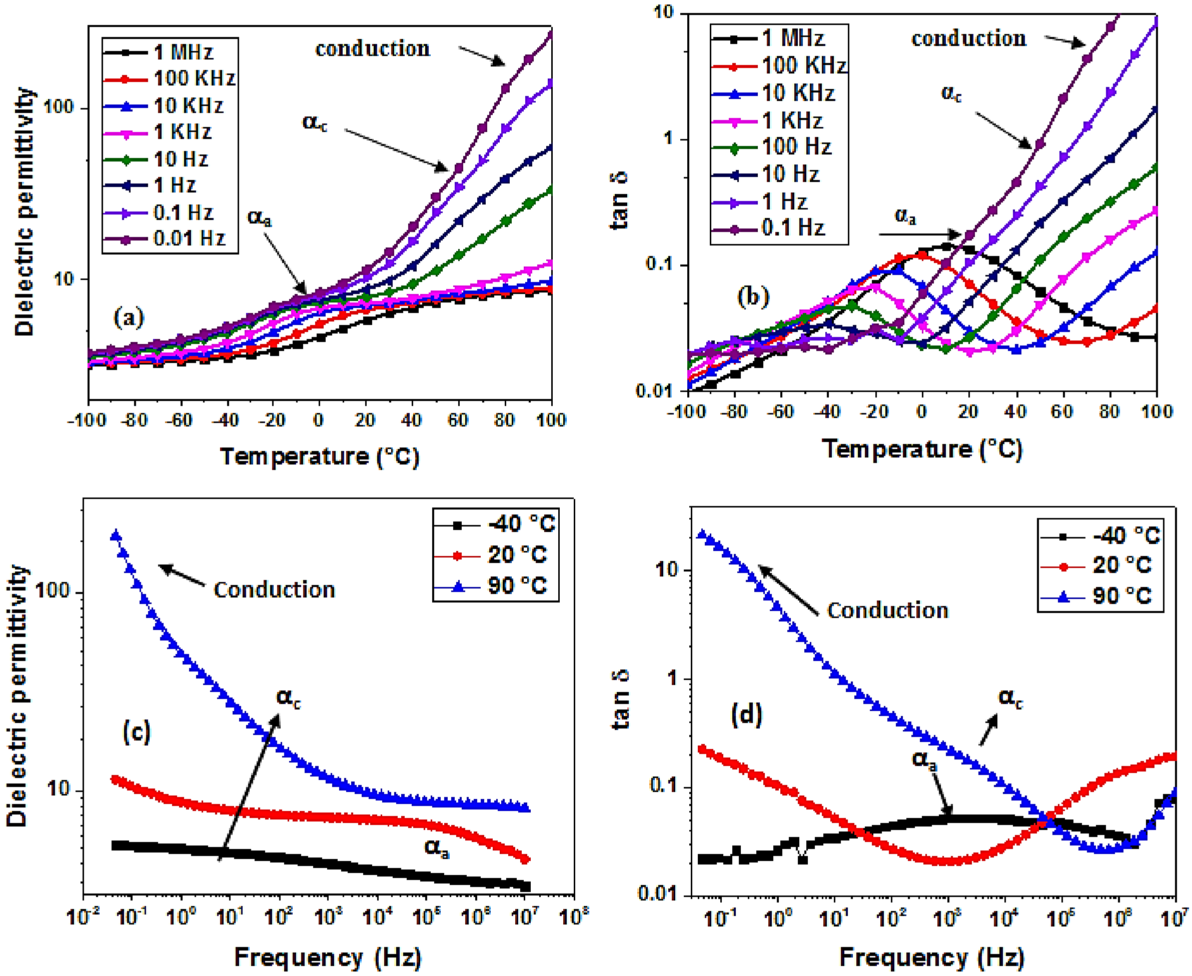

Figure 6. Dielectric permittivity (ε′) and loss tangent (tan δ) of P(VDF-HFP) versus temperature at different frequencies (a, b) and versus frequency at selected temperatures (c, d).

Two relaxation peaks are observed for P(VDF-HFP) which appear around and above the glass transition temperature (T_g, ca. -36 °C, the data from Arkema corporation) (Figs 6a-b). The α_a relaxation, due to segmental motions in the amorphous phase [43], appears in the temperatures range from -40 °C to about 0 °C and is defined as the primary or glass-rubber relaxation [43]. From a dipolar point of view, it results from large-range dipole relaxation motions due to microbrownian segmental motion of polymer chain. Under temperatures around the glass transition temperature of P(VDF-HFP), the dipoles have enough mobility to realign to electric field and contribute to the increase of permittivity (Fig 6a). At low frequencies, the real part of permittivity ε′ presents an inflection associated with α_c relaxation, as shown by arrows in Figure 6a. This α_c relaxation, associated with relaxations within the crystalline phase in P(VDF-HFP), occurs above 0 °C until 40 °C [43,44]. Additionally, in low frequency part of tan δ (Fig. 6d), the characteristic contribution of dc conductivity, σ_{dc}

(reciprocal of frequency), due to the drift of ionic impurities is responsible for the upturn of the low frequency isochronal tan δ scan at high temperature can be observed (*i.e.* tan δ =10.5 at 90 °C and 0.1 Hz, Fig. 6d). This conduction mechanism was affected by an electrode polarization (EP) which is proved by a rapid increase in the real part of the permittivity (ε'=100 at 90°C and 0.1 Hz, Fig 6c). This mechanism is related to the existence of free charge carriers (ions) which can drift under the applied electric field towards the electrode/sample interfaces where they accumulate and lead to an apparent large macroscopic polarization much greater than that taking place in the volume of the material. This conductivity contribution progressively overlaps with that of the α_c-relaxation, hindering an easy visualization of the relaxation scenario (Fig 6b-d). Fig. 6a shows that in the glassy state (below T_g), the dipolar orientation is mainly blocked. The dielectric constant values of different P(VDF-HFP) copolymer (3 mol% of HFP) are low, almost independent of both the temperature and frequency, and dominated by the high frequency permittivity ($\varepsilon'_\infty \approx 3.5$ at 10 Hz and -100 °C) that is a quite typical value for the atomic and electronic polarization [45]. Above T_g (-20 to 40 °C), the dielectric permittivity of P(VDF-HFP) increases with increasing temperature and lowering frequencies and presents a dielectric permittivity of ca. 8 at 1 kHz and room temperature which is close to that reported in literature ($\varepsilon < 10$), that depends on HFP content in the P(VDF-HFP) copolymer (Fig 6a) [46–49]. This increasing permittivity is due to the increase in segmental motions of dipole units the P(VDF-HFP) copolymer related to the α_a and α_c relaxations.

V.3.5.2. Dielectric properties of core-double shell PVDF-g-BT/P(VDF-HFP) nanocomposites

The dielectric properties of nanocomposites were measured as a function of frequency and temperature. All composites exhibit some similar tends. Figure 7 shows for example ε' and tan δ of the nanocomposite film 20-20 *versus* temperature at different frequencies (characteristic plots of samples 10-10, 10-20 and 20-10 are depicted in the Appendix II (Figure A2)).

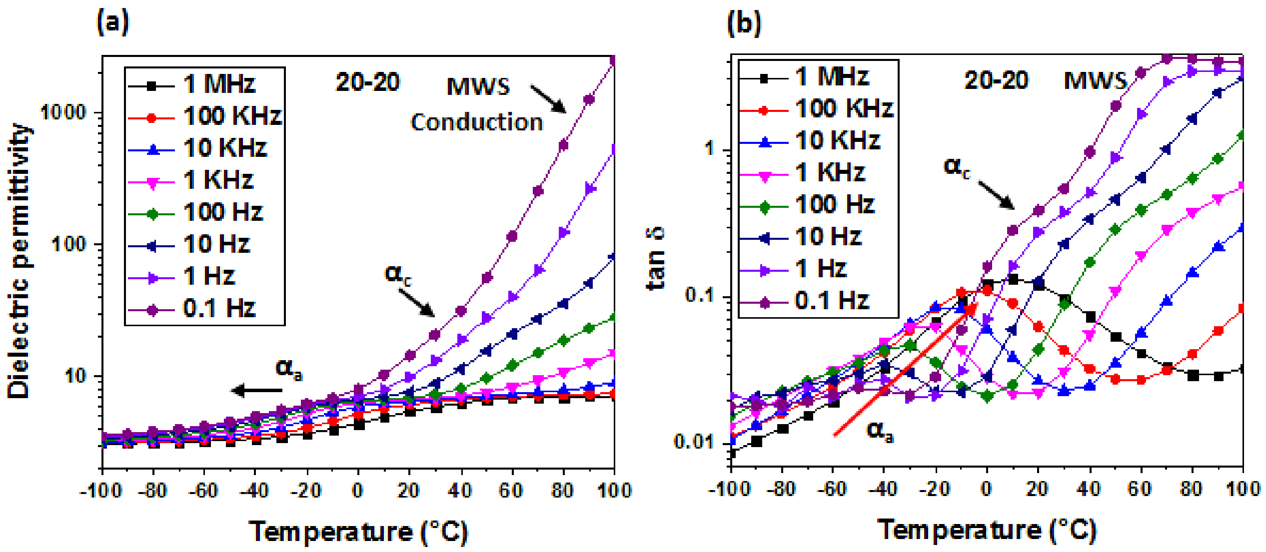

Figure 7. Dielectric permittivity, ε′, (a) and loss tangent, tan δ, (b) of nanocomposite film 20-20 versus temperature at different frequencies.

At low frequencies, the real part of permittivity ε′ presents two inflections associated with two relaxation processes, α_α around T_g (-40 - 0 °C) and α_c above T_g (0 - 60°C), as shown by arrows in Figure 7a and corresponding to the dipole relaxations of P(VDF-HFP) attributed to the amorphous and the crystalline phases of polymer matrix. Figure 7b showing the tangent loss (tan δ) *versus* temperature and frequencies. The relaxation peaks (α_α) were observed and shifted to high temperature when the frequency increases. Indeed, the tanδ presented an inflexion point corresponding to α_c relaxation which is hidden by the conductivity contribution (EP) and also the interfacial relaxation (MWS) at high temperature and lower frequency. This phenomenon is responsible of very high ε′ values at high temperature and low frequency (*i.e.* ε′= 1000 at 0.1 Hz and 90 °C, Fig 7a).

In Figure 8, selected representative isothermal spectra recorder for ε′ and tan δ of the nanocomposite film 20-20 are shown. Figure A3 (Appendix II) shows those corresponding to the 10-10, 10-2 and 20-10 nanocomposite films. Figure 8 shows the relaxations and conduction phenomena observed at selected isothermal temperatures -20 °C, 40 °C and 90 °C below and above T_g and confirmed the results obtained in at Figure 7.

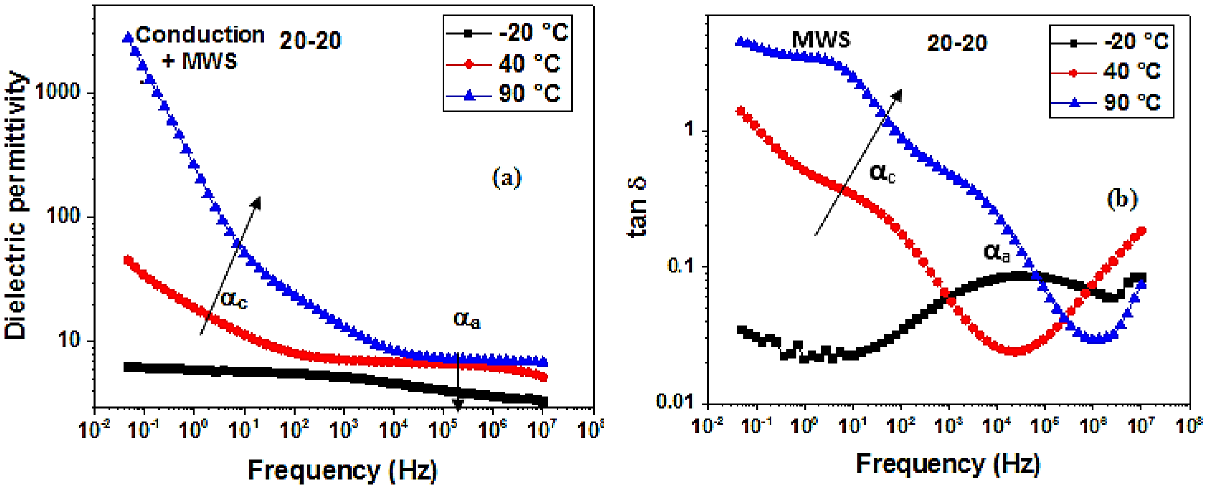

Figure 8. Dielectric permittivity, ε′, (a) and loss tangent, tan δ, (b) of nanocomposite film 20-20 versus frequency at -20 °C, 40 °C and 90 °C.

The electrode polarization is active in the lower frequency range and responsible for very high ε′ values, a phenomenon clearly observable for the higher temperature Isotherm (90 °C). At higher frequencies the same isotherms present a plateau, followed by a drop of ε′ (Figure 8a). On the other hand, and by increasing the frequency, dielectric permittivity decreased and this is due to the rotational motion of the polar segment, which cannot keep up with the external electric field [49]. While at 90 °C the plateau is broad and centered at 200 kHz, well within the region free from the electrode polarization, at lower temperatures the same plateau shifts to lower frequencies and a second step of ε′ with frequency is indicative of the presence of α_c relaxation, as discussed in the case of the reference P(VDF-HFP) polymer. At -20 °C the α_c relaxation occur at frequencies too low to be observed when the α_a relaxation was observed at high frequency. A more detailed picture can be obtained from a plot of tan δ (f, T) against the frequency, as shown in Figure 8 b. The contributions of α_a and α_c relaxations, respectively, are indicated by the arrows and shift at lower frequencies on cooling but with different temperature dependence; as a consequence, they tend to merge on approaching the glass transition temperature.

Indeed, the rapid increase of dielectric permittivity at 90 °C is associated to the enhanced interfacial polarization effect (MSW) overlapped by conduction which acts mainly in low frequency range because it takes longer time to polarize than other kind of polarizations [40]. Figure 8b shows also at low frequency and high temperature MWS polarization (T = 90 °C). This phenomenon can be explained by the large difference in electrical conductivity between the nanofillers and copolymer matrix, which leads to an accumulation of charge carriers at the interface of the different constituent of the nanocomposite film causing a large polarization and thus a high dielectric constant [50].

Figure 9 displays the frequency dependence of dielectric permittivity and dielectric loss tangent for the pristine P(VDF-HFP) copolymer and the core@double shell structured nanocomposites recorded at 20 °C.

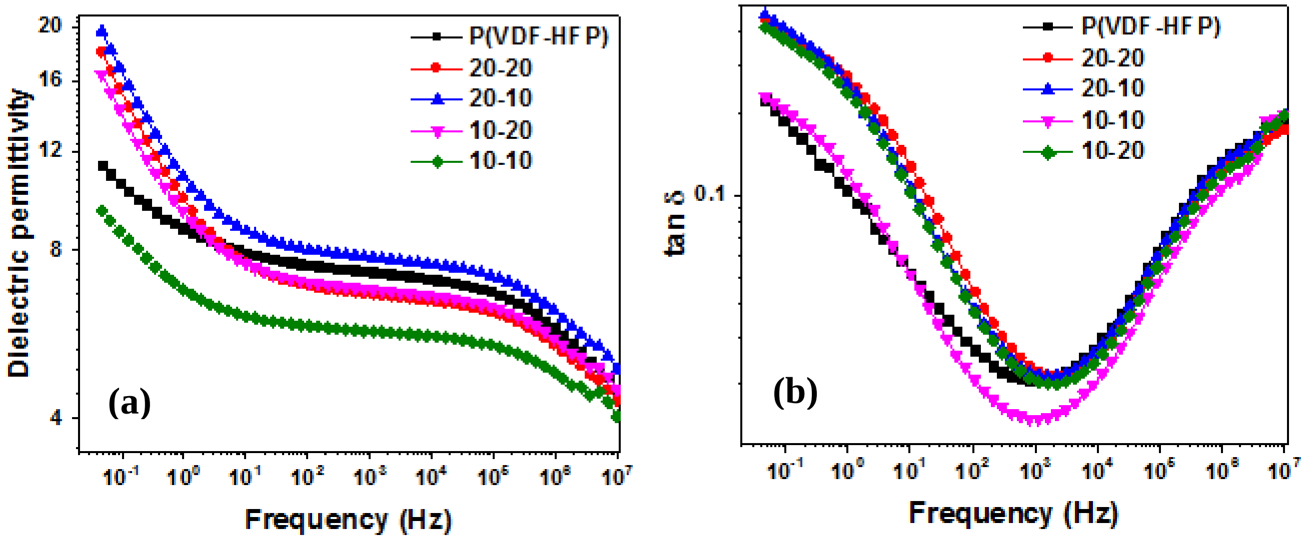

Figure 9. Frequency dependence of (a) dielectric permittivity and (b) dielectric loss tangent for the pristine P(VDF-HFP) copolymer and the core@double shell structured nanocomposites recorded at 20 °C.

Moreover, it was also found that the dielectric permittivity increases by increasing temperature for all samples as depicted in Figure 9. For example, and at 1 Hz and 60 °C, the dielectric permittivity increased from 20 for P(VDF-HFP) to 40 for 20-10 nanocomposite [PVDF-*g*-BT 20%/P(VDF-HFP)(10/90)]. This rapid increase of dielectric constant with different temperatures is related to the enhanced interfacial polarization effect, where the charges are accumulated at the interface of heterogeneous systems [51,52].

However, the results did not show clearly regularity as a function of volume fraction of the loaded nanocomposites. In fact, similar trends were observed in previous works [53–55]. For instance, Khodaparast *et al.* [53] prepared nanocomposites consisting of three different nanoparticles namely titania, silica and alumina embedded within PVDF matrix using a solution blending and casting method. These authors showed that even the fillers exhibit a high dielectric permittivity than that of the PVDF, the resulting nanocomposite could displays a dielectric constant lower than that of the pure polymer. They emphasized also the fact that the chemistry and the interactions between the fillers and the PVDF could be more important than dielectric permittivity of the filler in determining the dielectric permittivity of the resulting nanocomposite.

The rapid increase of permittivity at low frequencies is due to the electrode polarization and the effect of this latter can completely hinder the low frequency relaxations (Figures 6,7 and 8) [56]. To overcome this issue, McCrum *et al.*[57–60] have introduced the electric modulus formalism that suppresses the effect of electrode polarization, which can be expressed by the following equation (2):

$$M^* = \frac{1}{\varepsilon^*} = M' + jM'' = \frac{\varepsilon'}{\varepsilon'^2 + \varepsilon''^2} + j\,\frac{\varepsilon''}{\varepsilon'^2 + \varepsilon''^2} \qquad (2)$$

where M' and M" are the real and the imaginary parts of electric modulus, respectively, ε'and ε" are the real and the imaginary part of dielectric constant. The imaginary part of the electric modulus (Modulus"), which takes the form of loss curves, is usually adopted to interpret the bulk relaxation properties [50]. Figure A4 (Appendix II) presents the dielectric loss modulus (Modulus") of P(VDF-HFP) and for the nanocomposite films (10-10) as a function of frequency and in the range of temperature from 0 to 100 °C which the α_c and MSW relaxations were observed. It can be seen that in contrast to P(VDF-HFP) copolymer which exhibits two relaxation peaks, the nanocomposite films revealed a third relaxation process that can be attributed to interfacial polarization or Maxwell Wagner Sillars (MWS) polarization [61,62], that is associated with the accumulation of free charges generated at the interfaces between the fillers and the polymer shells [63].

Figure 10 shows M" *versus* frequency at selected temperature (-20 °C, 40 °C and 90 °C) around and above T_g for P(VDF-HFP) matrix and the corresponding nanocomposite 20-20 as example. Indeed, Figure A5 (Appendix II) displays the M" *versus* frequency at different range temperatures of 20-20 nanocomposite film. These figures confirm the dynamic molecular mobility of the matrix and the corresponding nanocomposites as reported above in terms of permittivity and tan δ. Figure 11 represents the comparison of M" of P(VDF-HFP) and their nanocomposites versus frequency at 20 °C and 90 °C and show both the relaxation in crystalline phase and MSW interfaciale polarization between the organomodified BT (PVDF-g-BT) and P(VDF-HFP)

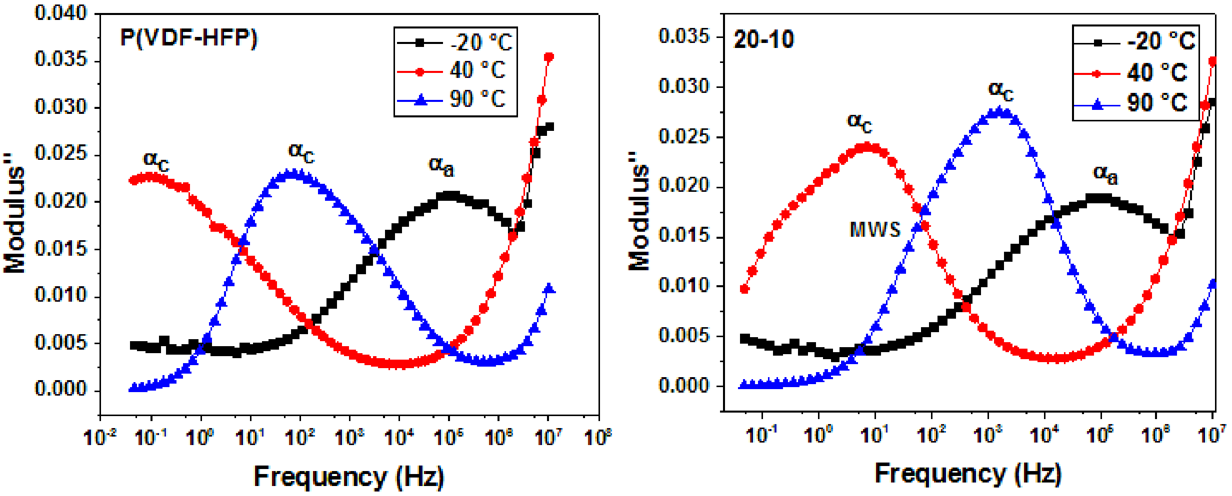

Figure 10. M" versus frequency at selected temperature (-20 °C, 40 °C and 90 °C for P(VDF-HFP) matrix ((left) and the corresponding nanocomposite 20-20 (right).

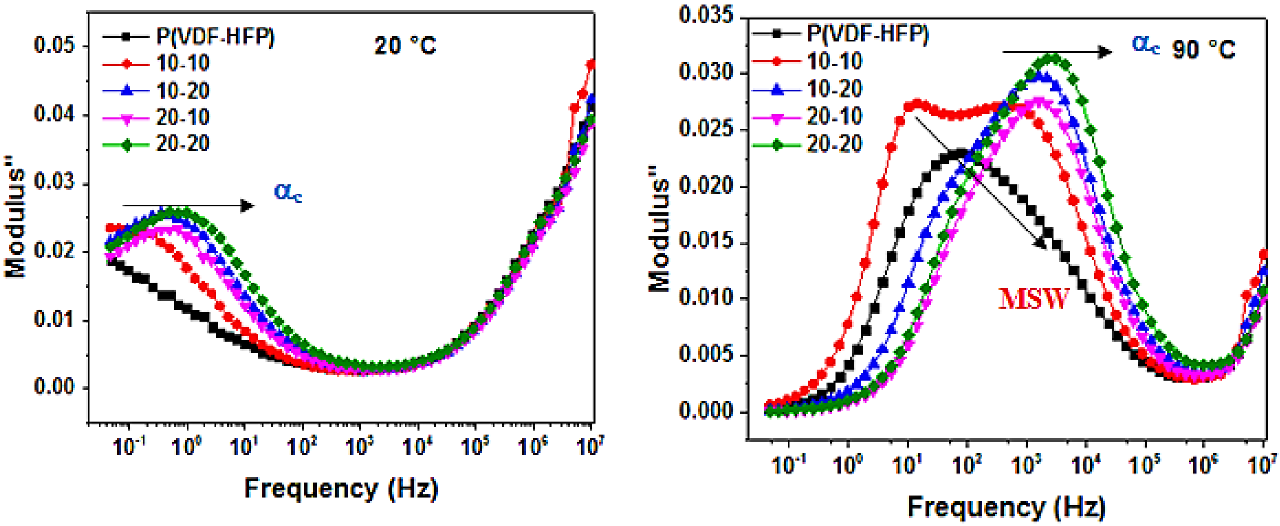

Figure 11. M" versus frequency for P(VDF-HFP) matrix and the corresponding nanocomposite films at selected temperature 20 °C (left) and 90 °C (right).

In order to analyze quantitatively the dielectric relaxations, the Havriliak-Negami (HN) function is used:

$$\varepsilon^*(f) = \Sigma\left[\frac{\Delta\varepsilon}{\left(1+\left(i\frac{f}{f_0}\right)^{\alpha}\right)^{\beta}}\right] \qquad (3)$$

where $\Delta\varepsilon$ is dielectric relaxation strength defined as $\Delta\varepsilon = \varepsilon_s - \varepsilon_\infty$ (ε_s and ε_∞ are the low- and the high-frequency limits of the real part of dielectric permittivity), α and β ($\alpha \geq 0$

and $\beta \leq 1$) are the parameters describing asymmetry and distribution width of relaxation times, respectively [44]. Table 3 summarizes the parameters of HN at T=20 °C where the α_c is the relaxation of these samples. We noticed that the increment dielectric ($\Delta\varepsilon$), related to the relaxation phenomena responsible for the increasing permittivity, is higher in the nanocomposites compared to the pristine P(VDF-HFP) matrix. Indeed, $\Delta\varepsilon$ increases when the % of PVDF-g-BT is high.

Table 4. HN parameters at T=20 °C for pure P(VDF-HFP) and its corresponding nanocomposite films.

Samples	***Log f_0***	***$\Delta\varepsilon$***	***α***	***β***
P(VDF-HFP)	-1.09	1.2	0.88	0.86
10-10	-1.92	9.0	0.69	0.62
10-20	-2.22	43.0	0.49	0.98
20-10	-2.20	50.3	0.57	0.81
20-20	-2.07	45.5	0.49	-

For more details about the α_a relaxation, we have selected the data tested at lower temperatures and made a fitting on dielectric loss *vs* log of frequency using equation 3 for all the samples. Figure 12 exhibits the logarithmic frequency (log fmax) as a function of inverse of temperature (1000/T).

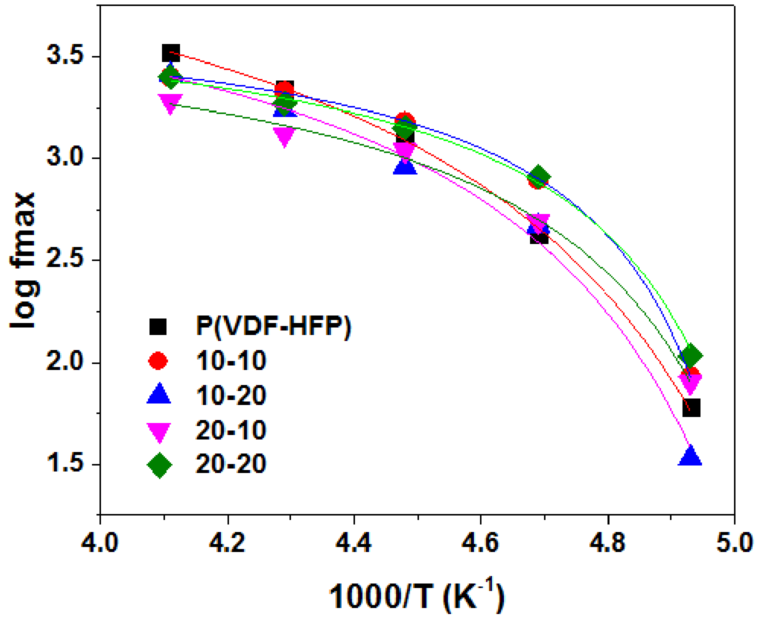

Figure 12. Variation of the logarithmic frequency versus the inverse of temperature for pristine P(VDF-HFP) copolymer and its corresponding nanocomposite films for α_a (VFT behavior).

It is observed that the corresponding relaxations were described by a Volgel-Fulcher-Tammann (VFT) equation:

$$f = f_0 \exp\left(\frac{-B}{T - T_v}\right) \qquad (4)$$

where f_0 and B are the fit parameters and T_v is the Vogel temperature, which is approximately 50 °C lower than the glass-transition temperature (T_g) [44]. Hence, that fitting enables to deduce such parameters and values in equation 4. The detailed calculated activation parameters for the observed relaxation processes are listed in Table 4.

Table 5. The relevant parameters obtained from fitting using equation 4.

Samples	***P(VDF-HFP)***	***10-10***	***10-20***	***20-10***	***20-20***
log f_0	4.5	4	4	4	4
B (K)	132	37	71	53	37
T_g (° C)	-42	-29	-33	-33	-30

BDS is an interesting tool to determinate the T_g of the samples from the figure12 ($T=T_g$ when τ=100s) which is not easy to calculate from the DSC thermograms. It can be seen that the pristine P(VDF-HFP) copolymer exhibits a glass transition temperature of -42 °C, and this value increases to -30 °C after introducing the nanocomposite films. This can be explained by two factors: i) after the introduction of PVDF-*g*-BT nanocomposites within the P(VDF-HFP) copolymer matrix, an overlapping of the immobile polymer regions around the fillers occurs and ii) the existence of the Rigid Amorphous Phase (RAP), which is the interphase between the crystalline and amorphous phases in the copolymer, leading to an increase in glass transition of the polymer [64–66]. In fact, Parodi *et al*. [67] investigated the influence of thermal history of polyamide 6 on glass transition and clearly demonstrated that a high content of the RAP in the polymer leads to an increase in T_g.

The Arrhenius relation describes the temperature dependence of the α_c and MWS relaxation times for the different samples (Figure 13):

$$lnf_{max} = lnf_0 - \frac{E_a}{RT} \qquad (5)$$

Where E_a is the activation energy for the relaxation process, R is the gas constant and T is the absolute temperature. Table 5 summarizes the activation energies obtained from the fits of each curve.

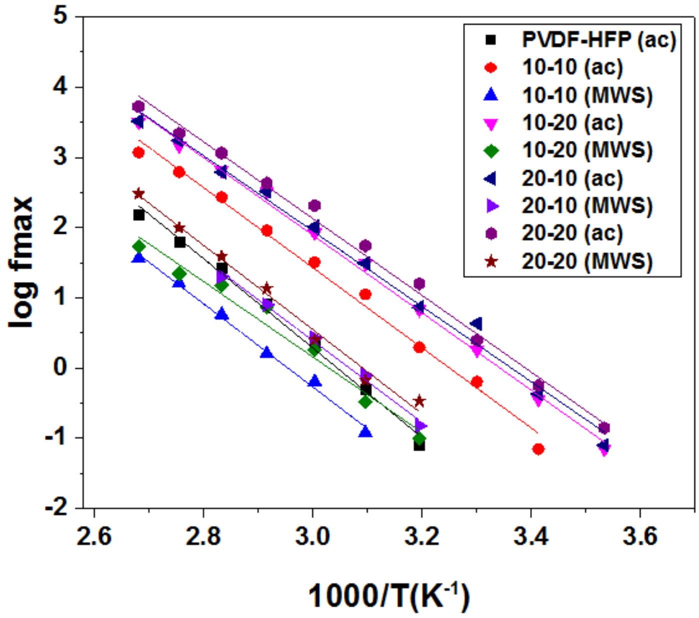

Figure 13. Variation of the logarithmic frequency versus the inverse of temperature for pristine P(VDF-HFP) copolymer and its corresponding nanocomposite films (VFT behavior).

Table 6.Arrhenius parameters of α_c and MWS relaxations.

Samples	***Log f_0***		***E (kJ.mol^{-1})***		***R-squares***	
	α_c	**MWS**	**α_c**	**MWS**	**αc**	**MWS**
P(VDF-HFP)	19.37	-	53.4	-	0.99	-
10-10	18.54	17.79	47.4	49.2	0.99	0.99
10-20	18.44	16.26	45.8	44.5	0.99	0.97
20-10	18.04	17.86	44.5	48.3	0.99	0.99
20-20	18.52	18.53	45.4	49.8	0.99	0.99

It was of interest to determine the conductivity of pristine P(VDF-HFP) and its corresponding nanocomposite films (Figure 14). The conductivity values can be deduced from equation 6:

$$\sigma = \varepsilon'' 2\pi \, \varepsilon_0 f \qquad (6)$$

where ε'', ε_0, and f stand for the loss factor, permittivity of free space and the frequency (Hz), respectively.

It can be clearly noted that the conductivity increases with the increase of frequency for the pristine copolymer as well as for its corresponding nanocomposite films. Moreover, the incorporation of PVDF-*g*-BT nanocomposites as fillers within the P(VDF-HFP) copolymer leads to a slight increase of conductivity at low frequency regions and becomes almost the same for high frequencies, which indicates the good insulating properties of the resulting nanocomposite films. Similar trends were observed previously [38,68]. For instance, Feng *et al.* [68] incorporated $BaTiO_3$ into P(VDF-HFP) matrix and investigated the dependence of electrical conductivity on the frequency at room temperature. It was found that the conductivity of the resulting nanocomposites shows a strong dependence on frequency because of their insulating properties.

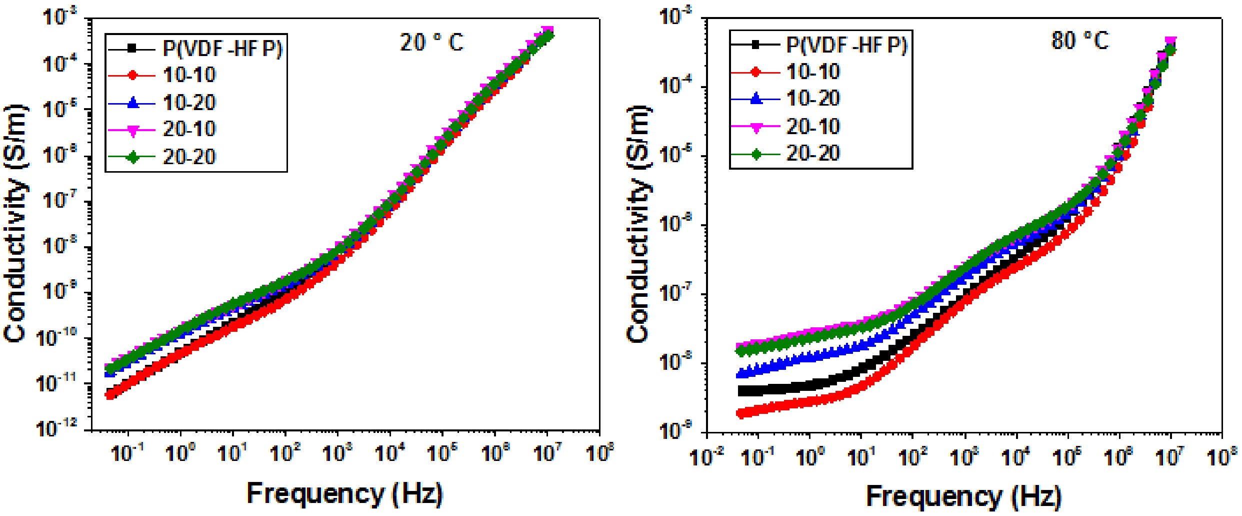

Figure 14. Frequency dependence of conductivity for P(VDF-HFP) copolymer and its corresponding nanocomposite films at 20 °C and 80 °C.

V.3.4. Mechanical properties

In order to investigate the mechanical properties of the nanocomposite films, uniaxial tensile tests were conducted on five samples. Figure 15 exhibits the strain=f(stress) curve of the pristine P(VDF-HFP) copolymer and of the prepared nanocomposite films. The samples exhibit a ductile behavior, which is more pronounced in the case of the pristine copolymer and becomes less important for the nanocomposite films.

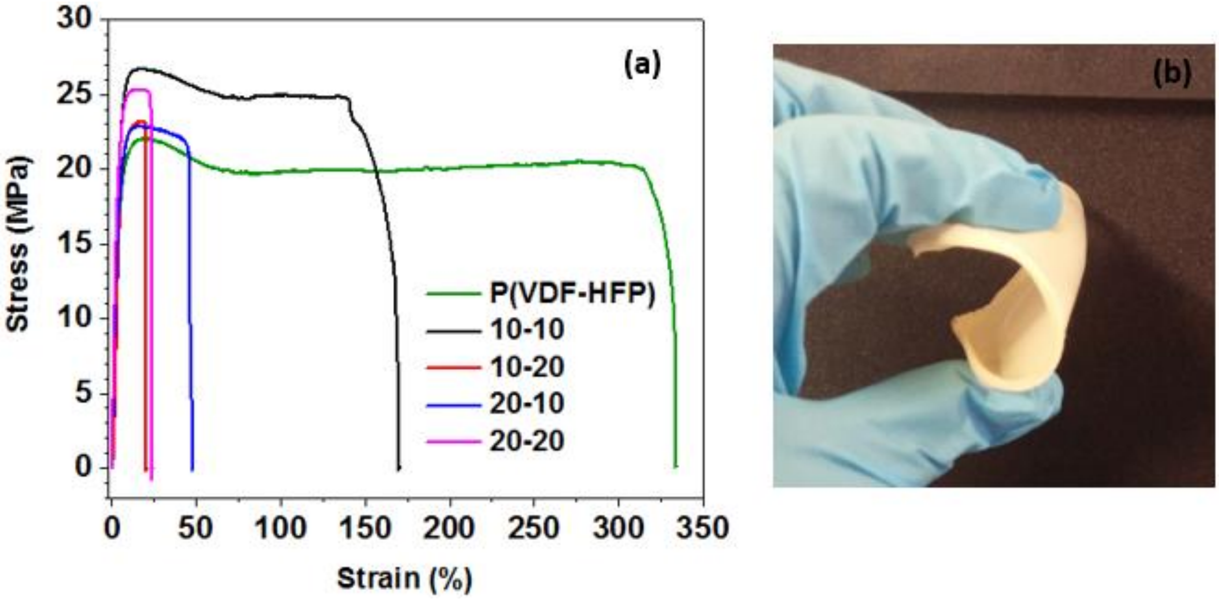

Figure 15. (a)Typical stress-strain curve of pristine P(VDF-HFP) copolymer and PVDF-*g*-BT@P(VDF-HFP) nanocomposite films and (b) Photograph showing the flexibility of the prepared nanocomposite films.

During the tests, four readings per sample were performed, which enable to determine the relevant parameters characterizing the mechanical performances of the resulting films. The Young's modulus together with the tensile strength are depicted in Figure 16.

The P(VDF-HFP) copolymer exhibit a tensile strength of 22 MPa with an elongation at break value of 507 %. While after adding 10 wt % of PVDF-g-BT nanocomposites filled with 10 wt % of $BaTiO_3$, the elongation at break decreased to 107 % with a tensile strength of 24 MPa. As compared to the pristine copolymer, the decrease in the elongation at break of the nanocomposite films is obvious and expected [69–72].

On the other hand, it was found that the Young's modulus of such materials follows the decreasing order 20-20 > 10-10 > 10-20> 20-10 > P(VDF-HFP). Indeed, the addition of PVDF-*g*-BT nanocomposites to P(VDF-HFP) matrix increased the stiffness of the resulting films. This is in a good agreement with Ponnamma *et al.*'s results [48] who prepared P(VDF-HFP) nanocomposites containing $BaTiO_3$ and hexagonal boron nitride by casting method. The mechanical measurements revealed an enhancement in both Young's modulus and tensile strength of the prepared nanocomposites as compared to the P(VDF-HFP) copolymer and a decrease of the elongation at break. The same behavior was reported by Tarhini *et al*. [73] who embedded graphene nanoflakes into P(VDF-HFP) matrix, and noted an enhancement of Young's modulus for nanocomposite films as compared to the pristine copolymer film. This improvement can be explained by the fact that the introduction of nanoparticles restricted the segmental movements of P(VDF-HFP) chains and also the uniform distribution of nanofillers having strong bonding with the matrix.

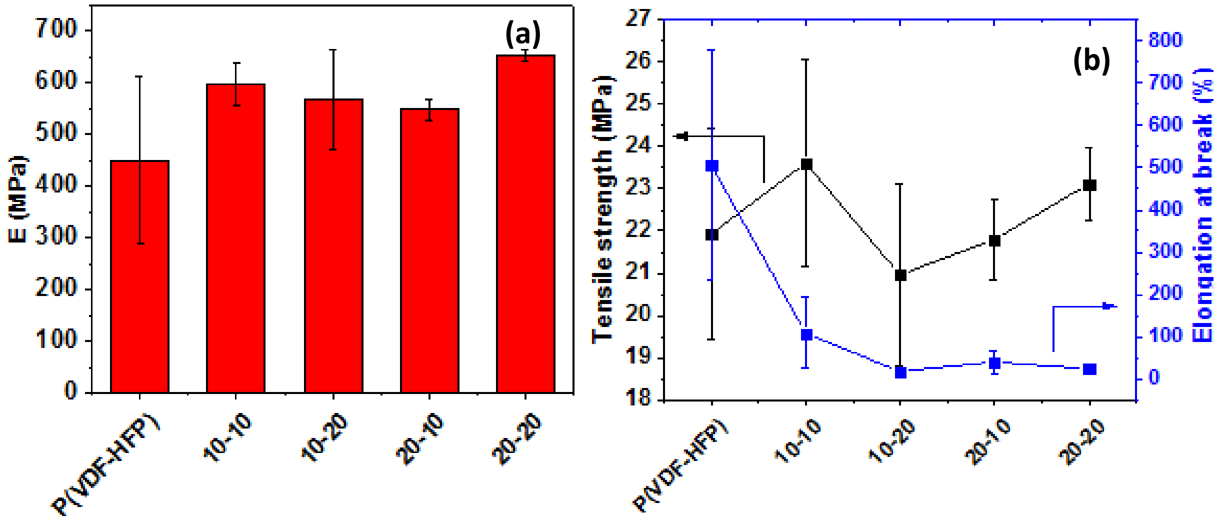

Figure 16. (a) Young's modulus and (b) Tensile strength with elongation at break for pristine P(VDF-HFP) copolymer and PVDF-*g*-BT@P(VDF-HFP) nanocomposite films.

V.5. Conclusion

A series of PVDF-*g*-BT@P(VDF-HFP) nanocomposite films were prepared using a solution blending method from pristine P(VDF-HFP) copolymer and PVDF-*g*-BT nanofillers. The resulting films were fully characterized with FT-IR, TGA, DSC and SEM. These analyses enabled to prove the successful introduction and the good dispersion of PVDF-*g*-BT nanocomposites within the P(VDF-HFP) matrix and also the enhancement of thermal properties of the system. The dielectric measurements showed that the addition of PVDF-*g*-BT nanocomposites to the copolymer matrix increased the dielectric permittivity of the films reaching 250 (at 60 °C and 10^{-2} Hz) which is more than five times the dielectric permittivity of the pristine P(VDF-HFP) at the same temperature and frequency. Moreover, mechanical analysis showed an enhancement in Young’s modulus and tensile strength of the prepared nanocomposite films as compared to the pristine copolymer, resulting in increased stiffness of the films. Thanks to the interesting properties shown by this nanocomposite films, they could find application as membranes or even binders in lithium-ion batteries.

V.6. References

[1] Z. Yao, Z. Song, H. Hao, Z. Yu, M. Cao, S. Zhang, M.T. Lanagan, H. Liu, Homogeneous/Inhomogeneous-Structured Dielectrics and their Energy-Storage Performances, Adv. Mater. 29 (2017) 1601727. https://doi.org/10.1002/adma.201601727.

[2] X. Huang, P. Jiang, Core-Shell Structured High-k Polymer Nanocomposites for Energy Storage and Dielectric Applications, Adv. Mater. 27 (2015) 546–554. https://doi.org/10.1002/adma.201401310.

[3] Q. Li, K. Han, M.R. Gadinski, G. Zhang, Q. Wang, High Energy and Power Density Capacitors from Solution-Processed Ternary Ferroelectric Polymer Nanocomposites, Adv. Mater. 26 (2014) 6244–6249. https://doi.org/10.1002/adma.201402106.

[4] S. Chen, X. Lv, X. Han, H. Luo, C.R. Bowen, D. Zhang, Significantly improved energy density of BaTiO3 nanocomposites by accurate interfacial tailoring using a novel rigid-fluoro-polymer, Polym. Chem. 9 (2018) 548–557. https://doi.org/10.1039/C7PY01914A.

[5] Z. He, Q. Cao, B. Jing, X. Wang, Y. Deng, Gel electrolytes based on poly(vinylidenefluoride-co-hexafluoropropylene)/thermoplastic polyurethane/poly(methyl methacrylate) with in situ SiO2 for polymer lithium batteries, RSC Adv. 7 (2017) 3240–3248. https://doi.org/10.1039/C6RA25062A.

[6] U. ur Rehman Farooqui, A. Latif Ahmad, N. Abdul Hameed, Influence of Solvent and Thickness Variation on the Performance of Poly(Vinylidene Fluoride-co-hexafluoropropylene) Polymer Membrane, J. Phys. Sci. 29 (2018) 125–132. https://doi.org/10.21315/jps2018.29.s1.16.

[7] A.L. Ahmad, U.R. Farooqui, N.A. Hamid, Effect of graphene oxide (GO) on Poly(vinylidene fluoride-hexafluoropropylene) (PVDF- HFP) polymer electrolyte membrane, Polymer (Guildf). 142 (2018) 330–336. https://doi.org/10.1016/J.POLYMER.2018.03.052.

[8] J. Yu, W. Wu, D. Dai, Y. Song, C. Li, N. Jiang, Crystal structure transformation and dielectric properties of polymer composites incorporating zinc oxide nanorods, Macromol. Res. 22 (2014) 19–25. https://doi.org/10.1007/s13233-014-2009-x.

[9] P. Martins, A.C. Lopes, S. Lanceros-Mendez, Electroactive phases of poly(vinylidene fluoride): Determination, processing and applications, Prog. Polym. Sci. 39 (2014) 683–706. https://doi.org/10.1016/J.PROGPOLYMSCI.2013.07.006.

[10] J.T. Goldbach, R. Amin-Sanayei, W. He, J. Henry, W. Kosar, A. Lefebvre, G. O’Brien, D. Vaessen, K. Wood, S. Zerafati, Chapter 6: Commercial Synthesis and Applications of Poly(Vinylidene Fluoride), in: RSC Polym. Chem. Ser., Royal Society of Chemistry, 2017: pp. 127–157. https://doi.org/10.1039/9781782629368-00127.

[11] Y. Song, Y. Shen, H. Liu, Y. Lin, M. Li, C.-W. Nan, Improving the dielectric constants and breakdown strength of polymer composites: effects of the shape of the BaTiO3 nanoinclusions, surface modification and polymer matrix, J. Mater. Chem. 22 (2012) 16491. https://doi.org/10.1039/c2jm32579a.

[12] B. Ameduri, From Vinylidene Fluoride (VDF) to the Applications of VDF-Containing Polymers and Copolymers: Recent Developments and Future Trends, Chem. Rev. 109 (2009) 6632–6686. https://doi.org/10.1021/cr800187m.

[13] Prateek, V.K. Thakur, R.K. Gupta, Recent Progress on Ferroelectric Polymer-Based Nanocomposites for High Energy Density Capacitors: Synthesis, Dielectric Properties, and Future Aspects, Chem. Rev. 116 (2016) 4260–4317. https://doi.org/10.1021/acs.chemrev.5b00495.

[14] Y. Song, Y. Shen, H. Liu, Y. Lin, M. Li, C.-W. Nan, Improving the dielectric constants and breakdown strength of polymer composites: effects of the shape of the BaTiO3 nanoinclusions, surface modification and polymer matrix, J. Mater. Chem. 22 (2012) 16491.

https://doi.org/10.1039/c2jm32579a.

[15] K. Yang, X. Huang, L. Fang, J. He, P. Jiang, Fluoro-polymer functionalized graphene for flexible ferroelectric polymer-based high-k nanocomposites with suppressed dielectric loss and low percolation threshold, Nanoscale. 6 (2014) 14740–14753. https://doi.org/10.1039/C4NR03957B.

[16] N. Guo, S.A. DiBenedetto, P. Tewari, M.T. Lanagan, M.A. Ratner, T.J. Marks, Nanoparticle, Size, Shape, and Interfacial Effects on Leakage Current Density, Permittivity, and Breakdown Strength of Metal Oxide−Polyolefin Nanocomposites: Experiment and Theory, Chem. Mater. 22 (2010) 1567–1578. https://doi.org/10.1021/cm902852h.

[17] T. Zhou, J.-W. Zha, R.-Y. Cui, B.-H. Fan, J.-K. Yuan, Z.-M. Dang, Improving Dielectric Properties of BaTiO3/Ferroelectric Polymer Composites by Employing Surface Hydroxylated BaTiO3 Nanoparticles, ACS Appl. Mater. Interfaces. 3 (2011) 2184–2188. https://doi.org/10.1021/am200492q.

[18] B.P. Kim, S.C. Jones, P.J. Hotchkiss, J.N. Haddock, B. Kippelen, S.R. Marder, J.W. Perry, Phosphonic Acid-Modified Barium Titanate Polymer Nanocomposites with High Permittivity and Dielectric Strength, Adv. Mater. 19 (2007) 1001–1005. https://doi.org/10.1002/adma.200602422.

[19] P. Kim, N.M. Doss, J.P. Tillotson, P.J. Hotchkiss, M.-J. Pan, S.R. Marder, J. Li, J.P. Calame, J.W. Perry, High Energy Density Nanocomposites Based on Surface-Modified BaTiO3 and a Ferroelectric Polymer, ACS Nano. 3 (2009) 2581–2592. https://doi.org/10.1021/nn9006412.

[20] J. Defebvin, S. Barrau, J. Lyskawa, P. Woisel, J.-M. Lefebvre, Influence of nitrodopamine-functionalized barium titanate content on the piezoelectric response of poly(vinylidene fluoride) based polymer-ceramic composites, Compos. Sci. Technol. 147 (2017) 16–21. https://doi.org/10.1016/j.compscitech.2017.05.001.

[21] C. Guo, M. Fuji, Effect of silicone coupling agent on dielectric properties of barium titanate/silicone elastomer composites, Adv. Powder Technol. 27 (2016) 1162–1172. https://doi.org/10.1016/J.APT.2016.03.028.

[22] S. Liu, S. Xue, W. Zhang, J. Zhai, Enhanced dielectric and energy storage density induced by surface-modi fi ed BaTiO 3 nano fi bers in poly (vinylidene fl uoride) nanocomposites, 40 (2014) 15633–15640. https://doi.org/10.1016/j.ceramint.2014.07.083.

[23] S. Dalle Vacche, F. Oliveira, Y. Leterrier, V. Michaud, D. Damjanovic, J.-A.E. Månson, Effect of silane coupling agent on the morphology, structure, and properties of poly(vinylidene fluoride–trifluoroethylene)/BaTiO3 composites, J. Mater. Sci. 49 (2014) 4552–4564. https://doi.org/10.1007/s10853-014-8155-x.

[24] J. Wang, F. Guan, L. Cui, J. Pan, Q. Wang, L. Zhu, Achieving high electric energy storage in a polymer nanocomposite at low filling ratios using a highly polarizable phthalocyanine interphase, J. Polym. Sci. Part B Polym. Phys. 52 (2014) 1669–1680. https://doi.org/10.1002/polb.23554.

[25] X. Zhang, S. Zhao, F. Wang, Y. Ma, L. Wang, D. Chen, C. Zhao, W. Yang, Improving dielectric properties of BaTiO3/poly(vinylidene fluoride) composites by employing core-shell structured BaTiO3@Poly(methylmethacrylate) and BaTiO3@Poly(trifluoroethyl methacrylate) nanoparticles, Appl. Surf. Sci. 403 (2017) 71–79. https://doi.org/10.1016/j.apsusc.2017.01.121.

[26] X. Du, Y. Liu, J. Wang, H. Niu, Z. Yuan, S. Zhao, X. Zhang, R. Cao, Y. Yin, N. Li, C. Zhang, Y. Xing, W. Xu, C. Li, Improved Triboelectric Nanogenerator Output Performance through Polymer Nanocomposites Filled with Core–shell-Structured Particles, ACS Appl. Mater. Interfaces. 10 (2018) 25683–25688. https://doi.org/10.1021/acsami.8b05966.

[27] K. Yang, X. Huang, Y. Huang, L. Xie, P. Jiang, Fluoro-Polymer@BaTiO3 Hybrid Nanoparticles Prepared via RAFT Polymerization: Toward Ferroelectric Polymer

Nanocomposites with High Dielectric Constant and Low Dielectric Loss for Energy Storage Application, Chem. Mater. 25 (2013) 2327–2338. https://doi.org/10.1021/cm4010486.

[28] K. Yang, X. Huang, M. Zhu, L. Xie, T. Tanaka, P. Jiang, Combining RAFT Polymerization and Thiol–Ene Click Reaction for Core–Shell Structured Polymer@BaTiO3 Nanodielectrics with High Dielectric Constant, Low Dielectric Loss, and High Energy Storage Capability, ACS Appl. Mater. Interfaces. 6 (2014) 1812–1822. https://doi.org/10.1021/am4048267.

[29] X. Zhang, H. Chen, Y. Ma, C. Zhao, W. Yang, Preparation and dielectric properties of core–shell structural composites of poly(1H,1H,2H,2H-perfluorooctyl methacrylate)@BaTiO3 nanoparticles, Appl. Surf. Sci. 277 (2013) 121–127. https://doi.org/10.1016/J.APSUSC.2013.03.178.

[30] K. Qian, X. Lv, S. Chen, H. Luo, D. Zhang, Interfacial engineering tailoring the dielectric behavior and energy density of BaTiO3/P(VDF-TrFE-CTFE) nanocomposites by regulating a liquid-crystalline polymer modifier structure, Dalt. Trans. 47 (2018) 12759–12768. https://doi.org/10.1039/C8DT02626B.

[31] J. Zhang, J. Ma, L. Zhang, C. Zong, A. Xu, Y. Zhang, B. Geng, S. Zhang, Enhanced breakdown strength and suppressed dielectric loss of polymer nanocomposites with BaTiO3 fillers modified by fluoropolymer, RSC Adv. 10 (2020) 7065–7072. https://doi.org/10.1039/c9ra10591c.

[32] J. Ma, U. Azhar, C. Zong, Y. Zhang, A. Xu, C. Zhai, L. Zhang, S. Zhang, Core-shell structured PVDF@BT nanoparticles for dielectric materials: A novel composite to prove the dependence of dielectric properties on ferroelectric shell, Mater. Des. 164 (2019) 107556. https://doi.org/10.1016/J.MATDES.2018.107556.

[33] F.E. Bouharras, M. Raihane, G. Silly, C. Totee, B. Ameduri, Core shell structured Poly(Vinylidene Fluoride) -grafted- BaTiO3 nanocomposites prepared via Reversible Addition fragmentation chain transfer (RAFT) polymerization of VDF for high energy storage capacitors, Polym. Chem. 10 (2019) 891–904. https://doi.org/10.1039/C8PY01706A.

[34] F.E. Bouharras, M. Raihane, B. Ameduri, Recent progress on core-shell structured BaTiO3@polymer/fluorinated polymers nanocomposites for high energy storage: Synthesis, dielectric properties and applications, Prog. Mater. Sci. 113 (2020) 100670. https://doi.org/10.1016/j.pmatsci.2020.100670.

[35] A. Kelarakis, S. Hayrapetyan, S. Ansari, J. Fang, L. Estevez, E.P. Giannelis, Clay nanocomposites based on poly(vinylidene fluoride-co-hexafluoropropylene): Structure and properties, Polymer (Guildf). 51 (2010) 469–474. https://doi.org/10.1016/J.POLYMER.2009.11.057.

[36] P. Kumar, S. Yu, F. Shahzad, S.M. Hong, Y.-H. Kim, C.M. Koo, Ultrahigh electrically and thermally conductive self-aligned graphene/polymer composites using large-area reduced graphene oxides, Carbon N. Y. 101 (2016) 120–128. https://doi.org/10.1016/j.carbon.2016.01.088.

[37] X. Tian, X. Jiang, Poly(vinylidene fluoride-co-hexafluoropropene) (PVDF-HFP) membranes for ethyl acetate removal from water, J. Hazard. Mater. 153 (2008) 128–135. https://doi.org/10.1016/j.jhazmat.2007.08.029.

[38] Y. Jiang, Z. Zhang, Z. Zhou, H. Yang, Q. Zhang, Enhanced Dielectric Performance of P(VDF-HFP) Composites with Satellite-Core-Structured Fe2O3@BaTiO3 Nanofillers, Polymers (Basel). 11 (2019). https://doi.org/10.3390/polym11101541.

[39] J.M. Tarascon, A.S. Gozdz, C. Schmutz, F. Shokoohi, P.C. Warren, Performance of Bellcore's plastic rechargeable Li-ion batteries, Solid State Ionics. 86–88 (1996) 49–54. https://doi.org/10.1016/0167-2738(96)00330-X.

[40] Q. Zhang, Y. Jiang, E. Yu, H. Yang, Significantly enhanced dielectric properties of P(VDF-HFP) composite films filled with core-shell BaTiO3@PANI nanoparticles, Surf.

Coatings Technol. 358 (2019) 293–298. https://doi.org/10.1016/j.surfcoat.2018.11.056.

[41] D. Yu, N.X. Xu, L. Hu, Q.L. Zhang, H. Yang, Nanocomposites with BaTiO3-SrTiO3 hybrid fillers exhibiting enhanced dielectric behaviours and energy-storage densities, J. Mater. Chem. C. 3 (2015) 4016–4022. https://doi.org/10.1039/c4tc02972k.

[42] F. Kremer, A. (Andreas) Schönhals, Broadband Dielectric Spectroscopy, Springer Berlin Heidelberg, Berlin, 2003. http://93.174.95.29/_ads/DCE7FDA58FE208CFB20309F0A3F5B416 (accessed September 24, 2019).

[43] X. Zhao, W. Liu, X. Jiang, K. Liu, G. Peng, Z. Zhan, Exploring the relationship of dielectric relaxation behavior and discharge efficiency of P(VDF-HFP)/PMMA blends by dielectric spectroscopy, Mater. Res. Express. 3 (2016) 75304. https://doi.org/10.1088/2053-1591/3/7/075304.

[44] V. V. Kochervinskij, I.A. Malyshkina, N.P. Bessonova, S.N. Suljanov, K.A. Dembo, Effect of recrystallization on the molecular mobility of a copolymer of vinylidene fluoride and hexafluoropropylene, J. Appl. Polym. Sci. 120 (2011) 13–20. https://doi.org/10.1002/app.32993.

[45] V. Castelvetro, S. Capaccioli, M. Raihane, S. Atlas, Complex Dynamics of a Fluorinated Vinylidene Cyanide Copolymer Highlighted by Dielectric Relaxation Spectroscopy, Macromolecules. 49 (2016) 5104–5114. https://doi.org/10.1021/acs.macromol.6b00683.

[46] G. Peng, X. Zhao, Z. Zhan, S. Ci, Q. Wang, Y. Liang, M. Zhao, New crystal structure and discharge efficiency of poly(vinylidene fluoride-hexafluoropropylene)/poly(methyl methacrylate) blend films, RSC Adv. 4 (2014) 16849–16854. https://doi.org/10.1039/c3ra47462c.

[47] P. Frübing, F. Wang, M. Wegener, Relaxation processes and structural transitions in stretched films of polyvinylidene fluoride and its copolymer with hexafluoropropylene, Appl. Phys. A. 107 (2012) 603–611. https://doi.org/10.1007/s00339-012-6838-1.

[48] D. Ponnamma, M.A.A. Al-Maadeed, Influence of BaTiO3 /white graphene filler synergy on the energy harvesting performance of a piezoelectric polymer nanocomposite, Sustain. Energy Fuels. 3 (2019) 774–785. https://doi.org/10.1039/c8se00519b.

[49] Z.D. Liu, Y. Feng, W.L. Li, High dielectric constant and low loss of polymeric dielectric composites filled by carbon nanotubes adhering BaTiO3 hybrid particles, RSC Adv. 5 (2015) 29017–29021. https://doi.org/10.1039/C5RA00639B.

[50] Y. Li, X. Huang, Z. Hu, P. Jiang, S. Li, T. Tanaka, Large Dielectric Constant and High Thermal Conductivity in Poly(vinylidene fluoride)/Barium Titanate/Silicon Carbide Three-Phase Nanocomposites, ACS Appl. Mater. Interfaces. 3 (2011) 4396–4403. https://doi.org/10.1021/am2010459.

[51] X. Zhao, C. Li, T. Zhu, N. Ren, X. Han, G. Peng, Study on relaxation process of fluorinated graphite/poly(vinylidene fluoride-hexafluoropropylene) composites by dielectric relaxation spectroscopy, Mater. Res. Express. 6 (2019) 065323. https://doi.org/10.1088/2053-1591/ab1030.

[52] N. Xu, L. Hu, Q. Zhang, X. Xiao, H. Yang, E. Yu, Significantly Enhanced Dielectric Performance of Poly(vinylidene fluoride-co-hexafluoropylene)-based Composites Filled with Hierarchical Flower-like TiO2 Particles, ACS Appl. Mater. Interfaces. 7 (2015) 27373–27381. https://doi.org/10.1021/acsami.5b08987.

[53] P. Khodaparast, Z. Ounaies, On the dielectric and mechanical behavior of metal oxide-modified PVDF-based nanocomposites, in: ASME 2013 Conf. Smart Mater. Adapt. Struct. Intell. Syst. SMASIS 2013, American Society of Mechanical Engineers, 2013. https://doi.org/10.1115/SMASIS2013-3302.

[54] K. Venkata Sahithya, D. Kavitha, M. Balachandran, M. Kumar, Polymer

Nanocomposite Containing High Permittivity Nanoparticles for Energy Storage Application, 2017. http://www.ripublication.com (accessed November 21, 2019).

[55] K. Yu, Y. Bai, Y. Zhou, Y. Niu, H. Wang, K. Yu, Y. Bai, Y. Zhou, Y. Niu, H. Wang, Poly(vinylidene fluoride) polymer based nanocomposites with enhanced energy density by filling with polyacrylate elastomers and BaTiO3 nanoparticles, Appl. Phys. Lett. 104 (2014) 0–4. https://doi.org/10.1063/1.4866585.

[56] C. V. Chanmal, J.P. Jog, Dielectric relaxations in PVDF/BaTiO3 nanocomposites, Express Polym. Lett. 2 (2008) 294–301. https://doi.org/10.3144/expresspolymlett.2008.35.

[57] G.M. Tsangaris, N. Kouloumbi, S. Kyvelidis, Interfacial relaxation phenomena in particulate composites of epoxy resin with copper or iron particles, Mater. Chem. Phys. 44 (1996) 245–250. https://doi.org/10.1016/0254-0584(96)80063-0.

[58] G.. Psarras, E. Manolakaki, G.. Tsangaris, Electrical relaxations in polymeric particulate composites of epoxy resin and metal particles, Compos. Part A Appl. Sci. Manuf. 33 (2002) 375–384. https://doi.org/10.1016/S1359-835X(01)00117-8.

[59] A.C. Patsidis, G. Psarras, Dielectric behaviour and functionality of polymer matrix-ceramic BaTiO3 composites, Polym. Lett. 2 (2008) 718–726. https://doi.org/10.3144/expresspolymlett.2008.85.

[60] G.A. Kontos, A.L. Soulintzis, P.K. Karahaliou1, G.C. Psarras, S.N. Georga, C.A. Krontiras, M.N. Pisanias, Electrical relaxation dynamics in TiO2 – polymer matrix composites, Polym. Lett. 1 (2007) 781–789. https://doi.org/10.3144/expresspolymlett.2007.108.

[61] S. Liu, S. Xue, B. Shen, J. Zhai, Reduced energy loss in poly(vinylidene fluoride) nanocomposites by filling with a small loading of core-shell structured BaTiO3/SiO2 nanofibers, Appl. Phys. Lett. 107 (2015) 032907. https://doi.org/10.1063/1.4927330.

[62] N. Tohluebaji, C. Putson, N. Muensit, High Electromechanical Deformation Based on Structural Beta-Phase Content and Electrostrictive Properties of Electrospun Poly(vinylidene fluoride- hexafluoropropylene) Nanofibers, Polymers (Basel). 11 (2019) 1817. https://doi.org/10.3390/polym11111817.

[63] Y. Gong, W. Zhou, Z. Wang, L. Xu, Y. Kou, H. Cai, X. Liu, Q. Chen, Z.M. Dang, Towards suppressing dielectric loss of GO/PVDF nanocomposites with TA-Fe coordination complexes as an interface layer, J. Mater. Sci. Technol. 34 (2018) 2415–2423. https://doi.org/10.1016/j.jmst.2018.06.007.

[64] P. Da Hong, W.T. Chuang, W.J. Yeh, T.L. Lin, Effect of rigid amorphous phase on glass transition behavior of poly(trimethylene terephthalate), Polymer (Guildf). 43 (2002) 6879–6886. https://doi.org/10.1016/S0032-3861(02)00617-1.

[65] H. Rekik, Z. Ghallabi, I. Royaud, M. Arous, G. Seytre, G. Boiteux, A. Kallel, Dielectric relaxation behaviour in semi-crystalline polyvinylidene fluoride (PVDF)/TiO2 nanocomposites, Compos. Part B Eng. 45 (2013) 1199–1206. https://doi.org/10.1016/J.COMPOSITESB.2012.08.002.

[66] G. Calleja, A. Jourdan, B. Ameduri, J.P. Habas, Where is the glass transition temperature of poly(tetrafluoroethylene)? A new approach by dynamic rheometry and mechanical tests, in: Eur. Polym. J., 2013: pp. 2214–2222. https://doi.org/10.1016/j.eurpolymj.2013.04.028.

[67] E. Parodi, L.E. Govaert, G.W.M. Peters, Glass transition temperature versus structure of polyamide 6: A flash-DSC study, Thermochim. Acta. 657 (2017) 110–122. https://doi.org/10.1016/j.tca.2017.09.021.

[68] Y. Feng, W.L. Li, Y.F. Hou, Y. Yu, W.P. Cao, T.D. Zhang, W.D. Fei, Enhanced dielectric properties of PVDF-HFP/BaTiO3-nanowire composites induced by interfacial polarization and wire-shape, J. Mater. Chem. C. 3 (2015) 1250–1260. https://doi.org/10.1039/c4tc02183e.

[69] T.D. Fornes, D.L. Hunter, D.R. Paul, Nylon-6 Nanocomposites from Alkylammonium-Modified Clay: The Role of Alkyl Tails on Exfoliation, (2004). https://doi.org/10.1021/ma0305481.

[70] P.J. Yoon, D.L. Hunter, D.R. Paul, Polycarbonate nanocomposites. Part 1. Effect of organoclay structure on morphology and properties, Polymer (Guildf). 44 (2003) 5323–5339. https://doi.org/10.1016/S0032-3861(03)00528-7.

[71] F. Chavarria, D.R. Paul, Comparison of nanocomposites based on nylon 6 and nylon 66, Polymer (Guildf). 45 (2004) 8501–8515. https://doi.org/10.1016/j.polymer.2004.09.074.

[72] D.R. Paul, L.M. Robeson, Polymer nanotechnology: Nanocomposites, Polymer (Guildf). 49 (2008) 3187–3204. https://doi.org/10.1016/j.polymer.2008.04.017.

[73] A.A. Tarhini, A.R. Tehrani-Bagha, Graphene-based polymer composite films with enhanced mechanical properties and ultra-high in-plane thermal conductivity, Compos. Sci. Technol. 184 (2019) 107797. https://doi.org/10.1016/J.COMPSCITECH.2019.107797.

Appendix II

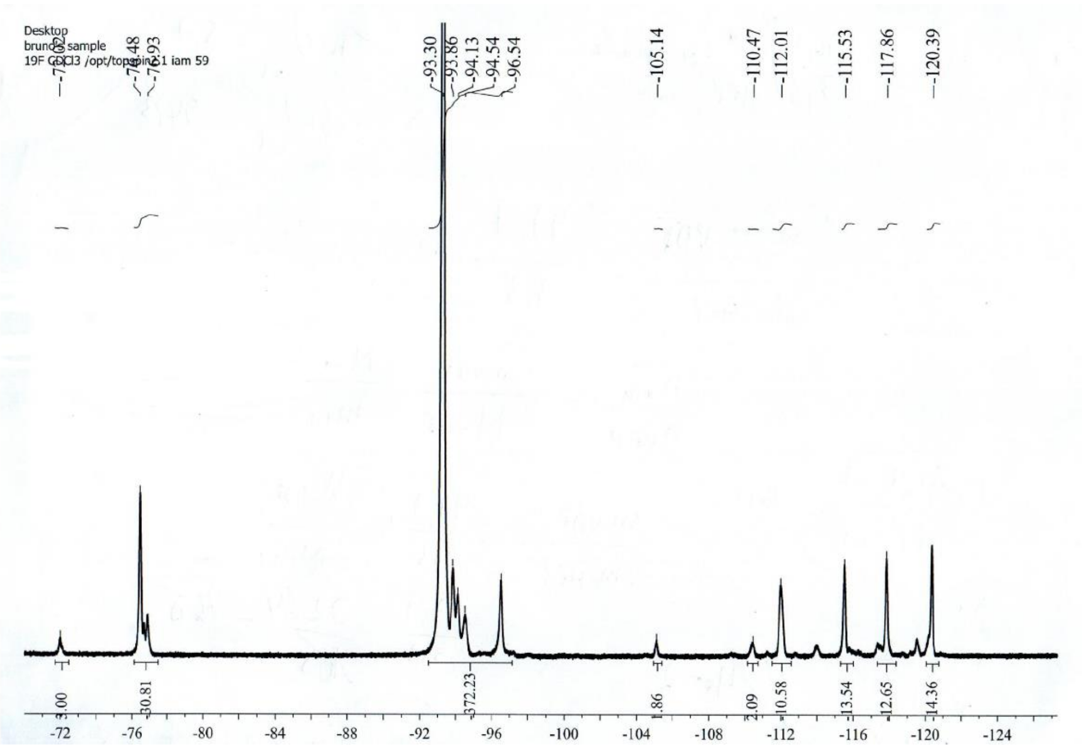

Figure A39. ^{19}F NMR spectrum of commercially available P(VDF-HFP) recorded in $CDCl_3$.

The VDF content was determined using the equation 1, and was estimated to be 97 mol %.

$$\% VDF = \frac{\int_{-92.0}^{-119} VDF/2}{\int_{-92.0}^{-119} VDF/2 + \int_{-119.5}^{-120.5} HFP/2} \qquad (1)$$

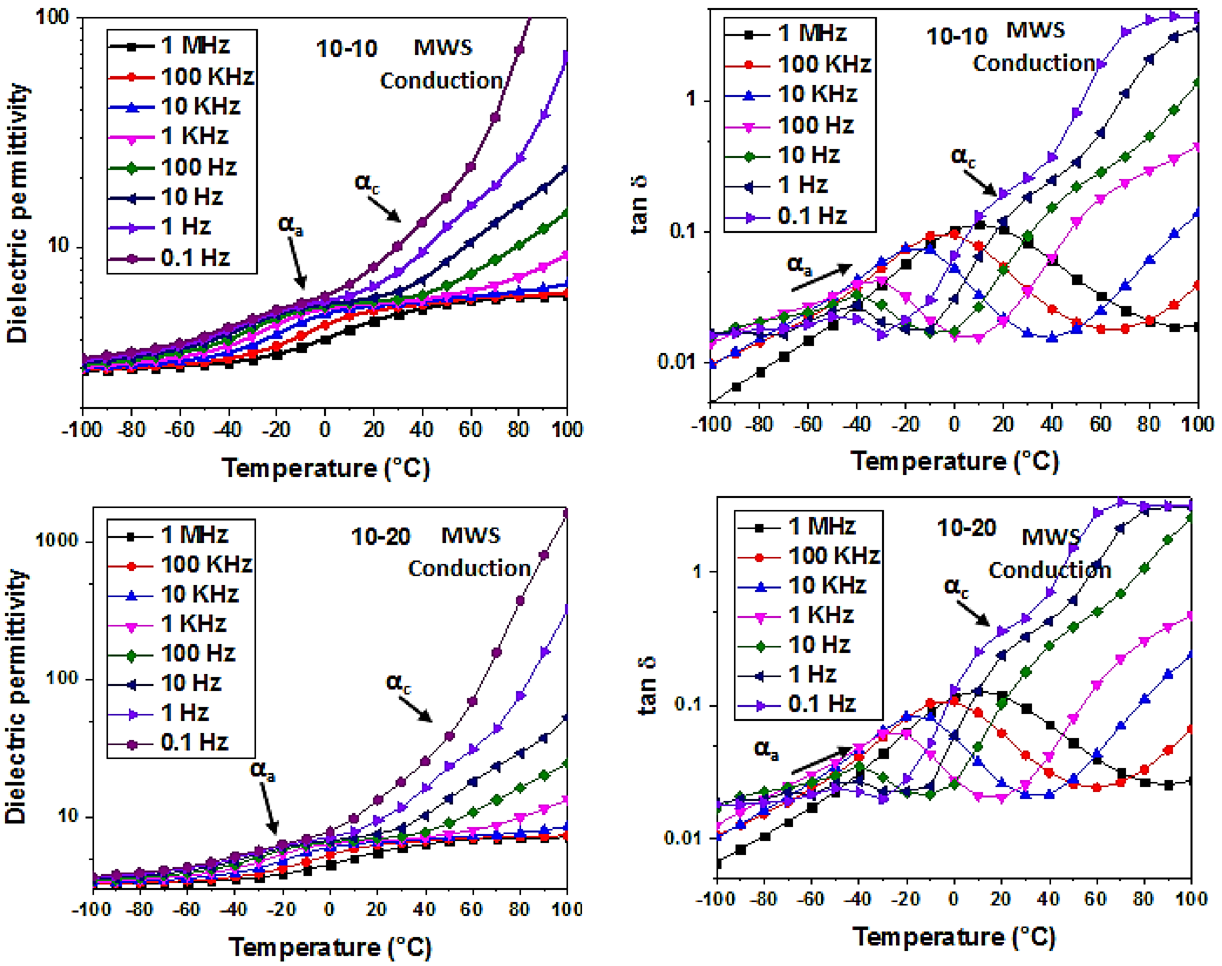

Figure A2. Dielectric permittivity, ε′, (left) and loss tangent, tan δ, (right) of nanocomposites films 10-10, 10-20 and 20-10 versus temperature at different frequencies.

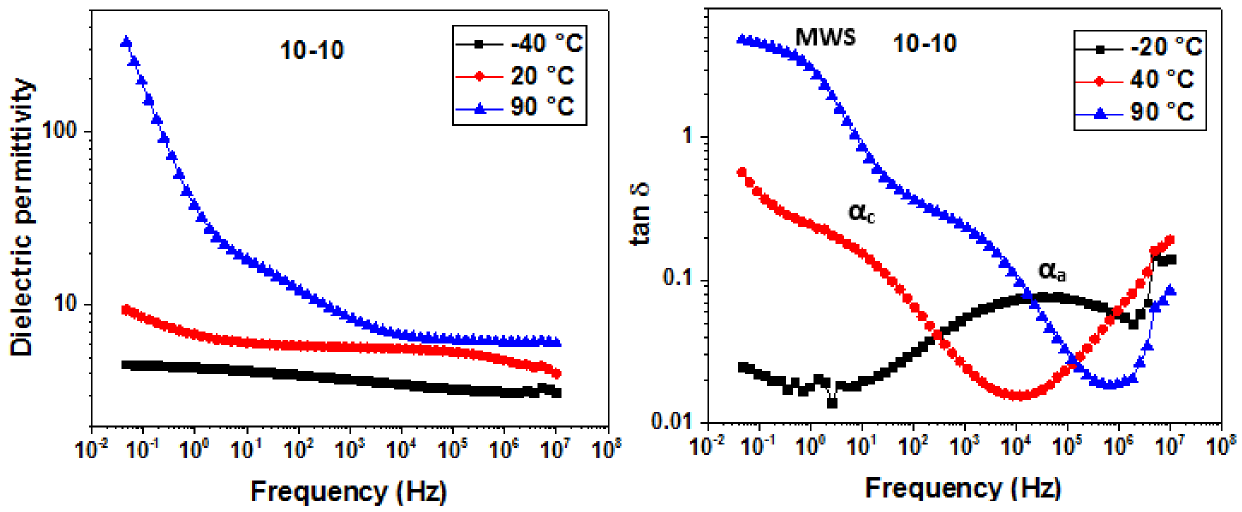

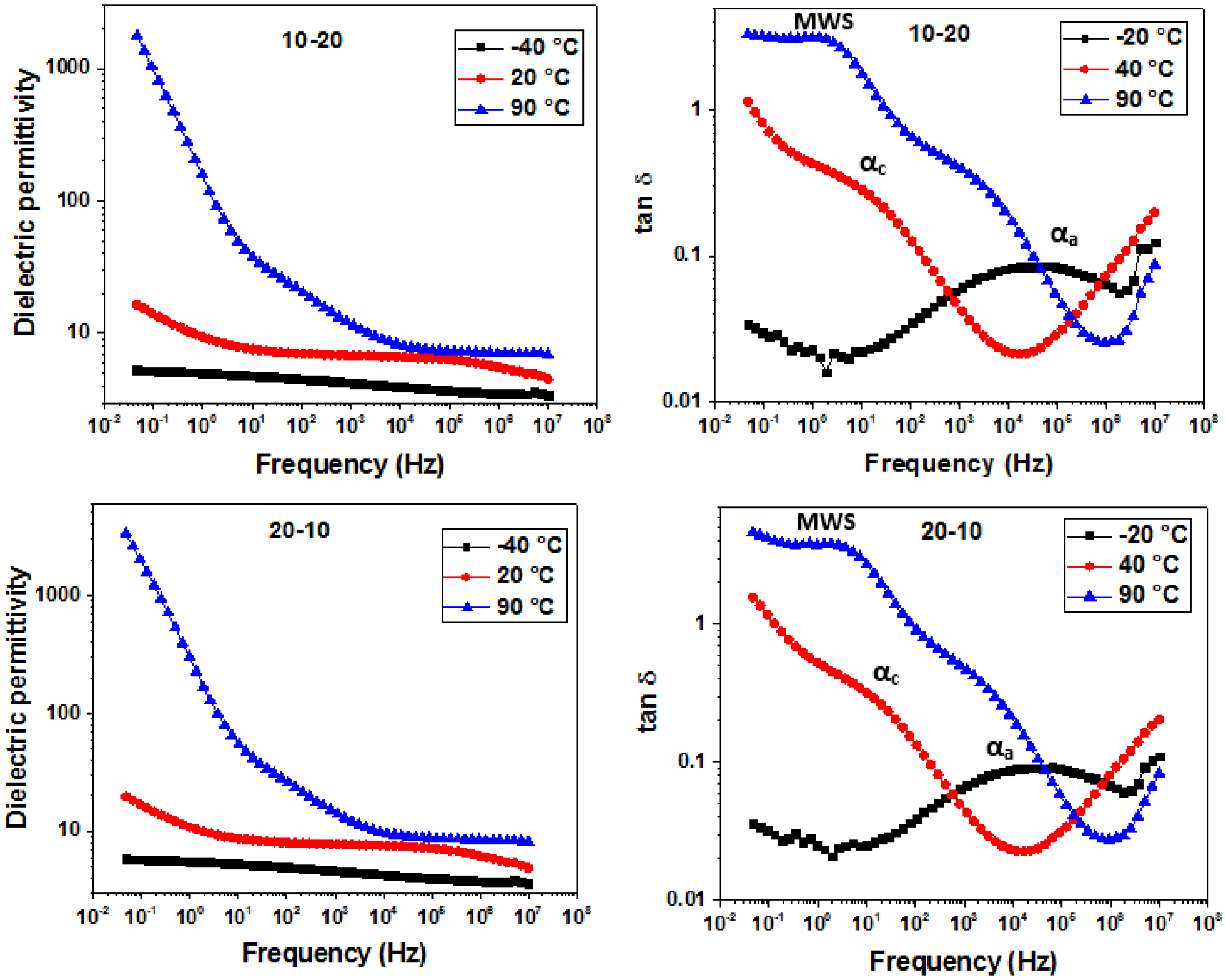

Figure A3. Selected representative isothermal spectra recorder for ε′ and tan δ of the nanocomposite films10-10, 10-20 and 20-10.

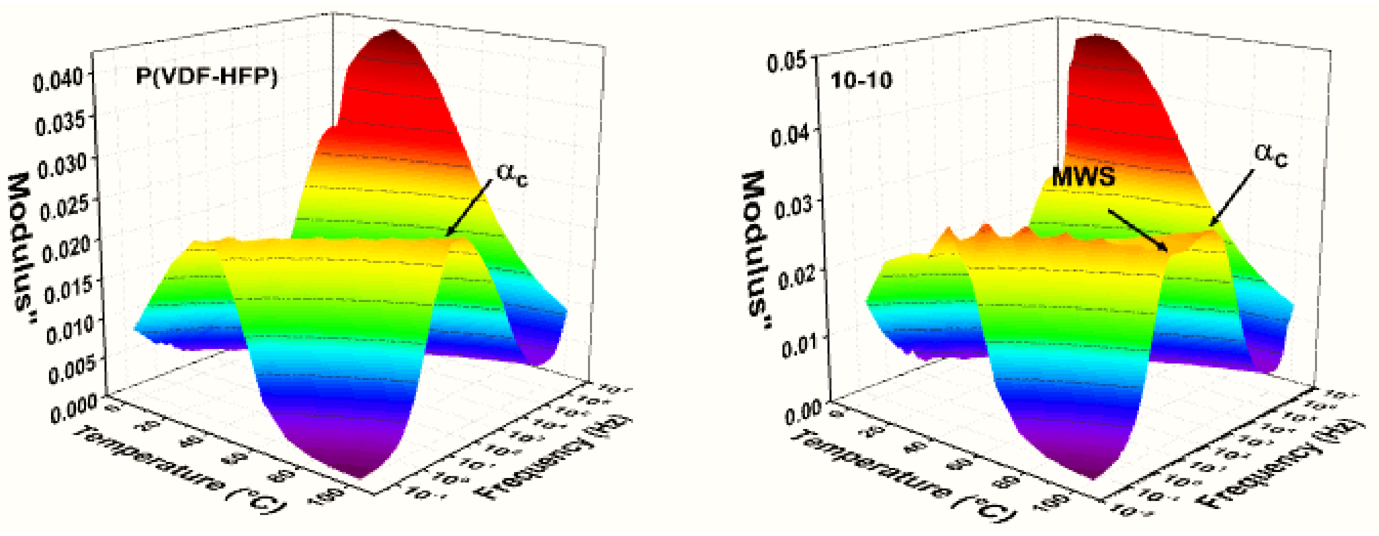

Figure A4. Frequency dependence dielectric loss modulus (Modulus") of the nanocomposite films (10-20, 20-10 and 20-20) at different temperatures.

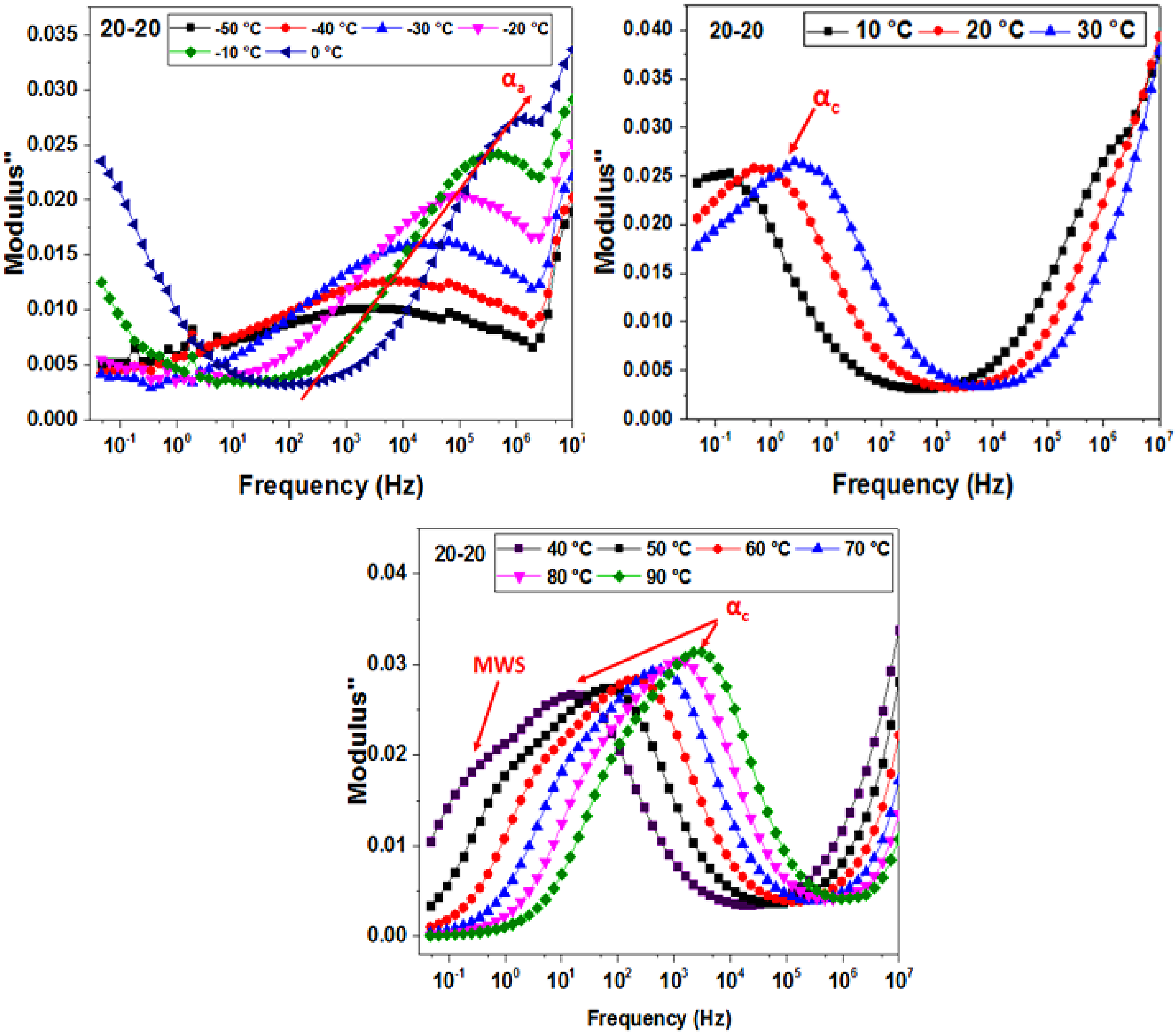

Figure A5. M” versus frequency at different range temperatures of 20-20 nanocomposite film.

[1] F.E. Bouharras, M. Raihane, G. Silly, C. Totee, B. Ameduri, Core shell structured Poly(Vinylidene Fluoride) -grafted- BaTiO3 nanocomposites prepared via Reversible Addition fragmentation chain transfer (RAFT) polymerization of VDF for high energy storage capacitors, Polym. Chem. 10 (2019) 891–904. doi:10.1039/C8PY01706A.

Chapter VI: Evaluation of core–shell poly(vinylidene fluoride)-*grafted*-Barium titanate (PVDF-*g*-BaTiO$_3$) nanocomposites as a cathode binder in batteries

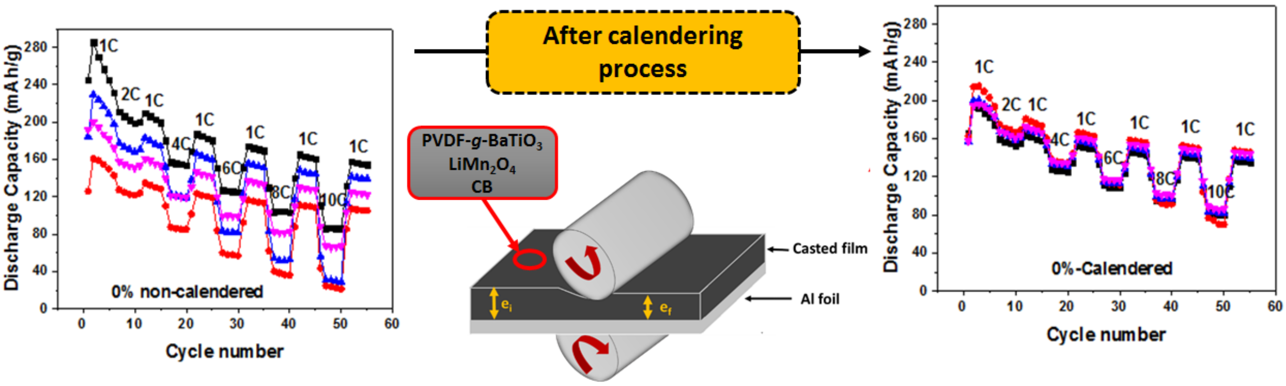

VI.1. Introduction

The increasing number of electronic devices represents a challenge for the industry. Actually, the design of a passive electronic component having high performances with moderate production costs, light weight and small size requires great efforts in the field of research and development [1],[2]. In this goal, and since it is possible to combine several materials to achieve optimum properties, studies on nanocomposite materials made by polymers and fillers such as ceramics have received much attention since this technique combines the low temperature processing and both the light weight of polymers and the high dielectric constant of ceramics (*e.g*, $BaTiO_3$) [3]. Thereby, the combination of polymer and ceramic may give the nanocomposites some advantages from both sides by a certain design and preparation [4]. Actually, polymer nanocomposite systems with high dielectric permittivity have attracted significant attention in the recent years due to their wide range use in electronic industry, such as in multilayer, embedded and high energy density capacitors [5–8]. Another important application of polymer nanocomposites deals with lithium ion batteries [9]. Having a great potential of achieving very high energy density and low environmental impact, lithium ion batteries become the most used secondary rechargeable storage systems [10].

A typical electrode fabrication consists on the active material, conductive agent, binder and the solvent that are mixed to form a slurry. This later is then casted onto an aluminum or copper foil and dried at room temperature to form the electrode. In order to remove all the remaining solvent(s), the prepared electrode is further dried under vacuum before making the cell.

In order to enhance the battery performances, several studies have been reported on active material, binder or even electrolyte, in which polymer nanocomposites have been widely used [11]. For example, Kumar *et al*. [12] used $BaTiO_3$ as a filler in poly(VDF-HFP) co-polymer based composite solid polymer electrolyte (CSPE) prepared by solution casting. The results show that the highest DC conductivity was 2.19×10^{-6} S cm^{-1} at 300 K, which increases to 8.89×10^{-6} S cm^{-1} after adding 4 wt.% of $BaTiO_3$. Other works have been also reported using other kind of fillers. Giselle et *al.* [13] synthesized polymer-clay nanocomposites and tested them as possible candidates as electrolytes in lithium-ion cells. The obtained films displayed excellent mechanical strength with conductivity comparable to more traditional polymer electrolytes made with added lithium salts. Ferrari *et al*. [14] reported the use of different types of fillers (*e.g.*, ceramics, metal oxides, glass…) that can be incorporated into the polymer matrix or formed in situ by different synthetic strategies.

On the other hand, and although they are electrochemically inactive material, the binder can have significant influence on the electrode performance [11]. In fact, various kinds of binders have been attempted, such as poly(vinyl alcohol) [15], poly(acrylic acid) [16], poly (methyl methacrylate) [17], carboxymethyl cellulose [11] and natural cellulose [18]. Besides the listed polymers, polyvinylidene fluoride, PVDF, and its blend copolymers are considered to be the most common and widely used binder material in lithium ion batteries, thanks to their good electrochemical stability and strong adhesion properties as well [17,19]. Zheng *et al.*[20] studied the effect of PVDF modified with blending copolymer polyethylene-block-poly(ethylene glycol) co-polymer and poly (propylene carbonates) (PPCs), used as binder material using $LiCoO_2$ as active material and carbon black as conductive agent. It was found that the modified PVDF improves the dispersion of carbon black compared to the pure PVDF binder, leading to enhanced uniformity of the electrode composite.

Apart from the polymer binder nature, molar mass of the used polymer is also an important factor. Wang *et al.*[21] investigated the effect of molar mass of PVDF binder on the electrochemical performances of $LiNi_{0.33}Co_{0.33}Mn_{0.33}O_2$ (NMC) electrodes made by a dry powder coating process. The authors found that the PVDF form a thin layer around the NMC particles surface after heating it to above its melting temperature, and by increasing the molar mass of the polymer, the PVDF layer becomes more porous, improving the high rate capacity of the electrodes. Wang *et al.* [22] also studied the effect of PVDF molar mass on electrode performances using a wet-slurry procedure. In contrast to Wang *et al.*'s strategy, it was found that the smallest molar masses had the best performances.

Herein, modified PVDF was used to prepare electrodes based on $LiMn_2O_4$ as the active material and carbon black as the conductive agent. This binder, named as PVDF-*g*-BT, was obtained from a reversible addition fragmentation chain transfer polymerization (RAFT) of VDF from the surface of $BaTiO_3$ nanoparticles leading to a well-structured nanocomposite materials. The electrochemical tests, including cyclic voltammetry, charge-discharge capacity and rate performance were investigated on the prepared cells.

VI.2. Cells preparation

The binders tested are commercial polyvinylidene fluoride (Solef® 5130/1001 PVDF) purchased from Solvay and modified polyvinylidene fluoride-*grafted*-Barium titanate (PVDF-*g*-BT) nanocomposites filled with 5 wt% of $BaTiO_3$. PVDF-*g*-$BaTiO_3$ nanocomposites synthesized by RAFT polymerization of VDF [23] (Reported in Chapter III). The cathode films were prepared using 70 wt% $LiMn_2O_4$, 18 wt% of Carbon black (C65), 12 wt% of the binder (PVDF or PVDF-*g*-BT nanocomposite or both) (Table 1).

Table 1. Formulations used to prepare electrode materials for batteries with active material.

Formulations	*Wt % PVDF*	*Wt% PVDF-g-BT*
0%	12	0
4%	8	4
8%	4	8
12%	0	12

PVDF-*g*-$BaTiO_3$ nanocomposite filled with 5 wt% of $BaTiO_3$ was used as binder material in Lithium ion batteries to test its effect on electrochemical behavior. In a first step, four formulations were chosen based on PVDF, CB and modified PVDF (Table 2).

Table 2. Formulations used to prepare electrode materials for batteries without active material.

Formulations	*Wt % PVDF*	*Wt% CB*	*Wt% PVDF-g-BT*
A	33	33	33
B	12	18	70
C	40	60	0
D	50	50	0

In the case where the active material was not used, the slurry was prepared as previously reported according to the precursors listed in Table 2 and spread in a copper foil instead of the aluminum. After drying at room temperature for 48 h, the obtained films were punched to discs with 12.7 mm in diameter and further dried at 80 °C for 3h.

VI.3. Results and discussions

IV.3.1. Cells made without active material

VI.3.1.1. Cyclic voltammetry

The first step aimed to explore the electrochemical behavior of cells made by the modified PVDF to check whether it will affect the electrochemical performances of the battery. The obtained electrodes (Table 2) were tested by cyclic voltammetry as shown in Figure 1.

Figure 1 exhibits that all the electrodes either made from PVDF-*g*-$BaTiO_3$ or not, display a quite similar evolution and the presence of a slight peak is attributed to carbon black activity. Furthermore, by comparing voltammograms of electrodes made with (*e.g.*, A) and without (*e.g.*, D) nanocomposites, no big differences are noted which indicate that the introduction of PVDF-*g*-$BaTiO_3$ nanocomposites as a binder material in the electrode does not involve any activity and therefore does not affect the electrochemical stability of the cell.

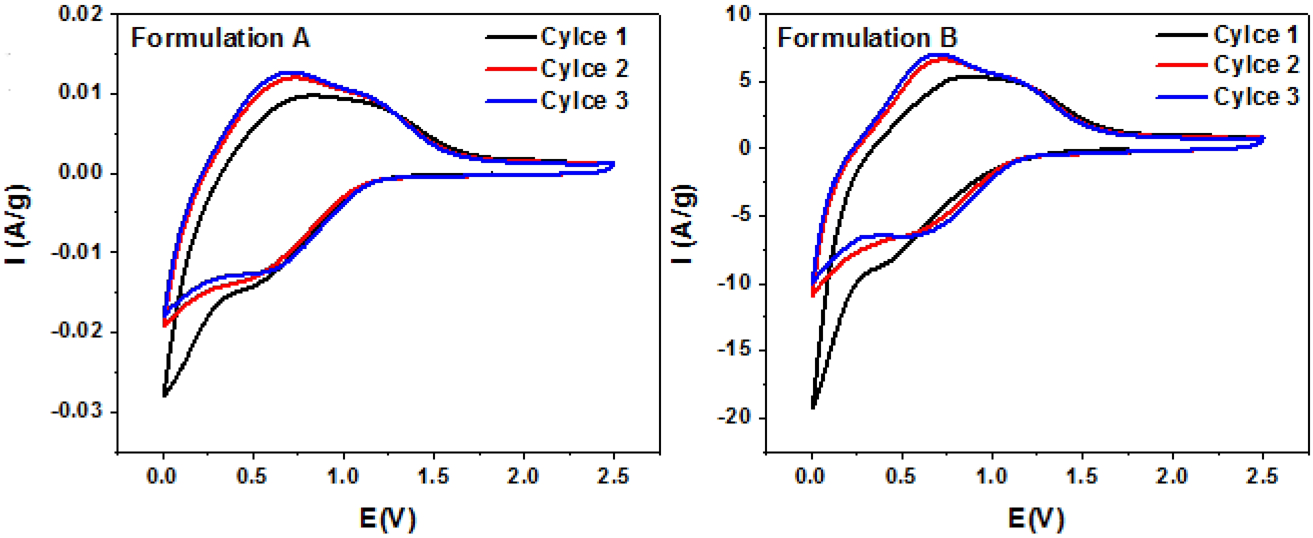

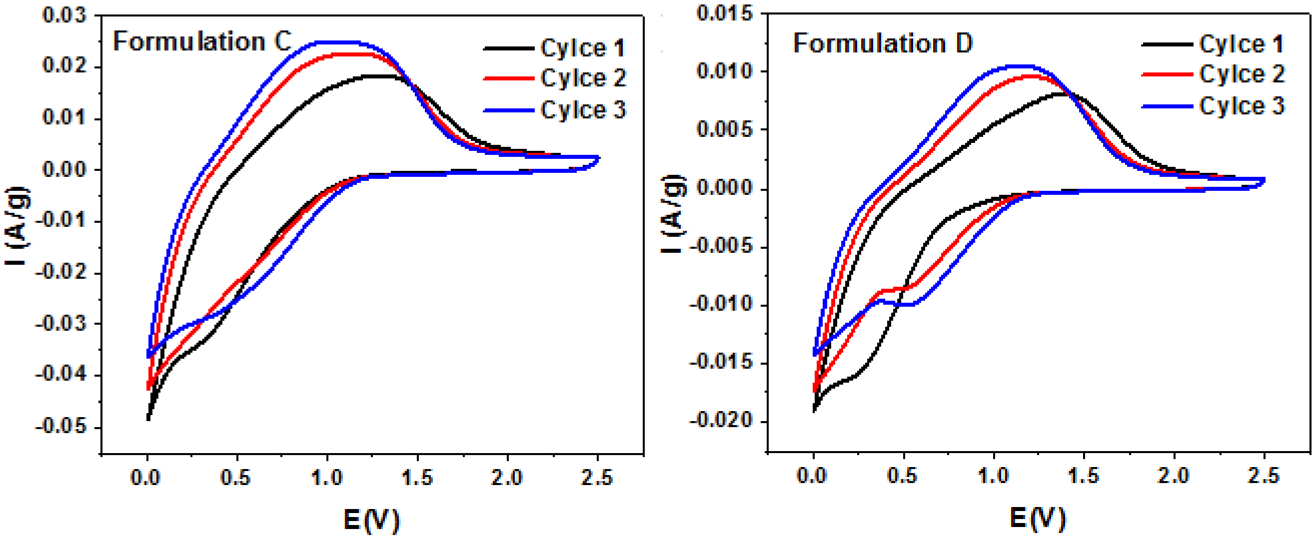

Figure 1. Cyclic voltammograms of the prepared electrode with (A and B) and without (C and D) PVDF-*g*-$BaTiO_3$ nanocomposites.

VI.3.1.2. Impedance measurements

Table 3 presents the resistance of the cells prepared with and without PVDF-*g*-BT nanocomposites, obtained from impedance measurements.

Table 3. Resistance values of the cells made with and without PVDF-*g*-BT nanocomposites at different temperatures.

Formulations	***R at RT (Ohm)***	***R at 40 °C (Ohm)***	***R at 60 °C (Ohm)***	***R at 80 °C (Ohm)***
A	42.9	28.3	4.61	0.73
B	47.5	21.4	5.45	0.98
C	16.4	16.2	3.99	0.58
D	27,1	16,8	2.89	0.76

For all samples, the resistance decreases by increasing the temperature. In addition, it is noted that the cells prepared with the nanocomposites exhibit higher resistance in comparison to those made from commercially available PVDF. This indicates that the introduction of modified ceramics with PVDF into the cell increases the resistance of the system and thus decreases the electrical conductivity. Based on the thicknesses of the casted films, the conductivity was determined using equation 1:

$$\sigma = \frac{e}{R \times S} \qquad (1)$$

where e and S stand for the thickness of the casted film and its surface area, respectively.

Figure 2 shows that the cells prepared with PVDF-*g*-BT exhibit conductivities quite similar as those achieved from commercially available PVDF at lower temperatures. However, the difference becomes prominent when the temperature increases up to 40 °C. In fact, the role of the binder consists on holding the electrode particles (*i.e.* active material and conductive agent) together and bond the active material to the current collector [24]. However, a lack of PVDF binder needed to hold these particles leads to decreased conductivity [25], and this explained the fade of conductivity in formulations made with the modified PVDF, where the amount of polymer is lower.

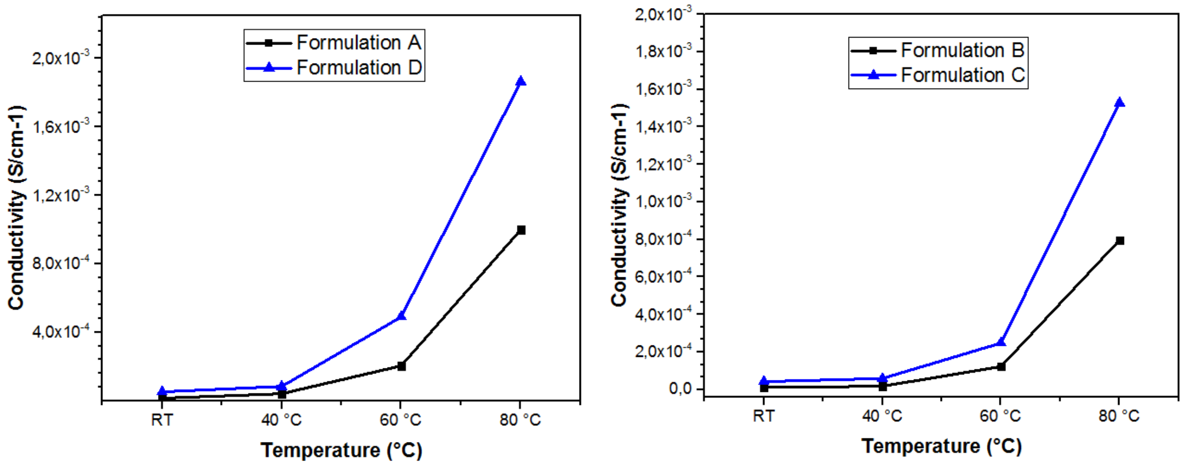

Figure 2. Conductivities of the cells at different temperatures made without the active material corresponding to formulations listed in Table 2.

VI.3.2. Cells made with active material

After exploring the electrochemical behavior of PVDF-*g*-BT nanocomposites and knowing that they do not affect the electrochemical stability of the prepared cells, new cells were prepared with another configuration using the active material (LMO) according to Table 1.

VI.3.2.1. Calendering procedure

In order to obtain uniform thickness, better particles dispersion and thus homogeneous structure, films calendering was adopted (Figure 3). In fact, the calendering process consists in placing the casted film or the electrode between two rolls working in opposite directions, where the gap size is significantly smaller than the electrode thickness in order to insure the desired compaction of the electrode coating [26].

This technique was found to enhance not only the mechanical and physical characteristics, but also the electrochemical performances of the electrode as well [27]. Indeed, it is believed that the calendering enables to increase the contact between particle to particle and particle to current collector in the electrode, leading to an improvement in both electrical and thermal conductivities [28].

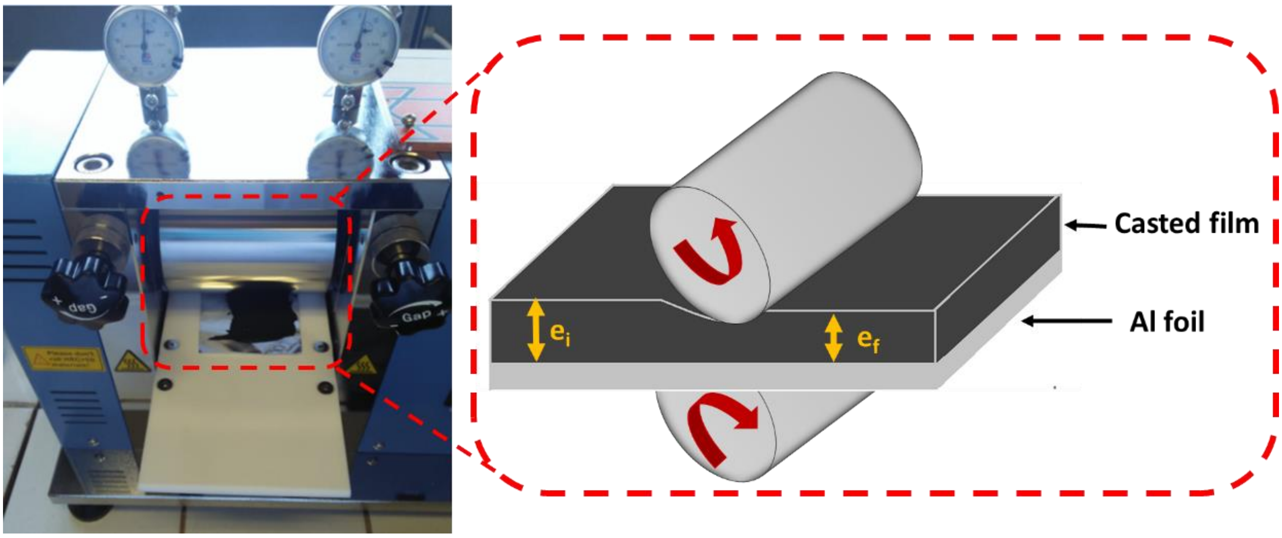

Figure 3. Picture and sketch illustrating the calendering procedure used to process the resulting electrodes based on the active material.

In the present work, formulations based on the active material were calendered before assembling the cells (Figure 3). Thicknesses of the films were measured using digital micrometer (IP 65, Mitutoyo) before and after calendering by picking six different points (Three measurements on the border and three in the middle of each film) as shown in Figure 11-b of Chapter II.

Table 4 displays the average thicknesses of the electrodes before and after calendering. It is clearly seen that calendering procedure enables to decrease the thickness of the prepared films by 4.5, 2.3, 9.0 and 7.7 µm for formulations made by 0, 4, 8 and 12 wt% of modified PVDF, respectively.

Table 4. Average thicknesses of the different electrodes before and after calendering in µm.

Samples	***Before calendering*** **(e_i (μm))**	***After calendering*** **(e_f (μm))**
0 %	49.5	45.0
4 %	46.7	44.3
8 %	46.3	37.3
12 %	44.5	36.8

However, it is worth mentioning that the thickness of the calendered films is still higher than that of the roll thickness fixed at 30 µm, and this can be explained by the elastic recovery (ER) of the electrode when the pressure is removed. Figure 4 exhibits the elastic recovery determined from equation (2):

$$ER = \frac{e_f - e_r}{e_i} \qquad (2)$$

where e_f, e_g and e_i refer to final, in-between the roll and initial thicknesses, respectively [28].

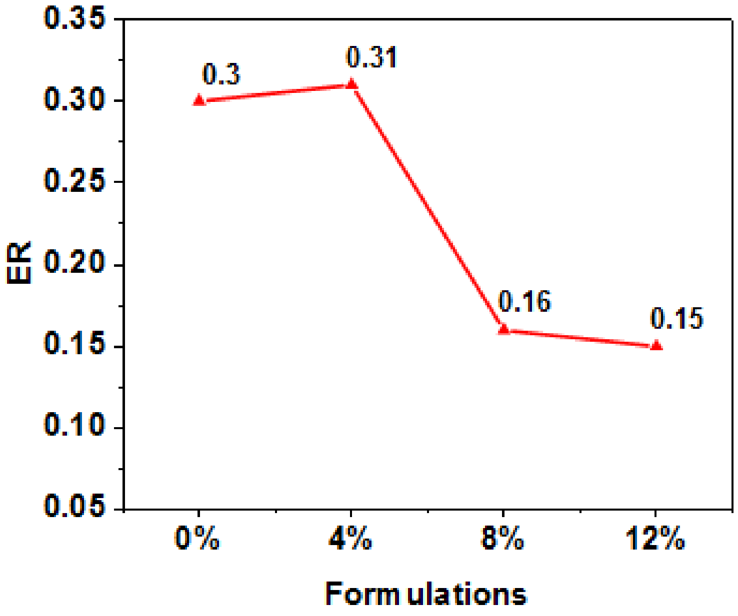

Figure 4. Elastic recovery (ER) determined from equation (2), for the different formulations based on the active material.

From Figure 4, the elasticity of the films decreases as the feed amount of modified PVDF in the formulation increased. For instance, the ER decreased from 0.3 for formulation made by commercially available PVDF to 0.15 when modified PVDF (12 wt%) is used. This variance comes from the difference in PVDF structure and namely in molar masses. In fact, the commercial PVDF presents a molar mass (~1,200,000 g/mol) higher than that of the modified one (~3200 g/mol), and thus carrying long polymer chains. Those latter confine to the film an elastic deformation that dominates the densification process when the calendering is applied, leading to increased elastic recovery (ER).

VI.3.2.2. Scanning electronic microscopy

In order to further explore the effect of calendering process, the films were characterized by scanning electronic microscopy (SEM). Figure 5 exhibits the SEM images of non-calendered (0NC %) and calendered films (0, 4, 8 and 12 %).

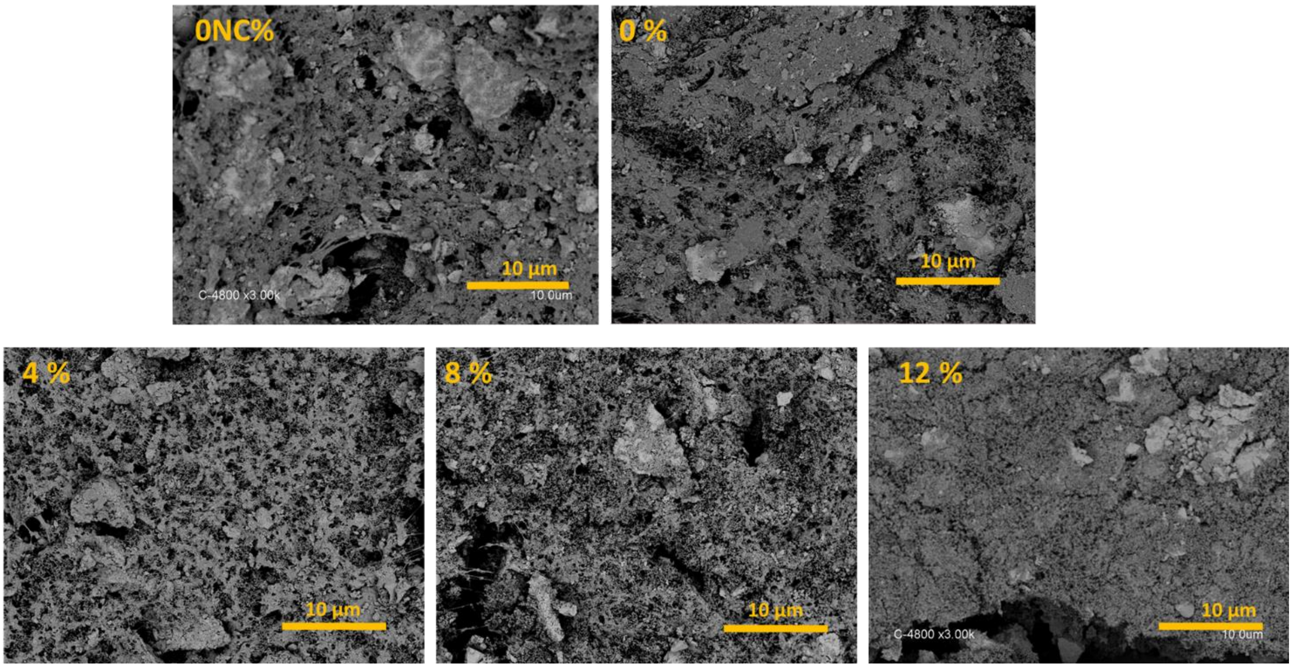

Figure 5. SEM images of non-calendered (0NC %) and calendered films (0, 4, 8 and 12 %).

By comparing the SEM images of the non-calendered (0NC%) and calendered (0 %) films, it seems that this procedure induces a change in the structure evidenced by obtaining a film with less pores and voids. Moreover, and in all the samples, particles are well dispersed in the film and it is worth to note the presence of some aggregates that could be related to $LiMn_2O_4$. Figure 6 provides low magnification (600 µm) SEM images of the different films. After calendering the sample with 0% of modified PVDF, the obtained film presents a softer surface as compared to that of the non-calendered one. However, after adding 8 wt%, the film surface presents cracks that could be due to the low PVDF content responsible to bind all the particles together on the current collector, resulting in cracked surface. It is believed that calendering procedure renders the structure of the film more compact and thus reducing the pores and voids leading to enhanced electrochemical performances.

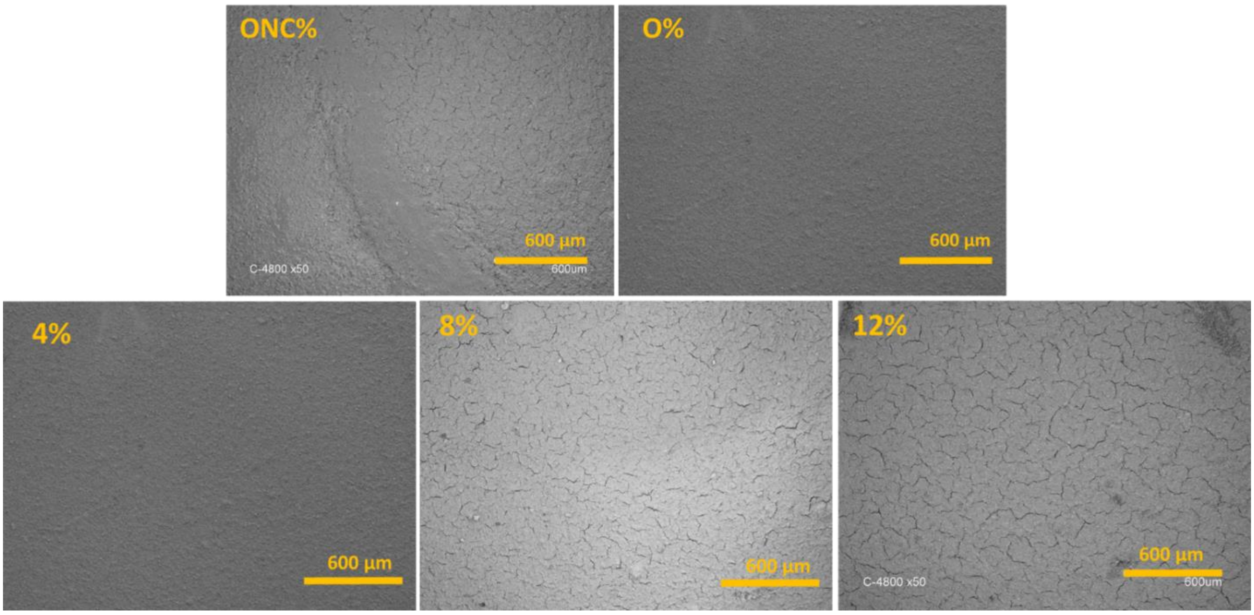

Figure 6. SEM images of non-calendreded (0NC %) and calendreded (0 %, 4 %, 8 % and 12 %) films at low magnification (600µm).

Zheng *et al.*[29] studied the effect of calendering on the morphology of cathode laminates based on Li $[Ni_{1/3}Mn_{1/3}Co_{1/3}]O_2$, 8 %wt of PVDF and 7 %wt of acetylene black. The prepared films were compressed to the desired thickness corresponding to the searched porosity, which was adjusted from the free standing (50 %) to 40, 30, 20, 10 and 0 %. For the sample having 50 % of porosity, SEM images revealed the presence of several pores and micro-fractures. Moreover, it was shown that the inactive material (PVDF and acetylene black) occupied a large volume fraction in the electrode, leading to low volumetric energy density, and this is due to the low volumetric fraction of the active material. However, when the porosity was sited at 30 %, the morphology changed and since the material was not crashed by calendering, the decrease of film thickness was attributed to the shrinkage of the inactive material.

VI.3.2.3. Cyclic voltammetry measurements

To compare the electrochemical behavior of the prepared cells made with the active material, cyclic voltammetry measurements were conducted at a scan rate of 0.5 mV/s between 3.2 and 4.5 V (Figure 7).

For all formulations, and before calendering, two pairs of separated redox peaks are observed: two oxidation peaks located at about 4.1 V and 4.2 V, and two reduction peaks located at about 3.9 V and 4.04 V, characterizing lithium ions extraction-insertion from-into the tetrahedral sites of $LiMn_2O_4$ [30]. In fact, the first peak is attributed to the removal of Li^+ from half of the spinel framework where Li-Li interactions exist ($LiMn_2O_4/Li_{0.5}Mn_2O_4$), while the second peak is assigned to the removal of Li^+ from the other tetrahedral sites ($Li_{0.5}Mn_2O_4$/ γ-MnO_2) in which such interaction does not exist [30–32]. However, after calendering procedure, it is observed that: i) the separation between two redox pairs became less discernable; ii) a higher peak current was obtained after calendering which is more prominent in the 0% sample and iii) the ΔE (separation between Ea and Ec) became more important (Table 5).

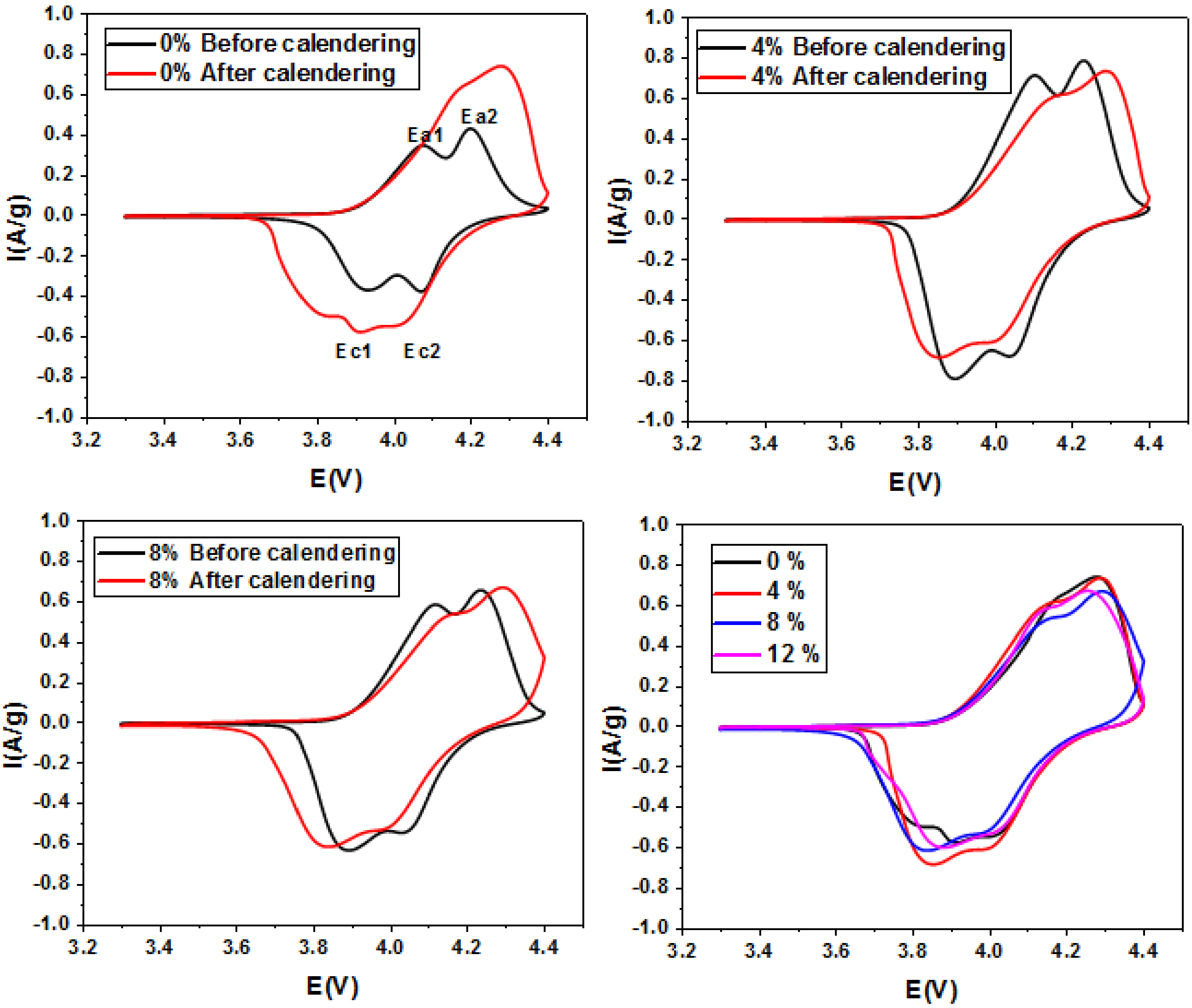

Figure 7. Cyclic voltammograms of the prepared cells using LMO as active material performed at a scan rate of 0.5 mV/s.

Assuming that the intercalation reaction is controlled by the solid-state diffusion of Li^+, the diffusion coefficient could be determined from the peak current I_p intensity using the following equation [33,34] :

$$I_P = 2.69 \times 10^5 \times n^{3/2} \times A \times D_{Li}^{1/2} \times v^{1/2} \times C_{Li}^0 \qquad (3)$$

Where v is the scan rate, n is the number of electrons per reaction species (n~1 for $LiMn_2O_4$), A is the surface area of the electrode and C_{Li}^0 is the bulk concentration of Li^+ in the electrode (given as 0.02378 mol cm^{-3} from the theoretical density of spinel).

Table 5. Summary of CV results at the potential scanning rate of 0.5 mV/s and the determined diffusion coefficients (D_{a1} and D_{a2}) before and after calendering.

	Before calendering				**After calendering**			
	ΔE_a (V)	ΔE_c (V)	D_{a1} (cm^2/s)	D_{a2} (cm^2/s)	ΔE_a (V)	ΔE_c (V)	D_{a1} (cm^2/s)	D_{a2} (cm^2/s)
0%	0.14	0.12	3.70×10^{-9}	5.65×10^{-9}	0.26	0.27	1.18×10^{-8}	1.69×10^{-8}
4%	0.21	0.19	1.53×10^{-8}	1.70×10^{-8}	0.3	0.29	1.15×10^{-8}	1.67×10^{-8}
8%	0.23	0.19	9.15×10^{-9}	1.31×10^{-9}	0.32	0.32	8.72×10^{-9}	1.36×10^{-8}
12%	-	-	-	-	0.26	0.22	1.01×10^{-8}	1.36×10^{-8}

From Table 5, it can be seen that the calendering procedure enables to enhance the diffusion coefficient of Li^+ ions for cells made by 0% of modified PVDF. For instance, the diffusion coefficient at the first anodic peak in 0% sample was 3.70×10^{-9} cm^2/s, and slightly increases to 1.18×10^{-8} cm^2/s after calendering the film.

VI.3.2.4. Galvanostatic electrochemical characterizations

In order to further investigate the effect of calendering procedure on the electrochemical performances of the films, four electrodes were prepared from each formulation. The effect of modified PVDF was also studied. The cells were charged and discharged for 55 cycles from 2.5 to 4.5 V at various current densities, and the current rate was increased from 1C to 10 C in steps. The comparison of the cycling performance of the calendered films at different charge and discharge rates is depicted in Figures 8 and 9.

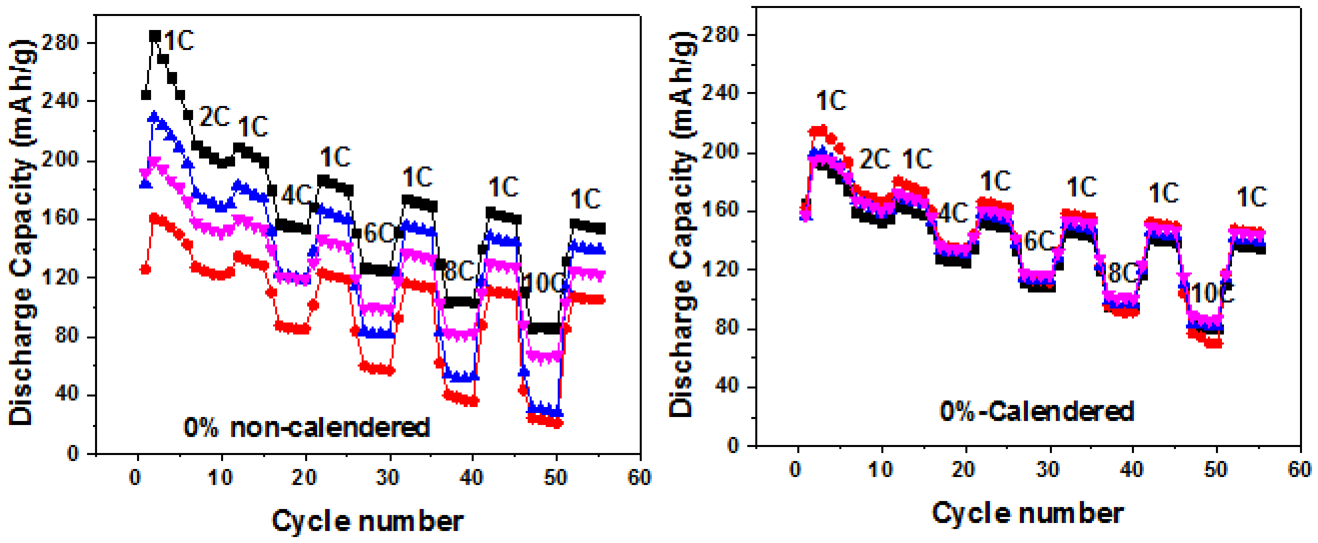

Figure 8. Discharge capacity as a function of cycle number for non-calendered and calendered films made by 0 % of modified PVDF.

It is worth mentioning that the calendering process enables to obtain a uniform structure, and this is well seen in the almost reproducible tests performed on the different cells of same formulation. Besides the reduction of volumetric density of the electrode film, the calendering process has an effect on other physical properties, including the interparticle contacts. Thus, the enhancement seen in cycling performance after calendering procedure could be explained by the increased ohmic contact area at the electrode-current collector interface [35].

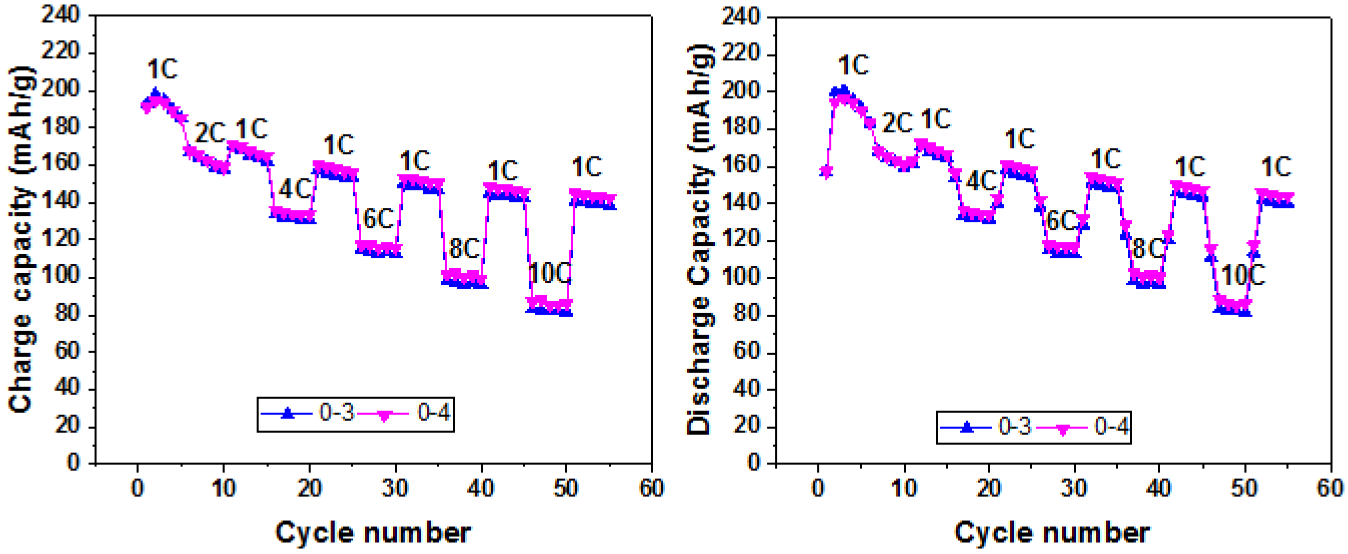

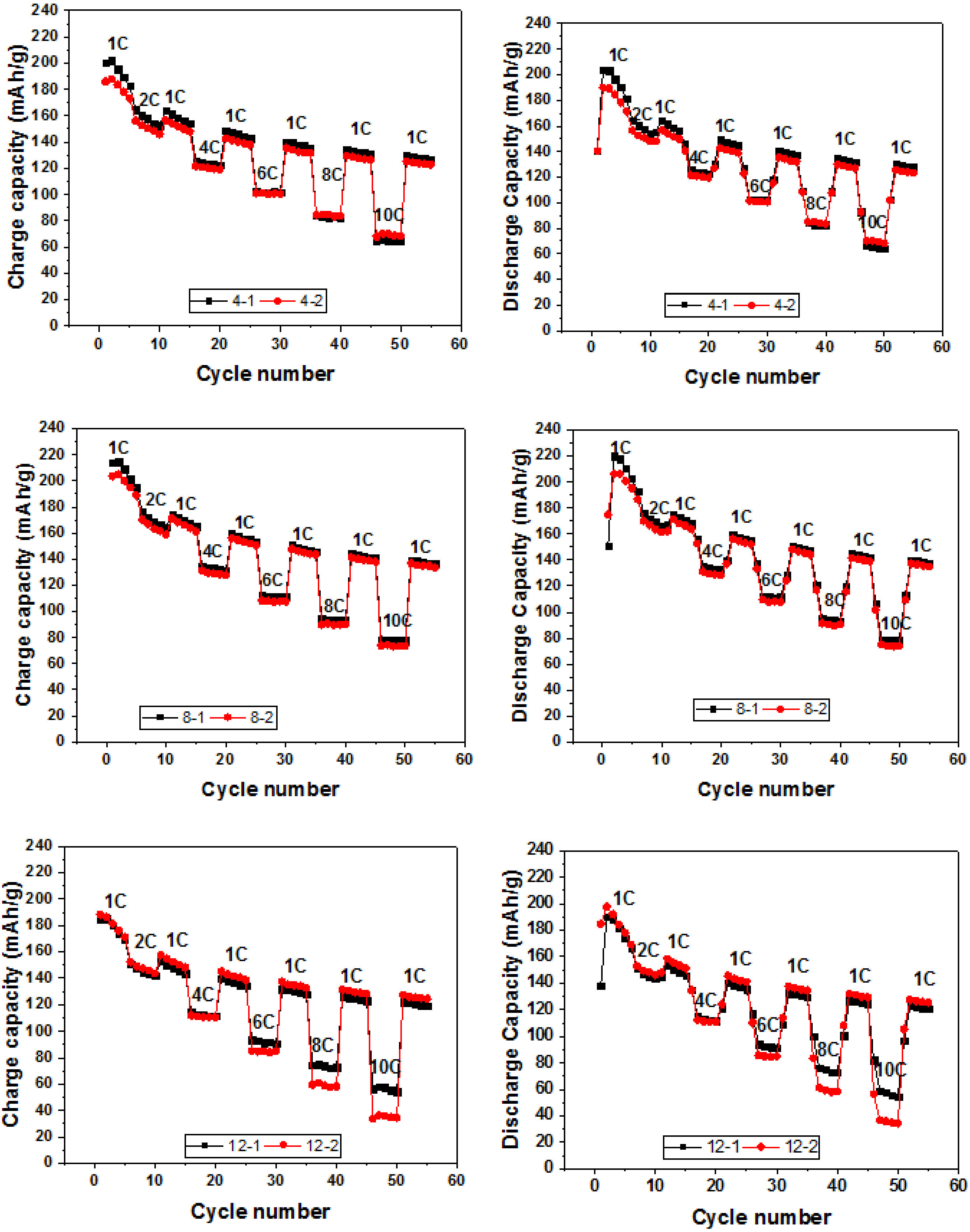

Figure 9. Charge and discharge capacity versus cycle number for all calendered formulations.

Figure 9 exhibits the charge and discharge capacities as a function of cycle number for all formulations after calendering process. It is observed that as the C-rate increases, there is a sharp decrease in the electrochemical performances of the prepared cells. For instance, for 0% sample and at 1 C, the discharge capacity is 194.6 mAh/g and decreases as the current rate increases to 167.3, 135.5, 117.5, 102.2 and 88.4 mAh/g at 2 C, 4 C, 6 C, 8 C and 10 C, respectively. This fade of capacity could be attributed to the structural change of the spinel $LiMn_2O_4$ due to Jahn-Teller effect as ($2Mn^{3+} \rightarrow Mn^{2+} + Mn^{4+}$) and the loss of active material with dissolution of Mn^{2+} into electrolyte [36]. However, even with the increase of charge-discharge rate to 10 C, the capacity can be approximately recovered when the current density returned to 1 C for all the samples, revealing the good reversibility of the structure.

Furthermore, it is observed that the specific capacity at 1 C and 2 C is higher than the theoretical capacity of LMO (148 mAh/g) for all samples and this could be explained by the capacitive behavior of nanosized electrode materials as it was reported previously [37,38]. Another explanation of this phenomenon could be given from Figure 10, which presents the first charge-discharge curve of non-calendered 0NC% sample at 1C.

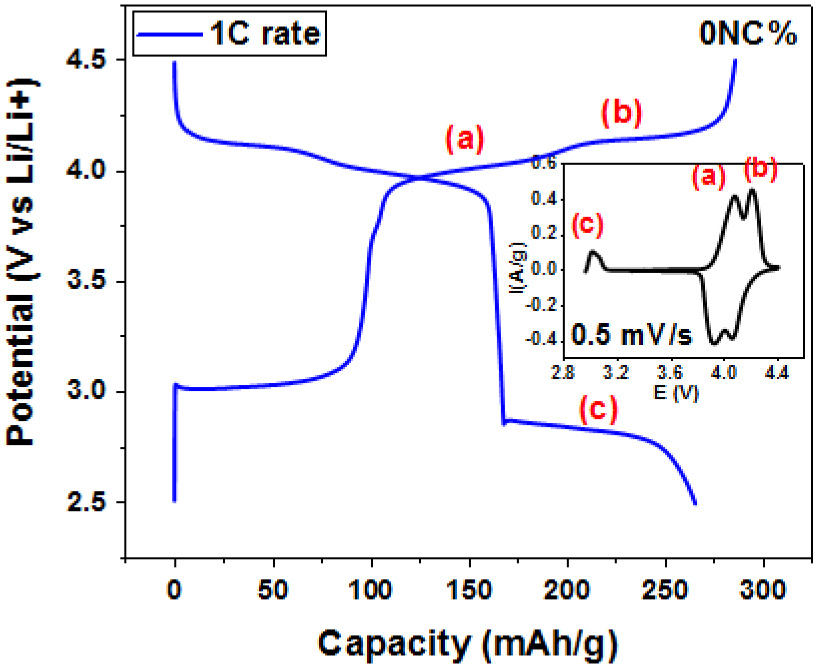

Figure 10. First charge-discharge curve of 0NC% at 1C; the inset refers to the CV plot of the same sample at 0.5 mV/s.

Two distinguished plateaus ((a) and (b) in Figure 10) could be identified corresponding to the two pairs of redox peaks in the CV plots. However, at low potentials, another reversible phase transformation occurs at around 2.99 V, assigned to the reversible transformation of $LiMn_2O_4$ to $Li_2Mn_2O_4$ [39] and this latter could have an effect on the cell performances since the cycling was performed from 2.5 to 4.5 V. In contrast to the mentioned measurement, Kim *et al*. [40] performed cycling measurements for commercial LMO in the voltage range of 3.4-4.3 V, and did not perceived the additional curve that appears for low voltage and thus discharge and charge capacities were less than the theoretical capacity of LMO.

Figure 11 exhibits the delivered discharge capacity, normalized with respect to the nominal one as a function of current scan for all calendered electrode films. It can be seen that the capacity retention decreases with increasing the scan rate for all the samples, and this could be explained by the Li^+ ion diffusion that occurs in the cathode material.

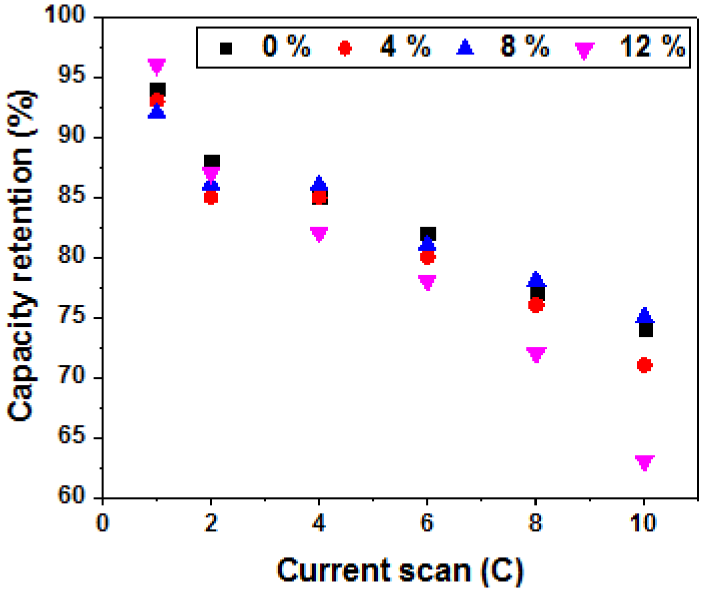

Figure 11. Capacity retention versus the current scan for different calendered formulations.

Figure 12 exhibits the cycling performance established in the voltage range of 3.4-4.3 V for non-calendered (ONC) and calendered (0 %) films made by only commercial PVDF. In contrast to the previous measurements, those later showed a specific capacity lower than that of the theoretical capacity of LMO (148 mAh/g). This confirms the effect of the transformation of $LiMn_2O_4$ to $Li_2Mn_2O_4$ that occurs at low potentials, on the cycling performances. On the other hand, Figure 12 highlights the importance of calendering process on enhancing the cycling performance of the prepared films. It can be seen also that as the C-rate increases, a sharp decrease in rate capability was observed, which is especially noted when C-rates are grater than or equal to 4C for non-calendered films.

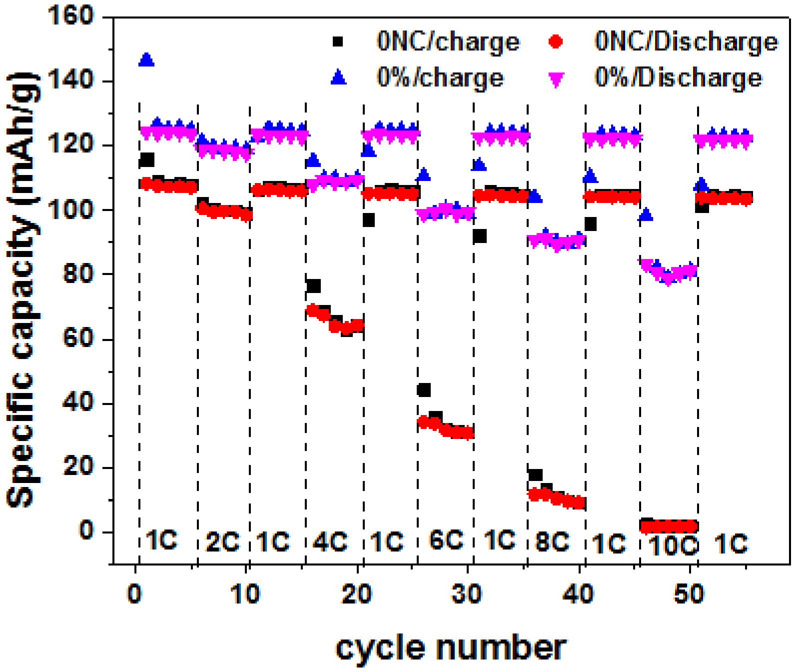

Figure 12. Charge and discharge capacity as a function of cycle number for non-calendered (0NC) and calendered (0%) films made by only commercial PVDF.

Figure 13 exhibits the charge and discharge capacities recorded for calendered films achieved from 0, 4 and 8 % of modified PVDF. It can be seen that formulation made by 4% of modified PVDF shows a similar behavior as the one made by commercial PVDF, while the sample with 8% was less performant. For instance, at 1C, the initial charge capacities were 146, 140 and 130 mAh/g and decreased to 98, 88 and 80 mAh/g at 10 C for films made by 0, 4 and 8 % of modified PVDF, respectively.

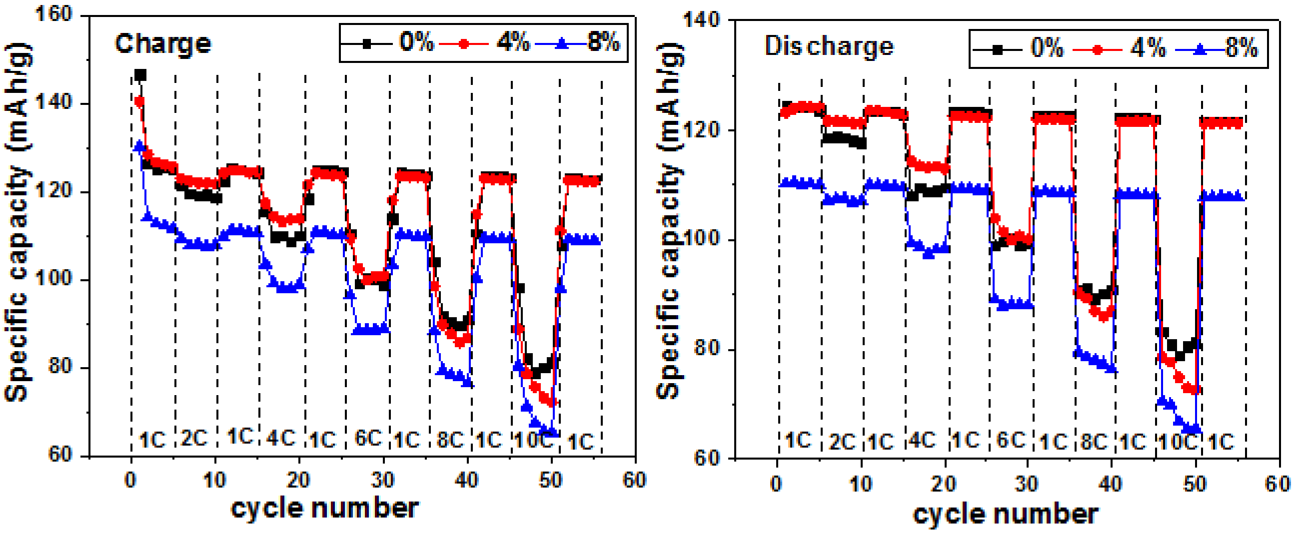

Figure 13. Charge and discharge capacities for calendered films processed from 0, 4 and 8% of modified PVDF.

VI.4. Conclusion

In this work, poly(vinylidene fluoride)-*grafted*-Barium titanate (PVDF-*g*-BaTiO$_3$) nanocomposites was used as binder to prepare cathode material and its effect on the electrochemical performances was investigated. Four formulations were prepared by varying the amount of modified PVDF in the formulation starting with 0, 4, 8 and 12 % of PVDF-*g*-BaTiO$_3$. Cells processed with 4 % of modified PVDF showed similar cycling performances as the ones made by only commercially available PVDF (0 %) while the sample with 8 and 12% were less performant. This could be explained by the low amount and the low molar mass of PVDF in the nanocomposite compared to that of the commercial one. On the other hand, and in order to obtain a uniform structure, the prepared films were calendered. This process induced an enhancement in cycling performances. For instance, the initial discharge capacity at 1C was 124 and 108 mAh/g, and decreased to 82 and 2 mAh/g at 10 C for calendered and non-calendered sample made with commercial PVDF, respectively. In conclusion, calendering procedure proves to have a positive effect on the cycling performances and is worthy to be applied. Moreover, PVDF with high molar mass is also desirable in order to bind well all the particles together on the current collector.

VI.6. References

[1] L. Ramajo, M. Reboredo, M. Castro, Dielectric response and relaxation phenomena in composites of epoxy resin with BaTiO3 particles, Compos. Part A. 36 (2005) 1267–1274. doi:10.1016/j.compositesa.2005.01.026.

[2] Jiongxin Lu, C. Wong, Recent advances in high-k nanocomposite materials for embedded capacitor applications, IEEE Trans. Dielectr. Electr. Insul. 15 (2008) 1322–1328. doi:10.1109/TDEI.2008.4656240.

[3] Y. Kobayashi, T. Tanase, T. Tabata, T. Miwa, M. Konno, Fabrication and dielectric properties of the BaTiO 3 – polymer nano-composite thin films, J. Eur. Ceram. Soc. 28 (2008) 117–122. doi:10.1016/j.jeurceramsoc.2007.05.007.

[4] D. Sinha, P.K.C. Pillai, Ceramic—polymer composites as potential capacitor material, J. Mater. Sci. Lett. 8 (1989) 673–674. doi:10.1007/BF01730438.

[5] L. Zhu, Q. Wang, Novel Ferroelectric Polymers for High Energy Density and Low Loss Dielectrics, Macromolecules. 45 (2012) 2937–2954. doi:10.1021/ma2024057.

[6] Q. Wang, L. Zhu, Polymer Nanocomposites for Electrical Energy Storage, (2011) 1421–1429. doi:10.1002/polb.22337.

[7] Prateek, V.K. Thakur, R.K. Gupta, Recent Progress on Ferroelectric Polymer-Based Nanocomposites for High Energy Density Capacitors: Synthesis, Dielectric Properties, and Future Aspects, Chem. Rev. 116 (2016) 4260–4317. doi:10.1021/acs.chemrev.5b00495.

[8] X. Huang, P. Jiang, Core-Shell Structured High-k Polymer Nanocomposites for Energy Storage and Dielectric Applications, Adv. Mater. 27 (2015) 546–554. doi:10.1002/adma.201401310.

[9] C. Yang, H. Wei, L. Guan, J. Guo, Y. Wang, X. Yan, X. Zhang, S. Wei, Z. Guo, Polymer nanocomposites for energy storage, energy saving, and anticorrosion, J. Mater. Chem. A. 3 (2015) 14929–14941. doi:10.1039/c5ta02707a.

[10] K. Ding, H. Gu, C. Zheng, L. Liu, L. Liu, X. Yan, Z. Guo, Octagonal prism shaped lithium iron phosphate composite particles as positive electrode materials for rechargeable lithium-ion battery, Electrochim. Acta. 146 (2014) 585–590. doi:10.1016/j.electacta.2014.08.141.

[11] J. Xu, S.L. Chou, Q.F. Gu, H.K. Liu, S.X. Dou, The effect of different binders on electrochemical properties of LiNi 1/3Mn1/3Co1/3O2 cathode material in lithium ion batteries, J. Power Sources. 225 (2013) 172–178. doi:10.1016/j.jpowsour.2012.10.033.

[12] A. Kumar, R. Sharma, M.K. Das, P. Gajbhiye, K.K. Kar, Impacts of ceramic filler and the crystallite size of polymer matrix on the ionic transport properties of lithium triflate/poly (vinylidene fluoride-co-hexafluoropropene) based polymer electrolytes, Electrochim. Acta. 215 (2016) 1–11. doi:10.1016/J.ELECTACTA.2016.08.087.

[13] P. Meneghetti, S. Qutubuddin, Synthesis, thermal properties and applications of polymer-clay nanocomposites, Thermochim. Acta. 442 (2006) 74–77. doi:10.1016/j.tca.2006.01.017.

[14] S. Ferrari, J.R. Nair, Y. Zhou, C. Wan, Polymer nanocomposites for lithium battery applications, in: Polym. Nanocomposites Energy Environ. Appl., Elsevier, 2018: pp. 283–313. doi:10.1016/B978-0-08-102262-7.00010-6.

[15] S. Komaba, T. Ozeki, K. Okushi, Functional interface of polymer modified graphite anode, J. Power Sources. 189 (2009) 197–203. doi:10.1016/j.jpowsour.2008.09.092.

[16] J. Chong, S. Xun, H. Zheng, X. Song, G. Liu, P. Ridgway, J.Q. Wang, V.S. Battaglia, A comparative study of polyacrylic acid and poly(vinylidene difluoride) binders for spherical natural graphite/LiFePO 4 electrodes and cells, J. Power Sources. 196 (2011) 7707–7714. doi:10.1016/j.jpowsour.2011.04.043.

[17] V.H. Nguyen, W.L. Wang, E.M. Jin, H.B. Gu, Impacts of different polymer binders on electrochemical properties of LiFePO 4 cathode, Appl. Surf. Sci. 282 (2013) 444–449. doi:10.1016/j.apsusc.2013.05.149.

[18] S.S. Jeong, N. Böckenfeld, A. Balducci, M. Winter, S. Passerini, Natural cellulose as binder for lithium battery electrodes, J. Power Sources. 199 (2012) 331–335. doi:10.1016/j.jpowsour.2011.09.102.

[19] M.J. Lacey, F. Jeschull, K. Edstro, D. Brandell, Porosity Blocking in Highly Porous Carbon Black by PVdF Binder and Its Implications for the Li−S System, (2014). doi:10.1021/jp508137m.

[20] M. Zheng, X. Fu, Y. Wang, J. Reeve, L. Scudiero, W.-H. Zhong, Poly(Vinylidene Fluoride)-Based Blends as New Binders for Lithium-Ion Batteries, ChemElectroChem. 5 (2018) 2288–2294. doi:10.1002/celc.201800553.

[21] M. Wang, J. Hu, Y. Wang, Y.-T. Cheng, The Influence of Polyvinylidene Fluoride (PVDF) Binder Properties on LiNi 0.33 Co 0.33 Mn 0.33 O 2 (NMC) Electrodes Made by a Dry-Powder-Coating Process , J. Electrochem. Soc. 166 (2019) A2151–A2157. doi:10.1149/2.1171910jes.

[22] R. Wang, L. Feng, W. Yang, Y. Zhang, Y. Zhang, W. Bai, B. Liu, W. Zhang, Y. Chuan, Z. Zheng, H. Guan, Effect of Different Binders on the Electrochemical Performance of Metal Oxide Anode for Lithium-Ion Batteries, Nanoscale Res. Lett. 12 (2017). doi:10.1186/s11671-017-2348-6.

[23] F.E. Bouharras, M. Raihane, G. Silly, C. Totee, B. Ameduri, Core shell structured Poly(Vinylidene Fluoride) -grafted- BaTiO3 nanocomposites prepared via Reversible Addition fragmentation chain transfer (RAFT) polymerization of VDF for high energy storage capacitors, Polym. Chem. 10 (2019) 891–904. doi:10.1039/C8PY01706A.

[24] J. Chen, J. Liu, Y. Qi, T. Sun, X. Li, Unveiling the roles of binder in the mechanical integrity of electrodes for lithium-ion batteries, J. Electrochem. Soc. 160 (2013). doi:10.1149/2.088309jes.

[25] G. Liu, H. Zheng, A.S. Simens, A.M. Minor, X. Song, V.S. Battaglia, Optimization of acetylene black conductive additive and PVDF composition for high-power rechargeable lithium-ion cells, J. Electrochem. Soc. 154 (2007). doi:10.1149/1.2792293.

[26] C. Meyer, H. Bockholt, W. Haselrieder, A. Kwade, Characterization of the calendering process for compaction of electrodes for lithium-ion batteries, J. Mater. Process. Technol. 249 (2017) 172–178. doi:10.1016/j.jmatprotec.2017.05.031.

[27] C. Meyer, M. Kosfeld, W. Haselrieder, A. Kwade, Process modeling of the electrode calendering of lithium-ion batteries regarding variation of cathode active materials and mass loadings, J. Energy Storage. 18 (2018) 371–379. doi:10.1016/j.est.2018.05.018.

[28] C. Sangrós Giménez, B. Finke, C. Schilde, L. Froböse, A. Kwade, Numerical

simulation of the behavior of lithium-ion battery electrodes during the calendaring process via the discrete element method, Powder Technol. 349 (2019) 1–11. doi:10.1016/j.powtec.2019.03.020.

[29] H. Zheng, L. Tan, G. Liu, X. Song, V.S. Battaglia, Calendering effects on the physical and electrochemical properties of Li[Ni 1/3Mn 1/3Co 1/3]O 2 cathode, J. Power Sources. 208 (2012) 52–57. doi:10.1016/j.jpowsour.2012.02.001.

[30] Y. Cai, Y. Huang, X. Wang, D. Jia, W. Pang, Z. Guo, Y. Du, X. Tang, Facile synthesis of LiMn2O4 octahedral nanoparticles as cathode materials for high capacity lithium ion batteries with long cycle life, J. Power Sources. 278 (2015) 574–581. doi:10.1016/j.jpowsour.2014.12.082.

[31] P. Ragupathy, H.N. Vasan, N. Munichandraiah, Microwave driven hydrothermal synthesis of LiMn2O4 nanoparticles as cathode material for Li-ion batteries, Mater. Chem. Phys. 124 (2010) 870–875. doi:10.1016/j.matchemphys.2010.08.014.

[32] H. Şahan, H. Göktepe, Ş. Patat, A Novel Method to Improve the Electrochemical Performance of LiMn2O4 Cathode Active Material by CaCO3 Surface Coating, J. Mater. Sci. Technol. 27 (2011) 415–420. doi:10.1016/S1005-0302(11)60084-4.

[33] D. Guo, B. Li, Z. Chang, H. Tang, X. Xu, K. Chang, E. Shangguan, X.Z. Yuan, H. Wang, Facile synthesis of LiAl 0.1 Mn 1.9 O 4 as cathode material for lithium ion batteries: Towards rate and cycling capabilities at an elevated temperature, Electrochim. Acta. 134 (2014) 338–346. doi:10.1016/j.electacta.2014.04.117.

[34] Y. Xia, H. Takeshige, H. Noguchi, M. Yoshio, Studies on an LiMnO spinel system (obtained by melt-impregnation) as a cathode for 4 V lithium batteries part 1. Synthesis and electrochemical behaviour of LixMn2O4, J. Power Sources. 56 (1995) 61–67. doi:10.1016/0378-7753(95)80009-6.

[35] C.F. Oladimeji, P.L. Moss, M.H. Weatherspoon, Analyses of the Calendaring Process for Performance Optimization of Li-Ion Battery Cathode, Adv. Chem. 2016 (2016) 1–7. doi:10.1155/2016/7395060.

[36] A.M. Hashem, S.M. Abbas, X. Hou, A.E. Eid, A.E. Abdel-Ghany, Facile one step synthesis method of spinel LiMn2O4 cathode material for lithium batteries, Heliyon. 5 (2019). doi:10.1016/j.heliyon.2019.e02027.

[37] Y. Huang, H. Yang, Y. Zhang, Y. Zhang, Y. Wu, M. Tian, P. Chen, R. Trout, Y. Ma, T.-H. Wu, Y. Wu, N. Liu, A safe and fast-charging lithium-ion battery anode using MXene supported Li 3 VO 4 †, (2019). doi:10.1039/c9ta02037c.

[38] Q. Li, Q. Wei, J. Sheng, M. Yan, L. Zhou, W. Luo, R. Sun, L. Mai, Mesoporous Li3VO4/C Submicron-Ellipsoids Supported on Reduced Graphene Oxide as Practical Anode for High-Power Lithium-Ion Batteries, Adv. Sci. 2 (2015). doi:10.1002/advs.201500284.

[39] J.M. Tarascon, D. Guyomarb, Li Metal-Free Rechargeable Batteries Based on Li1+xMn2O4 Cathodes (0 ≤ x ≤ 1) and Carbon Anodes, J. Electrochem. Soc. 138 (1991) 2864–2868. doi:10.1149/1.2085331.

[40] S. Kim, M. De, J.G. Alauzun, N. Louvain, N. Brun, D.J. Macquarrie, L. Stievano, B. Boury, L. Monconduit, P.H. Mutin, Alginic acid-derived mesoporous carbon (Starbon®) as template and reducing agent for the hydrothermal synthesis of mesoporous LiMn 2 O 4 grafted with carbonaceous species, J. Mater. Chem. A. 6 (2018) 14392–14399.

doi:10.1039/c8ta04128h.

Conclusions and perspectives

This PhD thesis work investigated the synthesis and characterization of core-shell structured nanocomposites based on $BaTiO_3$ nanoparticles and fluoropolymers as well as the investigation of their dielectric properties and their applications in batteries. Though several nanocomposite systems based on $BaTiO_3$ have been studied previously, Chapter I highlights various strategies, properties and applications on the design of $BaTiO_3$@polymer/Fluorinated polymer nanocomposites. In order to obtain promising performances for energy storage application, major efforts have been conducted to combine the efficient properties and high dielectric constant of ceramics with the flexibility and easy processing of polymers. Actually, it is obvious that the dielectric features of both ceramics and polymers will have an influence on the dielectric properties of the resulting nanocomposites. Nevertheless, it is worth mentioning that the processing method used to get such a material will also have an effect. Indeed, several strategies have been used to prepare these nanocomposites including the hot pressing, spin coating and melt stretching.

However, before combining the inorganic fillers with the organic polymer matrix, the surface functionalization of the ceramic must be first achieved. Indeed, this surface modification is a crucial step in the synthesis process by allowing good compatibility and dispersion of ceramic nanofiller into polymer matrix

In the present work, the "grafting from" strategy was adopted to prepare nanocomposites based on PVDF-*g*-$BaTiO_3$ using RAFT polymerization of VDF, and the synthesis and characterizations of such a nanocomposite was described in detail in Chapter 3. The as received $BaTiO_3$ nanoparticles were first surface modified to create xanthate functions for the RAFT polymerization using potassium ethyl xanthate, such decorated xanthates acting as original chain transfer agent. Then, the grafting of PVDF onto the functionalized nanoparticles was achieved by RAFT polymerization of vinylidene fluoride (VDF) using different $BaTiO_3$ concentrations starting from 3, 5, 10 and 20 wt%. Additionally, the effect of such a percentage was carefully studied on the properties of the nanocomposite. Results and especially High Resolution Magic Angle Spinning (HRMAS) spectroscopy and thermogravimetric (TGA) analyses revealed the successful grafting of PVDF onto the functionalized $BaTiO_3$ ceramic. Thermal analysis showed an enhanced thermal stability of the resulting nanocomposites compared to that of pure PVDF polymer. Moreover, HRMAS NMR spectroscopy was used and for the first time to characterize such nanocomposites and evidenced the successful grafting of PVDF onto $BaTiO_3$ surface. The presence of PVDF is also confirmed by Infrared spectroscopy as well as X-ray diffraction, which indicates that the PVDF was produced in its α form.

Chapter 4 presents a detailed study on the dielectric characterization of the aforementioned nanocomposites as well as of the pure PVDF. It was found that all the samples studied exhibited two main relaxations which fits well with the Arrhenius fitting. The first relaxation is the well-known β secondary relaxation in PVDF, while the second one is assigned to the crystalline fraction in the polymer. By applying the electric modulus formalism, that enables to suppress the effect of electrode polarization, a third relaxation appeared in the low frequency region. It is assigned to interfacial polarization resulting from the presence of fillers or even impurities in the system. However, the relaxation related to glass transition temperature could not be observed due to the high crystallinity of the polymer. It was also found that the conductivity of the prepared nanocomposites was independent of the volume fraction of the nanofillers and was close to that of the PVDF, indicating the good insulation properties of these nanocomposites.

In order to further improve the final properties of the prepared nanocomposites, the "core-double shell" approach was used. It consisted on a simple blending and casting of PVDF-*g*-$BaTiO_3$ with poly(VDF-*co*-HFP) copolymer from the use of solvent that enabled the blending and with a suitable low boiling point. The prepared films were fully characterized using spectroscopic, thermal and morphological analyses. Dielectric measurements revealed the existence of three relaxations; α_a assigned to the glass transition, α_c related to crystalline fraction in the copolymer and the one attributed to the conductivity process. Mechanical analysis showed an enhancement in Young's modulus of the nanocomposite films compared to that of the pristine copolymer, which results from the uniform distribution of PVDF-*g*-$BaTiO_3$ nanocomposites having strong interactions with poly(VDF-*co*-HFP) copolymer matrix.

Last but not least, the prepared PVDF-*g*-$BaTiO_3$ nanocomposites were tested as a binder to prepare cathode material for batteries, and this study is reported in Chapter 6. First, the effect of modified PVDF (*i.e.* PVDF-*g*-$BaTiO_3$) on the electrochemical performances was investigated showing that this later does not involve any electrochemical activity. Then, formulations based on 70 wt% of active material ($LiMn_2O_4$), 18 wt% of conductive agent (carbon black) and 12 wt% of binder (commercially available PVDF, modified PVDF or both) were processed. Four formulations were prepared by varying the amount of modified PVDF starting with 0, 4, 8 and 12 wt% of PVDF-*g*-$BaTiO_3$. It was found that cells made with

4 wt% of modified PVDF exhibited similar cycling performances as the ones made only with commercial PVDF (0 wt%), while the samples with 8 and 12 wt% demonstrated a less important behaviour. This was explained by the low amount and the low molar mass of PVDF present in the nanocomposite materials compared to that of the commercial one.

In order to obtain homogenous films and to get a better dispersity of nanoparticles, calendering procedure was used. This technique enabled to obtain electrode films with uniform structure, and this was well noted in the almost reproducible tests performed on the different cells of the same formulation. Besides the reduction of volumetric density of the electrode film, the calendering has an effect on other physical properties, including the interparticle contacts. Thus, the enhancement seen in cycling performances after calendering procedure could be explained by the increased ohmic contact area at the electrode-current collector interface.

On the light of the above results, this thesis work focused on the synthesis, characterization and possible application of nanocomposite materials in the field of energy storage. The energy density characterizing the storage capacity of a dielectric material is related to both its dielectric permittivity and electric breakdown strength. In the present work, only dielectric properties of the prepared nanocomposites were studied and, in order to get better performances, it is required to: i) use a filler (*e.g.* $BaTiO_3$) with a different shape (*e.g.* nanowires or nanorods instead of spherical one as disclosed in that present study) that make straightforward the dipole orientation when a current is applied leading to enhanced dielectric constant and ii) promote the formation of β phase of PVDF in the nanocomposite either by stretching or applying high voltage.

In the present study, we were unable to visualize the relaxation attributed to the glass transition temperature in the prepared PVDF-*g*-$BaTiO_3$ nanocomposites, and this was explained by the high crystallinity of the formed PVDF. However, an extensive study can be conducted using dilatometry analysis to verify the presence of the aforementioned relaxation.

Other strategies to prepare nanocomposite materials based on fluorinated polymers could be also adapted (*e.g.* click chemistry and ATRP polymerization). Moreover, it would be of interest to use fluorinated coupling agents to modify the filler surface in order to enhance the interface between the filler and polymer matrix.

Then, in order to enhance the use of these nanocomposites as binders in batteries, it is required to have PVDF grafted onto $BaTiO_3$ with high molar mass, to ensure high binding of all particles together on the current collector.

Résumé Général de la Thèse en Français

Résumé Général de la Thèse

1. Contexte général

Les matériaux diélectriques à constantes diélectriques élevées ont attiré une attention significative ces dernières années en raison de leur large éventail d'applications potentielles dans l'industrie électronique, notamment dans les dispositifs de stockage de l'énergie [1–4]. En effet, la densité d'énergie, Ue, caractérisant la capacité de stockage des matériaux diélectriques, peut être définie comme $Ue = 1 / 2\varepsilon\varepsilon_0 E_b^2$, où E_b, ε et ε_0 désignent respectivement la résistance au claquage électrique, la constante diélectrique et la constante diélectrique sous vide des matériaux [5–7]. Par conséquent, la densité d'énergie peut être améliorée soit en augmentant la constante diélectrique, soit en augmentant la résistance au claquage électrique des matériaux.

En effet, une valeur de permittivité diélectrique élevée peut être obtenue à partir de matériaux céramiques tel que les titanates de Barium ($BaTiO_3$). Cependant, ces dernières possèdent, généralement une faible résistance à la rupture. Comparés à leurs homologues en céramique, les polymères diélectriques présentent des résistances à la rupture diélectrique (claquage) plus élevées et une plus grande fiabilité, ils sont légers et peuvent être mise en forme sous des configurations complexes, et sont par conséquent un choix idéal pour de nombreuses applications en électronique de puissance. Cependant, leur faible valeur de permittivité diélectrique (les polymères hydrocarbonés possèdent généralement des permittivités de 2-5) limite toujours la densité d'énergie de stockage et ainsi leurs applications dans la prochaine génération de dispositifs de stockage d'énergie [8]. Ainsi, l'approche nanocomposite capitalise sur l'idée que la combinaison de matériaux inorganiques (par exemple, $BaTiO_3$) de grande permittivité avec des polymères de haute résistance à la rupture peut conduire à des matériaux ayant une grande capacité de stockage d'énergie. De plus, les nanocomposites polymères sont légers, mécaniquement souples et conservent une excellente performance diélectrique et capacitive après des cycles de flexion intensifs. Ces résultats permettent d'élargir le domaine d'utilisation des matériaux organiques dans les dispositifs électroniques de stockage de l'énergie à haute température.

En effet, les propriétés physico-chimiques uniques (par exemple, une grande énergie de surface) des nanoparticules provoquent inévitablement une agrégation et une inhomogénéité dans la matrice polymère [9], en particulier dans le cas où une concentration élevée en nanoparticules est utilisée. Il est bien connu que l'agrégation de nanoparticules donne lieu à une très faible résistance à la rupture et des vides indésirables entraînant une détérioration des propriétés électriques des nanocomposites polymères [10]. Les défis typiques impliquent la réalisation de dispersions homogènes de nanoparticules et l'adaptation de l'interface polymère/nanoparticules. Par conséquent, leur modification de surface et leur fonctionnalisation, y compris par des agents de couplage ou des polymères flexibles [11–14], est un outil puissant pour améliorer la compatibilité nanoparticules-polymère, entraînant une dispersion homogène des nanoparticules et donc une augmentation significative de la densité énergétique des nanocomposites résultants.

Les nanocomposites à base de polymères fluorés ferroélectriques (par exemple, poly (fluorure de vinylidène), PVDF) ont reçu beaucoup d'attention dans les applications de haute technologie telle que l'utilisation de matériaux à haute densité d'énergie en raison de leurs constantes diélectriques élevées (~10 à 1 kHz) [15–17]. Malgré leurs nombreux avantages potentiels, les propriétés finales de ces nanocomposites sont étroitement associées aux méthodes de traitement des matériaux. Les méthodes de synthèse conventionnelles (par exemple, un simple mélange mécanique [18] et un mélange en solution [11]) entraînent des propriétés électriques indésirables (par exemple, une diminution de la résistance à la rupture). De nombreuses études ont été consacrées à la préparation et aux propriétés diélectriques des nanocomposites constitués de polymères à base de PVDF avec différentes modification de surface des nanoparticules $BaTiO_3$ [19–22]. Prateek *et al.* [23] ont examiné en détail l'utilisation du PVDF et ces copolymères binaires / ternaires (par exemple, poly (VDF-*co*-hexafluoropropène) poly(VDF-*co*-HFP), poly(VDF-*co*-trifluoroéthylène), poly(VDF-*co*-TrFE), poly(VDF-*co*-chlorotrifluoroéthylène), poly(VDF-*co*-CTFE) et poly(VDF-*ter*-TrFE-*ter* -CTFE) terpolymère)) / nanoparticules $BaTiO_3$ en tant que composants potentiels dans les matériaux nanocomposites diélectriques pour les applications de condensateurs à haute densité d'énergie. Cependant, les copolymères à base de VDF sont généralement non miscibles avec la plupart des matériaux organiques et inorganiques en raison de leur faible énergie de surface, et les stratégies traditionnelles (par exemple, le mélange en solution) utilisées pour la modification des nanoparticules par des agents hydrocarbonés conduisent toujours à une agglomération de charge et des vides dans le nanocomposite final [24].

Pour surmonter cet inconvénient, la fonctionnalisation de surface des nanoparticules de $BaTiO_3$ avec des agents de couplage fluorés (par exemple, le perfluoroalkylsilane [13] , l'acide fluorophtalique [25]) et les polymères fluorés (c'est-à-dire le poly(méthacrylate de 2,2,2-trifluoroéthyle)) [26], poly(méthacrylate de 1H, 1H, 2H, 2H-perfluorooctyle) [27], poly (acrylate de 2,2,2-trifluoroéthyle), poly(acrylate de 1H, 1H, 2H, 2H-hepta- décafluorodécyle) [28] et poly (2,5-bis [(4-trifluorométhoxyphényl) oxycarbonyl] styrène) [4]), ont été utilisés. Ces derniers conduisent à une amélioration de l'interface agents fluorés / polymères à base de PVDF en utilisant le procédé de mélange en solution. Cependant, même si les forces d'interaction entre les polymères PVDF et le $BaTiO_3$ modifié avec du fluor sont plus fortes que celles établies avec des agents non-fluorées, ces procédés ont encore certaines limites pour réaliser des nanocomposites de haute permittivité car les agents modifiants eux-mêmes ne jouent généralement pas un rôle significatif dans le stockage d'énergie [29].

Afin d’améliorer les propriétés des nanocomposites, des efforts importants ont été récemment consacrés sur la conception et la synthèse de nanocomposites core-shell. Plus récemment, la préparation de nanoparticules structurées à constante diélectrique élevée par polymérisation radicalaire contrôlée *in situ* (*e.g.* polymérisation radicalaire par transfert d'atomes (ATRP) [26,30] et polymérisation par transfert de chaîne réversible par addition-fragmentation (RAFT) [31,32]) a suscité beaucoup d'intérêt via la technique du «*grafting from*» [27,30]. Comparativement aux méthodes conventionnelles, cette technique offre de nombreux avantages tels que: (i) les couches du polymère greffé sur les surfaces des nanoparticules sont solidement liées sur les surfaces des nanoparticules (par des liaisons chimiques), résultant en une forte interface nanoparticule/matrice et empêchant l'agrégation des nanoparticules, (ii) la concentration en nanoparticules peut être ajustée en ajustant le rapport d'alimentation en nanoparticules fonctionnalisées/monomère.

Ainsi, l'objectif de ce travail de thèse consiste en la synthèse et la caractérisation de nanocomposites structurés à base de céramiques $BaTiO_3$ incorporés dans une matrice de polymères fluorés pour des applications de stockage d'énergie.

2. Synthèse de nanocomposites PVDF-*g*-$BaTiO_3$ par polymérisation RAFT

Dans une première partie, nous nous sommes intéressés à la préparation de nanocomposites structurés de type Core Shell PVDF-*g*-$BaTiO_3$ *via* une polymérisation par transfert de chaîne réversible par addition fragmentation (RAFT). La charge céramique est modifiée dans un premier temps par un agent RAFT afin de créer des fonctions xanthates sur sa surface. Ses fonctions ont permis par la suite le greffage du VDF à partir des sites fonctionnalisés. L'effet de l'addition de la charge sur les propriétés du nanocomposite est étudié en utilisant différentes teneurs en poids de $BaTiO_3$ à savoir, 3, 5 10 et 20 %. Les nanocomposites ainsi préparés ont été caractérisés par différentes techniques d'analyses.

La procédure générale de préparation des nanocomposites PVDF-*g*-$BaTiO_3$ *via* la polymérisation par transfert de chaîne par addition fragmentation réversible est illustrée par le Schéma 1.

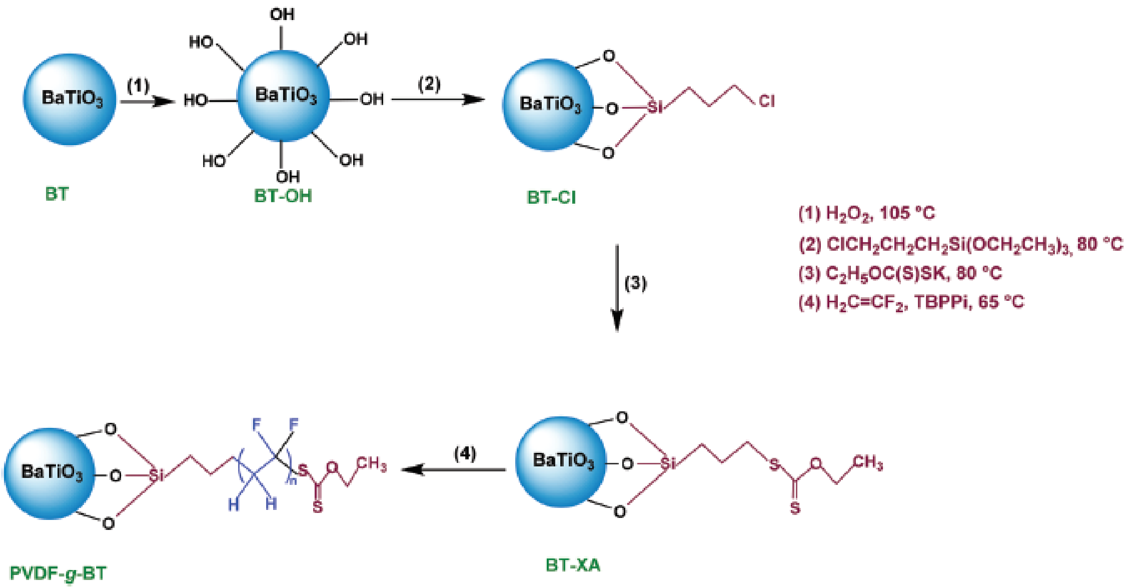

Schéma 1. Procédure générale pour la synthèse de nanocomposite PVDF-*g*-$BaTiO_3$ *via* la polymérisation RAFT.

La synthèse envisagée comprend quatre étapes : la première étape consiste en l'oxydation des nanoparticules $BaTiO_3$ en les dispersant dans l'eau oxygénée à 105 °C pendant 4 heures (étape 1, schéma 1). En fin de réaction, les nanoparticules sont récupérées par centrifugation puis séchées sous vide jusqu'à l'obtention d'une masse constante. La création des groupements OH sur la surface des nanoparticules a permis la fixation d'un agent silane (3-chloropropyl triéthoxysilane (CPTS)) dans une deuxième étape (étape 2, schéma 1). Cette réaction est à 80 °C pendant 12 heures pour conduire à des nanoparticules fonctionnalisées présentant une terminaison chlore qui vont permettre par la suite à la fixation de l'agent RAFT. Durant cette troisième étape, la réaction se produit à 80 °C pendant 12 heures (étape 3, schéma 1). Finalement, la dernière étape concerne la polymérisation du VDF amorcée par des peroxides et contrôlée par des fonctions xanthate fonctionnalisées sur le $BaTiO_3$ (étape 4, schéma 1).

Les nanoparticules $BaTiO_3$ possèdent peu de groupements OH sur leurs surface, ce qui rend difficile leurs manipulations [33]. Ainsi, la première étape étant l'oxydation de $BaTiO_3$, suivie par l'insertion des fonctions xanthates qui vont assurer le contrôle de la polymérisation du VDF amorcée par les peroxides [34–36]. Les nanocomposites PVDF-*g*-$BaTiO_3$ ont été préparés via une polymérisation RAFT du VDF à partir de BT-XA en utilisant le *tert*-butyl peroxypivalate comme amorceur à 65 °C pendant 15 h. Il a été reporté que la polymérisation RAFT est un outil qui permet de contrôler de contrôler l'épaisseur de l'écorce du nanocomposite en variant la teneur du polymère. En effet, Chen *et al.*[4] ont montré que l'épaisseur du Shell peut être contrôlée par le DPn lors la polymérisation RAFT. Dans ce travail, quatre ratio [BT-XA] :[VDF] ont été choisis (3,5, 10 et 20 wt %).

Les résultats ont montré que la modification de surface est réussie et le greffage de PVDF sur $BaTiO_3$ a conduit à des nanocomposites possédant des propriétés thermiques améliorées. En effet, tous les nanocomposites de PVDF-*g*-$BaTiO_3$ présentent une stabilité thermique significativement meilleure avec une augmentation de 52-76 °C des températures de début de dégradation, par rapport à celle du PVDF pur qui commence à se décomposer à 339 °C (Figure 1).

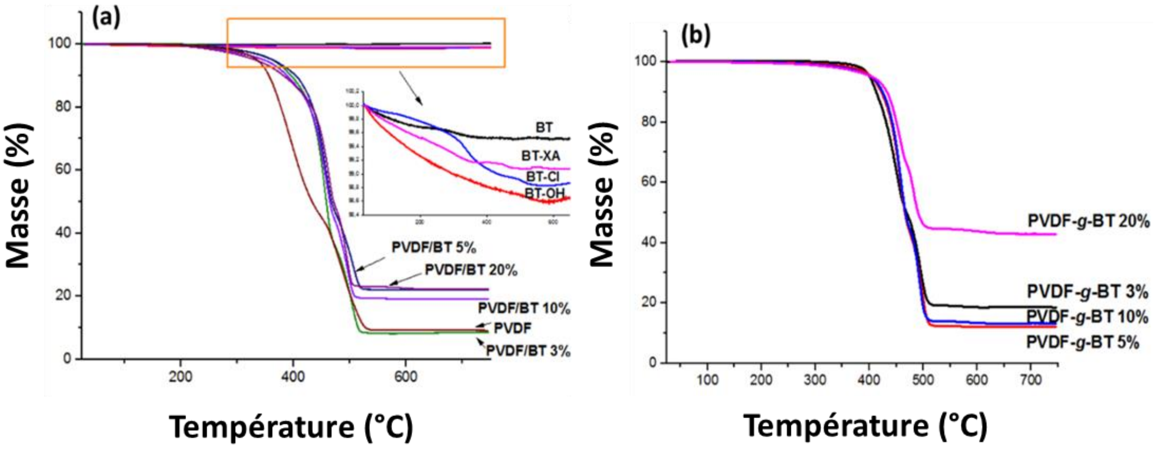

Figure 1. Thermogrammes ATG (sous air) de (a) nanoparticules BaTiO$_3$ modifiées et nanocomposites (BaTiO$_3$/PVDF) non purifié et (b) Thermogramme ATG des nanocomposites PVDF-*g*-BaTiO$_3$ purifiés après différents traitements de lavage.

En effet, l'incorporation des BaTiO$_3$ organomodifiés bien dispersées dans la matrice PVDF améliore la stabilité thermique du nanocomposite en agissant comme une barrière de transport de masse aux produits volatils générés lors de la décomposition [37]. De plus, l'augmentation des températures de décomposition des nanocomposites avec les grandes teneurs en BaTiO$_3$ peut être attribuée à la bonne dispersion et les pourcentages élevés des nanocharges. De plus, l'élimination du PVDF physisorbé de BaTiO$_3$/PVDF pendant le traitement de lavage conduit à une amélioration de la stabilité thermique du nanocomposite résultant où les chaines de PVDF sont liées de façon covalente au BaTiO$_3$. En effet, les décompositions thermiques des nanocomposites BaTiO$_3$ PVDF avant purification sont inférieures à celles du PVDF greffé sur BaTiO$_3$. Ceci peut être expliqué par la faible interaction physique entre le PVDF libre (un polymère fluoré difficilement « miscible » ou compatible avec d’autres matériaux) et le PVDF-*g*-BaTiO$_{3.}$

La meilleure preuve du succès du greffage du PVDF sur la surface de BT a été donnée par la spectroscopie RMN HRMAS. La RMN HRMAS de PVDF-g-BaTiO$_3$ dans le DMSO-d$_6$ fourni les signaux caractéristiques attribués aux divers groupements du PVDF (addition normales et inverses du VDF) et surtout l’unité VDF adjacente à la fonction xanthate située à -70 ppm attestant ainsi le greffage du PVDF. La Figure 2 montre le spectre HRMAS ^{19}F du nanocomposite PVDF-g-BaTiO$_3$ préparé avec 3% en poids de BaTiO$_3$.

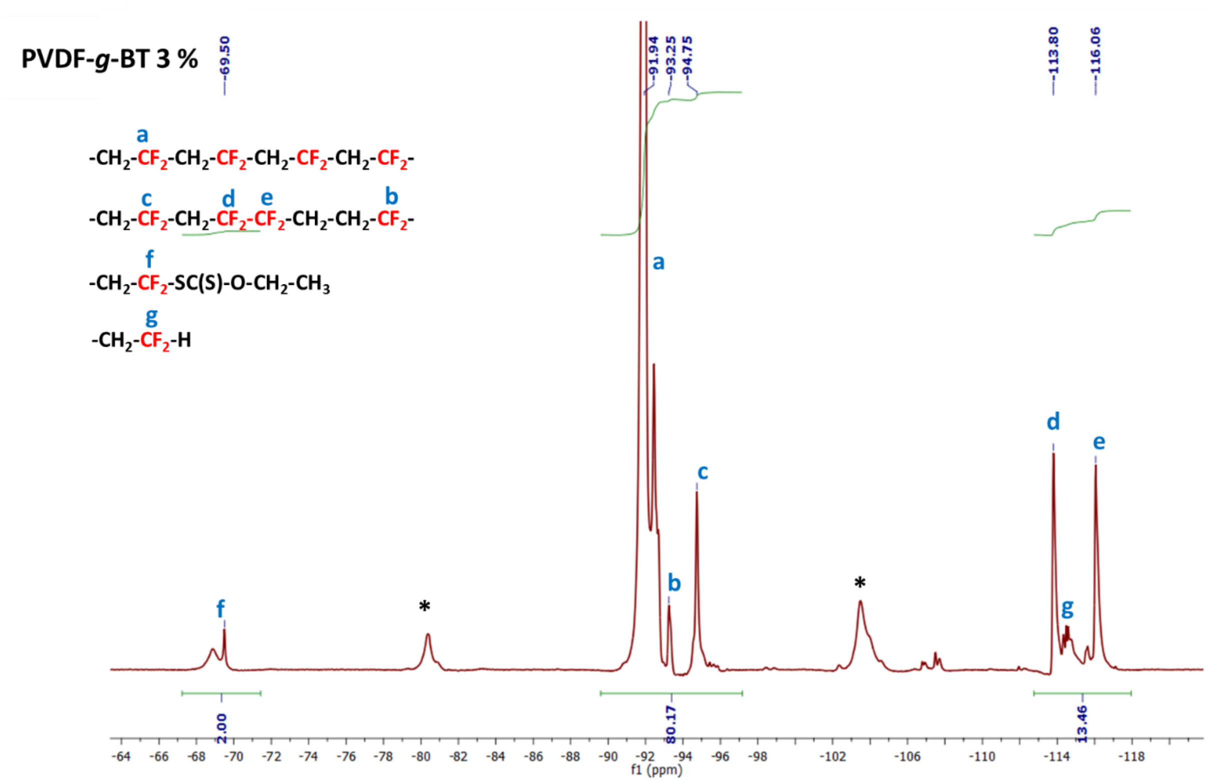

Figure 2. Expansion de la région -64 à -120 ppm du spectre ^{19}F HRMAS enregistré dans le d_6-DMSO du nanocomposite PVDF-*g*-$BaTiO_3$ contenant 3% en poids de $BaTiO_3$ (* correspondant aux bandes de rotation).

Ce spectre a été enregistré avec du DMF deutéré qui gonfle le PVDF situé à la surface de $BaTiO_3$. Le signal intense à -92 ppm est caractéristique de l'addition HT de VDF (-CH_2-**CF_2**-CH_2-**CF_2**-CH_2-**CF_2**-CH_2-**CF_2**-) [35,36,38,39]. Des signaux à -114 ppm et -116 ppm sont attribués à des défauts de chaîne causés par des ajouts inversés de VDF (-CH_2-CF_2-CH_2-**CF_2**-CF_2-CH_2-CH_2-CF_2-) et (-CH_2-CF_2-CH_2-CF_2-**CF_2**-CH_2-CH_2-CF_2-) respectivement [40]. Un signal à -70 ppm est relatif à l'addition HT normale adjacente au groupe xanthate -CH_2-**CF_2**-SCS-O-CH_3 [35,38,39].

Le succès de l'introduction du PVDF sur les nanoparticules fonctionnalisées a été aussi montré par analyses Infra-rouge et diffraction des rayons X, qui ont révélé que le PVDF existe uniquement sous sa forme cristalline α. L'épaisseur du shell déterminé par le microscope électronique à transmission (MET) indique que la diminution de la teneur de $BaTiO_3$ conduit à une augmentation de l'épaisseur de 2.2 nm à 5.1 nm pour les nanocomposites préparés respectivement avec 3 wt% et 20 wt% (Figure 3).

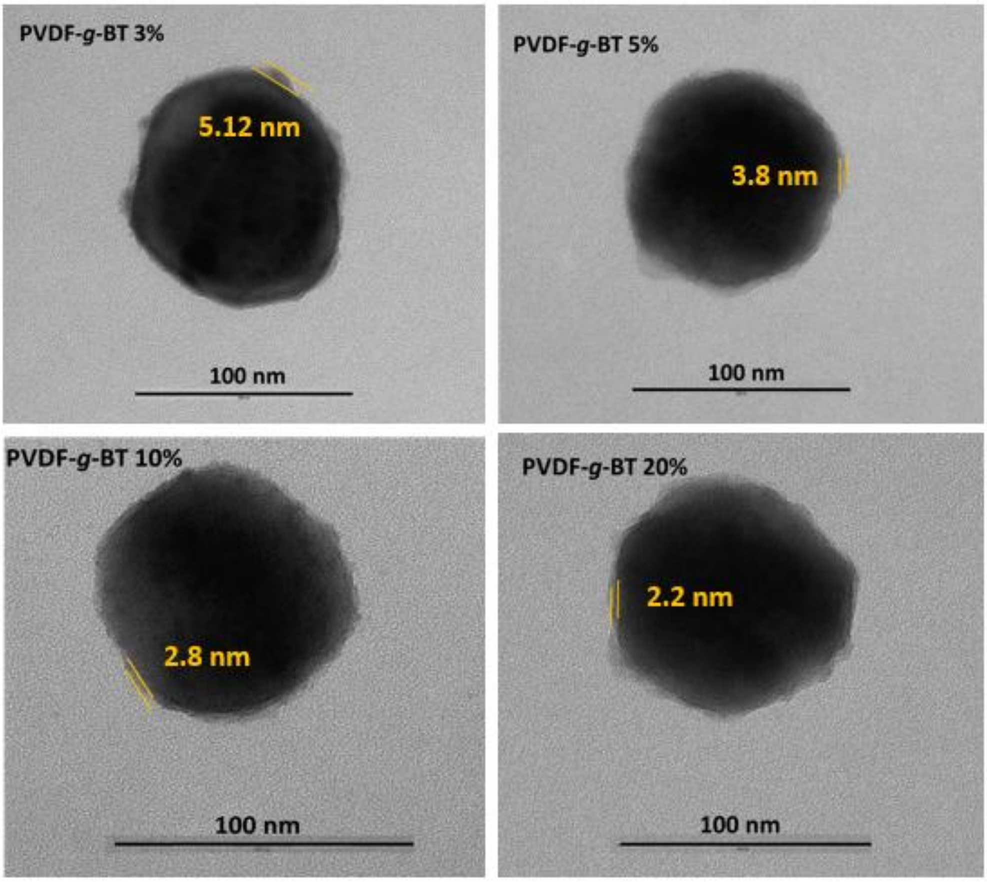

Figure 3. Images MET des nanocomposites PVDF-*g*-BT avec différentes teneurs en poids de $BaTiO_3$ (3, 5, 10 et 20 %).

3. Etude des propriétés diélectriques des nanocomposites PVDF-*g*-$BaTiO_3$

Après avoir prouvé le succès du greffage des chaines du PVDF sur les nanoparticules fonctionnalisées, une étude sur les caractérisations diélectriques des nanocomposites préparés a été menée. Figure 4-a présente la variation de la permittivité de tels composites en fonction de la fréquence à T=20 °C. Il est bien montré que la permittivité du PVDF ainsi que celle des nanocomposites diminue en augmentant la fréquence. Ceci peut être expliqué par le fait que lorsque la fréquence augmente, les dipôles des nanocharges et des polymères ne peuvent pas changer leurs orientations très rapidement, ce qui se traduit par une diminution de la permittivité diélectrique du système résultant. D'autre part, l'évolution de la tangente de perte en fonction de la fréquence, (Figure 4-b) présente deux relaxations observées pour le PVDF pur et les nanocomposites préparés à 10^0 Hz et 10^6 Hz. Le premier pic est attribué à la relaxation α_c dû à la phase non polaire du PVDF, tandis que le deuxième pic est relatif à la relaxation secondaire β du PVDF.

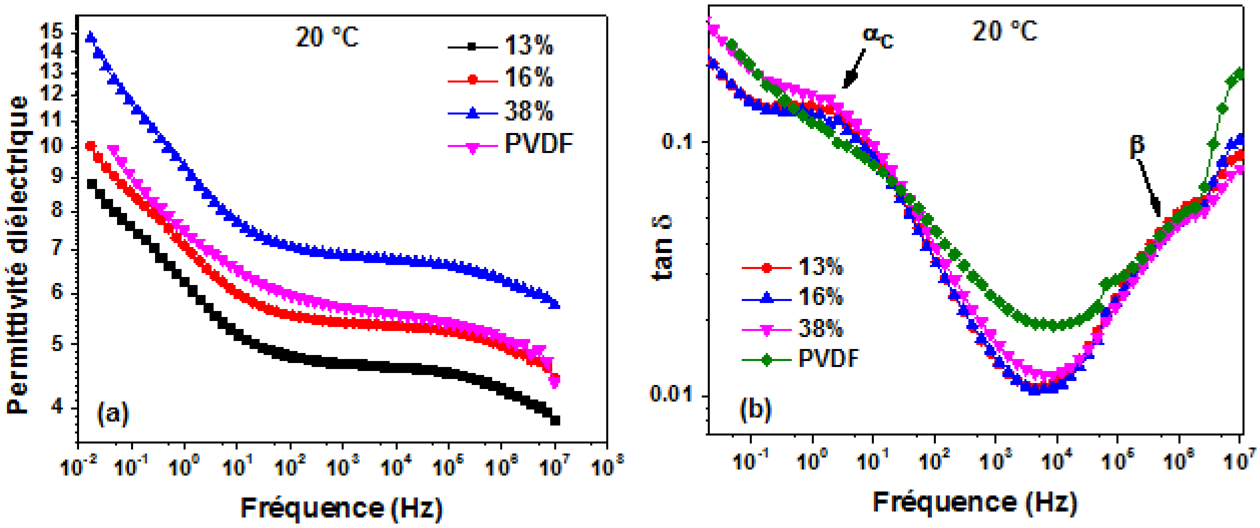

Figure 4. Evolution de la : (a) constante diélectrique et (b) de la tangente de perte pour le PVDF et ses nanocomposites PVDF-*g*-BT à 20 ° C.

En plus des relaxations susmentionnées, une polarisation interfaciale ou polarisation de Maxwell-Wagner-Sillars (MWS) peut également être observée dans ces nanocomposites [41]. En effet, l'augmentation rapide de la permittivité aux basses fréquences est attribuée à la polarisation des électrodes, et l'effet de cette dernière peut masquer complètement les relaxations aux basses fréquences [42]. Pour surmonter à ce problème, McCrum *et al.* [43–45] ont introduit le formalisme du module électrique qui permet la suppression de l'effet de la polarisation des électrodes. Il peut être exprimé par l'équation suivante :

$$M^* = \frac{1}{\varepsilon^*} = M' + jM'' \qquad (1)$$

Avec:

$$M' = \frac{\varepsilon'}{\varepsilon'^2 + \varepsilon''^2}\ , and\ \ M'' = \frac{\varepsilon''}{\varepsilon'^2 + \varepsilon''^2} \qquad (2)$$

La Figure 5 montre le module de perte diélectrique (M") du nanocomposite PVDF pur et des nanocomposites PVDF-*g*-BT en fonction de la fréquence à différentes températures. Contrairement à la Figure 4-b, qui ne révèle que deux pics de relaxation, la Figure 5 révèle trois pics de relaxation. En fait, le troisième pic de relaxation qui apparaît pour T ≥ 30 ° C est attribué à la polarisation interfaciale ou la polarisation MWS. On peut clairement voir que cette relaxation est présente dans le système nanocomposite PVDF-*g*-BT ainsi que dans le PVDF et qu'elle provient de la présence de charges ou même d'impuretés qui présentent des valeurs de permittivité et de conductivité différentes, ce qui se traduit par un système hétérogène [46]. Cependant, la relaxation relative à la transition vitreuse n'a pas été détectée dû à la partie cristalline très élevée dans la structure.

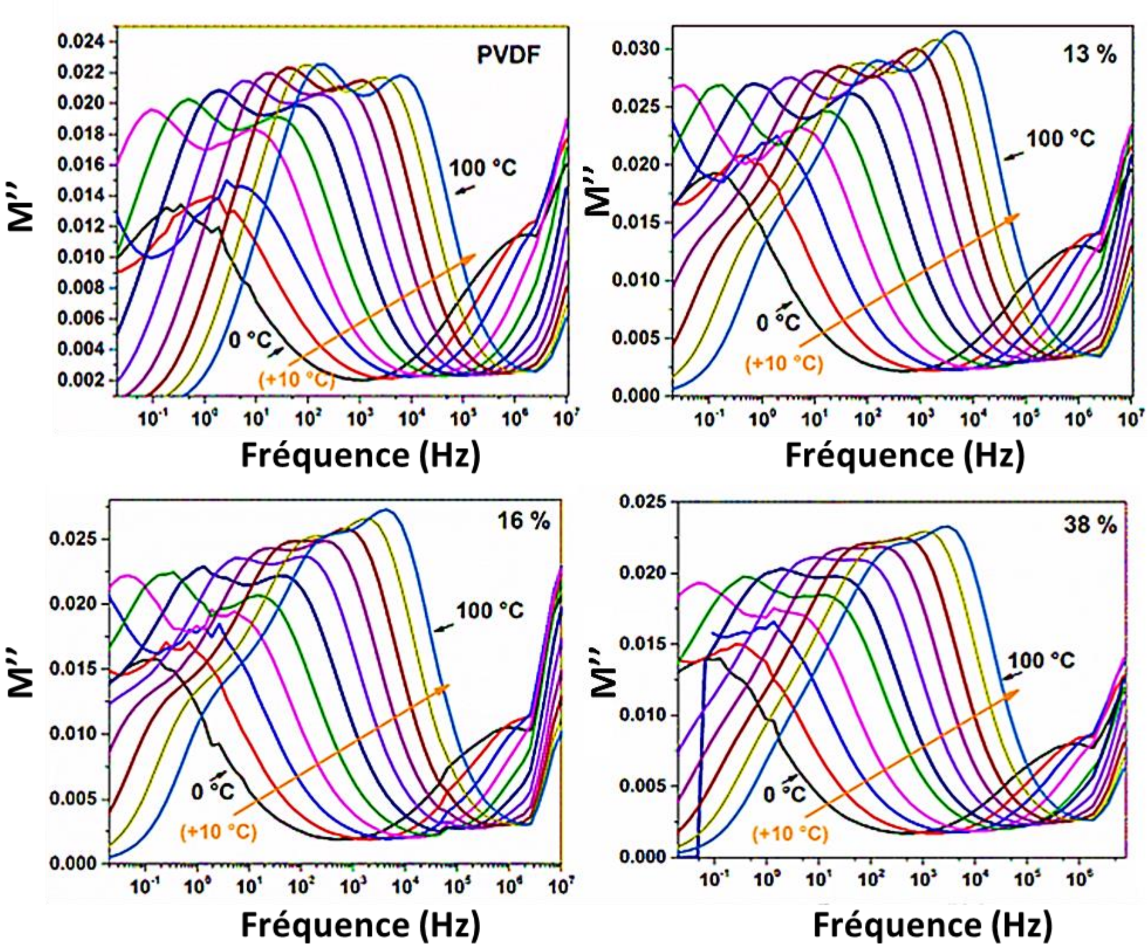

Figure 5. Module de perte diélectrique (M'') en fonction de la fréquence pour le PVDF +et pour les nanocomposites PVDF-*g*-BT à différentes températures.

La Figure 6 montre l'évolution de la conductivité, σ, en fonction de la fréquence pour le PVDF pur et des nanocomposites PVDF-*g*-BT, obtenue à partir de l'équation [47]:

$$\sigma = \varepsilon'' 2\pi f \, \varepsilon_0 \qquad (3)$$

où ε'' désigne le facteur de perte, ε_0 la permittivité de l'espace libre et f la fréquence (Hz).

A partir de la Figure 6, il est montré que la conductivité augmente avec l'augmentation de la fréquence et de la température pour tous les nanocomposites ainsi que pour le PVDF pur. De plus, à 20 °C et sur toute la gamme de fréquences, la conductivité est indépendante de la fraction volumique des charges et proche de celle du PVDF, indiquant les bonnes propriétés isolantes des nanocomposites préparés [48].

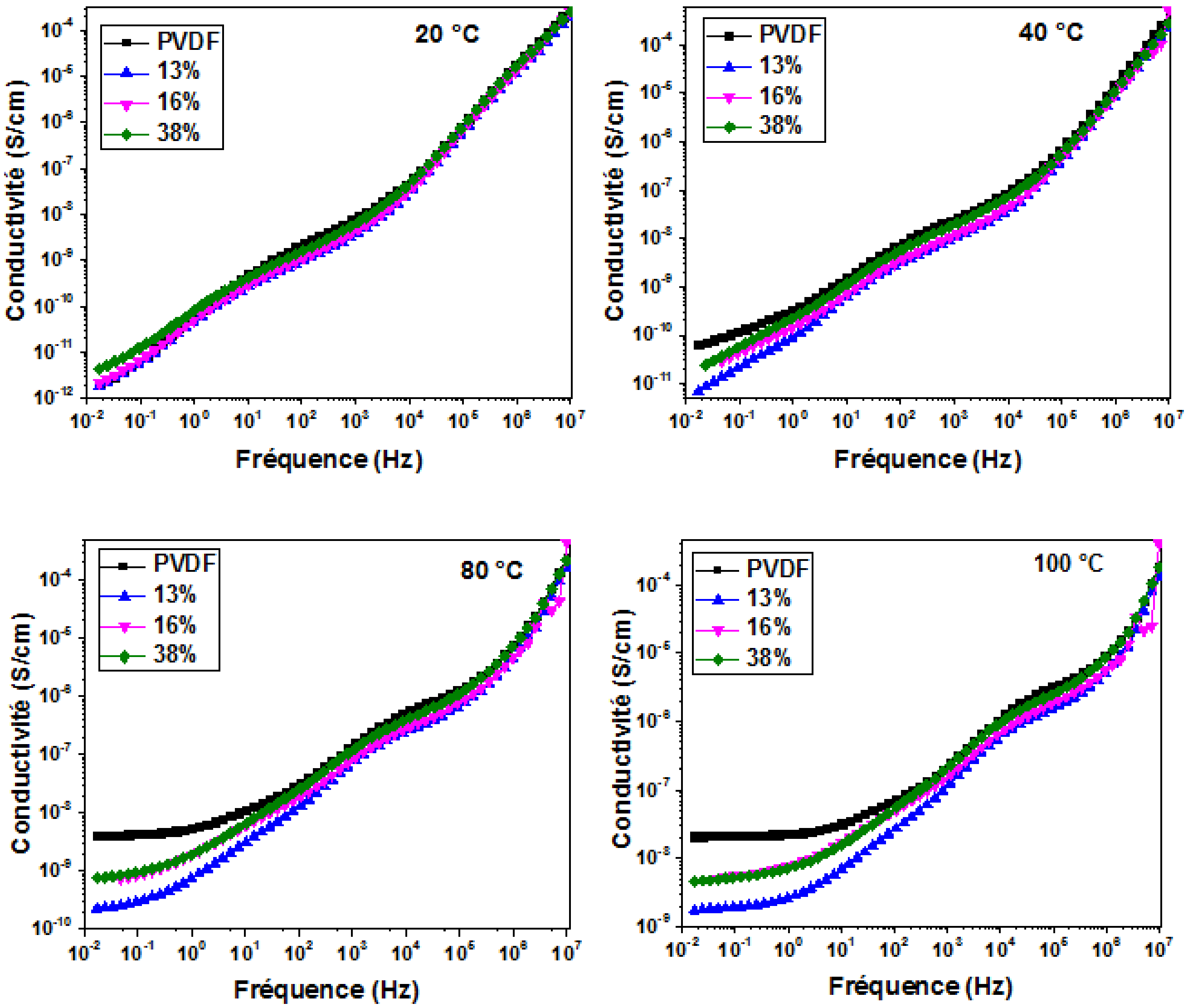

Figure 6. Évolution de la conductivité en fonction de la fréquence pour le PVDF pur et des nanocomposites PVDF-*g*-BT à différentes températures.

4. Synthèse et caractérisations de nanocomposites PVDF-*g*-BaTiO$_3$/Poly(VDF-*co*-HFP) préparé par le mélange en solution

Afin d'améliorer davantage les propriétés finales des nanocomposites préparés, l'approche core-double shell a été utilisée. Elle consistait en un simple mélange de PVDF-*g*-BaTiO$_3$ avec un copolymère de poly(VDF-*co*-HFP) (Figure 7). La nomenclature des films est donnée comme suit :

10-10: PVDF-*g*-BT 10% / Poly(VDF-*co*-HFP) (10/90)

10-20: PVDF-*g*-BT 10% / Poly(VDF-*co*-HFP) (20/80)

20-10: PVDF-*g*-BT 20% / Poly(VDF-*co*-HFP) (10/90)

20-20: PVDF-*g*-BT 20% / Poly(VDF-*co*-HFP) (20/80)

Les films préparés ont été entièrement caractérisés par analyses spectroscopique, thermique et morphologique.

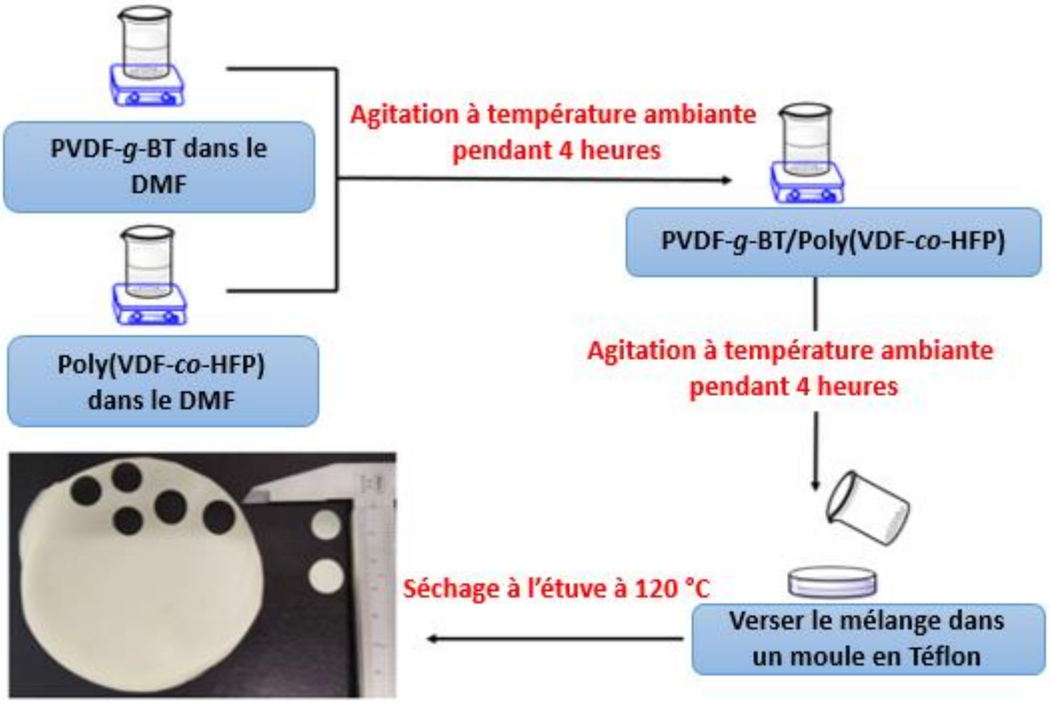

Figure 7. Schéma illustrant le processus de fabrication des différents films en utilisant la technique du mélange en solution.

La stabilité thermique des films a été étudiée par analyse thermogravimétrique. Le Tableau 1 présente les températures de début de dégradation ainsi que les pertes en poids pour les différents films préparés. Le copolymère pur enregistre une température de début de dégradation de 446 ° C pour atteindre 99,9% de perte de poids à 650 ° C. Dans des conditions similaires, la température de début de dégradation du PVDF-*g*-BT / Poly(VDF-*co*-HFP) a été augmentée à 459, 460, 462 et 464 ° C pour les films fabriqués, respectivement, à partir de 10-10, 10-20, 20-10 et 20-20 nanocomposites. Ainsi, l'introduction de nanocomposite PVDF-*g*-BT dans la matrice polymère conduit à une amélioration notable de la stabilité thermique du système.

Tableau 2. Récapitulatif des températures de début de dégradation (sous air) et des pertes de poids pour les films préparés.

Films	T_d *(1) (°C)*	*Perte de masse (%) à 650 °C*
P(VDF-HFP)	446	99.9
10-10	459	99.9
10-20	460	97.8
20-10	462	95.7
20-20	464	94.4

(1) T_d: *Température de début de dégradation.*

D'autres part, l'analyse calorimétrique différentielle a indiqué que la cristallinité des films augmentait de 18 % pour le copolymère pur et atteignait 25 % pour les films nanocomposites 20-20. Ceci suggère que les nanocomposites PVDF-*g*-BT offrent de nombreux sites de nucléation hétérogènes à la matrice poly(VDF-*co*-HFP) conduisant à une augmentation de la cristallinité.

La Figure 8 présente les images MEB des films obtenus pour le poly(VDF-*co*-HFP) ainsi que pour les nanocomposites obtenus. Pour tous les échantillons, il a été observé que les nanocomposites PVDF-*g*-BT sont bien incorporés à l'intérieur du copolymère poly(VDF-*co*-HFP). De plus, il convient de mentionner l'absence d'agglomérats, ce qui indique que les nanocomposites PVDF-*g*-BT sont bien dispersés au sein de la matrice de copolymère.

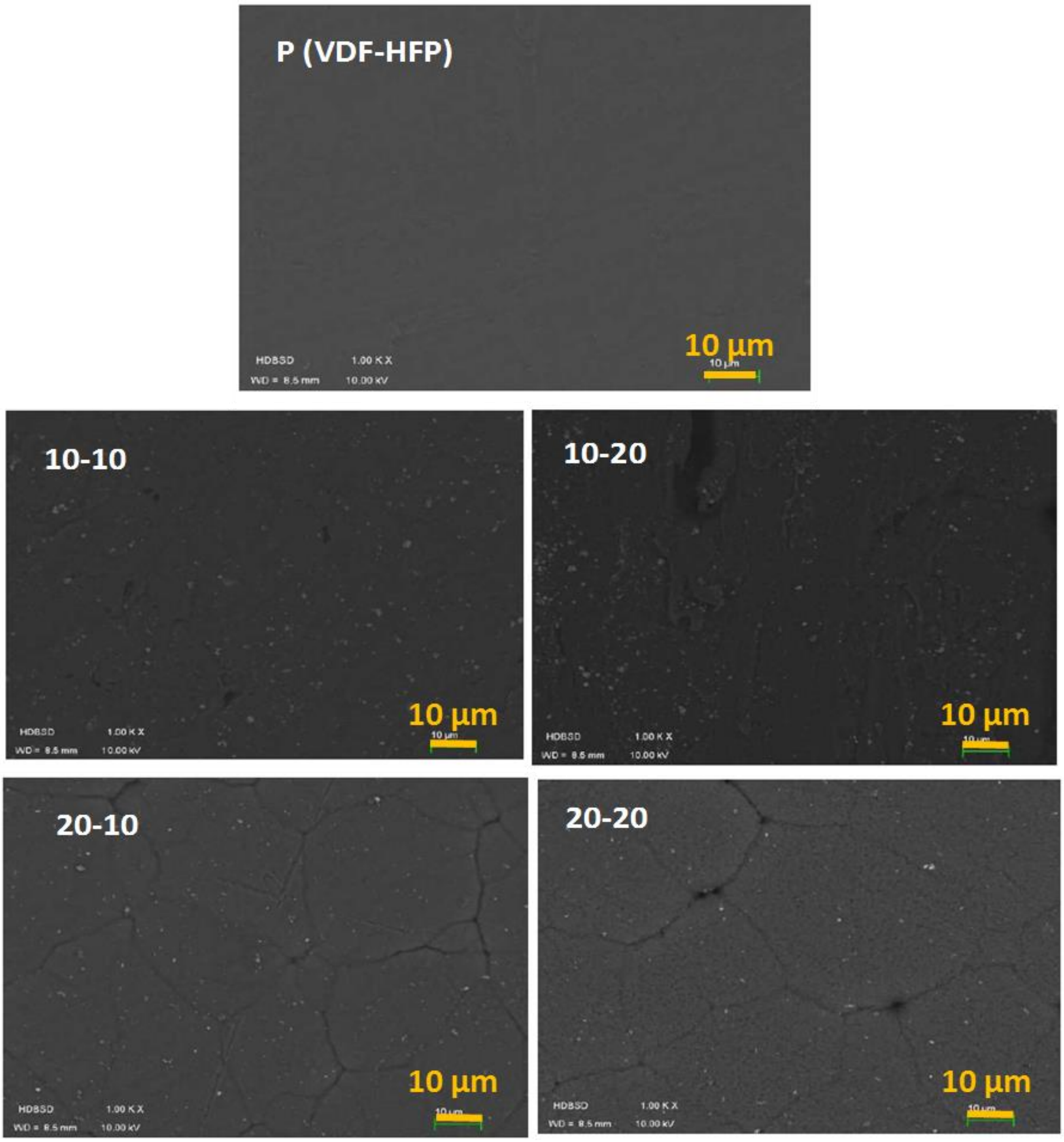

Figure 8. Microscopie électronique à balayage du copolymère poly(VDF-*co*-HFP) ainsi que des films nanocomposites PVDF-*g*-$BaTiO_3$/ poly(VDF-*co*-HFP) résultants.

Les mesures diélectriques effectués sur ces films ont révélé l'existence de trois relaxations (Figure 9) : α_a attribué à la transition vitreuse ; α_c liée à la fraction cristalline dans le copolymère tandis que la troisième a été assignée au processus de conductivité. De plus, l'analyse des spectres diélectrique a permis d'avoir une approximation des valeurs de la température de transition vitreuse (T_v) qui n'a pas pu été déterminé par DSC (comme il est souvent le cas pour le PVDF). La T_v du copolymère pur était de -42 °C et augmentait à -30 °C après l'introduction des nanocomposites PVDF-*g*-$BaTiO_3$, ce qui était envisageable.

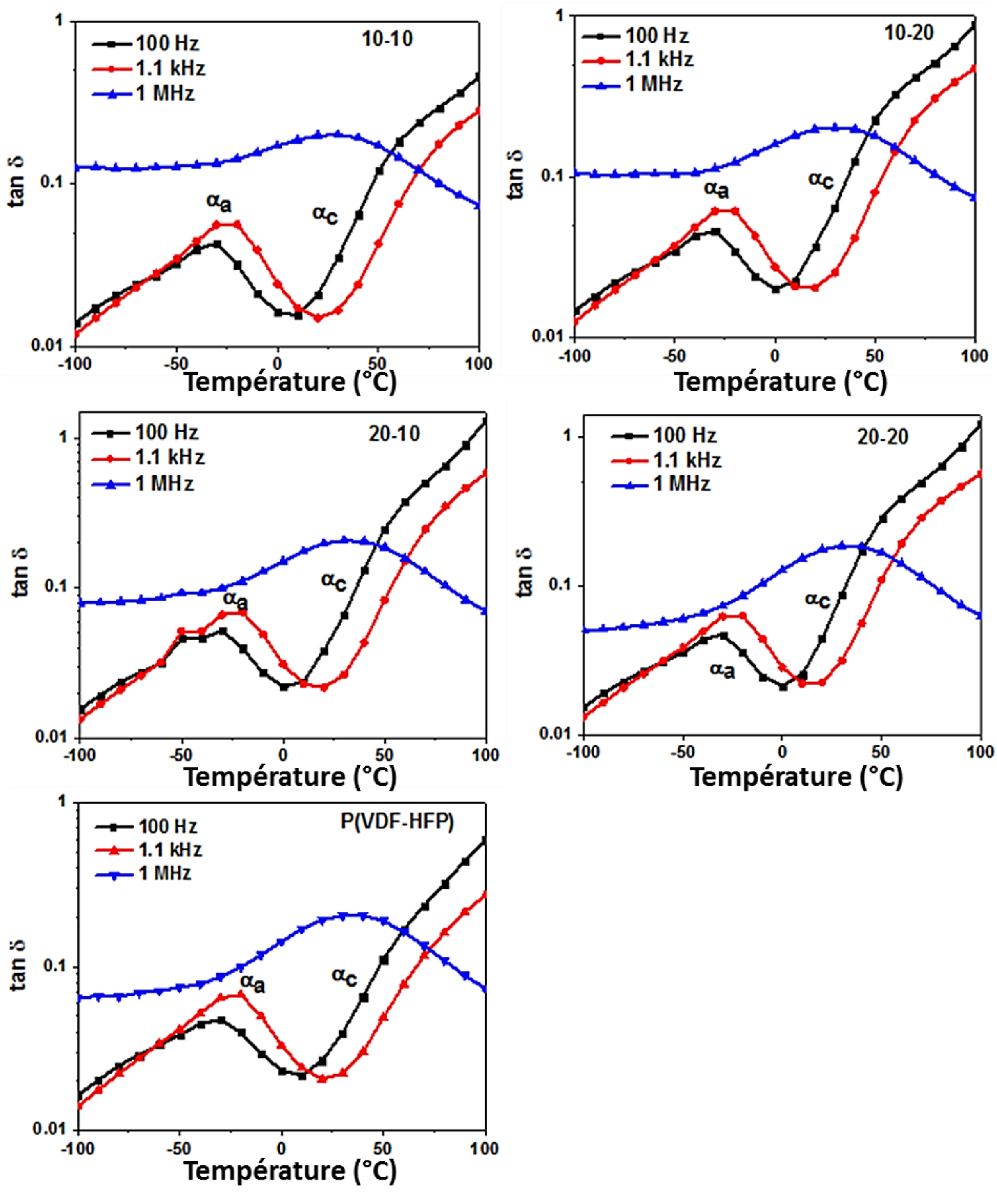

Figure 9. Evolutions de la tangente de perte en fonction de la température pour les différents films préparés à des fréquences différentes.

L'analyse mécanique a montré une amélioration du module de Young des films nanocomposites par rapport au copolymère vierge, et ceci résulte de la distribution uniforme des nanocomposites PVDF-*g*-BaTiO$_3$ présentant de fortes interactions avec la matrice copolymère poly (VDF-*co*-HFP).

5. Application des nanocomposites PVDF-*g*-BaTiO$_3$ comme matériaux liants dans les batteries Lithium-ion

Finalement, ces nanocomposites PVDF-*g*-BaTiO$_3$ ont aussi été testés comme liants pour préparer de nouveaux matériaux de cathode pour les batteries aux ions lithium. Premièrement, l'effet du PVDF modifié (c'est-à-dire PVDF-*g*-BaTiO$_3$) sur les performances électrochimiques a été étudié et les résultats ont montré que ce dernier n'entraine aucune activité électrochimique. Ensuite, des formulations à base de 70% en poids (70 wt%) de matériau actif (LiMn$_2$O$_4$), 18 wt% d'agent conducteur (noir de carbone) et 12 wt% de liant (PVDF commercial, PVDF modifié ou les deux) ont été réalisées. Quatre formulations ont été préparées en faisant varier la quantité de PVDF modifié de 0 à 4, 8 et 12 wt% de PVDF-*g*-BaTiO$_3$.

Afin d'obtenir des films homogènes et présenter une meilleure dispersion des nanoparticules, le calandrage des films a été utilisé. Cette technique a permis d'obtenir des films d'électrodes de structure uniforme, et cela a été bien mis en évidence dans les tests qui étaient reproductibles, effectués sur les différentes piles de la même formulation (Figure 10).

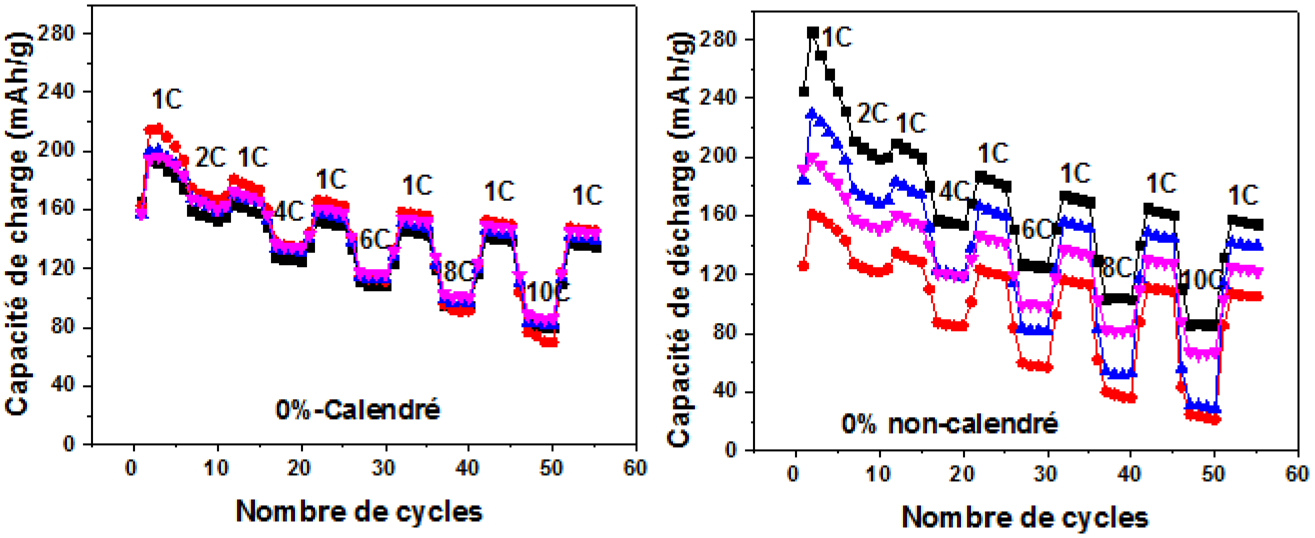

Figure 10. Capacités de charges et de décharge en fonction du nombre de cycle pour les formulations non-calandrées et calandrées préparées uniquement avec du PVDF commercial.

Outre la réduction de la densité volumétrique du film d'électrode, le calandrage a un effet sur d'autres propriétés physiques, et notamment favoriser les contacts entre les particules. Ainsi, l'amélioration observée dans les performances de cyclage après la procédure de calandrage pourrait s'expliquer par l'augmentation de la zone de contact ohmique à l'interface électrode-collecteur de courant.

De plus, Il a été constaté que les piles fabriquées avec 4 wt% de PVDF modifié présentaient des performances de cyclage similaires à celles réalisées uniquement avec du PVDF commercial (0 wt% de PVDF modifié), tandis que les échantillons avec 8 et 12 wt% étaient moins performant (Figure 11). Cela s'explique par la faible quantité ainsi que la faible masse molaire du PVDF présent dans les matériaux nanocomposites par rapport au PVDF commercial.

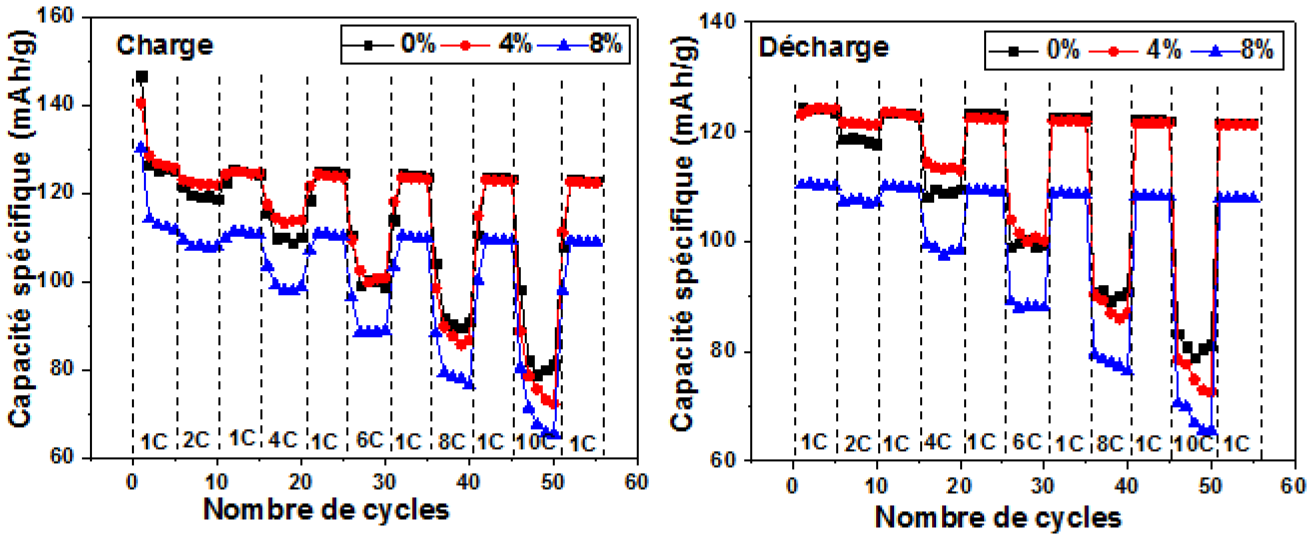

Figure 11. Capacités de charge et de décharge pour les films calandrés préparés avec 0, 4 et 8% de PVDF modifié.

6. Conclusion et perspectives

Au terme de ce travail, des nanocomposites à base de PVDF greffé sur des nanoparticules de $BaTiO_3$ ont été synthétisés par polymérisation RAFT du VDF. Le matériau préparé a été entièrement caractérisé démontrant ainsi le succès du greffage du PVDF. Les propriétés diélectriques des nanocomposites obtenus ont été étudiées. En vue d'améliorer davantage la permittivité diélectrique du nanocomposite obtenu, il serait préférable d'utiliser des charges céramiques ayant des morphologies unidimensionnelles sous formes de nano-fils ou nano-tiges par exemple. Lors de l'application d'un champ électrique, l'orientation des dipôles selon sa direction serait plus facile que dans le cas des nanoparticules sphériques, conduisant à une permittivité améliorée [9,49]. De plus, il serait souhaitable de favoriser la formation de la phase β du PVDF dans le nanocomposite soit par étirement soit en appliquant une haute tension sur le nanocomposite.

Dans notre étude, nous n'avons pas pu visualiser la relaxation attribuée à la température de transition vitreuse dans les nanocomposites PVDF-*g*-$BaTiO_3$ préparés, et ceci a été expliqué par la grande cristallinité du PVDF formé. Cependant, une étude plus approfondie peut être menée en utilisant l'analyse dilatométrique afin de vérifier la présence de la dite relaxation.

D'autres stratégies de préparation des matériaux nanocomposites à base de polymères fluorés peuvent être également utilisées (par exemple, « la click chemistry » et la polymérisation ATRP). De plus, il serait intéressant d'utiliser des agents de couplage fluorés pour modifier la surface de la charge afin d'améliorer l'interface entre la charge et la matrice polymère.

Finalement, afin d'améliorer l'utilisation de ces nanocomposites comme liants dans les batteries, il est nécessaire que le PVDF greffé sur les nanoparticules $BaTiO_3$ possède une masse molaire élevée, pour assurer une bonne adhésion des différentes particules sur le collecteur de courant.

7. Références

[1] Dang Z-M, Yuan J-K, Yao S-H, Liao R-J. Flexible Nanodielectric Materials with High Permittivity for Power Energy Storage. Adv Mater 2013;25:6334–65. doi:10.1002/adma.201301752.

[2] Fan Y, Huang X, Wang G, Jiang P. Core-Shell Structured Biopolymer@BaTiO3 Nanoparticles for Biopolymer Nanocomposites with Significantly Enhanced Dielectric Properties and Energy Storage Capability. J Phys Chem C 2015;119:27330–9. doi:10.1021/acs.jpcc.5b09619.

[3] Li Q, Han K, Gadinski MR, Zhang G, Wang Q. High Energy and Power Density Capacitors from Solution-Processed Ternary Ferroelectric Polymer Nanocomposites. Adv Mater 2014;26:6244–9. doi:10.1002/adma.201402106.

[4] Chen S, Lv X, Han X, Luo H, Bowen CR, Zhang D. Significantly improved energy density of BaTiO3 nanocomposites by accurate interfacial tailoring using a novel rigid-fluoro-polymer. Polym Chem 2018;9:548–57. doi:10.1039/C7PY01914A.

[5] Wang Q, Zhu L. Polymer nanocomposites for electrical energy storage. J Polym Sci Part B Polym Phys 2011;49:1421–9. doi:10.1002/polb.22337.

[6] Zhu L, Wang Q. Novel Ferroelectric Polymers for High Energy Density and Low Loss Dielectrics. Macromolecules 2012;45:2937–54. doi:10.1021/ma2024057.

[7] Chu B, Xin Z, Kailiang R, Bret N, Minren L, Qing W, et al. A Dielectric Polymer with High Electric Energy Density and Fast Discharge Speed. Science (80-) 2006;313:334–6.

doi:10.1126/science.1127798.

[8] Pan J, Li K, Li J, Hsu T, Wang Q. Dielectric characteristics of poly(ether ketone ketone) for high temperature capacitive energy storage. Appl Phys Lett 2009;95:22902. doi:10.1063/1.3176219.

[9] Guo N, DiBenedetto SA, Tewari P, Lanagan MT, Ratner MA, Marks TJ. Nanoparticle, Size, Shape, and Interfacial Effects on Leakage Current Density, Permittivity, and Breakdown Strength of Metal Oxide−Polyolefin Nanocomposites: Experiment and Theory. Chem Mater 2010;22:1567–78. doi:10.1021/cm902852h.

[10] Seo M, Hillmyer MA. Reticulated Nanoporous Polymers by Controlled Polymerization-Induced Microphase Separation. Science (80-) 2012;336:1422–5. doi:10.1126/science.1221383.

[11] Kim BP, Jones SC, Hotchkiss PJ, Haddock JN, Kippelen B, Marder SR, et al. Phosphonic Acid-Modified Barium Titanate Polymer Nanocomposites with High Permittivity and Dielectric Strength. Adv Mater 2007;19:1001–5. doi:10.1002/adma.200602422.

[12] Guo C, Fuji M. Effect of silicone coupling agent on dielectric properties of barium titanate/silicone elastomer composites. Adv Powder Technol 2016;27:1162–72. doi:10.1016/J.APT.2016.03.028.

[13] Zhang X, Ma Y, Zhao C, Yang W. High dielectric constant and low dielectric loss hybrid nanocomposites fabricated with ferroelectric polymer matrix and BaTiO3 nanofibers modified with perfluoroalkylsilane. Appl Surf Sci 2014;305:531–8. doi:10.1016/J.APSUSC.2014.03.131.

[14] Toor A, So H, Pisano AP. Improved Dielectric Properties of Polyvinylidene Fluoride Nanocomposite Embedded with Poly(vinylpyrrolidone)-Coated Gold Nanoparticles. ACS Appl Mater Interfaces 2017;9:6369–75. doi:10.1021/acsami.6b13900.

[15] Song Y, Shen Y, Liu H, Lin Y, Li M, Nan C-W. Improving the dielectric constants and breakdown strength of polymer composites: effects of the shape of the BaTiO3 nanoinclusions, surface modification and polymer matrix. J Mater Chem 2012;22:16491. doi:10.1039/c2jm32579a.

[16] Tang H, Lin Y, Sodano HA. Synthesis of High Aspect Ratio BaTiO3 Nanowires for High Energy Density Nanocomposite Capacitors. Adv Energy Mater 2013;3:451–6. doi:10.1002/aenm.201200808.

[17] Zhu L. Exploring Strategies for High Dielectric Constant and Low Loss Polymer Dielectrics. J Phys Chem Lett 2014;5:3677–87. doi:10.1021/jz501831q.

[18] Subodh G, Deepu V, Mohanan P, Sebastian MT. Dielectric response of high permittivity polymer ceramic composite with low loss tangent. Appl Phys Lett 2009;95:62903. doi:10.1063/1.3200244.

[19] Liu S, Xue S, Zhang W, Zhai J. Enhanced dielectric and energy storage density induced by surface-modified BaTiO3 nanofibers in poly(vinylidene fluoride) nanocomposites. Ceram Int 2014;40:15633–40. doi:10.1016/J.CERAMINT.2014.07.083.

[20] Gao L, He J, Hu J, Li Y. Large Enhancement in Polarization Response and Energy Storage Properties of Poly(vinylidene fluoride) by Improving the Interface Effect in Nanocomposites. J Phys Chem C 2014;118:831–8. doi:10.1021/jp409474k.

[21] Zhou T, Zha J-W, Cui R-Y, Fan B-H, Yuan J-K, Dang Z-M. Improving Dielectric Properties of BaTiO3/Ferroelectric Polymer Composites by Employing Surface Hydroxylated BaTiO3 Nanoparticles. ACS Appl Mater Interfaces 2011;3:2184–8. doi:10.1021/am200492q.

[22] Yu K, Niu Y, Xiang F, Zhou Y, Bai Y, Wang H. Enhanced electric breakdown strength and high energy density of barium titanate filled polymer nanocomposites. J Appl Phys 2013;114:174107. doi:10.1063/1.4829671.

[23] Prateek, Thakur VK, Gupta RK. Recent Progress on Ferroelectric Polymer-Based Nanocomposites for High Energy Density Capacitors: Synthesis, Dielectric Properties, and Future Aspects. Chem Rev 2016;116:4260–317. doi:10.1021/acs.chemrev.5b00495.

[24] Li JY, Zhang L, Ducharme S. Electric energy density of dielectric nanocomposites. Appl Phys Lett 2007;90:132901. doi:10.1063/1.2716847.

[25] Yu K, Niu Y, Xiang F, Zhou Y, Bai Y, Wang H. Enhanced electric breakdown strength and high energy density of barium titanate filled polymer nanocomposites. J Appl Phys 2013;114:174107. doi:10.1063/1.4829671.

[26] Zhang X, Zhao S, Wang F, Ma Y, Wang L, Chen D, et al. Improving dielectric properties of BaTiO3/poly(vinylidene fluoride) composites by employing core-shell structured BaTiO3@Poly(methylmethacrylate) and BaTiO3@Poly(trifluoroethyl methacrylate) nanoparticles. Appl Surf Sci 2017;403:71–9. doi:10.1016/j.apsusc.2017.01.121.

[27] Zhang X, Chen H, Ma Y, Zhao C, Yang W. Preparation and dielectric properties of core–shell structural composites of poly(1H,1H,2H,2H-perfluorooctyl methacrylate)@BaTiO3 nanoparticles. Appl Surf Sci 2013;277:121–7. doi:10.1016/J.APSUSC.2013.03.178.

[28] Yang K, Huang X, Huang Y, Xie L, Jiang P. Fluoro-Polymer@BaTiO3 Hybrid Nanoparticles Prepared via RAFT Polymerization: Toward Ferroelectric Polymer Nanocomposites with High Dielectric Constant and Low Dielectric Loss for Energy Storage Application. Chem Mater 2013;25:2327–38. doi:10.1021/cm4010486.

[29] Huang X, Jiang P. Core-Shell Structured High-k Polymer Nanocomposites for Energy Storage and Dielectric Applications. Adv Mater 2015;27:546–54. doi:10.1002/adma.201401310.

[30] Ejaz M, Puli VS, Elupula R, Adireddy S, Riggs BC, Chrisey DB, et al. Core-Shell Structured Poly (glycidyl methacrylate)/ BaTiO 3 Nanocomposites Prepared by Surface-Initiated Atom Transfer Radical Polymerization : A Novel Material for High Energy Density Dielectric Storage 2015:719–28. doi:10.1002/pola.27485.

[31] Zhu M, Huang X, Yang K, Zhai X, Zhang J, He J, et al. Energy Storage in Ferroelectric Polymer Nanocomposites Filled with Core–Shell Structured Polymer@BaTiO3 Nanoparticles: Understanding the Role of Polymer Shells in the Interfacial Regions. ACS Appl Mater Interfaces 2014;6:19644–54. doi:10.1021/am504428u.

[32] Yang K, Huang X, Xie L, Wu C, Jiang P, Tanaka T. Core-shell structured polystyrene/BaTiO3 hybrid nanodielectrics prepared by in situ RAFT polymerization: A route to high dielectric constant and low loss materials with weak frequency dependence. Macromol Rapid Commun 2012;33:1921–6. doi:10.1002/marc.201200361.

[33] Huang X, Xie L, Yang K, Wu C, Jiang P, Li S, et al. Role of interface in highly filled epoxy/BaTiO3 nanocomposites. Part II-effect of nanoparticle surface chemistry on

processing, thermal expansion, energy storage and breakdown strength of the nanocomposites. IEEE Trans Dielectr Electr Insul 2014;21:480–7. doi:10.1109/TDEI.2013.004166.

[34] Kostov G, Boschet F, Buller J, Badache L, Brandsadter S, Ameduri B. First Amphiphilic Poly(vinylidene fluoride-co-3,3,3-trifluoropropene)-b-oligo(vinyl alcohol) Block Copolymers as Potential Nonpersistent Fluorosurfactants from Radical Polymerization Controlled by Xanthate. Macromolecules 2011;44:1841–55. doi:10.1021/ma102679f.

[35] Girard E, Marty J-D, Ameduri B, Destarac M. Direct Synthesis of Vinylidene Fluoride-Based Amphiphilic Diblock Copolymers by RAFT/MADIX Polymerization. ACS Macro Lett 2012;1:270–4. doi:10.1021/mz2001143.

[36] Banerjee S, Patil Y, Gimello O, Ameduri B. Well-defined multiblock poly(vinylidene fluoride) and block copolymers thereof: a missing piece of the architecture puzzle. Chem Commun 2017;53:10910–3. doi:10.1039/C7CC06122F.

[37] Ejaz M, Puli VS, Elupula R, Adireddy S, Riggs BC, Chrisey DB, et al. Core-shell structured poly(glycidyl methacrylate)/BaTiO3 nanocomposites prepared by surface-initiated atom transfer radical polymerization: A novel material for high energy density dielectric storage. J Polym Sci Part A Polym Chem 2015;53:719–28. doi:10.1002/pola.27485.

[38] Patil Y, Ameduri B. First RAFT/MADIX radical copolymerization of tert-butyl 2-trifluoromethacrylate with vinylidene fluoride controlled by xanthate. Polym Chem 2013;4:2783. doi:10.1039/c3py21139h.

[39] Guerre M, Campagne B, Gimello O, Parra K, Ameduri B, Ladmiral V. Deeper Insight into the MADIX Polymerization of Vinylidene Fluoride. Macromolecules 2015;48:7810–22. doi:10.1021/acs.macromol.5b01528.

[40] Asandei AD, Adebolu OI, Simpson CP. Mild-Temperature Mn (CO)10 - Photomediated Controlled Radical Polymerization of Vinylidene Fluoride and Synthesis of Well-Defined Poly(vinylidene fluoride) Block Copolymers. J Am Chem Soc 2012;134:6080–3. doi:10.1021/ja300178r.

[41] Mittal V. Characterization Techniques for Polymer Nanocomposites. Wiley-VCH; 2012. doi:10.1002/9783527654505.

[42] Chanmal C V., Jog JP. Dielectric relaxations in PVDF/BaTiO3 nanocomposites. eXPRESS Polym Lett 2008;2:294–301. doi:10.3144/expresspolymlett.2008.35.

[43] Tsangaris GM, Kouloumbi N, Kyvelidis S. Interfacial relaxation phenomena in particulate composites of epoxy resin with copper or iron particles. Mater Chem Phys 1996;44:245–50. doi:10.1016/0254-0584(96)80063-0.

[44] Psarras G., Manolakaki E, Tsangaris G. Electrical relaxations in polymeric particulate composites of epoxy resin and metal particles. Compos Part A Appl Sci Manuf 2002;33:375–84. doi:10.1016/S1359-835X(01)00117-8.

[45] Patsidis AC, Psarras G. Dielectric behaviour and functionality of polymer matrix-ceramic BaTiO3 composites. Polym Lett 2008;2:718–26. doi:10.3144/expresspolymlett.2008.85.

[46] TSANGARIS GM, PSARRAS GC, KOULOUMB N. Electric modulus and interfacial polarization in composite polymeric systems. J Mater Sci 1998;33:2027–37.

doi:10.1023/A:1004398514901.

[47] Feng Y, Li WL, Hou YF, Yu Y, Cao WP, Zhang TD, et al. Enhanced dielectric properties of PVDF-HFP/ BaTiO 3-nanowire composites induced by interfacial polarization and wire-shape 2015. doi:10.1039/c4tc02183e.

[48] Zhou W, Dong L, Sui X, Wang Z, Zuo J, Cai H, et al. High dielectric permittivity and low loss in PVDF filled by core-shell Zn@ZnO particles. J Polym Res 2016;23:45. doi:10.1007/s10965-016-0941-5.

[49] Song Y, Shen Y, Liu H, Lin Y, Li M, Nan C-W. Improving the dielectric constants and breakdown strength of polymer composites: effects of the shape of the BaTiO3 nanoinclusions, surface modification and polymer matrix. J Mater Chem 2012;22:16491. doi:10.1039/c2jm32579a.